Copyright

by

Paul Robert Abel

2014

The Dissertation Committee for Paul Robert Abel Certifies that this is the approved version of the following dissertation:

Chemical Modification of Nanocolumnar Semiconductor Electrodes for Enhanced Performance as Lithium and Sodium-Ion Battery Anode Materials

Committee:

C. Buddie Mullins Supervisor

Adam Heller

Brian Korgel

Arumugam Manthiram

Keith Stevenson

Chemical Modification of Nanocolumnar Semiconductor Electrodes for Enhanced Performance as Lithium and Sodium-Ion Battery Anode Materials

by

Paul Robert Abel, B.S. Ch. E.

Dissertation

Presented to the Faculty of the Graduate School of

The University of Texas at Austin

in Partial Fulfillment

of the Requirements

for the Degree of

Doctor of Philosophy

The University of Texas at Austin

August 2014

Dedication

To my parents

for planting the seed of lifelong learning.

Acknowledgements

The work presented in this dissertation would not have been possible without the help and support of many people. First, I would like to acknowledge my advisor Prof. C. Buddie Mullins for his guidance and direction in both my personal and professional development during graduate school. I would also like to thank Prof. Adam Heller for the wisdom and insight that he imparted on me during our years of close collaboration.

I am also grateful for the tireless work of the departmental support staff. Without their efforts, my research would have come to a screeching halt on many occasions. I would especially like to thank Butch Cunningham for the countless parts that he machined for me over the years, Eddie Ibarra for his help purchasing all the large and small lab equipment and supplies, Jim Smitherman for his help keeping the labs in good working order, Mike Ronalter for his services in the glass shop, Kevin Haynes for keeping us stocked with all the necessary compressed gases, and Randy Rife for keeping our computers backed up and operating smoothly.

I'd like to thank all the people who manage the user facilities. Having well-maintained equipment available for my research was invaluable to my success. I'd especially like to thank Dr. Hugo Celio who continuously improved the x-ray photoelectron spectrometer over the years and whose vacuum transfer capsule made several of my studies possible.

I would also like to acknowledge the many friends and colleagues that I've had the pleasure of working with in my studies: Dr. Yong-Mao Lin, Dr. Sean Berglund, Dr. Tyler Elko-Hansen, Dr. Vince Holmberg, Kyle Klavetter, Alex Rettie, and the many others past and present members of the Mullins' group.

I owe a huge debt of gratitude to my family for their love and support through my time in graduate school. My parents, Connie and Clayton, and my wife Chia never doubted me even when I doubted myself.

And for financial support, I would like to thank the Fannie and John Hertz Foundation for a graduate fellowship. I would also like to thank the University of Texas at Austin Cockrell School of Engineering for the Thrust 2000 - Harry P. Whitworth Endowed Graduate Fellowship in Engineering.

Chemical Modification of Nanocolumnar Semiconductor Electrodes for Enhanced Performance as Lithium and Sodium-Ion Battery Anode Materials

Paul Robert Abel, Ph.D.

The University of Texas at Austin, 2014

Supervisor: C. Buddie Mullins

The successful commercialization of lithium-ion batteries is responsible for the ubiquity of personal electronics. The continued development of battery technology, as well as its application to new emerging markets such as electric vehicles, is dependent on developing safer, higher energy density, and cheaper electrode materials and battery chemistries. The focus of this dissertation is on identifying, characterizing and optimizing new materials for lithium- and sodium-ion batteries.

Batteries are incredibly complex engineered systems with each electrode composed of conductive additive and polymeric binder in addition to the active material. All of these components must work together for the electrode system to function properly. In this work, glancing angle deposition (GLAD) and reactive ballistic deposition (RBD) are employed to grow thin films of novel materials with reproducible morphology for use as battery electrodes. The use of these thin film electrodes eliminated

the need for conductive additives and polymer binders allowing for the active materials themselves to be studied rather than the whole electrode system.

Two techniques are employed to modify the chemical properties of the electrode materials grown by RBD and GLAD: Alloying (Si-Ge alloys for Li-ion batteries and Sn-Ge alloys for Na-ion batteries) and partial chalcogenation (partial oxidation of silicon, and partial sulfidation and selenidation of germanium for Li-ion batteries). Both of these techniques are successfully employed to enhance the electrochemical properties of the materials presented in this dissertation.

Table of Contents

List of Tables

List of Figures

Chapter 1: Introduction

THE NEED FOR ENERGY STORAGE

Electrical energy storage is an enabling technology. The successful commercialization of the lithium-ion (Li-ion) battery is responsible for the ubiquity of personal electronics. Li-ion batteries are the current gold standard in electrochemical energy storage based on their high gravimetric and volumetric energy densities. A comparison of the energy densities of several battery chemistries is shown in Figure 1.1. Consumer demand for smaller, lighter and longer-lasting devices is driving the development of battery technology; however improvements in electrochemical energy storage have not kept pace with Moore's Law – the doubling of transistors in integrated circuits every 18 months. While growth in computational power has been exponential, increases in the energy density of Li-ion batteries has been much more modest over the 23 years since their commercialization. The basic chemistry of the Li-ion battery has remained essentially unchanged since its introduction in 1991 and provides a fundamental limitation of the energy density of the batteries. Current Li-ion chemistries are nearing their theoretical limit.[1]

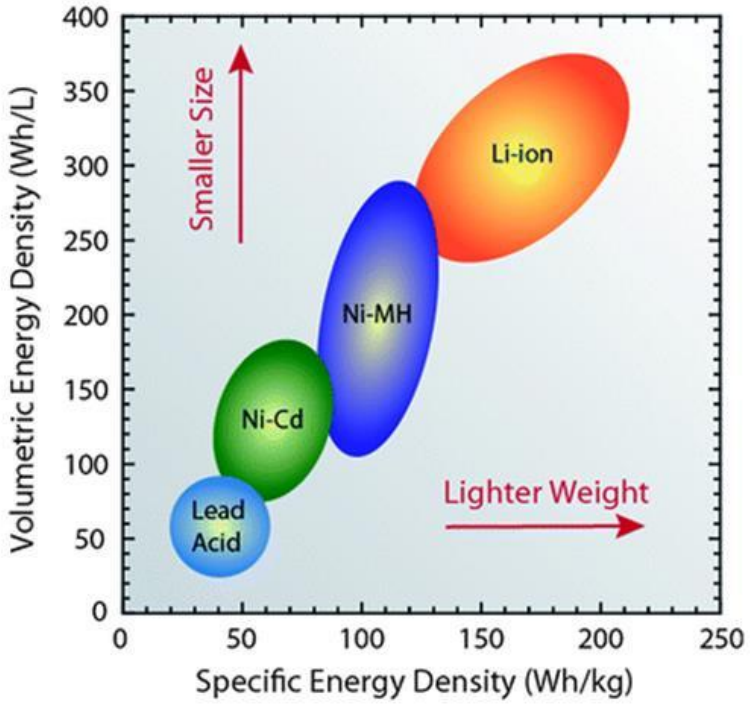

Figure 1.1. The energy density of several battery chemistries on both a gravimetric and volumetric basis.[2]

A new emerging market for Li-ion batteries is electric vehicles (EV). Well-to-wheel analysis indicates that electric vehicles are significantly more efficient than those powered by gasoline.[3] This efficiency advantage, as well as consolidating distributed tailpipe emissions to a single power plant – allowing for economies of scale for pollution control – makes EVs attractive for environmental reasons. However, the cost of Li-ion batteries and concerns over the safety of the necessarily large battery packs make it difficult for EVs to compete directly with gasoline powered vehicles. The continued development of battery technology, as well as its application to new emerging markets

such as EV's, is dependent on identifying safer, higher energy density, and cheaper electrode materials and battery chemistries.

INTRODUCTION TO ALKALI-ION BATTERIES

Lithium-Ion Batteries

Lithium is an attractive material for batteries because it has a very negative reduction potential (-3.04V vs. SHE) and lithium metal has a very low density (0.534 g cm^{-3}). While these characteristics have allowed for the development of high energy density primary battery chemistries such as Li-MnO_2 and Li-FeS_2, lithium metal was found to be unsuitable for use as an anode in secondary batteries because dendrite formation on recharge posed a significant safety hazard. In 1983, Yazami and Touzain showed that lithium-graphite intercalation compounds could be formed electrochemically and could be used as a battery electrode.[4] This provided a suitable anode material to be paired with any one of several lithium insertion cathodes which had been previously identified. Commercial Li-ion batteries use a graphite anode and a $LiCoO_2$[5] or $LiFePO_4$[6] cathode as lithium insertion hosts. A lithium salt, typically $LiPF_6$, dissolved in organic carbonates is used as the electrolyte. A diagram of such a battery is shown in Figure 1.2.

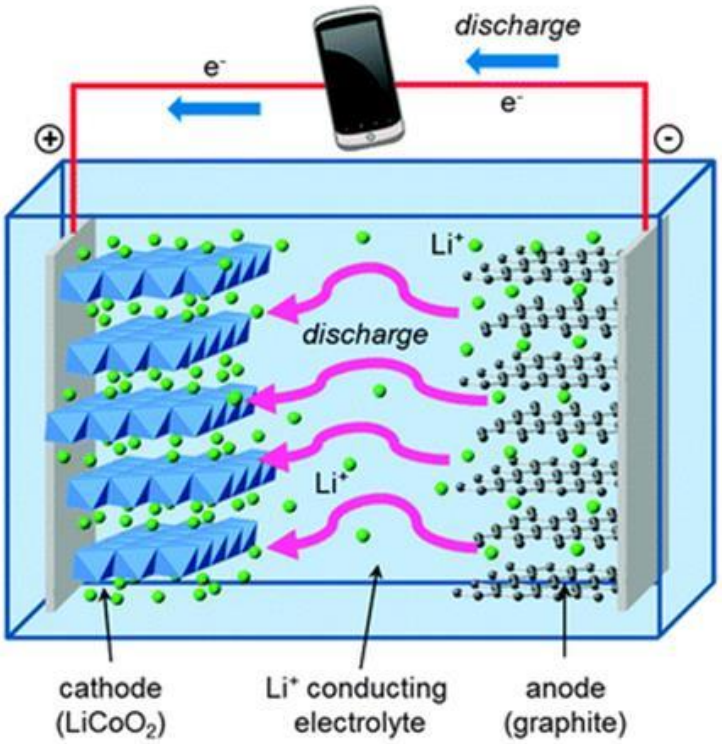

Figure 1.2. Schematic diagram of a Li-ion battery utilizing graphite as the anode material and LiCoO2 as the cathode material.[7]

The electrode reactions that occur during discharge of the battery can be written as follows:

Anode: $Li_xC_6 \rightarrow C_6 + x\ Li^+ + x\ e^-$ (1.1)

Cathode: $Li_{1-x}CoO_2 + x\ Li^+ + x\ e^- \rightarrow LiCoO_2$ (1.2)

As the reaction progresses, lithium ions diffuse from anode to cathode through the electrolyte while the electrons pass through the external circuit where they are free to do work. When an external voltage is applied, lithium ions are removed from the cathode and inserted back into the anode, thus recharging the cell.

An energy diagram of a lithium ion battery is shown in Figure 1.3. The open circuit potential of the cell is determined by the difference in electrochemical potential between the cathode (μ_C) and the anode (μ_A). Given that the stored energy in a cell is the product of the total stored charge (cell capacity) and the average cell voltage, having a high μ_A (low voltage) is advantageous for high energy density cells. μ_A is bounded by the Li/Li^+ reduction potential, which is the point where electrodeposition of lithium on the surface of the electrode becomes thermodynamically favorable. One criterion for stable operation of a battery is that the μ_A must lie below the lowest unoccupied molecular orbital (LUMO) of the electrolyte to prevent reduction of the electrolyte species on the anode surface. Conversely μ_C must lie above the highest occupied molecular orbital (HOMO) of the electrode to prevent electrolyte oxidation on the cathode surface. The energy gap between the HOMO and LUMO define the electrochemical stability window of the electrolyte.

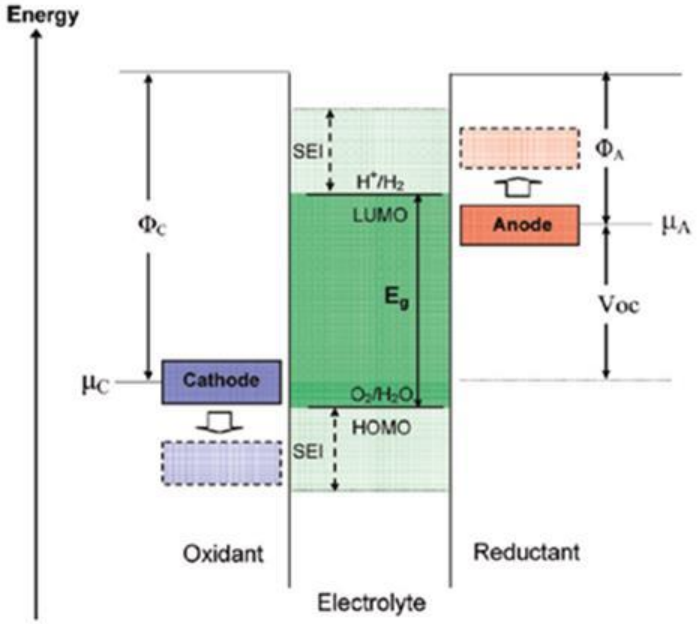

Figure 1.3. Schematic energy diagram of a lithium ion battery.[8]

Typical Li-ion battery electrolyte solvents undergo reduction at potentials around 1.5 V vs Li/Li+ (1.36 V for ethylene carbonate, 1.32V for diethyl carbonate and dimethyl carbonate, and 1.6 V for propylene carbonate).[9] Currently used cathode materials will not oxidize the electrolyte, but lithiated graphite, having a potential of ~100 mV, will spontaneously reduce electrolyte with which it comes in contact. This process, however is self-limiting, with the reduction products forming an ion conducting but electrically insulating solid electrolyte interphase (SEI) layer on the electrode surface. The stability of the SEI layer is critical to the stable operation of Li-ion batteries, and electrolyte solvents are often chosen in order to improve the quality of the SEI layer for more stable cell operation.[10-15]

Li-ion batteries have been extremely successful commercially, yet they still have many shortcomings that are the subject of current research. Safety is always critical for consumer products but the thermodynamics and kinetics of the graphite anode have led to serious safety problems. The potential of the graphite anode is close to the Li/Li^+ reduction potential and lithium intercalation into graphite can be kinetically limited, so the overpotentials required to charge a Li-ion battery at high rates can lead to electrodeposition of metallic lithium. This leads to dendrite formation which can cause internal shorting of the cell and thermal runaway.[16-18] Additionally, high rates of charging can lead to exfoliation of the SEI layer on graphite.[19] For these reasons, new anode materials are sought.

Preventing lithium electrodeposition on the anode can be accomplished by either increasing the voltage of the electrode, or improving the rate of lithium transport in the electrode material. While increasing the voltage of the electrode can significantly improve safety, it decreases the energy density of the cell. This can be offset by increasing the specific capacity of the electrode material. However, as the anode capacity is increased, the total cell capacity approaches an asymptotic limit for a given cathode material. The total cell capacity as a function of anode capacity for two cathode capacities is shown in Figure 1.4.[20] In both cases, there are diminishing returns for anode capacities above approximately 1000 mAh/g.

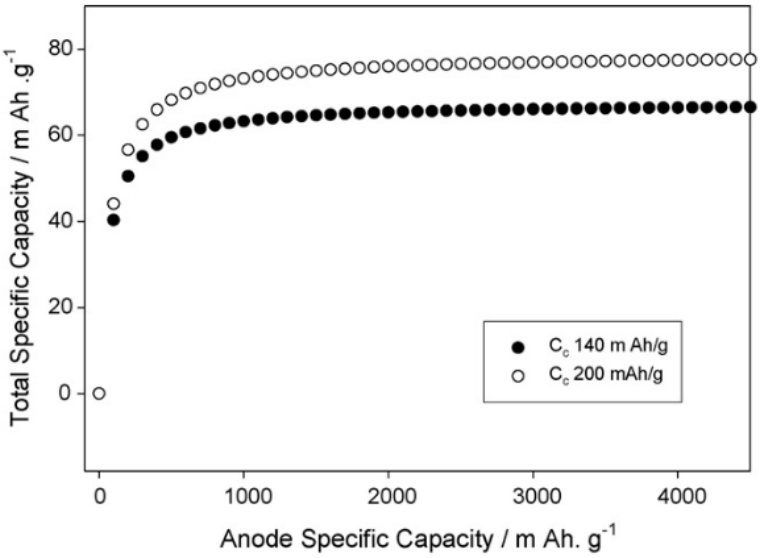

Figure 1.4. Total cell capacity as a function of anode capacity for two cathode capacities.[20]

The specific capacity and lithium reduction potential of many candidate anode materials including composites,[21-23] transition-metal oxides[24-27] and nitrides[28-29] are shown in Figure 1.5.[30] Lithium alloys have also attracted significant attention because of their large specific capacities. Silicon,[15, 31-33] germanium,[14, 34-36] and tin[37-39] will all form binary alloy with lithium up to terminal composition of $Li_{15}M_4$ (M = Si, Ge) or $Li_{22}Sn_5$. The large lithium storage capacity (3579 mAh/g for Si, 1384 mAh/g for Ge and 996 mAh/g for Sn) is accompanied by large volumetric expansion which can lead to pulverization of the active material and rapid degradation of the electrode.[20] Nanostructures, which are much more effective than bulk materials at accommodating large strains,[40] have been successfully applied to these materials to help stabilize their performance. The capacities

of Si and Ge, however, are much higher than the 1000 mAh/g figure necessary to effectively maximize cell capacity, so methods which sacrifice specific capacity in order to enhance other attributes of the electrode can be pursued without detriment to total capacity. The work in this dissertation explores chemical modification of these alloy type electrodes, specifically partial chalcogenation and ternary alloy formation, in order to enhance aspects of their electrochemical performance such as stability, high-rate capability, and electrode potential.

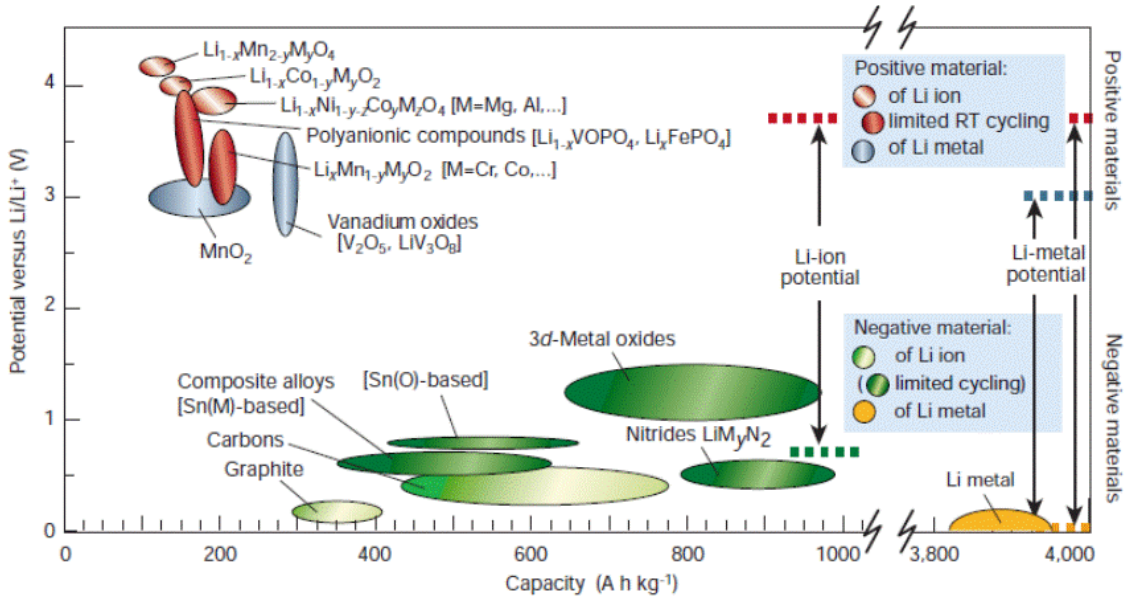

Figure 1.5 Potential and Capacity of candidate anode and cathode materials for lithium-ion batteries.[30]

The materials in this work necessarily react with lithium at potentials above the reduction potential of lithium, so they will function as a cathode, thermodynamically

speaking, when tested against a lithium foil counter electrode. The lithium redox potential of these materials is, however, suitable for use as an anode when paired with a traditional Li-ion battery cathode material. For clarity, the materials in this dissertation will only be referred to as anode materials throughout the work.

Sodium-Ion Batteries

The high cost of Li-ion batteries and the cost targets for energy storage have renewed interest in alternative battery chemistries. The abundance of proven sodium reserves has made it an attractive candidate as a charge carrier.[41] The operation of Na-ion batteries is expected to be analogous to that of Li-ion chemistries with Na^+ ions shuttled back and forth between an insertion anode and an insertion cathode. The Na/Na^+ redox couple is only ~300mV positive of Li/Li^+, so only a small fraction of the open circuit potential is sacrificed when switching from lithium to sodium chemistries. Sodium secondary battery chemistries have previously been developed for low-cost electrical energy storage,[42-43] however they operate at high temperatures making them impractical for portable and on-demand applications. The recent development of sodium insertion cathodes has increased interest in developing a room temperature sodium-ion (Na-ion) battery.[44-46] Sodium, unlike lithium, will not intercalate into graphite,[47] so alternative materials are sought. As with lithium, sodium will alloy with elements such as Ge,[48-49] Sn,[50-51] Sb,[52] and Pb.[53] This dissertation explores germanium and tin-germanium alloys as possible anode materials for Na-ion batteries.

DISSERTATION OVERVIEW

This dissertation contains eight chapters. Chapter 1 provides an introduction to subject of alkali-ion (specifically lithium- and sodium-ion) batteries. It covers the basic chemistry and physics that govern the inner workings of lithium and sodium secondary batteries and outlines the limitations that must be overcome in order to engineer better batteries. Chapters 2 through 7 each consist of a study, either published in, submitted to, or in preparation for submission to a peer-reviewed journal. Each study is aimed at improving one or more of the limitations of an individual anode chemistry. Anode materials for Li-ion batteries are the subject of Chapters 2 through 5, whereas anode materials for Na-ion batteries are the subject of Chapters 6 and 7. Chapter 8 contains conclusions based on the work in this dissertation and recommendations on directions for future research.

In Chapter 2, the performance of silicon and partially oxidized silicon thin films with nanocolumnar morphology, synthesized by evaporative deposition at a glancing angle, was evaluated as Li-ion battery anode materials. The incorporated oxygen concentration was controlled by varying the partial pressure of water during the deposition and monitored by quartz crystal microbalance, x-ray photoelectron spectroscopy, and electrochemical methods. In addition to bulk oxygen content, surface oxidation and annealing at low temperature affected the cycling stability and lithium storage capacity of the films. By optimizing all three to maximize cycle life, a material with a lithium storage capacity of ~2200 mAh/g was synthesized. Coin cells with anodes of the optimized material were reversibly cycled for ~120 cycles with virtually no

capacity fade. Subsequent cycling resulted in a loss of ~0.15% per cycle. After 300 cycles, 80% of the initial reversible capacity was retained. The work has been previously published in *ACS Nano*.[23]

Chapter 3 deals with silicon-germanium alloys for lithium-ion batteries. Both silicon and germanium are candidates to replace the carbon anode of lithium ions batteries. Silicon is attractive because of its high lithium storage capacity while germanium, a superior electronic and ionic conductor, can support much higher charge/discharge rates. Here we investigate the electronic, electrochemical and optical properties of $Si_{(1-x)}Ge_x$ thin films with x = 0, 0.25, 0.5, 0.75 and 1. Glancing angle deposition provided amorphous films of reproducible nanostructure and porosity. The film's composition and physical properties were investigated by x-ray photoelectron spectroscopy, four-point probe conductivity, Raman, and UV-Vis absorption spectroscopy. The films were assembled into coin cells to test their electrochemical properties as a lithium-ion battery anode material. The cells were cycled at various C-rates to determine the upper limits for high rate performance. Adjusting the composition in the $Si_{(1-x)}Ge_x$ system demonstrates a tradeoff between rate capability and specific capacity. We show that high-capacity silicon anodes and high-rate germanium anodes are merely the two extremes; the composition of $Si_{(1-x)}Ge_x$ alloys provides a new parameter to use in electrode optimization. This work has been previously published in *ACS Nano.*[24]

The synthesis, characterization and electrochemical performance of germanium sub-selenide, an anode material capable of supporting high charge/discharge rates, is reported in Chapter 4. The time it takes a user of a lithium ion battery powered device to

re-charge the battery is determined by the rate of charging of the anode. For safety, lithium ion batteries are charged at rates that do not exceed the rate of transport of lithium into their lithium alloying or intercalating anode material. Most batteries are charged at rates of 1 C or less, i.e., it takes an hour or longer to fully lithiate their anode. When charged at a higher rate, their coulombic efficiency drops and, more importantly, electrodeposition of metallic lithium dendrites increase the risk of fire. In today's science and engineering of advanced anode materials of high coulombic capacity, i.e., greater than 1 Ahr g^{-1}, charging and discharging at a 10 C rate with a loss of about $2/3^{rd}$ of the coulombic capacity is considered to be a significant development. Here we report that an amorphous nanocolumnar germanium sub-selenide $Ge_{0.9}Se_{0.1}$, provides 1.2 Ahr g^{-1} coulombic capacity and retains 70% of its capacity when charged at a 50 C rate, and 40 % of its capacity when charged at a 100 C rate, i.e., when it is lithiated in 36 seconds. After 1000 cycles at a 50 C rate the material retains approximately 70% of its maximum observed capacity. Its rate of discharge is even faster: when discharged at a rate of 1100 C, (delithiation in 3.3 seconds) 75 % of the coulombic capacity is retained. At this rate the specific current is 1.34 kA g^{-1} (kiloampere per gram); at a rate of 1800 C the material retains 36 % of its 1.2 Ahr g^{-1} capacity. This work has been accepted for publication in the *Journal of Physical Chemistry C.*[56]

Chapter 5 builds on the work presented in chapter 4, showing that sub-stoichiometric germanium sulfide also exhibits the favorable high-rate performance of sub-stoichiometric germanium selenide. Sulfur, has a lower atomic mass than selenium, so an equivalent mole fractions of sulfur is a lower mass fraction of sulfur. This increases

the gravimetric specific capacity of sulfur-containing films compared to selenium-containing films. We report that amorphous, nanocolumnar $Ge_{0.95}S_{0.05}$ has a reversible capacity of 1200 mAh/g and retains ~85% of this capacity when cycled at 20C, or 3 minutes per charge or discharge half-cycle. The material is also stable at high rates, retaining 88% of its initial 20C capacity after 500 cycles at that rate. TEM imaging indicates that the sulfur phase segregates on the first cycle to form poorly crystallized, nanoscale Li_2S inclusions. We postulate that these inclusions are responsible for the high-rate performance as diffusion along grain or phase boundaries is substantially faster than through bulk materials. A manuscript detailing this study is in preparation.

Chapter 6 details nanocolumnar and dense germanium thin films, synthesized by evaporative deposition, tested as a potential anode material for sodium-ion batteries. The reversible capacity of the nanocolumnar films was found to be 430 mAh/g, which is higher than the theoretical capacity of 369 mAh/g. The nanocolumnar films retained 88% of their initial capacity after 100 cycles at C/5, whereas the dense films began to deteriorate after ~15 cycles. Additionally, the nanocolumnar films were stable at charge/discharge rates up to 27C (10 A/g). The diffusion coefficient for sodium in germanium was estimated, from impedance analysis of the dense films, to be $\sim 10^{-13}$ cm^2 s^{-1}. Modeling of diffusion in the sodium- germanium system predicts that sodium diffusion in the near-surface layers of the material is significantly faster than in the bulk. These results show that small feature sizes are critical for rapid, reversible electrochemical sodiation of germanium. This work has been published in the *Journal of Physical Chemistry C*.[57]

In Chapter 7, the sodium electrochemistry of evaporatively deposited tin, germanium, and alloys of the two elements is reported. Limiting the sodium stripping voltage window to 0.75V versus Na/Na^+ improves the stability of the tin and tin-rich compositions on repeated sodiation/de-sodiation cycles whereas the germanium and germanium-rich alloys were stable up to 1.5V. The stability of the electrodes could be correlated to the surface mobility of the alloy species during deposition suggesting that tin must be effectively immobilized in order to be successfully utilized as a stable electrode. While the stability of the alloys is greatly increased by the presence of germanium, the specific coulombic capacity of the alloy decreases with increasing germanium content due to the lower coulombic capacity of germanium. Additionally, the presence of germanium in the alloy suppresses the formation of intermediate phases present in the electrochemical sodiation of tin. Four-point probe resistivity measurements of the different compositions show that electrical resistivity increases with germanium content. Pure germanium is the most resistive yet exhibited the best electrochemical performance at high current densities which indicates that electrical resistivity is not rate limiting for any of the tested compositions. This work has been submitted for publication in *ACS Applied Materials and Interfaces.*

A summary of this work and conclusions drawn from it are presented in Chapter 8. Additionally, recommendations on future research directions are given.

REFERENCES

1. Zu, C.-X.; Li, H., *Energy & Environmental Science* **2011,** *4*, 2614-2624.

2. Landi, B. J.; Ganter, M. J.; Cress, C. D.; DiLeo, R. A.; Raffaelle, R. P., *Energy & Environmental Science* **2009,** *2*, 638-654.

3. Kromer, M. A.; Heywood, J. B. *Electric Powertrains: Opportunities and*

Challenges in the U.S. Light-Duty Vehicle Fleet Massachusetts Institute of Technology: Sloan Automotive Laboratory, 2007.

4. Yazami, R.; Touzain, P., *J. Power Sources* **1983,** *9*, 365-371.

5. Mizushima, K.; Jones, P. C.; Wiseman, P. J.; Goodenough, J. B., *Mater. Res. Bull.* **1980,** *15*, 783-789.

6. Padhi, A. K.; Nanjundaswamy, K. S.; Goodenough, J. B., *J. Electrochem. Soc.* **1997,** *144*, 1188-1194.

7. Islam, M. S.; Fisher, C. A. J., *Chem. Soc. Rev.* **2014,** *43*, 185-204.

8. Goodenough, J. B.; Kim, Y., *Chem. Mater.* **2009,** *22*, 587-603.

9. Zhang, X.; Kostecki, R.; Richardson, T. J.; Pugh, J. K.; Ross, P. N., *J. Electrochem. Soc.* **2001,** *148*, A1341-A1345.

10. Chen, L.; Wang, K.; Xie, X.; Xie, J., *J. Power Sources* **2007,** *174*, 538-543.

11. Aurbach, D.; Gamolsky, K.; Markovsky, B.; Gofer, Y.; Schmidt, M.; Heider, U., *Electrochim. Acta* **2002,** *47*, 1423-1439.

12. Jeong, S.-K.; Inaba, M.; Mogi, R.; Iriyama, Y.; Abe, T.; Ogumi, Z., *Langmuir* **2001,** *17*, 8281-8286.

13. Nakai, H.; Kubota, T.; Kita, A.; Kawashima, A., *J. Electrochem. Soc.* **2011,** *158*, A798-A801.

14. Klavetter, K. C.; Wood, S. M.; Lin, Y.-M.; Snider, J. L.; Davy, N. C.; Chockla, A. M.; Romanovicz, D. K.; Korgel, B. A.; Lee, J.-W.; Heller, A.*, et al.*, *J. Power Sources* **2013,** *238*, 123-136.

15. Lin, Y.-M.; Klavetter, K. C.; Abel, P. R.; Davy, N. C.; Snider, J. L.; Heller, A.; Mullins, C. B., *Chem. Commun.* **2012,** *48*, 7268-7270.

16. Manthiram, A., *J. Phys. Chem. Lett.* **2011,** *2*, 176-184.

17. Scrosati, B., *J. Electrochem. Soc.* **1992,** *139*, 2776-2781.

18. Zaghib, K.; Brochu, F.; Guerfi, A.; Kinoshita, K., *J. Power Sources* **2001,** *103*, 140-146.

19. Ning, G.; Haran, B.; Popov, B. N., *J. Power Sources* **2003,** *117*, 160-169.

20. Kasavajjula, U.; Wang, C.; Appleby, A. J., *J. Power Sources* **2007,** *163*, 1003-1039.

21. Derrien, G.; Hassoun, J.; Panero, S.; Scrosati, B., *Adv. Mater.* **2007,** *19*, 2336-2340.

22. Zhong, C.; Wang, J.; Chen, Z.; Liu, H., *J. Phys. Chem. C* **2011,** *115*, 25115-25120.

23. Huang, H.; Kelder, E. M.; Schoonman, J., *J. Power Sources* **2001,** *97–98*, 114-117.

24. Cabana, J.; Monconduit, L.; Larcher, D.; Palacín, M. R., *Adv. Mater.* **2010,** *22*, E170-E192.

25. Hariharan, S.; Saravanan, K.; Balaya, P., *Electrochem. Solid St.* **2010,** *13*, A132-A134.

26. Poizot, P.; Laruelle, S.; Grugeon, S.; Dupont, L.; Tarascon, J. M., *Nature* **2000,** *407*, 496-499.

27. Lin, Y.-M.; Abel, P. R.; Heller, A.; Mullins, C. B., *J. Phys. Chem. Lett.* **2011,** *2*, 2885-2891.

28. Shodai, T.; Okada, S.; Tobishima, S.-i.; Yamaki, J.-i., *Solid State Ionics* **1996,** *86–88, Part 2*, 785-789.

29. Rowsell, J. L. C.; Pralong, V.; Nazar, L. F., *J. Am. Chem. Soc.* **2001,** *123*, 8598-8599.

30. Tarascon, J. M.; Armand, M., *Nature* **2001,** *414*, 359-367.

31. Chan, C. K.; Peng, H.; Liu, G.; McIlwrath, K.; Zhang, X. F.; Huggins, R. A.; Cui, Y., *Nat. Nanotechnol.* **2008,** *3*, 31-35.

32. Hatchard, T. D.; Dahn, J. R., *J. Electrochem. Soc.* **2004,** *151*, A838-A842.

33. Beattie, S. D.; Larcher, D.; Morcrette, M.; Simon, B.; Tarascon, J. M., *J. Electrochem. Soc.* **2008,** *155*, A158-A163.

34. Baggetto, L.; Notten, P. H. L., *J. Electrochem. Soc.* **2009,** *156*, A169-A175.

35. Laforge, B.; Levan-Jodin, L.; Salot, R.; Billard, A., *J. Electrochem. Soc.* **2008,** *155*, A181-A188.

36. Chockla, A. M.; Klavetter, K. C.; Mullins, C. B.; Korgel, B. A., *ACS Appl. Mater. Interfaces* **2012,** *4*, 4658-4664.

37. Winter, M.; Besenhard, J. O., *Electrochim. Acta* **1999,** *45*, 31-50.

38. Noh, M.; Kwon, Y.; Lee, H.; Cho, J.; Kim, Y.; Kim, M. G., *Chem. Mater.* **2005,** *17*, 1926-1929.

39. Bazin, L.; Mitra, S.; Taberna, P. L.; Poizot, P.; Gressier, M.; Menu, M. J.; Barnabé, A.; Simon, P.; Tarascon, J. M., *J. Power Sources* **2009,** *188*, 578-582.

40. Arico, A. S.; Bruce, P.; Scrosati, B.; Tarascon, J.-M.; van Schalkwijk, W., *Nat Mater* **2005,** *4*, 366-377.

41. Survey, U. S. G. *Mineral Commodity Summaries 2013*; U.S. Geological Survey: 2013.

42. Sudworth, J. L., *J. Power Sources* **1994,** *51*, 105-114.

43. Lu, X.; Xia, G.; Lemmon, J. P.; Yang, Z., *J. Power Sources* **2010,** *195*, 2431-2442.

44. Lu, Y.; Wang, L.; Cheng, J.; Goodenough, J. B., *Chem. Commun.* **2012,** *48*, 6544-6546.

45. Barpanda, P.; Ye, T.; Nishimura, S.-I.; Chung, S.-C.; Yamada, Y.; Okubo, M.; Zhou, H.; Yamada, A., *Electrochem. Commun.* **2012,** *24*, 116-119.

46. Lim, S. Y.; Kim, H.; Shakoor, R. A.; Jung, Y.; Choi, J. W., *J. Electrochem. Soc.* **2012,** *159*, A1393-A1397.

47. Stevens, D. A.; Dahn, J. R., *J. Electrochem. Soc.* **2001,** *148*, A803-A811.

48. Abel, P. R.; Lin, Y.-M.; de Souza, T.; Chou, C.-Y.; Gupta, A.; Goodenough, J. B.; Hwang, G. S.; Heller, A.; Mullins, C. B., *Journal of Physical Chemistry C* **2013,** *117*, 18885-18890.

49. Baggetto, L.; Keum, J. K.; Browning, J. F.; Veith, G. M., *Electrochem. Commun.* **2013,** *34*, 41-44.

50. Ellis, L. D.; Hatchard, T. D.; Obrovac, M. N., *J. Electrochem. Soc.* **2012,** *159*, A1801-A1805.

51. Datta, M. K.; Epur, R.; Saha, P.; Kadakia, K.; Park, S. K.; Kumta, P. N., *J. Power Sources* **2013,** *225*, 316-322.

52. Farbod, B.; Cui, K.; Kalisvaart, W. P.; Kupsta, M.; Zahiri, B.; Kohandehghan, A.; Lotfabad, E. M.; Li, Z.; Luber, E. J.; Mitlin, D., *ACS Nano* **2014**.

53. Jow, T. R.; Shacklette, L. W.; Maxfield, M.; Vernick, D., *J. Electrochem. Soc.* **1987,** *134*, 1730-1733.

54. Abel, P. R.; Lin, Y.-M.; Celio, H.; Heller, A.; Mullins, C. B., *ACS Nano* **2012,** *6*, 2506-2516.

55. Abel, P. R.; Chockla, A. M.; Lin, Y.-M.; Holmberg, V. C.; Harris, J. T.; Korgel, B. A.; Heller, A.; Mullins, C. B., *ACS Nano* **2013,** *7*, 2249-2257.

56. Abel, P. R.; Klavetter, K. C.; Heller, A.; Mullins, C. B., *J. Phys. Chem. C* **2014**.

57. Abel, P. R.; Lin, Y.-M.; de Souza, T.; Chou, C.-Y.; Gupta, A.; Goodenough, J. B.; Hwang, G. S.; Heller, A.; Mullins, C. B., *J. Phys. Chem. C* **2013,** *117*, 18885-18890.

Chapter 2: Improving the Stability of Nanostructured Silicon Thin Film Lithium-Ion Battery Anodes Through Their Controlled Oxidation

INTRODUCTION

Lithium ion batteries are widely used in portable devices and are being developed for use in zero-emission vehicles. In the latter, simultaneous demands for safety and increased energy and power density continues to outpace the improvements in battery technology. The current graphite anode is limited with respect to its safety and capacity (372 mAh/g). For this reason, a massive search for new anode materials is in progress. Silicon has received a lot of attention because of its high lithium storage capacity – it alloys with lithium up to a thermodynamic limit of $Li_{22}Si_5$ which gives 4200 mAh/g storage capacity.[1] This capacity has been realized in high temperature experiments, but at room temperature only $Li_{15}Si_4$ (3579 mAh/g) has been reached.[2-3] Either value represents an order of magnitude improvement over the theoretical capacity of graphite anodes. The lithium insertion potential is low - ~120 mV for lithiation of crystalline silicon – which allows for the construction of high voltage (~3.8 V for a cell utilizing a $LiCoO_2$ cathode), and thusly high energy density cells. However, increased anode capacity yields diminishing returns in overall cell capacity with current cathode materials. Analysis by Kasavajjula *et al.* showed that the overall cell capacity is only marginally improved once the anode capacity is increased above ~1200 mAh/g when it is paired with a currently available high capacity cathode (~200 mAh/g).[4] With the inherent lithium storage capacity of silicon far exceeding this value, there is excess capacity available that can be

sacrificed in order to optimize other properties of the electrode, such as safety and stability.

Due to the high potential payoff of a successful silicon based electrode, much work has been done on the subject. Li *et al.* showed that crystalline silicon undergoes a transition to amorphous on lithium insertion but the order/disorder transition is reversible, allowing for recrystallization of the silicon upon removal of lithium[5]. However, further work by Hatchard and Dahn showed that this behavior was grain size dependent, that nano-scale silicon remained amorphous through the entire lithium insertion and removal cycle and that avoiding recrystallization of the silicon extended the cycle life of the electrodes.[2]

Silicon anodes can degrade rapidly by pulverization leading to loss of electrical contact between their particles .[6] However, superplastically deforming small grained materials are well known. Metals that would fail at 20 % elongation persevere at > 200 % elongation when made of small grains. Consequently, it is recognized that nano-scale materials can be reversibly deformed far beyond the limit of large-grained materials.[7-8] In order to overcome the rapid loss of capacity, nano-scale silicon morphologies have been extensively investigated. The studies include nanoparticles,[9] nanorods,[10] nanowires,[11-13] nanospheres,[14] and thin films[15-16]. Despite any superplasticity imparted by the nano scale dimensions, electrodes comprised of nano-scale silicon are still not stable. This inherent instability led Beattie *et. al.* to the investigation of electrodes containing large concentrations of binder[17] intended to buffer the volumetric expansion associated with the lithium alloying reaction. They succeeded in reversibly cycling 100 nm silicon

powder anodes by reducing the weight percentage of silicon to 33 weight %. Their electrodes, with ~600mAh/g capacity, were stable for 140 cycles.

Buffering the excessive expansion/shrinkage through active/inactive silicon heterostructures has also been investigated. Zhou *et al.* used a $TiSi_2$ nanonet as a silicon support.[18] This system operated reversibly as long as the lower cutoff potential was high enough to avoid the reduction of $TiSi_2$. Magasinski *et al.* used high surface area, dendritic carbon-black as a support for CVD silicon.[18-19] The electrodes cycled well for 100 cycles with a specific capacity of ~1600 mAh/g.

Other methods for stabilizing the silicon electrode include coatings such as carbon[11, 20] and copper[13] and chemical surface treatments such as hydrogen termination, and ligand capping[21] and while these do affect the lithium storage dynamics and improve the cycle life, they are insufficient to completely stabilize the electrode.

This study considers the chemical modification of silicon by controlled oxidation. Gao *et al.* showed that SiO_2 nanoparticles react reversibly with lithium given sufficiently high potential to drive the reverse reaction.[22] Yang *et al.* showed that SiO_x ($0.8<x<1.1$) electrodes could be reversibly cycled and lower oxygen content increased the reversible capacity, but decreased the electrod stability.[23] This was confirmed by Kim *et al.* with SiO_x where $0.18<x<0.5$.[24] Morita and Takami then showed that composite electrodes composed of disproportionated SiO and carbon retained ~90% of their initial ~700 mAh/g capacity after 200 cycles.[25] It has also been shown that disproportionated SiO forms Si in an SiO_2 matrix leading to active – inactive structures that help buffer the strain during cycling.[26] Additional work on SiO_x/C composites by Hu *et al.* showed that

capacities of 1100 mAh/g could be realized without sacrificing stability.[27] Park *et al.* showed that the extent of disproportionation in SiO is temperature dependent, and partially disproportionated SiO provides superior performance as an anode material.[28] Yoo *et al.* reported the synthesis of Si/SiOx core – shell structures with a reversible lithium storage capacity of ~2000 mAh/g and good stability for 70 cycles.[29] The disproportionation may help buffer strain, but the presence of SiO_2 hinders both electrical and ionic transport. Due to the poor transport properties of SiO_2, we focus our investigation on SiO_x where $0<x<0.2$ in order to minimize the detrimental effects of large quantities of SiO_2. In addition to oxygen contained in the bulk of the material, we look at the effect of the native surface oxide on the stability of our material. Recent studies by Xun *et al.*[30] and McDowell *et al.*[31] show that the reversible capacity of nano-scale silicon is decreased by the presence of a thick surface oxide layer. Our results agree with these findings; however McDowell *et al.* also report that an oxide layer is detrimental to cycling stability. Our work shows the opposite trend, with a significant increase in cycling stability with the addition of a surface oxide layer.

Silicon and its oxide have been well studied by the semiconductor industry, and it has been found that two types of oxides are easily created on a clean silicon surface. Dry oxides, where the silicon is oxidized using molecular oxygen, have higher density and dielectric strength, and have a slower growth rate due to slow diffusion of oxygen through the oxide layer.[32] Steam oxides, where water is used as the oxidizer, have a slightly lower density due to the expansion of the lattice from Si-H and Si-OH groups formed during oxidation. This expanded lattice increases the ionic conductivity through

the steam oxide. In our study, we use water as the oxidizer for the bulk material in order to minimize any increase in ionic resistance from the increased oxygen content.

We employ two related evaporative deposition techniques in this study. Glancing angle deposition (GLAD), also known as oblique angle deposition, is vacuum evaporative deposition at high angles of incidence, where the angle can be used to control the morphology of the material being synthesized.[33-34] Dense films are grown at deposition angles close to the surface normal, while nanocolumnar morphology emerges as the deposition angle is increased to more glancing angles. Evaporation in high vacuum onto a substrate at room temperature is a form of ballistic deposition. The presence of a reactive gas during the deposition alters the chemical composition of the deposit *via* a process known as reactive ballistic deposition (RBD).[35-39] RBD provides reproducible nanostructured morphologies with tunable composition, and has been used to synthesize materials for use in energy storage [16, 40] and conversion.[41-42] This study builds on the work of Fleischauer *et al.*[16] who deposited silicon films at glancing angles with promising results. We use RBD at glancing angles to synthesize nanostructured silicon thin films with varying oxygen content by evaporating silicon in a water ambient. The oxygen content is varied from 0 to 17 atomic % (at%) without affecting the morphology allowing compositional effects to be studied. We show that the addition of oxygen to the nanostructured films significantly increases their cycling stability but lowers their reversible capacity relative to pristine silicon films.

EXPERIMENTAL METHODS

Film Preparation

Silicon and partially oxidized silicon films were deposited on 15.8mm, 300 series stainless steel disks (MTI Corp.) by evaporating silicon under high vacuum (~10^{-7} Torr) or in a background of water vapor (2 – 4x10^{-6} Torr). The vacuum chamber was first evacuated to below 5x10^{-8} Torr. The pressure rose to ~1x10^{-7} Torr when the evaporator was in use. A cylinder protruding into the chamber was filled with liquid nitrogen during deposition of un-oxidized films in order to condense background water and oxygen. Quadrupole mass spectra (Stanford Research Systems, RGA200) indicate that most of the residual gas in the chamber was hydrogen. A precision leak valve was used to backfill the chamber with water vapor up to 2 – 4x10^{-6} Torr. Total pressure was measured using a nude ionization gauge (MDC with a Stanford Research Systems Controller). Silicon shot or ingot (Alfa Aesar 99.999%) was evaporated from a tantalum crucible using an electron beam evaporator (Telemark model 118). The substrate was mounted on a rotary probe, allowing the deposition angle to be adjusted between 0° and 90° (between surface normal and parallel). The crucible to substrate distance was approximately 28 cm. A quartz crystal microbalance (Inficon) was used to measure the deposition rate and the total mass of silicon deposited on a substrate. Cross sectional images of three pristine films with identical mass as measured by QCM are shown in Figure A.1. The deviation in thickness between the films is quite small, only ~1%, giving confidence that the QCM is an accurate method for measuring total film mass. Once deposited, the silicon films were transferred to an argon filled glovebox (MBraun Unilab) with oxygen content less than

0.1 ppm and water content less than 2ppm. A sealed vacuum transfer container was used to transport some films from the vacuum chamber to the glovebox without exposure to air. Once in the glovebox, the samples were assembled into coin cells as deposited or annealed to 200°C for 2 hours prior to assembly. Other samples were removed from the vacuum chamber and annealed to 200°C for 2 hours in air before being introduced to the glovebox.

The QCM was also used to estimate the concentration of oxygen incorporated into the films during deposition. The mass rate of deposition was monitored as water was introduced into the chamber and the increase in deposition rate for a given partial pressure of water was taken to be the mass of oxygen incorporated into the film. We assumed that the mass of hydrogen incorporated into the film was negligible.

Film Characterization

SEM imaging was performed using a Hitachi S-5500 scanning transmission electron microscope (STEM) using a 30 kV accelerating voltage. XPS spectra were recorded using a commercial X-ray photoelectron spectrometer (Kratos Axis Ultra), utilizing a monochromated Al-Kα X-ray source ($h\nu$ = 1486.5 eV). An automated charge neutralizer was employed for analysis. Casa XPS analysis software was used to determine the stoichiometry of samples from corrected peak areas, employing Kratos sensitivity factors for each element of interest. The analysis of films exposed to air was performed on samples deposited at 70°, but the analysis of films not exposed to air was performed on dense films, grown at normal incidence in order to allow cleaning of the

surface by argon ion sputtering to better measure the true bulk composition of the material.

Transfer of samples to the XPS machine was done using the Reduce Oxidation (RoX) interface – an interface for transporting air sensitive samples from a glove box to an ultra-high vacuum chamber for X-ray photoelectron spectroscopy analysis. It was built at the Surface Analysis Laboratory of the Texas Materials Institute (TMI) at UT-Austin. The design of the interface contains a set of built-in figure of merits that were used to verify that samples were not exposed to traces of oxygen and water during transport.

Coin Cell Assembly and Electrochemical Testing

Samples were assembled into coin cells inside the glove box. Substrates were assembled into type 2032 coin cells against a lithium metal (Alfa Aesar 99%) counter/reference electrode. The electrolyte was 5 wt% vinylene carbonate (Alfa-Aesar, 97%) added to 1M LiPF6 in EC:DMC 1:1 (EMD Chemicals). A 25μm thick polypropylene film separator (Celguard 2400) was used. After assembly into coin cells, the electrochemical behavior of samples was tested on a multi-channel battery tester (Arbin BT2143). Cells were cycled between 5mV and 1.5V at various currents with a 5 minute rest period between charge/discharge half cycles. Films were tested for 10 cycles at C/10 followed by 10 cycles each at C/5, C/2, C, and then a final 10 cycles at C/10 to examine how the samples recovered from the high rate tests. C-rates were calculated based on a theoretical capacity of 4200 mAh/g. The best performing films were then subjected to extended cycling – 300 cycles – at C/5. Electrochemical testing of some electrodes was stopped after 10 cycles. These cells were disassembled, soaked in DMC

for 24 hours to remove lithium salts, and then dipped in 1 mM acetic acid for 30 seconds to remove the SEI. These electrodes were then imaged by SEM.

RESULTS AND DISCUSSION

Materials Characterization

SEM images of silicon GLAD and RBD films deposited with an incident angle of 70^{o} are shown in Figure 2.1. The films are nanocolumnar, and as seen in Figure 2.1b, the diameter of the individual columns is on the order of 10 nm. The SEM micrograph in Figure 2.1c is that of a film deposited at 70^{o} and at $2x10^{-6}$ Torr partial pressure H_2O and subsequently annealed to $200^{o}C$ in air for two hours. Figure 1d shows a film deposited under similar conditions, but at a partial pressure of $4x10^{-6}$ Torr H_2O, similarly annealed to $200^{o}C$ in air for two hours. Figures 2.1c and 2.1d show that the morphologies of the films deposited in a water-containing environment are not altered from that of the films deposited in the absence of water (Figures 2.1a and 2.1b). Oxygen incorporation in the films during their deposition and annealing increases their electrical resistance, allows their charging and exaggerates the apparent contrast of the individual columns in Figures 2.1c and d. Because the structures of the films are invariant, the differences in their electrochemical behavior can be rigorously associated with changes in their composition. The porous morphology allows electrolyte to penetrate into the electrode and provides a high surface area for the reduction of lithium. Additionally, the small diameter of the individual columns minimizes the lithium diffusion length during the alloying/de-alloying reaction. The high surface area is also available for native oxide formation when

the films are annealed in air, and a measurable fraction of the material is oxidized during this process.

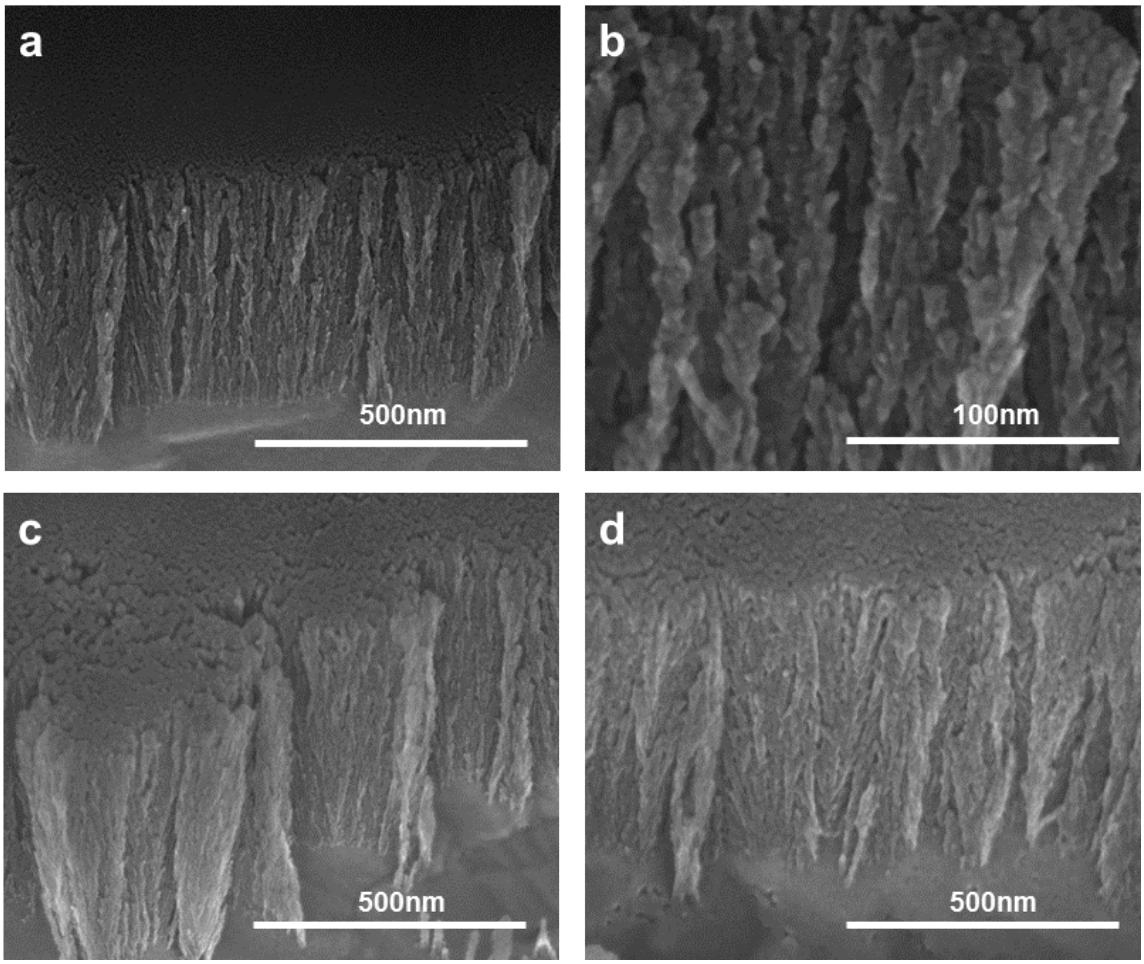

Figure 2.1. SEM micrographs of silicon GLAD and RBD films deposited at 70°. a) and b) deposited in high vacuum, c) deposited in $2x10^{-6}$ Torr H_2O and annealed in air at 200°C for 2 hours, and d) deposited in $4x10^{-6}$ Torr H_2O and annealed in air at 200°C for 2 hours.

Figure 2.2 shows x-ray photoelectron (XPS) spectra of the silicon films. Figure 2.2a shows the spectra for dense films deposited at an incident angle of 0^{o} (normal to the substrate surface) in the absence of water vapor (labeled "pristine"), with a partial pressure of $2x10^{-6}$ Torr H_2O, and with a partial pressure of $4\ x10^{-6}$ Torr H_2O. Because the composition of the bulk of the films is independent of the deposition angle, films deposited at normal incidence were employed so that their surface would be flat and readily cleaned by argon ion sputtering. These films were never exposed to air, and they had only a sub-monolayer of surface oxide when introduced into the XPS chamber. Their surface was sputtered prior to analysis in order to remove any surface contaminants. Quantitative analysis of the O 1s and Si 2p peaks showed the oxygen content of the pristine film to be 3 at% (attributable to surface-adsorbed H_2O, CO or CO_2) whereas the oxygen content of the films deposited in a partial pressure of $2x10^{-6}$ and $4x10^{-6}$ Torr H_2O were found to be 13 and 17 at%. Repeated sputtering of the film – removing additional material to measure the oxygen concentration at points deeper in the film – did not change the measured oxygen content which indicates that oxygen is homogeneously incorporated into the film.

Irrespective of their morphologies, the oxygen content of the films was determined solely by the fluxes of silicon atoms and water molecules to the substrate during film deposition. The 13 and 17 atom % oxygen content values agreed with quartz crystal microbalance (QCM) measured deposited mass differences between silicon deposited in high vacuum at constant evaporator power and at a particular partial pressure of water. The C 1s feature indicated 2 at% carbon on the surface of the pristine film and 6

at% carbon on the films deposited in $2x10^{-6}$ Torr H_2O and 4 $x10^{-6}$ Torr H_2O. The intensity of the carbon peak increased with the time delay between sputtering and analysis, indicating that the carbon is due to adsorbed carbon containing species (see figure A.2). Figure 2.2b shows spectra for a pristine film, a film deposited in a partial pressure of $2x10^{-6}$ Torr H_2O, and in a partial pressure of $4x10^{-6}$ Torr H_2O, but subsequently annealed in air at 200°C for two hours. The films were deposited at 70° from surface normal. Quantitative analysis of the annealed films deposited in high vacuum (labeled "pristine"), $2x10^{-6}$ Torr H_2O, and $4x10^{-6}$ Torr H_2O shows 56, 55, and 57 at% oxygen, respectively, on the surface of each sample. This is less than the 66 at% expected for a silicon native oxide; however XPS is a surface analysis technique that gathers information from the top few nanometers of the material. The thickness of a silicon native oxide layer is ~1 nm and the 200°C anneal is not hot enough to significantly increase the thickness of this layer. The measured oxygen content determined from Figure 2.2b is therefore the average oxygen content of the native oxide and the material beneath it.

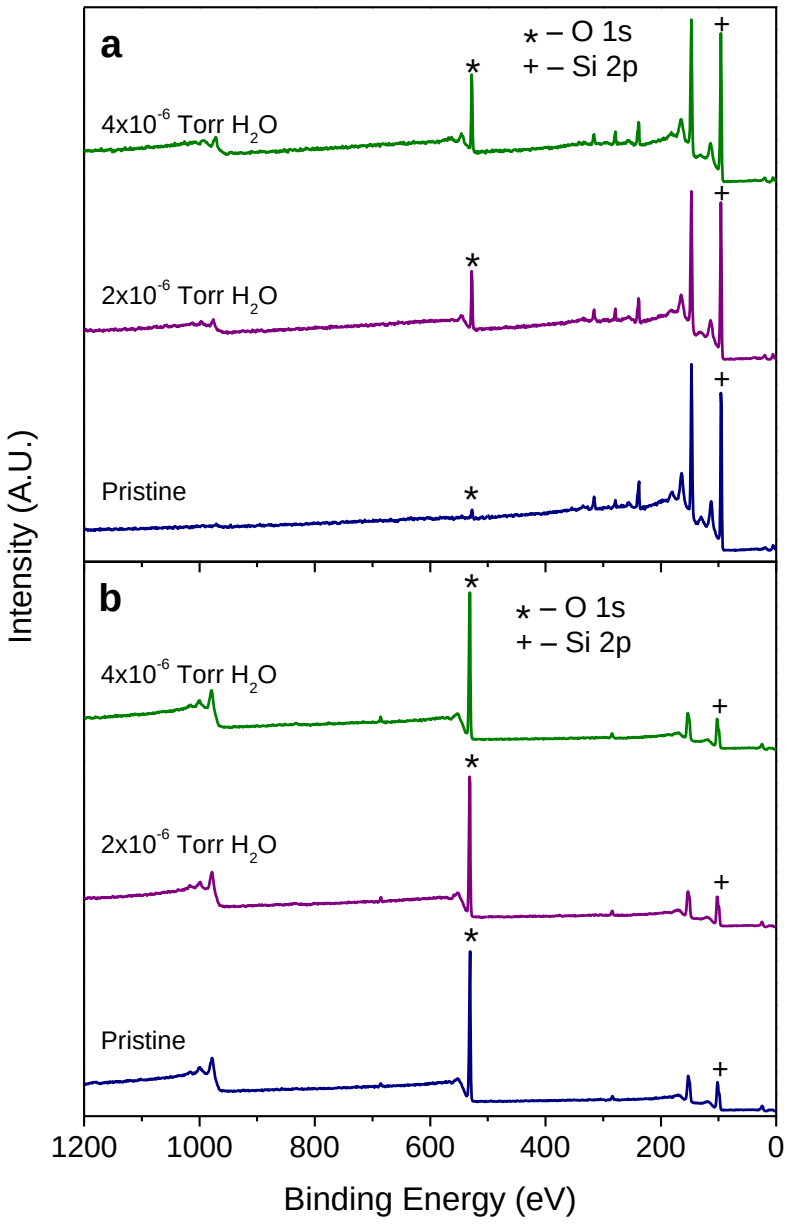

Figure 2.2. XPS spectra of a) dense films grown at 0° from surface normal and lacking surface oxide and b) films grown at 70° from surface normal and annealed in air. Quantitative analysis shows 3, 13, and 17 at% oxygen for the pristine, $2x10^{-6}$ and $4x10^{-6}$ Torr H_2O films from a). Analysis shows 56, 55, and 57 at% oxygen for the vacuum deposited, $2x10^{-6}$ and $4x10^{-6}$ Torr H_2O films from b).

High-resolution measurements of the Si 2p peak shows that the feature is the convolution of the Si^{o}, Si^{1+} and Si^{2+} peaks with the Si^{o} peak further split due to spin-orbit coupling. Line broadening of the oxidized silicon peaks due to the amorphous nature of the material and compositional effects prevented the resolution of the individual spin states. Figure 2.3 shows this high-resolution measurement and the de-convolution of the measurement into its component peaks. The pristine film is nearly entirely composed of Si^{o}, but as the background water pressure during deposition increases, a shoulder appears and grows in magnitude, indicating higher fractions of silicon existing in the Si^{1+} and Si^{2+} states. The fraction of Si^{o} relative to Si^{1+} and Si^{2+} is consistent with the QCM measurements regarding oxygen content and quantitative analysis using the O 1s feature. The lack of Si^{3+} and Si^{4+} features indicates that oxygen is incorporated randomly into the film during deposition, and that the sub-oxide does not spontaneously disproportionate into silicon and SiO_2. Since the oxygen is incorporated randomly into the film, the probability of fully oxidizing individual silicon atoms is low. The individual components that make up the Si 2p feature are all broad, having FWHM >0.8 eV, which is much broader than the ultimate resolution of the instrument, and is indicative of an amorphous material as is expected for GLAD and RBD films.[36, 42]

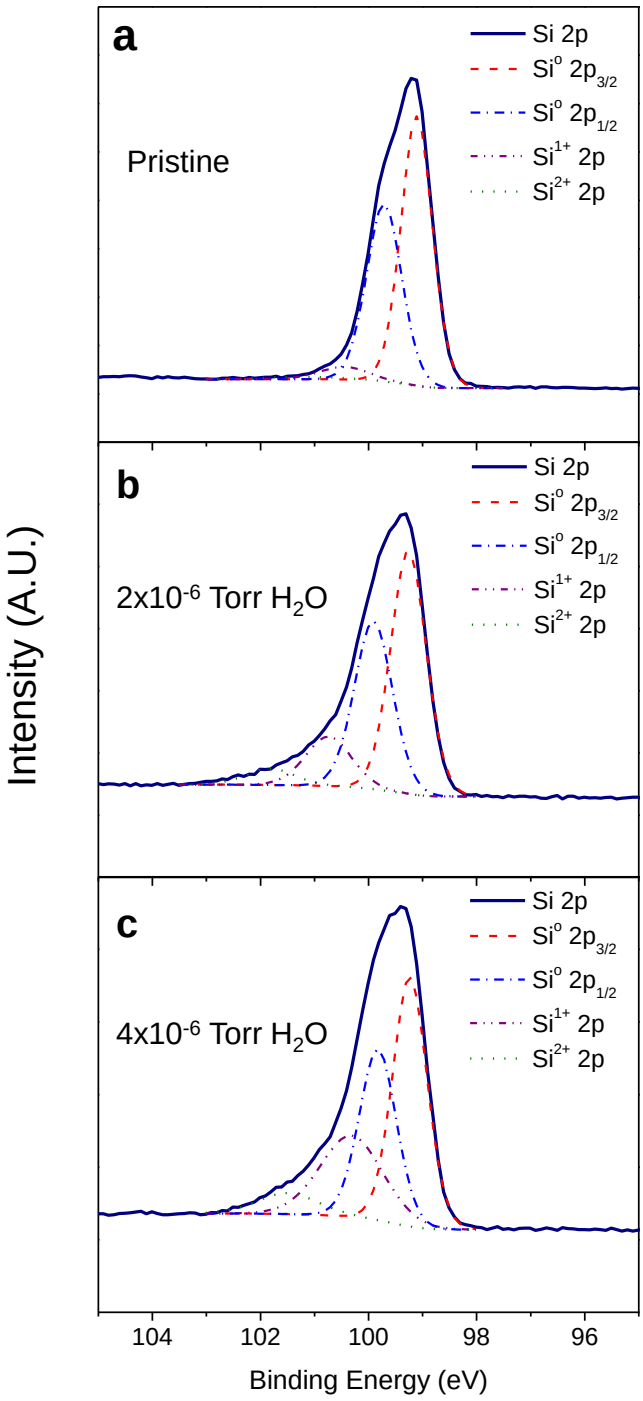

Figure 2.3. High resolution XPS of the Si 2p feature of a) pristine silicon, b) silicon grown in 2x10^{-6} Torr H_2O, c) silicon grown in 4x10^{-6} Torr H_2O. The fraction of silicon in the 1+ and 2+ states increases with increasing water pressure during deposition.

Electrochemical Characterization

Films with 100 μg total combined mass of silicon and oxygen grown in high vacuum, and at $2x10^{-6}$ Torr H_2O, or at $4x10^{-6}$ Torr H_2O were transferred from the vacuum chamber to a glovebox without exposure to air in a sealed vacuum transfer interface where they were then assembled into coin cells. XPS measurements indicate that this transfer method only allowed a sub-monolayer surface oxide to form on these samples before assembly into coin cells. Once assembled, the cells were cycled at constant current for 10 cycles at C/10 followed by 10 cycles each at C/5, C/2, C and then a final 10 cycles at C/10. The lithium storage capacity as a function of cycle number is shown in Figure 2.4. The pristine film, deposited in high vacuum without exposure to water, had a first cycle lithium insertion capacity of 3966 mAh/g. This is above the theoretical capacity for silicon at room temperature, but some charge is consumed in the first cycle by parasitic side reactions such as solid electrolyte interface (SEI) formation. The initial reversible capacity was 2839 mAh/g. This capacity had dropped to 929 mAh/g by the 10^{th} cycle, indicating rapid degradation of the electrode. The degradation continued at the higher C-rate cycles, with a modest recovery at cycle 41. After 50 cycles, the capacity was reduced to 343 mAh/g – roughly 10% of the initial reversible capacity. The film deposited in a partial pressure of $2x10^{-6}$ Torr H_2O, while having a similar 1^{st} cycle lithium insertion capacity showed a slower rate of degradation, retaining a capacity of 1787 mAh/g after 10 cycles. The capacity after 50 cycles was ~812 mAh/g, however there was very little capacity recovery when the charge/discharge rate was reduced from C to C/10. The

increased oxygen content of the film deposited in a partial pressure of $4x10^{-6}$ Torr H_2O showed slower decay in the first 10 cycles, but the rate of degradation increased in subsequent cycles, and the capacity after 50 cycles was 507 mAh/g. This behavior suggests that up to a point, oxygen incorporated into silicon electrodes increases their cycling stability, but is detrimental beyond that limit. Based on the oxygen content of the films deposited in $2x10^{-6}$ Torr H_2O and $4x10^{-6}$ Torr H_2O, the amount of oxygen past which the effect becomes detrimental appears to be roughly 15 at%.

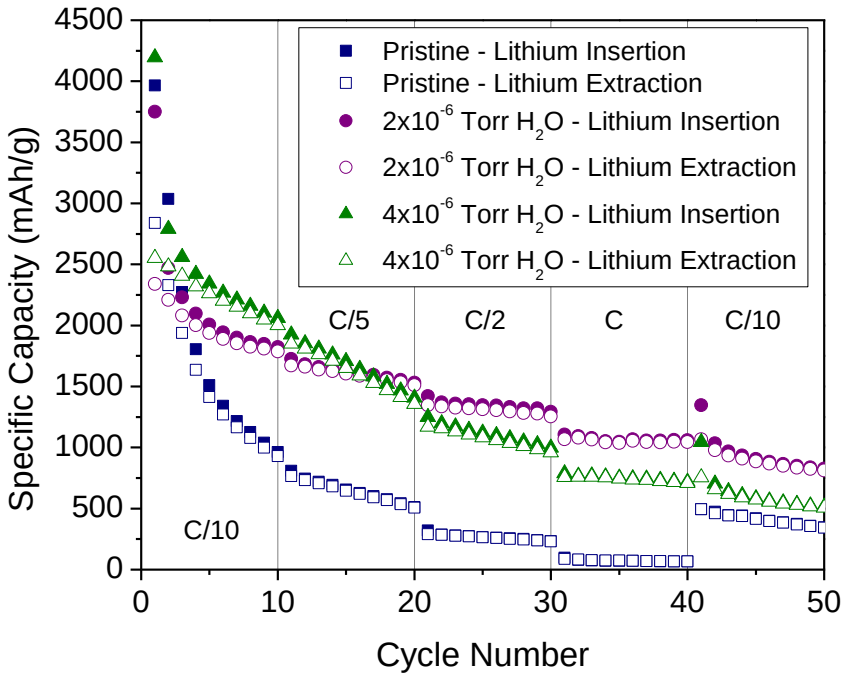

Figure 2.4. Silicon GLAD and RBD films deposited at 70° are cycled at various c-rates. The capacity retention of the films is poor, with the film deposited in $2x10^{-6}$ Torr H_2O degrading the least.

Low temperature annealing of silicon/metal heterostructures promotes the interdiffusion of the two elements at the interface, stabilizing silicon/iron layered thin film electrodes.[43] Correspondingly, films grown in high vacuum and at a defined partial pressure of water were transferred from the vacuum chamber to the glove-box using the sealed vacuum transfer interface, but were then annealed to 200°C for two hours in the oxygen and water free environment of the glovebox before being assembled into coin cells. Once assembled into coin cells, they were tested as above. The cycling data are shown in Figure 2.5. Surprisingly, the stability of the pristinely deposited film was not improved by the inert atmosphere annealing. After 50 cycles, the capacity was 315 mAh/g – slightly less than the un-annealed film. The film deposited in $2x10^{-6}$ Torr H_2O also cycled poorly. The annealing process helped to stabilize the film deposited in a partial pressure of $4x10^{-6}$ Torr H_2O. This electrode had an initial reversible capacity of 2362 mAh/g. After 10 cycles, the capacity had degraded to 2096 mAh/g and the capacity was down to 1918 mAh/g after 50 cycles. The improved stability of the film deposited in a partial pressure of $4x10^{-6}$ Torr H_2O and no improvements in the films with lower oxygen content suggests that random incorporation of oxygen into the silicon is not the optimal configuration and that the higher oxidation states of silicon are involved in stabilizing the films. Figure 2.3 indicates that there is a significant increase in the concentration of Si^{2+} in the film when the background pressure of water is increased from $2x10^{-6}$ Torr to $4x10^{-6}$ Torr. Low temperature annealing may promote a structural relaxation that improves the cycling stability of the film.

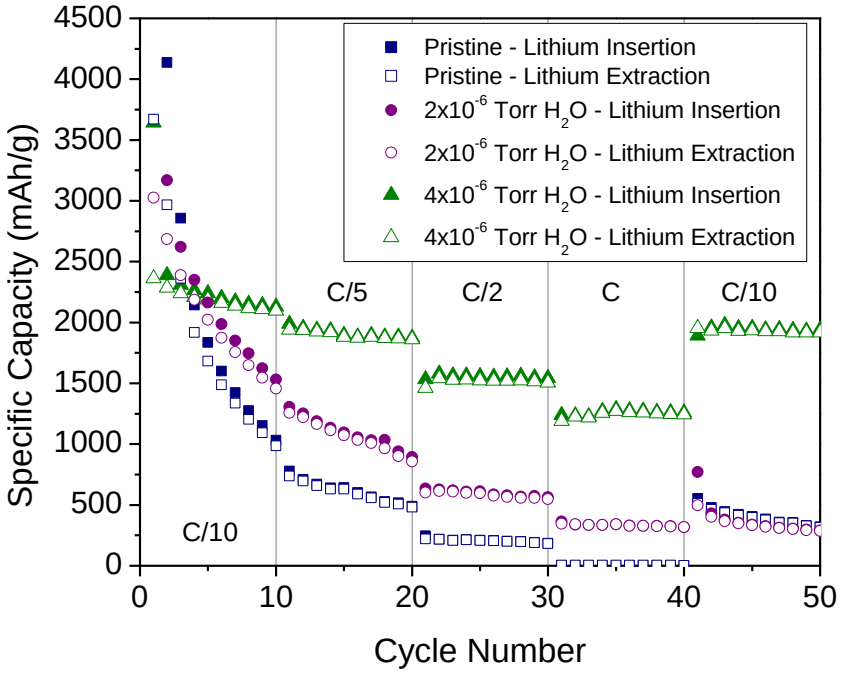

Figure 2.5. Silicon GLAD and RBD films deposited at 70° and annealed to 200°C for 2 hours in an inert atmosphere are cycled at various c-rates. The capacity retention of the films is better than the un-annealed films, the best performing film – deposited in $4x10^{-6}$ Torr H_2O – was at ~80% of initial capacity after 50 cycles.

In the electrode deposited in high vacuum as well as in electrodes deposited in $2x10^{-6}$ Torr H_2O or $4x10^{-6}$ Torr H_2O and annealed to 200°C for two hours in air a native oxide layer quickly formed, but at the low annealing temperature the oxide layer thickness did not increase significantly. The films were incorporated into coin cells and tested as above. The cycling was continued after the 50th cycle for the best performing film, with the additional cycling performed at C/5. The cycling data are shown in Figure 2.6. Figure 2.6a shows the first 50 cycles. The film deposited in high vacuum, in the absence of water, has an initial reversible capacity of ~2720 mAh/g. The cycling stability

was greatly improved over the films deposited in high vacuum and films subsequently annealed in an inert atmosphere. The capacity decayed slightly at higher C-rates but decayed rapidly beginning at cycle 41 when the C/10 rate was resumed. The film deposited at $2x10^{-6}$ Torr H_2O has an initial reversible capacity of ~2179 mAh/g, and cycles stably for 50 cycles. The capacity fade observed in the electrode deposited in high vacuum was absent; its absence is attributed to the presence of bulk silicon sub-oxide formed during deposition. The film deposited in a partial pressure of $4x10^{-6}$ Torr H_2O shows similar qualitative behavior, but lower specific capacity. The reversible capacity is ~1696 mAh/g at C/10, but drops to ~822 mAh/g at 1C. This is a larger decrease in capacity than the film deposited in $2x10^{-6}$ Torr H_2O which only degreases to ~1450 mAh/g when cycled at 1C. Figure 2.6b shows subsequent cycling of the film deposited in $2x10^{-6}$ Torr H_2O. Cycles 51 through 300 are conducted at C/5. The capacity remained relatively constant up to about cycle 120, at which point the capacity begins to degrade. A linear fit from cycle 200 to 300 indicates that the decay rate is ~2 mAh/g per cycle, or 0.15% per cycle. The average coulombic efficiency for these cycles is ~99.5%, indicating that lithium is being consumed in parasitic side reactions on each cycle. If the SEI layer is damaged as the film expands on lithiation, the exposed electrode surface will quickly react with the electrolyte to repair the damage. As some lithium is consumed in SEI formation, this could account for the less than ideal efficiency. If this process continued, SEI material would build up in the pores of the film, eventually filling them and leading to additional stresses on the active material. This may explain the delayed onset of capacity fade in these films.

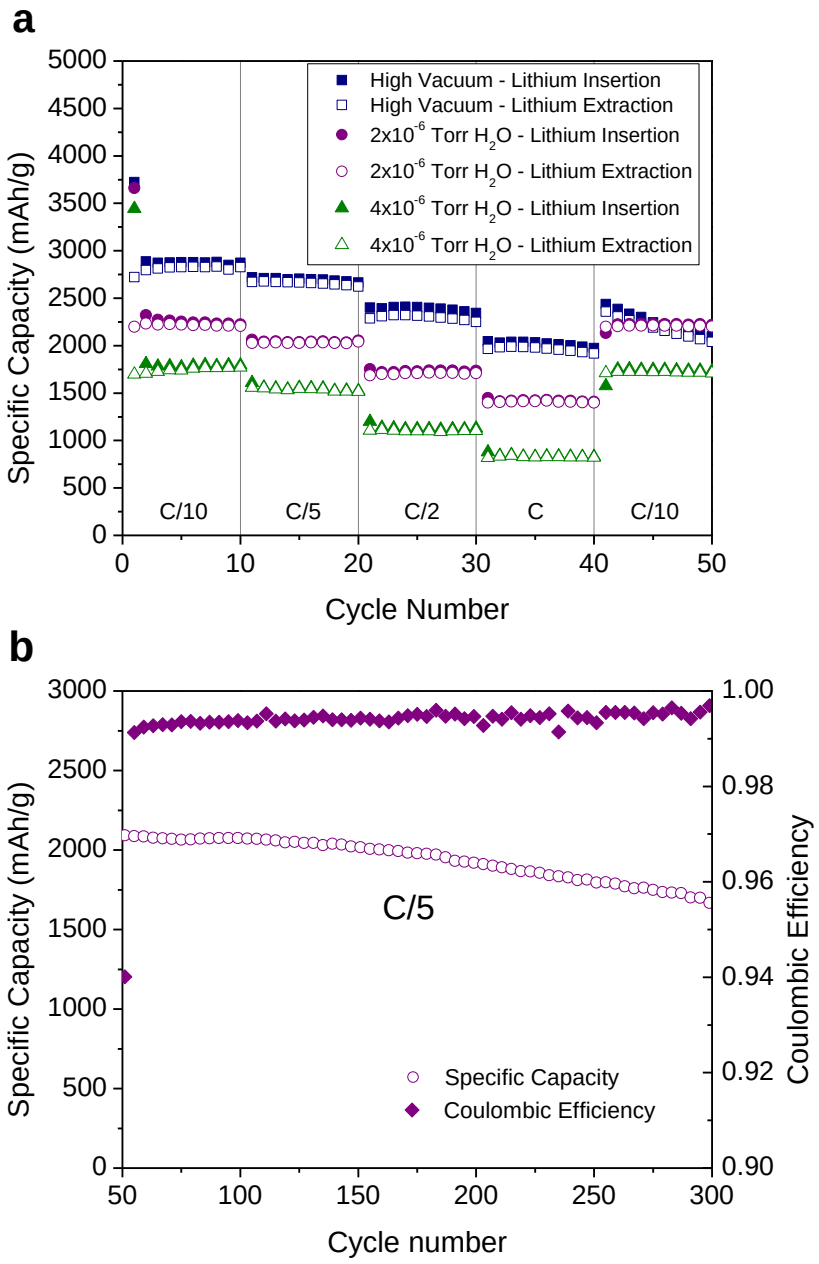

Figure 2.6. a) Silicon GLAD and RBD films that have been annealed to 200°C in air are cycled at various c-rates. b) Cycling is continued at C/5 for the film deposited in $2x10^{-6}$ Torr H_2O. The film remains stable up to cycle ~120 at which point it begins to degrade at ~0.15% per cycle.

For films annealed to 200ºC for two hours in air, incorporation of oxygen during deposition decreases the capacity and extends the cycle life. Films deposited in the absence of water, and containing little bulk oxygen, have higher initial capacity, but degrade relatively quickly, while films deposited in the presence of water and containing small amounts of oxygen in the bulk are stabilized and can undergo hundreds of cycles at a slightly reduced capacity. As can be seen with the cells deposited in a partial pressure of $4x10^{-6}$ Torr H_2O, excessive oxygen incorporation leads to lower specific capacity. However, given that overall cell capacity does not increase significantly for anode capacities above ~1200 mAh/g,[4] slightly reducing the capacity of silicon anodes in exchange for better cycle life is worthwhile with currently available cathodes.

Figure 2.7 shows SEM micrographs of electrodes after 10 cycles. Figures 2.7a, 2.7b and 2.7c show images of a pristine electrode, and electrodes deposited in $2x10^{-6}$ Torr H_2O and $4x10^{-6}$ Torr H_2O that were assembled without exposure to atmosphere. These films exhibit significant cracking with extreme damage and almost complete loss of active material in the pristine film and slightly less damage in the oxygen containing films. This is consistent with the capacity retained in these films after 10 cycles (see Figure 2.4). Figures 2.7d, 2.7e and 2.7f show images of a pristine electrode, and electrodes deposited in $2x10^{-6}$ Torr H_2O and $4x10^{-6}$ Torr H_2O that were annealed in air at 200ºC for 2 hours before assembly into coin cells. While these films still exhibit cracking, the extent of the damage is significantly less than their un-annealed counterparts. The crack density is seen to decrease as the bulk oxygen content increases. The annealed films show no capacity loss after 10 cycles (see figure 2.6a) indicating that,

although the films are cracked, no material has become disconnected from the substrate. In addition to the lower crack density in the oxygen containing annealed films, the active material appears to be better adhered to the substrate. In the un-annealed films and the oxygen free annealed film, shown in figure 2.7a-2.7d, the edges of silicon islands are pulled back from the substrate indicating that they are partially delaminated. Examination of the crack edges in the partially oxidized and annealed silicon films, shown in figure 2.7e and 2.7f, shows that the material remains well adhered to the substrates despite the presence of cracks in the films.

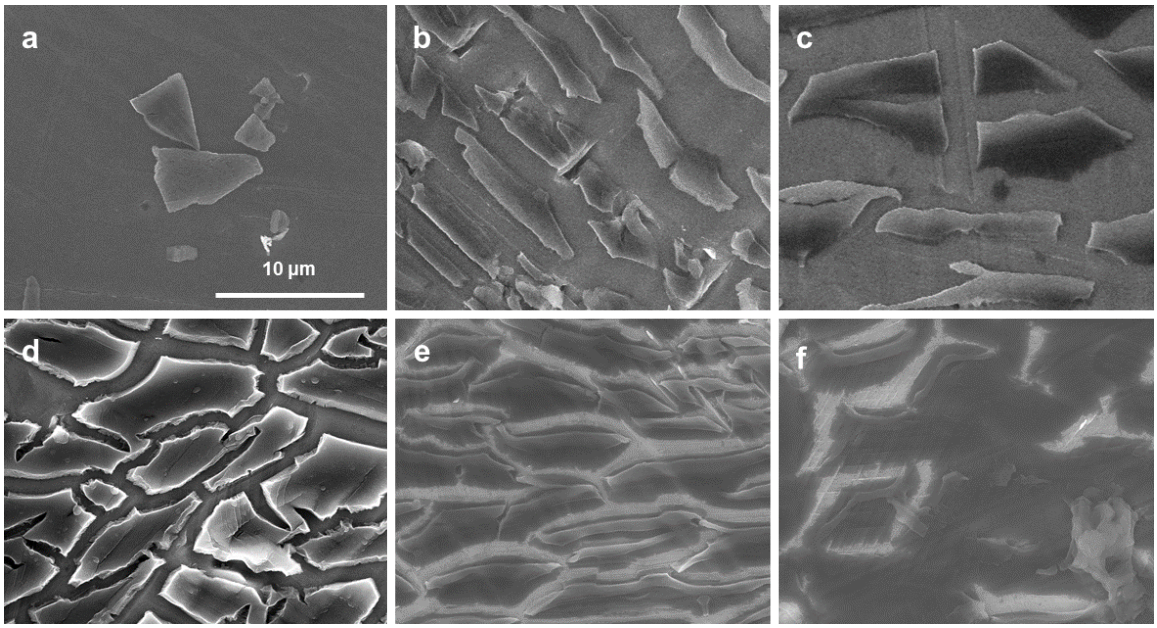

Figure 2.7. SEM images of silicon and partially oxidized silicon RBD electrodes after 10 cycles. a) Pristine b) $2x10^{-6}$ Torr H_2O, and c) $4x10^{-6}$ Torr H_2O without exposure to atmosphere, and d) pristine e) $2x10^{-6}$ Torr H_2O, and f) $4x10^{-6}$ Torr H_2O after annealing in air at 200°C for 2 hours. The 10 µm scale bar applies to all images.

We attribute the increased stability of the partially oxidized films to three factors. We postulate that presence of oxygen incorporated into the film creates a lithium inactive phase that anchors the structures during cycling. This helps prevent damage during the expansion/contraction associated with cycling. Secondly, the presence of oxygen decreases the specific capacity of the material. Lower capacity decreases the strain during cycling and helps prevent loss of integrity at the interface with the substrate. Thirdly, computational modeling of amorphous silicon sub-oxides shows that Si-O-Si bonds exhibit a wider range of bond angles than Si-Si bonds.[44] This additional conformational freedom may help the relieve stresses in the material during lithium alloying and de-alloying.

Despite the damage to the films at the micron scale, all of the electrodes retained a nano-structured morphology after cycling, indicating that delamination from the substrate and loss of electrical contact, rather than material pulverization is the failure mechanism in these films. High magnification SEM micrographs of the cycled electrodes are shown in figure 2.8.

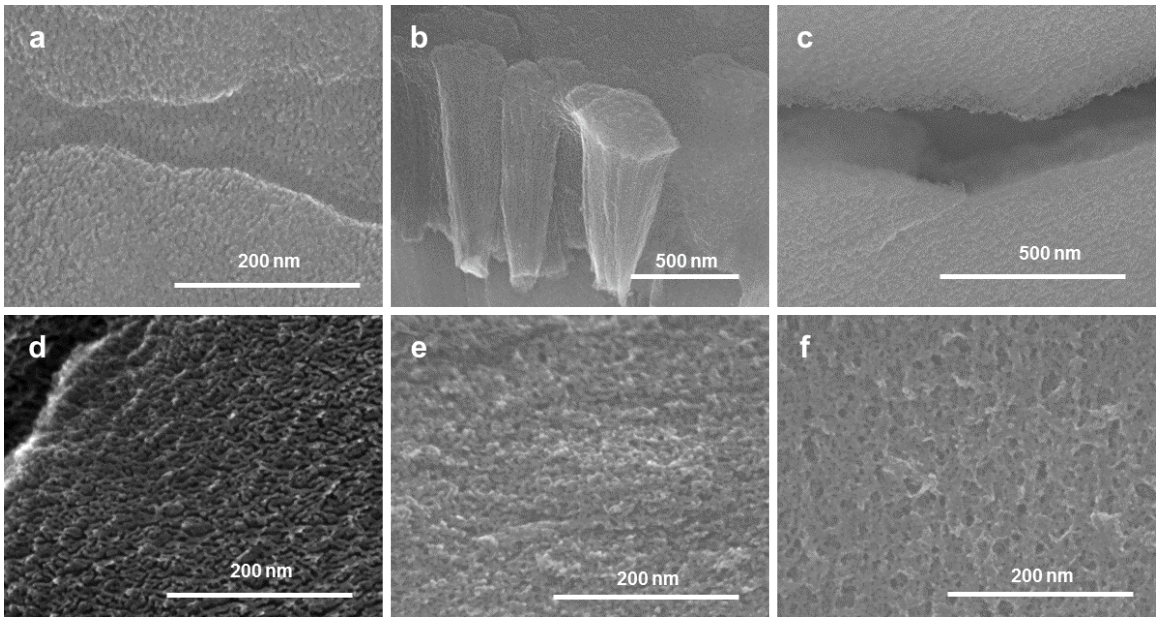

Figure 2.8. High magnification SEM micrographs of partially oxidized silicon RBD electrodes after 10 cycles. a) Pristine b) $2x10^{-6}$ Torr H_2O, and c) $4x10^{-6}$ Torr H_2O without exposure to atmosphere, and d) pristine e) $2x10^{-6}$ Torr H_2O, and f) $4x10^{-6}$ Torr H_2O after annealing in air at 200°C for 2 hours. Despite damage to the films at the micron scale, nano-scale morphology is retained.

Additional information is obtained by examining the cycling voltage profiles shown in differential form in Figures 2.9 and 2.10. The profiles of un-annealed films (corresponding to Figure 2.4) –a pristine film deposited in high vacuum, and films deposited in $2x10^{-6}$ Torr H_2O and 4 $x10^{-6}$ Torr H_2O, then transferred in the vacuum transfer interface – are shown in Figure 2.9. The pristine film exhibits interesting behavior on the first cycle. It shows two broad lithium insertion features at ~100mv and ~250 mV, but the higher voltage feature, while broad had a sharp onset, attributed to the pristine nature of the film's surface. Similar behavior is seen also on the first lithium extraction cycle, a sharp onset to a broad lithium extraction feature. After the first cycle,

the film shows features indicative of amorphous silicon. The intensity of the features decreases with cycling as the capacity of the film degrades (see Figure 2.4). Films deposited in water ambient contain an additional feature at 400mV during the first lithium insertion. This feature is attributed to the reaction between lithium and the silicon oxide. This peak has disappeared by the second cycle indicating that the reaction between lithium and the SiO_x species is irreversible. We conclude that this feature is due to the reaction of lithium with oxygen in the film rather than SEI formation for two reasons. First, the feature is absent in films carefully prepared without exposure to oxygen. Preventing the incorporation of oxygen into the bulk material as well as surface oxidation completely removes this feature. Secondly, the magnitude of this feature correlates to the bulk oxygen content of the films as measured by XPS and QCM measurements. By integrating the charge contained in this feature, the oxygen content of the films can be estimated. This charge can be related to oxygen concentration if we assume that lithium reacts with oxygen to form Li_2O. This method yields oxygen concentrations of 14 and 20 at% for films deposited in a partial pressure of $2x10^{-6}$ Torr H_2O and $4x10^{-6}$ Torr H_2O. This is in good agreement with the XPS and QCM measurements of oxygen content (See Figure A.3).

Figure 2.10 shows data for the films annealed to 200°C in air (corresponding to Figure 2.6). The first cycle has the characteristic features of amorphous silicon plus the ~400mV feature due to the reaction between lithium and SiO_x. Additionally, there is a tail on that feature which extends out to 900 mV due to the reaction between lithium and the native oxide layer. The magnitude of tail increases slightly with increasing bulk oxygen

content. This feature is detailed in Figure A.4. As can be seen by comparing the first cycle capacity of un-annealed films versus those of annealed films deposited under identical conditions, the presence of a native oxide layer adversely affects the electrode's reversible capacity.

The position of the lithium insertion and extraction features in the un-annealed films (Figure 2.9) do not change with increasing bulk oxygen content indicating that the presence of oxygen homogeneously incorporated into the material does not hinder electrical or ionic transport. Annealed films (Figure 2.10), however exhibit peak positions that shift toward higher overpotentials with increasing oxygen content. This indicates a synergistic effect between the bulk oxygen and the surface oxide where increased bulk oxygen increases the resistivity of the electrodes.

The features corresponding to the lithiation of SiO_x have disappeared by the second cycle which indicates that the reaction is irreversible. The material undergoes additional irreversible changes in subsequent cycles. In the 3rd cycle, the lower voltage lithium insertion peak splits, and the relative magnitude of the two components of this doublet shift up through the 10th cycle. This peak splitting is likely due to a symmetry breaking in the lithium storage sites due to the presence of oxygenated lithium species. The fact that the material is still changing up to the 10th cycle is interesting in that the specific capacity of the material is not changing over these cycles, wherefore the changes in the insertion voltages are attributed to internal re-arrangement.

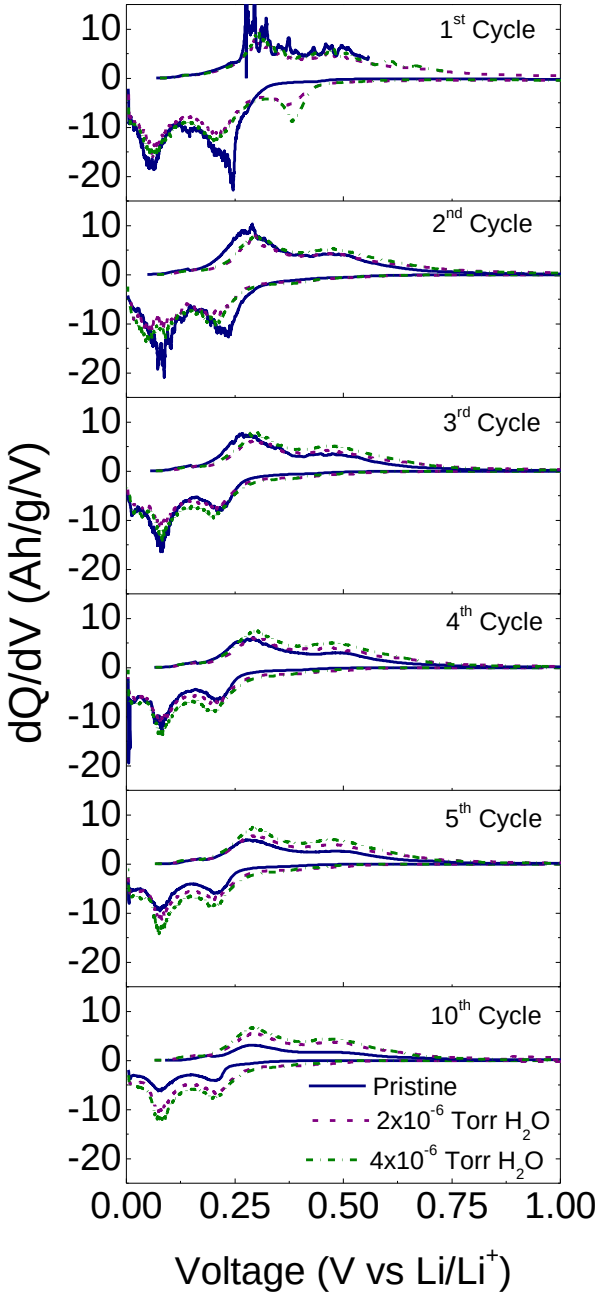

Figure 2.9. Differential capacity plots of silicon electrodes deposited in high vacuum, $2x10^{-6}$ Torr H_2O, and $4x10^{-6}$ Torr H_2O. The electrodes were never exposed to air. Irrespective of oxygen content, all three electrodes behave like amorphous silicon after the first cycle.

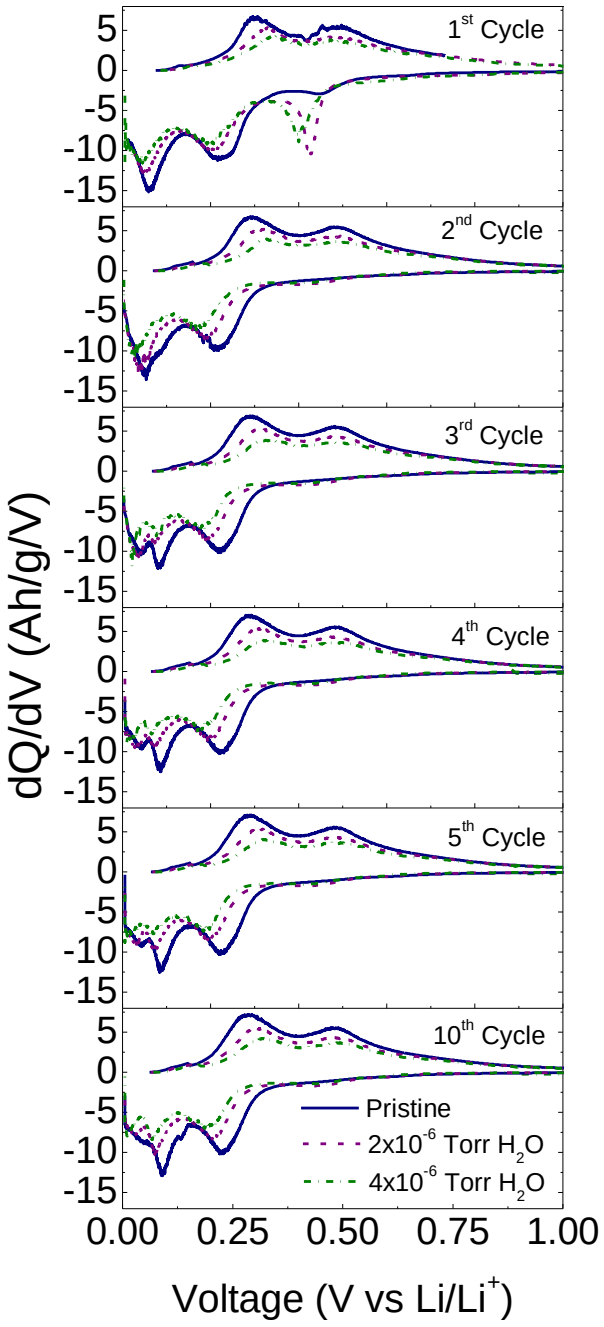

Figure 2.10. Differential capacity plots of silicon electrodes deposited in high vacuum, $2x10^{-6}$ Torr H_2O, and $4x10^{-6}$ Torr H_2O and subsequently annealed to 200°C for 2 hours in air. The lower voltage feature for lithium insertion into amorphous silicon splits after the second cycle. The relative intensity of the two new peaks changes in subsequent cycles. Additionally, the peak positions shift with increasing oxygen content.

CONCLUSIONS

The introduction of small amounts of oxygen (>20 at%) during synthesis of nanostructured silicon thin films increases their cycling stability when used as a lithium ion battery anode. Low temperature annealing further improves the electrode stability. The combination of homogeneous oxygen incorporation during the synthesis of the films and surface oxidation by low temperature annealing in air provides the best cycling stability. When both bulk and surface oxides are present in an annealed film, a high capacity (2200 mAh/g) is realized with virtually no capacity loss for the first 120cycles and slight capacity fade (~0.15% per cycle) over cycles 150-300. This electrode retains ~80% of its original capacity after 300 cycles. At a rate of 1C the capacity is 1450 mAh/g. The excellent cycling stability and high capacity make oxygen containing silicon a promising candidate material for lithium-ion battery research.

REFERENCES

1. Wen, C. J.; Huggins, R. A., *J. Solid State Chem.* **1981,** *37*, 271-278.

2. Hatchard, T. D.; Dahn, J. R., *J. Electrochem. Soc.* **2004,** *151*, A838-A842.

3. Obrovac, M. N.; Christensen, L., *Electrochem. Solid-State Lett.* **2004,** *7*, A93-A96.

4. Kasavajjula, U.; Wang, C.; Appleby, A. J., *J. Power Sources* **2007,** *163*, 1003-1039.

5. Li, H.; Huang, X.; Chen, L.; Zhou, G.; Zhang, Z.; Yu, D.; Jun Mo, Y.; Pei, N., *Solid State Ionics* **2000,** *135*, 181-191.

6. Ryu, J. H.; Kim, J. W.; Sung, Y.-E.; Oh, S. M., *Electrochem. Solid-State Lett.* **2004,** *7*, A306-A309.

7. Champion, Y.; Langlois, C.; Guérin-Mailly, S.; Langlois, P.; Bonnentien, J.-L.; Hÿtch, M. J., *Science* **2003,** *300*, 310-311.

8. Wu, B.; Heidelberg, A.; Boland, J. J., *Nat. Mater.* **2005,** *4*, 525-529.

9. Kim, H.; Seo, M.; Park, M.-H.; Cho, J., *Angew. Chem., Int. Ed.* **2010,** *49*, 2146-2149, S2146/1-S2146/4.

10. Hieu, N. S.; Lim, J. C.; Lee, J. K., *Microelectron. Eng.* **2011**.

11. Chan, C. K.; Patel, R. N.; O'Connell, M. J.; Korgel, B. A.; Cui, Y., *ACS Nano* **2010,** *4*, 1443-1450.

12. Chan, C. K.; Peng, H.; Liu, G.; McIlwrath, K.; Zhang, X. F.; Huggins, R. A.; Cui, Y., *Nat. Nanotechnol.* **2008,** *3*, 31-35.

13. Chen, H.; Xiao, Y.; Wang, L.; Yang, Y., *J. Power Sources 196*, 6657-6662.

14. Yao, Y.; McDowell, M. T.; Ryu, I.; Wu, H.; Liu, N.; Hu, L.; Nix, W. D.; Cui, Y., *Nano Lett.* **2011,** *11*, 2949-2954.

15. Maranchi, J. P.; Hepp, A. F.; Kumta, P. N., *Electrochem. Solid-State Lett.* **2003,** *6*, A198-A201.

16. Fleischauer, M. D.; Li, J.; Brett, M. J., *J. Electrochem. Soc.* **2009,** *156*, A33-A36.

17. Beattie, S. D.; Larcher, D.; Morcrette, M.; Simon, B.; Tarascon, J. M., *J. Electrochem. Soc.* **2008,** *155*, A158-A163.

18. Zhou, S.; Liu, X.; Wang, D., *Nano Lett.* **2010,** *10*, 860-863.

19. Magasinski, A.; Dixon, P.; Hertzberg, B.; Kvit, A.; Ayala, J.; Yushin, G., *Nat. Mater.* **2010,** *9*, 353-358.

20. Chen, H.; Dong, Z.; Fu, Y.; Yang, Y., *J. Solid State Electrochem.* **2010,** *14*, 1829-1834.

21. Xu, W.; Vegunta, S. S. S.; Flake, J. C., *J. Power Sources* **2011,** *196*, 8583-8589.

22. Gao, B.; Sinha, S.; Fleming, L.; Zhou, O., *Adv. Mater.* **2001,** *13*, 816-819.

23. Yang, J.; Takeda, Y.; Imanishi, N.; Capiglia, C.; Xie, J. Y.; Yamamoto, O., *Solid State Ionics* **2002,** *152-153*, 125-129.

24. Kim, K.; Park, J.-H.; Doo, S.-G.; Kim, T., *Thin Solid Films* **2010,** *518*, 6547-6549.

25. Morita, T.; Takami, N., *J. Electrochem. Soc.* **2006,** *153*, A425-A430.

26. Wang, J.; Zhao, H.; He, J.; Wang, C.; Wang, J., *J. Power Sources* **2011,** *196*, 4811-4815.

27. Hu, Y.-S.; Demir-Cakan, R.; Titirici, M.-M.; Mueller, J.-O.; Schloegl, R.; Antonietti, M.; Maier, J., *Angew. Chem., Int. Ed.* **2008,** *47*, 1645-1649.

28. Park, C.-M.; Choi, W.; Hwa, Y.; Kim, J.-H.; Jeong, G.; Sohn, H.-J., *J. Mater. Chem.* **2010,** *20*, 4854-4860.

29. Yoo, H.; Lee, J.-I.; Kim, H.; Lee, J.-P.; Cho, J.; Park, S., *Nano Lett. 11*, 4324-4328.

30. Xun, S.; Song, X.; Grass, M. E.; Roseguo, D. K.; Liu, Z.; Battaglia, V. S.; Liu, G., *Electrochem. Solid-State Lett.* **2011,** *14*, A61-A63.

31. McDowell, M. T.; Lee, S. W.; Ryu, I.; Wu, H.; Nix, W. D.; Choi, J. W.; Cui, Y., *Nano Lett.* **2011**, 4018–4025.

32. Ainger, F. W., *Journal of Materials Science* **1966,** *1*, 1-13.

33. Robbie, K.; Sit, J. C.; Brett, M. J., *J. Vac. Sci. Technol., B* **1998,** *16*, 1115-1122.

34. Hawkeye, M. M.; Brett, M. J., *J. Vac. Sci. Technol., A* **2007,** *25*, 1317-1335.

35. Dohnálek, Z.; Kimmel, G. A.; McCready, D. E.; Young, J. S.; Dohnálková, A.; Smith, R. S.; Kay, B. D., *J. Phys. Chem. B* **2002,** *106*, 3526-3529.

36. Flaherty, D. W.; Dohnálek, Z.; Dohnálková, A.; Arey, B. W.; McCready, D. E.; Ponnusamy, N.; Mullins, C. B.; Kay, B. D., *J. Phys. Chem. C* **2007,** *111*, 4765-4773.

37. Flaherty, D. W.; Hahn, N. T.; Ferrer, D.; Engstrom, T. R.; Tanaka, P. L.; Mullins, C. B., *J. Phys. Chem. C* **2009,** *113*, 12742-12752.

38. Flaherty, D. W.; May, R. A.; Berglund, S. P.; Stevenson, K. J.; Mullins, C. B., *Chem. Mater.* **2009,** *22*, 319-329.

39. Flaherty, D. W.; Hahn, N. T.; May, R. A.; Berglund, S. P.; Lin, Y.-M.; Stevenson, K. J.; Dohnalek, Z.; Kay, B. D.; Mullins, C. B., *Acc. Chem. Res.* **2011**.

40. Lin, Y.-M.; Abel, P. R.; Flaherty, D. W.; Wu, J.; Stevenson, K. J.; Heller, A.; Mullins, C. B., *J. Phys. Chem. C* **2011,** *115*, 2585-2591.

41. Berglund, S. P.; Flaherty, D. W.; Hahn, N. T.; Bard, A. J.; Mullins, C. B., *J. Phys. Chem. C* **2011,** *115*, 3794-3802.

42. Hahn, N. T.; Ye, H.; Flaherty, D. W.; Bard, A. J.; Mullins, C. B., *ACS Nano* **2010,** *4*, 1977-1986.

43. Kim, J.-B.; Lee, H.-Y.; Lee, K.-S.; Lim, S.-H.; Lee, S.-M., *Electrochem. Commun.* **2003,** *5*, 544-548.

44. Lee, S.; Bondi, R. J.; Hwang, G. S., *Phys. Rev. B* **2011,** *84*, 045202.

Chapter 3: Nanostructured $Si_{(1-x)}Ge_x$ for Tunable Thin Film Anodes

INTRODUCTION

Lithium ion batteries have enabled the widespread adoption of portable electronic devices but their continued development is limited by the electrode chemistries. Currently available cells utilize carbonaceous materials in the anode, but safety concerns as well as a limited capacity – especially at high charge/discharge rates – has led to the search for new, superior anode materials. Alloy type electrodes are a promising class of materials, which includes both silicon and germanium. These materials store lithium through the formation of a bulk lithiated alloy, and have capacities several times that of graphite. The thermodynamic limits for lithium alloy formation have been found to be $Li_{22}X_5$ (X=Si,Ge) which represents 4200 mAh g^{-1} for Si[1], and 1624 mAh g^{-1} for Ge[2] – these capacities have been realized at elevated temperatures, but studies on electrochemical lithiation of silicon at room temperature have shown that the highest accessible state is $Li_{15}Si_4$, which still represents a capacity of 3579 mAh g^{-1}.[3-4] There is still confusion about the accessible capacity for germanium. Baggetto *et al.* reports 1384 mAh g^{-1},[5] corresponding to $Li_{15}Ge_4$, but others report capacities close to 1624mAh g^{-1} indicative of $Li_{22}Ge_5$.[6] In either case, the capacity is significantly higher than that of the presently used graphitic material.

Silicon has been extensively studied due to its high capacity, low cost and abundance, with promising results.[7-14] Germanium has also attracted attention due to its favorable electronic conductivity, ionic diffusivity, and capacity.[6, 15-21] Germanium's

intrinsic electronic conductivity at room temperature is 2.1 S m^{-1}, three orders of magnitude higher than that of silicon.($1.6x10^{-3}$ S m^{-1})[22]. Additionally, the diffusivity of lithium in germanium is $6.25x10^{-12}$ cm^2 s^{-1}, two orders of magnitude higher than in silicon ($1.9x10^{-14}$ cm^2 s^{-1}).[23] However, the high cost and low abundance of germanium are hurdles to its widespread adoption. Both materials share the disadvantage of undergoing large volumetric expansion upon lithiation. Nanostructuring has been shown to prevent electrode pulverization in silicon and germanium independently and is expected to work for the alloy system as well. Here we use the term alloy to refer to only the silicon-germanium alloy. Lithium-silicon-germanium ternary compounds will be refered to as lithiated alloys.

Silicon and germanium are miscible over the entire compositional range. Additionally, the compositions of the terminal phases accesable through electrochemical lithiation have identical lithium content, are isostructural, and have similar lattice constants (10.777Å for $Li_{15}Si_4$[3] and 10.783Å for $Li_{15}Ge_4$,[24] each with 3.75 moles of lithium per mole of silicon or germanium). Assuming that the alloy is lithiated to $Li_{15}(Si_{(1-x)}Ge_x)_4$, the specific capacity of the alloy should scale with composition according to equation 1.

$$Specific\ \ Capacity\ \left(mA\cdot h\cdot g^{-1}\right) = \frac{\xi\ \ n\ \ F}{(1-x)M_{Si}+xM_{Ge}} \qquad (3.1)$$

Where ξ is the extent of reaction (taken to be 3.75 moles of lithium per mole of alloy – this corresponds to the formation of $Li_{15}(Si_{(1-x)}Ge_x)_4$), n is the charge carried by the lithium ion, F is the Faraday constant, x is the mole fraction of germanium in the alloy and M_{Si} and M_{Ge} are the molar masses of silicon and germanium.

Silicon-germanium alloys have been extensively studied for application to the semiconductor industry. The electrical conductivity of the alloy has been found to vary monotonically with composition between the bounds set by the pure species.[25] The intermediate electrical conductivity of silicon-germanium alloys should increase the high-rate performance of the alloy relative to the silicon baseline. Additionally, the ionic conductivity of lithium in the alloy has been studied at elevated temperature by Atabaev *et al.*[26] They found that, despite the higher ionic conductivity of germanium, the ionic conductivity of the alloy decreased with increasing germanium content over the compositional range 0 – 35 at% germanium. The trend was accentuated as the temperature was lowered (from 500ºC to 300ºC). The study did not investigate the behavior of alloys with high germanium content, but it would be expected that the ionic conductivity would increase as the composition becomes closer to pure germanium.

Several groups have investigated layered silicon-germanium systems.[27-29] However, alloy systems have not been well studied, and the reported results do not follow the expected trends. Hashimoto *et al.* used ball milling to create $Li_{4.4}Si_{(1-x)}Ge_x$ powder for use as an active material in all-solid-state batteries.[30] X-ray diffraction showed that the desired phases had been formed, but the material was cycled *versus* a lithiated cathode ($LiCo_{0.3}Ni_{0.7}O_2$). The authors state that the alloys reach a lithiated phase of $Li_ySi_{(1-x)}Ge_x$ with y ranging from 4.9 to 5.45 depending on the silicon to germanium ratio, but provide no evidence that the additional lithium was incorporated into the lithium-silicon-germanium alloy. Wang *et al.* investigated $Si_{(1-x)}Ge_x$ sputtered onto a copper nanowire array and found that capacity retention varied with composition, with the most stable

composition being $Si_{0.6}Ge_{0.4}$.[31] Further investigation of the properties of the silicon-germanium alloys was limited to this composition, so the changes in the electrochemical properties with material composition could not be tracked. Our results show a different trend in how capacity retention varies with composition, however this could be due to differences in the deposition techniques or substrate materials (and hence film adhesion).

In this work we synthesize nanostructured amorphous thin films by glancing angle deposition (GLAD). GLAD is a physical vapor deposition technique where the adatoms are directed at the substrate at high angles of incidence. In the early stages of deposition stochastic variations in deposition rate lead to surface roughening. The roughness is amplified by self-shadowing leading to the growth of nanocolumnar films. We employ multiple independently controlled evaporators to coevaporate silicon and germanium. Additional details regarding this technique are described elsewhere.[32-37] We vary the mole fraction of germanium in the alloy from 0 to 1. We show that the electronic conductivity increases with increasing germanium content and that the high-rate performance of the alloy increases with increasing germanium content, but the specific capacity decreases with increasing germanium content. These opposing trends provide application specific optimal compositions based on the needed specific capacity, C-rate performance, and material cost.

EXPERIMENTAL METHODS

Material Synthesis

Thin films of $Si_{(1-x)}Ge_x$ were synthesized in high vacuum ($<1x10^{-7}$ Torr) by evaporative deposition at normal or glancing angles. Total film mass densities of 50 μg cm^{-2} were used which corresponds to dense film thicknesses of 94 nm, 109 nm, 130 nm, 162 nm, and 215nm for Ge, $Si_{0.25}Ge_{0.75}$, $Si_{0.5}Ge_{0.5}$, $Si_{0.75}Ge_{0.25}$ and Si respectively. Silicon shot (99.999% Alfa Aesar) was evaporated using a Telemark 118 electron beam evaporator, and germanium was evaporated using a custom-built electron beam evaporator. The evaporators are operated independently with both evaporants directed at the center of the vacuum chamber. Each deposition rate could be individually controlled and independently measured using a quartz crystal microbalance (inficon SQM-160 with cool-drawer sensor feedthrough). The silicon deposition rate was monitored throughout the entire deposition, while the germanium deposition rate was measured before and after deposition. Variation in the germanium deposition rate between the two measurements was less than 10%. Films for electrochemical testing were deposited on 15.8mm, 300 series stainless steel disks (MTI Corp.), and films for *ex-situ* analysis were deposited on glass slide covers (Fisher Scientific). The substrate was mounted on a rotary probe, allowing the deposition angle to be adjusted between 0^o and 90^o (between surface normal and parallel).

Material Characterization

Imaging of the as deposited films was performed using a Hitachi S5500 in SEM mode with an acceleration voltage of 20 kV. The composition was measured by XPS using a commercial X-ray photoelectron spectrometer (Kratos Axis Ultra), utilizing a monochromatic Al-Kα X-ray source (hν = 1486.5 eV). An automated charge neutralizer was employed for analysis. Casa XPS analysis software was used to determine the stoichiometry of samples from corrected peak areas, employing Kratos sensitivity factors for each element of interest. Electrical conductivity was measured using a Lucas 302 four-point probe with a Keithly 220 programmable current source.

Raman spectroscopy was performed using a Renishaw inVia microscope equipped with a 514.5 nm argon ion laser in backscattering configuration. The Stokes Raman signal at 521 cm^{-1} for single-crystalline bulk Si oriented with the [110] direction normal to the laser was used to calibrate the instrument. The beam was focused using an optical microscope with a 50× objective lens. Spectra were taken on SiGe films deposited on glass slides by single scans at 5% laser power (0.2 mW). The films were annealed using 100% laser power to induce local crystallization, and spectra were taken again on the SiGe films using 5% laser power.

Absorptance measurements were made using a Cary 500 UV-Vis-NIR spectrophotometer attached to a Labsphere DRA-CA-5500 integrating sphere. Samples were suspended in the center of the integrating sphere using a clip-style center mount, and the total transmitted and reflected light were measured simultaneously. This transmittance + reflectance (transflectance) measurement gives the net percentage of light

transmitted through and reflected by the sample (T+R). The absorptance (A) of the sample is then given by equation 2.

$$A = 100\% - (T + R) \tag{3.2}$$

Electrochemical Testing

Samples were removed from the deposition chamber and exposed to atmosphere for 72 hours prior to being assembled into coin cells inside a glove box (MBraun Unilab). This allowed for the formation of a native oxide layer on the surface of the films. Substrates were assembled into type 2032 coin cells against a lithium metal (Alfa Aesar 99%) counter/reference electrode. The electrolyte was 1M LiPF6 in FEC:DEC 1:1 (Solvay Chemicals). Several studies have shown that FEC based electrolytes promote stable cycling with silicon and germanium electrodes.[13, 21, 38-40]. A 25μm thick polypropylene film separator (Celguard 2400) was used. After assembly into coin cells, the electrochemical behavior of samples was tested on a multi-channel battery tester (Arbin BT2143). Cells were cycled between 5mV and 1.5V at various currents with a 5 minute rest period between charge/discharge half cycles. Films were tested for 10 cycles at C/10 followed by 10 cycles each at C/5, C/2, C, 2C, 5C, and then a final 10 cycles at C/10 to examine how the samples recovered from the high rate tests. The cells that performed well at 5C were subjected to an additional 30 cycles with 10 cycles each at 5C, 10C, and 20C. C-rates were calculated for each composition based on Equation 1.

RESULTS AND DISCUSSION

Material Characterization

SEM images of $Si_{(1-x)}Ge_x$ films deposited with an incident angle of 70° from surface normal are shown in Figure 3.1. The films are nanocolumnar over the entire compositional range, but the feature size increases slightly with increasing germanium content. The column diameter is ~10 nm for the silicon film, but the diameter has increased to ~20 nm for the pure germanium film. As the germanium content increases the morphology changes: the individual columns become smoother, *i.e.*, they have fewer branches. This is likely due to germanium's lower melting point. As a general rule, nanostructuring can only be achieved if the substrate temperature is less than 30% of the material's melting point.[33] As the germanium content is increased, it becomes more difficult to grow the non-equilibrium nanocolumnar structures. Because there are morphological changes associated with the changes in composition, we cannot rigorously attribute all changes in electrochemical behavior to compositional effects, but the degree of change in morphology is small compared to the degree of change in measured material properties, so we attribute a majority of the electrochemical changes to changes in composition.

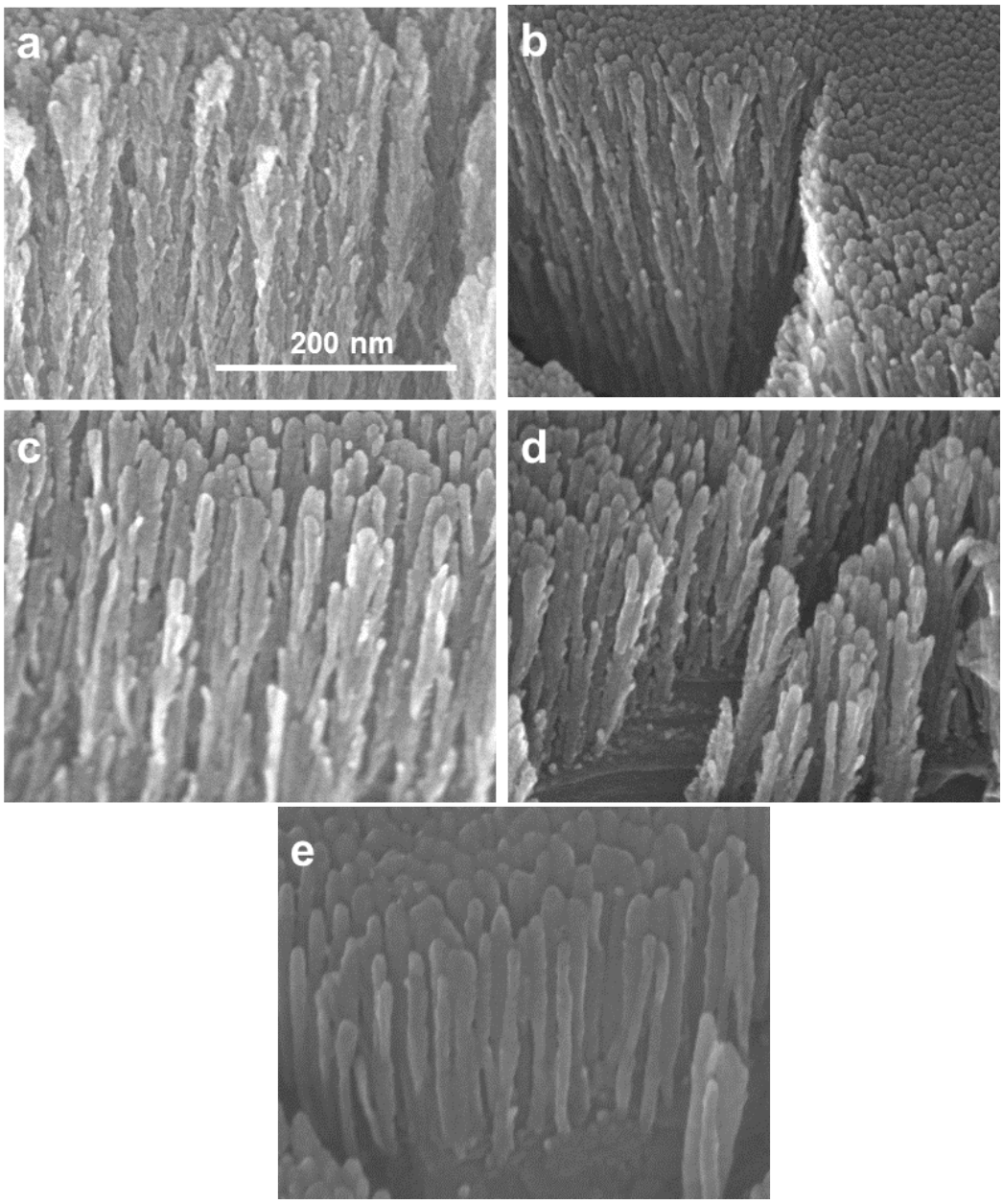

Figure 3.1. SEM Images of a) Si b) $Si_{0.75}Ge_{0.25}$ c) $Si_{0.5}Ge_{0.5}$ d) $Si_{0.25}Ge_{0.25}$ e) Ge thin films deposited at 70° from normal. The scale bar in a) applies to all images.

GLAD synthesis of high melting point materials has been shown to result in amorphous films, and in the case of multi-component depositions, the compositions have

been shown to be well mixed.[34, 37] The ability to grow non-equilibrium, nanocolumnar structures requires that surface diffusion of adatoms be limited. In contrast, phase segregation and crystallization require some degree of surface mobility during deposition to allow for energetically favorable order to develop. No x-ray diffraction peaks were observed for any of the as deposited films. High-resolution transmission electron microscope (HRTEM) imaging and energy-dispersive x-ray spectroscopy (EDS) was performed to ensure that the as deposited material was both amorphous and well mixed. Figure 3.2a shows the HRTEM image of an individual $Si_{0.25}Ge_{0.75}$ nanocolumn. There are no observable lattice fringes indicating that the material is, in fact, amorphous. An EDS line-scan was performed along the path indicated by the arrow in Figure 3.2a. The intensity of the silicon and germanium k_α transitions along that path are shown in Figure 3.2b. The line-scan shows that there are no spatial inhomogeneities in the composition. This confirms that the films are well mixed. Additionally, the film composition as measured by EDS was $Si_{0.26}Ge_{0.74}$, in good agreement with the nominal value determined by the silicon to germanium flux ratio during deposition.

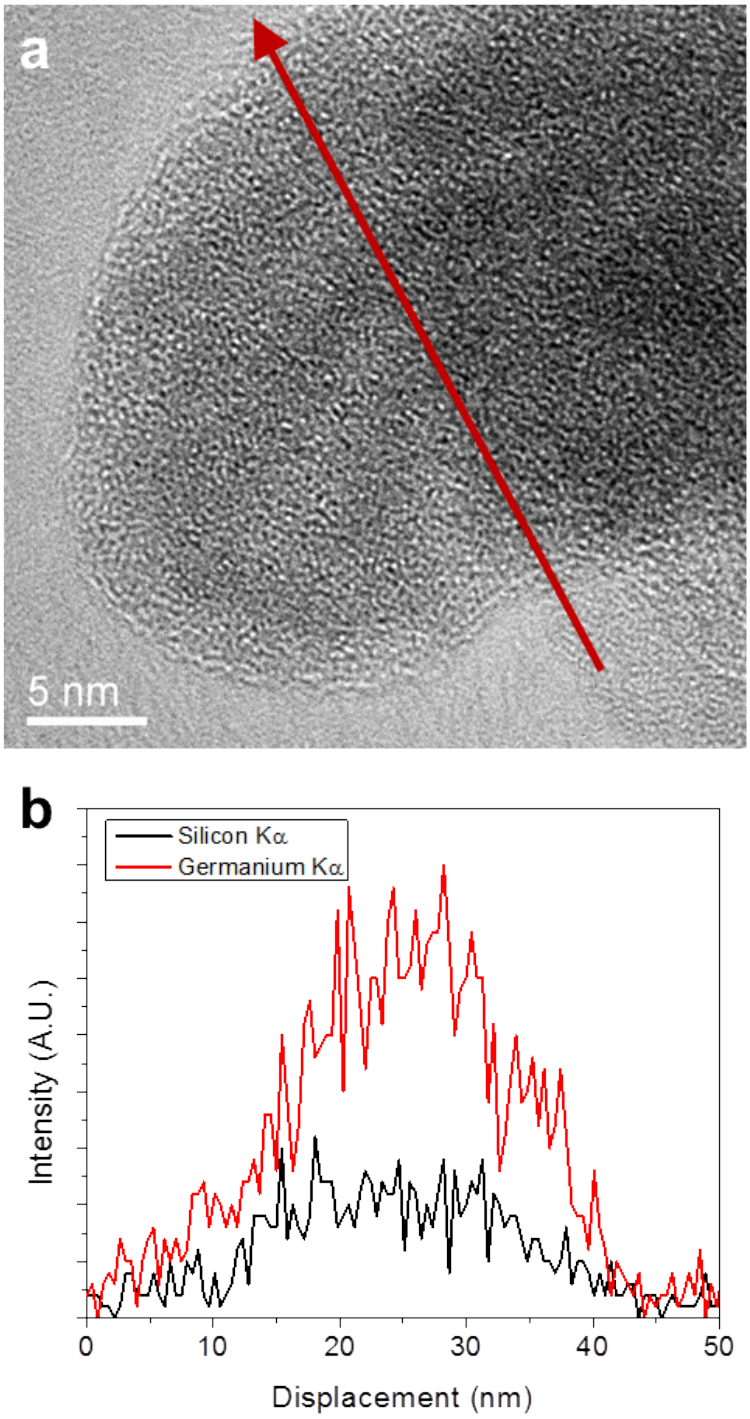

Figure 3.2. a) TEM image of a single $Si_{0.25}Ge_{0.75}$ nanocolumn; b) EDS line-scan across the nanocolumn.

Figure 3.3 shows the Si 2p and Ge 3d peaks of the x-ray photoelectron spectra for the $Si_{(1-x)}Ge_x$ films. The integrated areas of the peaks are used to confirm the nominal compositions of the films determined by the silicon and germanium fluxes measured during deposition. The compositions did not vary upon sputtering, *i.e.* as a function of depth and matched the nominal compositions within a few percent. The measured compositions of the alloy films were $Si_{0.75}Ge_{0.25}$, $Si_{0.48}Ge_{0.52}$, and $Si_{0.22}Ge_{0.78}$. The silicon and germanium films were found to be free of measurable contaminants.

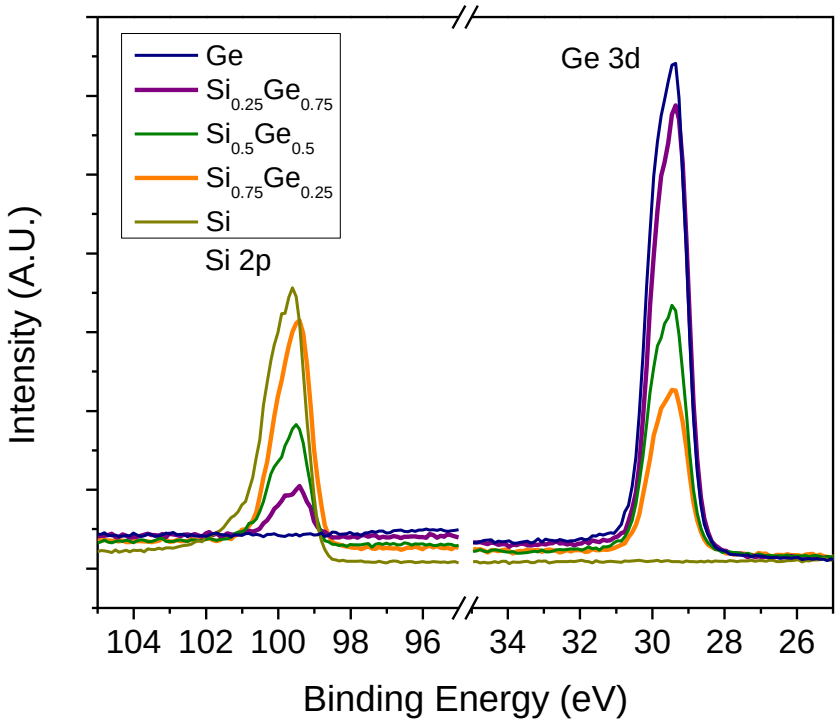

Figure 3.3. XPS spectra of dense $Si_{(1-x)}Ge_x$ films. Quantitative analysis of the Si 2p and Ge 3d peaks indicated that the composition of the films was within a few percentage points of the nominal values. The measurements were repeated at various depths in the films with no change in measured composition.

Figure 3.4 shows the electrical resistivity of dense $Si_{(1-x)}Ge_x$ films deposited on glass at normal incidence. In each case, the resistivity is significantly lower that the intrinsic values published for that composition. The resistivity of semiconductors, however, is very sensitive to impurities. In the manufacture of electronic devices, in the context of which the earlier values were measured, the purity is at least 99.9999%. In contrast, technical grade materials with 99.999% purity were used as the evaporation sources rather than the higher purity semiconductor grade materials. Lower purity could be responsible for the lower than intrinsic resistivity values if the impurities act as n- or p-type dopants rather than mid-gap states. While the level of impurities is still fat below the detection limit for XPS, it is enough to have a significant effect on the resistivity of the films. The lower resistivity of the materials is beneficial to the electrochemical performance of the electrodes, especially at high charge rates.

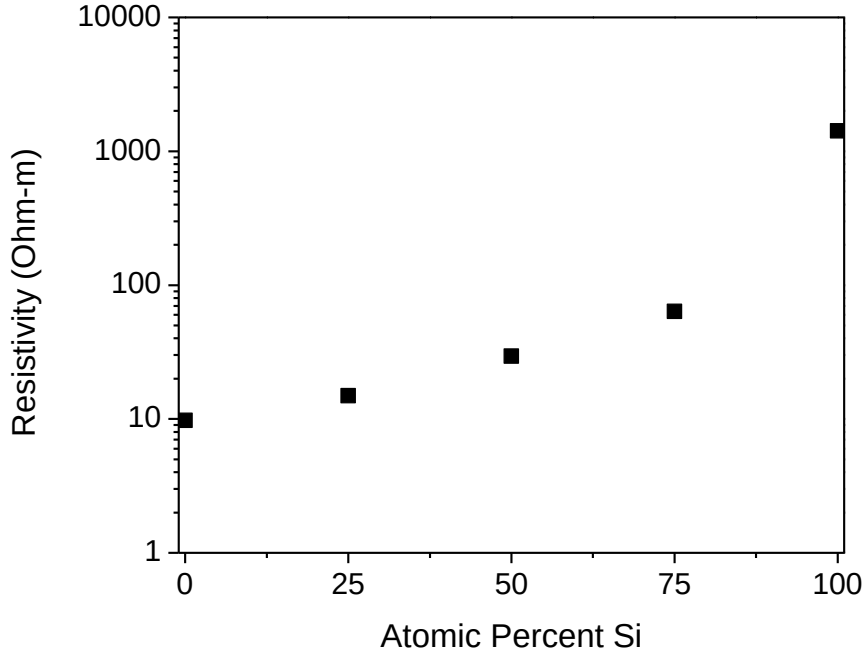

Figure 3.4. Electrical resistivities of dense $Si_{(1-x)}Ge_x$ thin films measured using a 4-pt probe.

The resistivity fell by nearly two orders of magnitude when 25 at. % germanium was incorporated in Si. As the fraction of germanium was increased further, the resistivity slowly fell to the value for pure germanium, *i.e.* the incremental drop in resistivity was largest for small germanium mole fractions. This indicates that a large benefit in electrical resistivity can be gained without sacrificing a large fraction of silicon's capacity.

Raman spectra of the dense $Si_{(1-x)}Ge_x$ films deposited on glass at normal incidence were measured. The spectra from the as deposited films are shown in Figure 3.5a. The features are diffuse as well as shifted ~30 cm^{-1} lower than the expected values for the pure crystalline materials (521 cm^{-1} for Si and 298 cm^{-1} for Ge). Both of these indicate

that the material is amorphous. Broad peaks characteristic of Si-Si, Si-Ge and Ge-Ge vibrations are present for the intermediate compositions. The features sharpen considerably after annealing the films with the Raman laser. Spectra of annealed films are shown in figure 3.5b. Expectedly, the pure silicon and pure germanium films show only vibrations of the homogeneous bonds, whereas the Si-Ge vibration is observed in the intermediate compositions. The peak intensities of the Si-Si, Si-Ge, and Ge-Ge vibrations are similar in the $Si_{0.5}Ge_{0.5}$ film, consistent with random bonding of silicon and germanium rather than preferred bonding of Si with Si or of Ge with Ge. The $Si_{0.75}Ge_{0.25}$ and $Si_{0.25}Ge_{0.75}$ films each had a strong peak for the majority component homogeneous bond and a minor peak for the heterogeneous bond. Additionally, the Si-Si peak shifts to lower wavenumbers as the germanium content of the film is increased. This is due to the germanium atoms disrupting the silicon lattice. The reciprocal is also true. The Ge-Ge peak shifts to lower wavenumbers as the silicon content of the films increases.

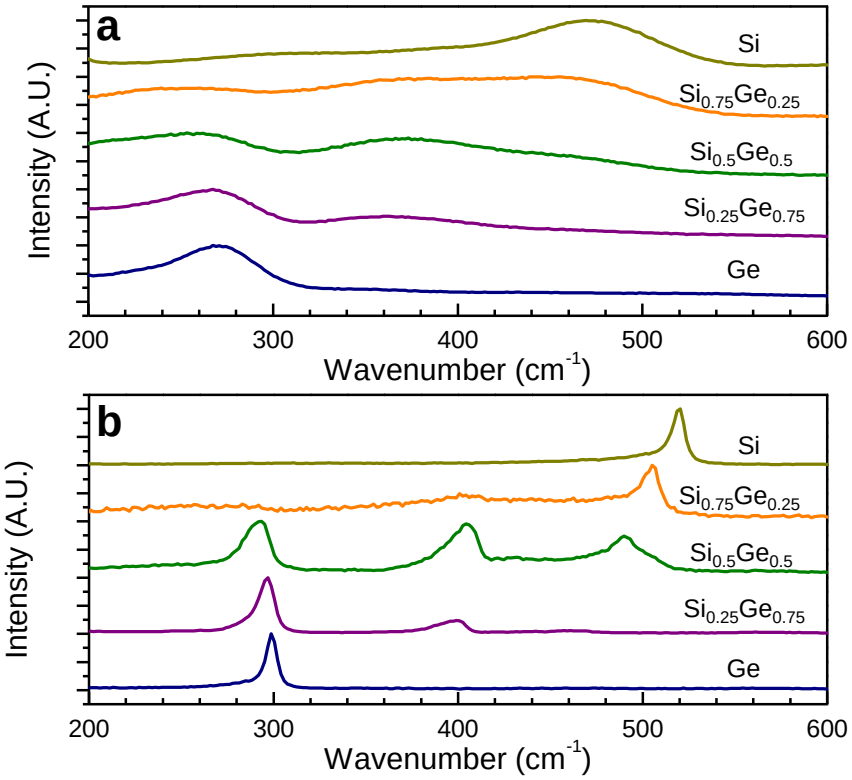

Figure 3.5. Raman spectra of $Si_{(1-x)}Ge_x$ films a) as deposited and b) Raman-laser annealed films.

Figure 3.6 shows absorptance measurements made on dense $Si_{(1-x)}Ge_x$ films deposited on glass at normal incidence. The band gap of a-Si is expected at 1.7 eV, however the band edge appears to start as low as 0.8 eV. Furthermore, there are multiple features in the Si spectrum. A shoulder begins between 1.1 and 1.2 eV, which corresponds to the band gap of c-Si. The curve steepens again around 1.6 eV to a peak centered at 1.8 eV near the value for the band gap of a-Si. Yet another peak begins around 2.0 eV which corresponds to the E_L transition in Si. The reason for the enhanced absorptance at low energies remains unclear, as the HRTEM measurements indicate that

the as deposited material is perfectly amorphous. Data from the electrochemical tests performed on this material are characteristic of a-Si, as well.

The pure Ge spectrum shows a band edge near the expected value of 0.67 eV. The absorptance begins at this point and increases monotonically to a value of ~50%, then levels off. There is a shallow peak centered around 1.2 eV that corresponds to the E_X transition in Ge. The absorption is expected to blueshift with increasing Si content.[41] However, the band edge for the intermittent $Si_{(1-x)}Ge_x$ compounds does not deviate from that of the Ge spectrum, and the Ge E_X transition peak location remains nearly constant as the composition is changed from Ge to $Si_{0.5}Ge_{0.5}$ with the only difference being the relative absorptance. This indicates a lack of compositional homogeneity at the atomic level – the $Si_{(1-x)}Ge_x$ materials synthesized in this study are disordered alloys rather than ordered intermetallics. The Raman data are also somewhat indicative of this feature, which becomes evident when examining the $Si_{0.5}Ge_{0.5}$ film. In an ordered film, the Si-Ge stretch is the only expected peak, as every Si atom would be bonded to a Ge atom, and vice-versa. The Si-Si and Ge-Ge stretches are still observed, however. In fact, the Ge-Ge stretch is evident in the Ge, $Si_{0.25}Ge_{0.75}$ and $Si_{0.5}Ge_{0.5}$ Raman spectra. The band edge for these films remains at the expected value for pure Ge. The $Si_{0.75}Ge_{0.25}$ Raman spectrum is dominated by the Si-Si stretch and shows little Si-Ge or Ge-Ge bonding.

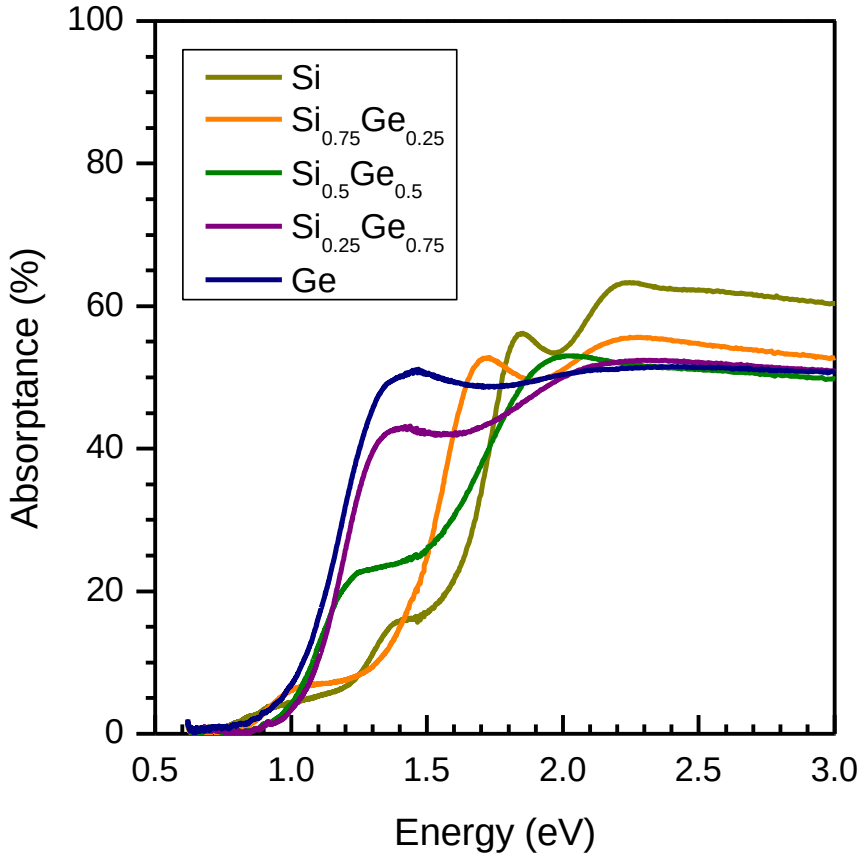

Figure 3.6. Absorptance spectra of $Si_{(1-x)}Ge_x$ films.

Electrochemical Testing

The results of charge/discharge cycling at rates up to 20C are shown in Figure 7a. The reversible capacity of the pure silicon film is 2640 mAh g^{-1}, which is lower than theoretical, but consistent with our previous results for silicon films.[9] The capacities of the $Si_{0.75}Ge_{0.25}$, $Si_{0.5}Ge_{0.5}$, $Si_{0.25}Ge_{0.75}$, and Ge films are 2121, 1883, 1652, and 1217 mAh g^{-1} respectively. These values are lower than expected based on the weighted combination of the capacities of the alloy's components. Specific capacity values were sensitive to the extent of surface oxidation. The films used in this study were exposed to air for 72 hours

before assembly into coin cells to allow the formation of a terminal native oxide layer. Additional films with minimum exposure to atmosphere between deposition and coin cell assembly showed capacities much closer to expected values, see Figures S1–S5. Returning to the data displayed in Figure 3.7, as the C-rate is increased, the performance of the films decreases with pure silicon degrading the most and pure germanium the least. The capacity of the silicon electrode is nearly zero at 5C. After cycling at 5C, the rate is decreased to 1C in order to determine the extent that the capacity recovers. All of the compositions show good capacity recovery. After the recovery cycles, cycling of the $Si_{0.5}Ge_{0.5}$, $Si_{0.25}Ge_{0.75}$, and Ge electrode was continued at 5C, 10C and then 20C rates. The germanium electrode retained a capacity of 644 mAh g^{-1} at 20C, over half of its C/10 capacity. Figure 3.7b shows the cycling data normalized to the maximum capacity of each material. Germanium retains the highest percentage of initial capacity at high rates; this is attributed to its high electronic and ionic conductivities. The retained capacity of the various alloys at a given C-rate decreases with decreasing germanium content; this is a reflection of the conductivity decreasing along with the germanium content. Figure 3.7c shows the same data presented in terms of moles of lithium stored per mole of alloy. Equation 3.1 assumed that each composition could store an equal 3.75 moles of lithium per mole of alloy, but this is not the case. The reversible lithium storage at low currents ranges from 2.75 for silicon to 3.75 for $Si_{0.25}Ge_{0.75}$. The extent of lithiation does not appear to be limited by charge transport or ionic diffusion, as germanium, the material with the highest capacity retention at high rates has an intermediate lithium storage capacity on a molar basis. Additionally, the trend does not appear to be mediated by

expansion-induced structural damage as silicon shows the largest capacity fade while having the lowest molar lithium storage capacity. At this point the reason for the differences in molar lithium storage capacity remains unclear.

The voltage profiles for the first two cycles for each composition are shown in Figure 3.8. The behavior of the films can be split into three groups, with Si and $Si_{0.75}Ge_{0.25}$ forming a group of silicon-like materials; $Si_{0.5}Ge_{0.5}$ exhibiting intermediate behavior; and $Si_{0.25}Ge_{0.75}$ and Ge forming a group of germanium-like materials. The silicon-like materials exhibit two broad lithium insertion and extraction pseudo-plateaus, these pseudo-plateaus are characteristic of single-phase lithiation where the lithium electrochemical potential in the host alloy is changing with composition as additional lithium is added. The germanium-like materials exhibit two lithium insertion pseudo-plateaus, but a single lithium extraction plateau. This single plateau is characteristic of a two-phase coexistence lithium deinsertion mechanism.

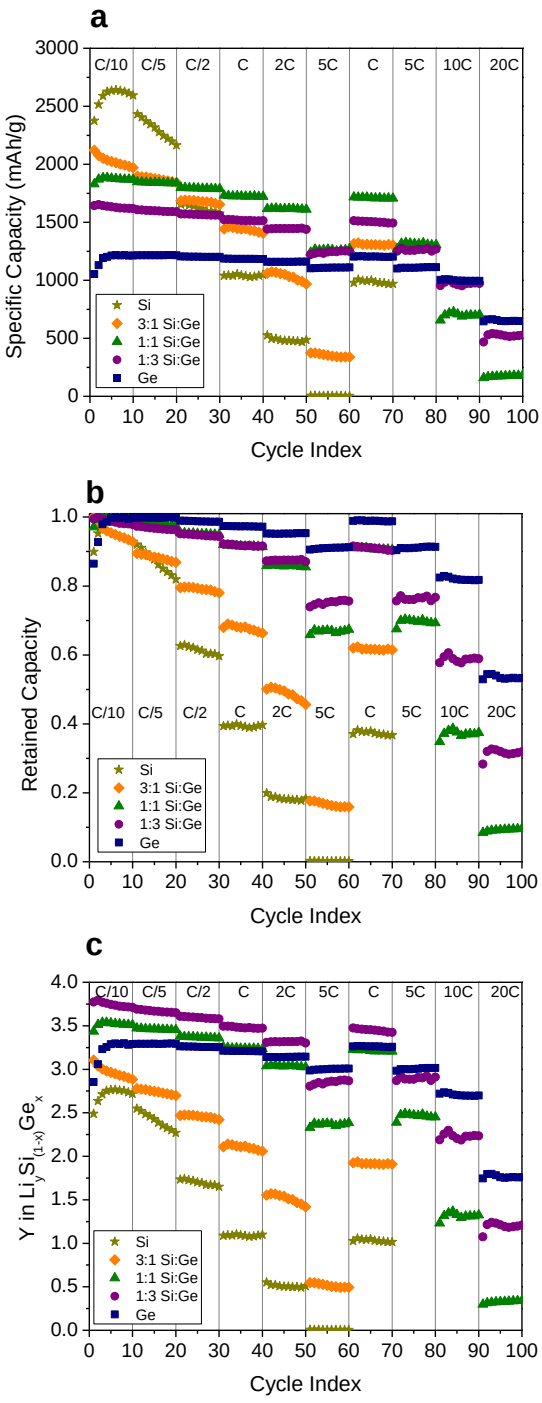

Figure 3.7. Cycling data of films. a) Specific capacity, b) retained capacity, and c) lithium content. Data for pure Si and $Si_{0.75}Ge_{0.25}$ are not shown for cycles 70-100 because the materials could not support the high charge/discharge rates.

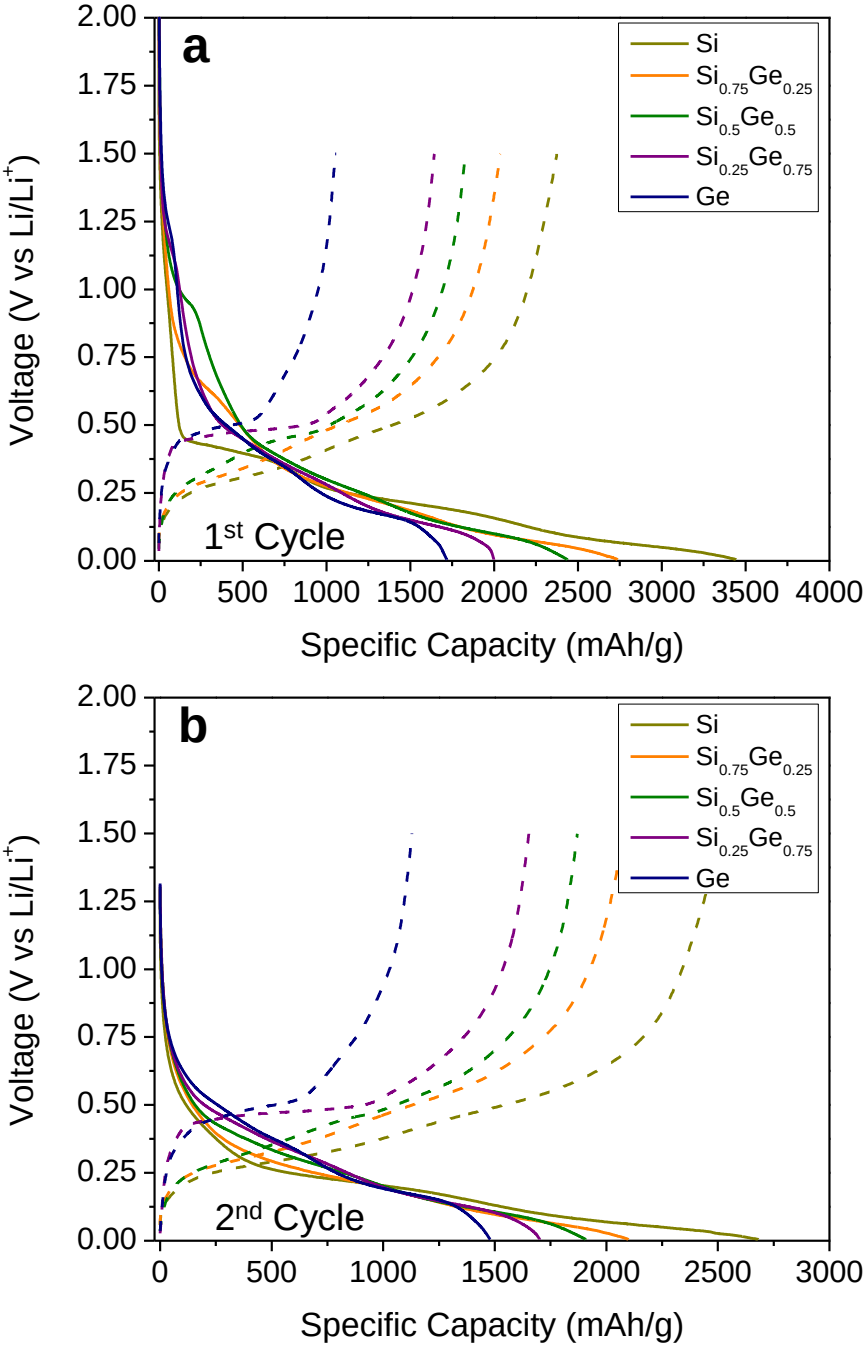

Figure 3.8. Voltage profiles for the a) first and b) second charge/discharge cycles of $Si_{(1-x)}Ge_x$ electrodes.

Additional insight into the separation of lithiation behaviors into distinct groups is obtained by looking at the voltage profiles in differential form as shown in Figure 3.9. The potential of the lithiation and delithiation features varies significantly with composition. During lithiation, each material exhibits broad features characteristic of single-phase lithiation of an amorphous material. However the features shift to more positive potentials as the mole fraction of germanium is increased. For pure silicon, the two broad lithiation features are at ~60 mV and ~220 mV. For germanium, these peaks are at ~170 mV one at ~370 mV. A third peak at ~510 mV is also present. No third peak is present in silicon. This is consistent with previous reports in the literature.[3, 5] For the alloys, the position of the two lithiation features, vary linearly with composition between these two extreme voltages set by the pure components. Additionally, the third germanium peak grows in as the germanium content is increased. The peak potentials for the first cycle lithiation features of the various alloys are plotted in Figure 3.10. The fact that the alloys exhibit shifts in peak position rather than multiple peaks corresponding to pure silicon and pure germanium is additional evidence that the alloys are well mixed at the atomic level.

The lithium extraction behavior of silicon and germanium are markedly different. Silicon undergoes a single-phase delithiation indicated by two broad oxidation features while germanium exhibits one very sharp feature indicating a two-phase mechanism. The silicon-like single-phase behavior of the $Si_{0.75}Ge_{0.25}$ alloy and the germanium-like two-phase behavior of the $Si_{0.25}Ge_{0.75}$ alloys are clearly visible, and the $Si_{0.5}Ge_{0.5}$ alloy shows a superposition of the two behaviors with a sharp germanium-like delithiation feature

growing out of the two broad silicon-like features. Baggetto *et. al* showed that this single lithium extraction peak in pure germanium was due to the fact that it crystallized into the $Li_{15}Ge_4$ phase at potentials below 110mV.[5] The presence of this feature in the germanium-like materials indicates similar behavior. Silicon has been known to crystalize into the $Li_{15}Si_4$ phase when lithiated to potentials below 50 mV, however the phenomenon is particle size dependent, and some morphologies do not crystallize even when held at 0 V.[3] Germanium undergoes crystallization at more positive potentials, thus enabling the formation of the crystalline phase. A small peak is observed at 85mV for germanium and at 65mV for $Si_{0.25}Ge_{0.75}$ that we attribute to the crystallization into the $Li_{15}(Si_{(1-x)}Ge_x)_4$ phase. This is analogous to the feature reported by Baggetto *et. al*.[5] Similar peaks are not present in the films with higher silicon content; most likely due to the more negative voltages required to form the crystalline phase in these films. We believe that the intermediate behavior of $Si_{0.5}Ge_{0.5}$ is due to the material being only partial crystallized at the lower cutoff voltage in the test. These differences can explain the fundamentally different behaviors of the silicon-like and germanium-like materials. Additionally, the lithium deinsertion peaks shift with material composition. The sharp two-phase coexistence peak shifts from 460mV in $Si_{0.5}Ge_{0.5}$ to 500mV in pure germanium. The broad single-phase deinsertion peak shifts from 300mV in pure silicon to 340mV in $Si_{0.5}Ge_{0.5}$.

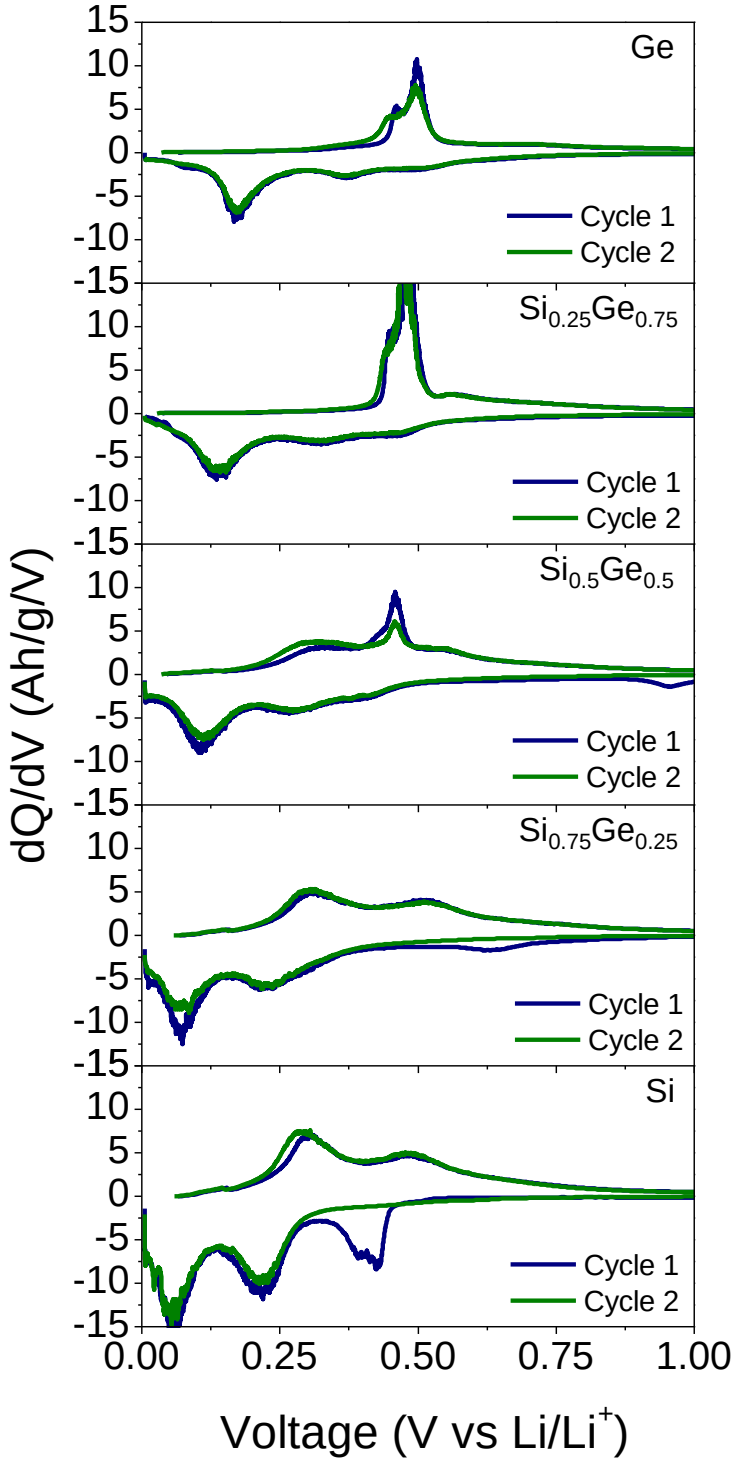

Figure 3.9. Differential capacity plots for the first and second cycles of $Si_{(1-x)}Ge_x$ films.

For pure silicon, there is another peak at ~400 mV which is attributed to the reaction of lithium with surface oxide.[9] Additional information on these oxide reduction peaks can be found in the supporting information. There is an analogous feature in the alloys and in the pure germanium film that shifts to higher voltages as germanium content is increased. This shift is also nearly linear with composition. The magnitude of the oxide reduction feature also decreases with increasing germanium content. This is consistent with the native oxide layer that forms on germanium being thinner than what forms on silicon. The shift in the oxide-reduction potential as a function of composition is also shown in figure 3.10.

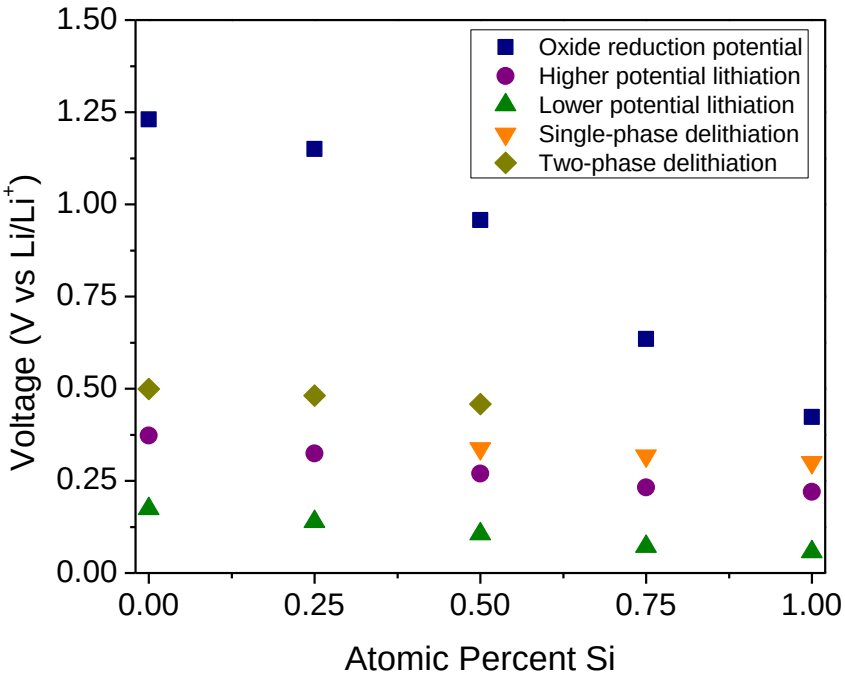

Figure 3.10. Dependence of the peak potentials for lithium insertion and deinsertion on material composition.

CONCLUSIONS

Silicon-germanium alloys of different compositions offer a range of high rate (up to 20C) and high specific capacity lithium-ion battery anodes. The electronic conductivity increases while the specific capacity decreases as germanium content is increased. Additionally, the high-rate performance of the material increases substantially with increasing germanium content. While the silicon films in this study retained almost zero capacity when cycled at 5C, the germanium films retained ~90% their initial capacity, $Si_{0.25}Ge_{0.75}$ retained ~75%, and $Si_{0.5}Ge_{0.5}$ retained ~68%. Silicon alloying mitigates the high cost of germanium and increases the specific capacity of the material. These benefits can outweight the loss of high rate performance – particularly if the maximum charge/discharge rate for the cell is below 5C. $Si_{(1-x)}Ge_x$ alloys give an additional parameter to adjust when tailoring the anode material to the specific current densities demanded by a given battery application.

REFERENCES

1. Wen, C. J.; Huggins, R. A., *J. Solid State Chem.* **1981,** *37*, 271-278.

2. St. John, M. R.; Furgala, A. J.; Sammells, A. F., *J. Electrochem. Soc.* **1982,** *129*, 246-250.

3. Hatchard, T. D.; Dahn, J. R., *J. Electrochem. Soc.* **2004,** *151*, A838-A842.

4. Obrovac, M. N.; Christensen, L., *Electrochem. Solid-State Lett.* **2004,** *7*, A93-A96.

5. Baggetto, L.; Notten, P. H. L., *J. Electrochem. Soc.* **2009,** *156*, A169-A175.

6. Graetz, J.; Ahn, C. C.; Yazami, R.; Fultz, B., *J. Electrochem. Soc.* **2004,** *151*, A698-A702.

7. Zhou, S.; Liu, X.; Wang, D., *Nano Lett.* **2010,** *10*, 860-863.

8. Magasinski, A.; Dixon, P.; Hertzberg, B.; Kvit, A.; Ayala, J.; Yushin, G., *Nat. Mater.* **2010,** *9*, 353-358.

9. Abel, P. R.; Lin, Y.-M.; Celio, H.; Heller, A.; Mullins, C. B., *ACS Nano* **2012,** *6*, 2506-2516.

10. Chan, C. K.; Patel, R. N.; O'Connell, M. J.; Korgel, B. A.; Cui, Y., *ACS Nano* **2010,** *4*, 1443-1450.

11. Chan, C. K.; Peng, H.; Liu, G.; McIlwrath, K.; Zhang, X. F.; Huggins, R. A.; Cui, Y., *Nat. Nanotechnol.* **2008,** *3*, 31-35.

12. Fleischauer, M. D.; Li, J.; Brett, M. J., *J. Electrochem. Soc.* **2009,** *156*, A33-A36.

13. Chockla, A. M.; Klavetter, K.; Mullins, C. B.; Korgel, B. A., *Chem. Mater.* **2012**.

14. Chockla, A. M.; Bogart, T. D.; Hessel, C. M.; Klavetter, K. C.; Mullins, C. B.; Korgel, B. A., *J. Phys. Chem. C* **2012,** *116*, 18079-18086.

15. Chan, C. K.; Zhang, X. F.; Cui, Y., *Nano Lett.* **2007,** *8*, 307-309.

16. Chockla, A. M.; Panthani, M. G.; Holmberg, V. C.; Hessel, C. M.; Reid, D. K.; Bogart, T. D.; Harris, J. T.; Mullins, C. B.; Korgel, B. A., *J. Phys. Chem. C* **2012,** *116*, 11917-11923.

17. Laforge, B.; Levan-Jodin, L.; Salot, R.; Billard, A., *J. Electrochem. Soc.* **2008,** *155*, A181-A188.

18. Liu, X. H.; Huang, S.; Picraux, S. T.; Li, J.; Zhu, T.; Huang, J. Y., *Nano Lett.* **2011,** *11*, 3991-3997.

19. Park, M.-H.; Cho, Y.; Kim, K.; Kim, J.; Liu, M.; Cho, J., *Angew. Chem. Int. Ed.* **2011,** *50*, 9647-9650.

20. Seo, M.-H.; Park, M.; Lee, K. T.; Kim, K.; Kim, J.; Cho, J., *Energy & Environmental Science* **2011,** *4*, 425-428.

21. Chockla, A. M.; Klavetter, K. C.; Mullins, C. B.; Korgel, B. A., *ACS Appl. Mater. Interfaces* **2012,** *4*, 4658−4664.

22. Conwell, E. M., *Proc. IRE* **1952,** *40*, 1327-1337.

23. Fuller, C. S.; Severiens, J. C., *Phys. Rev.* **1954,** *96*, 21-24.

24. Johnson, Q.; Smith, G. S.; Wood, D., *Acta Crystallogr.* **1965,** *18*, 131-132.

25. Levinshtein, M. E. R., Sergey L.; Shur, Michael S., *Properties of Advanced Semiconductor Materials: GaN, AlN, InN,NB,SiC, SiGe*. John Wiley and Sons: New York, 2001.

26. Atabaev, I.; Matchanov, N.; Bakhranov, É., *Phys. Solid State* **2001,** *43*, 2234-2236.

27. Hwang, C.-M.; Lim, C.-H.; Park, J.-W., *Thin Solid Films* **2011,** *519*, 2332-2338.

28. Hwang, C.-M.; Park, J.-W., *Electrochim. Acta* **2011,** *56*, 6737-6747.

29. Song, T.; Cheng, H.; Choi, H.; Lee, J.-H.; Han, H.; Lee, D. H.; Yoo, D. S.; Kwon, M.-S.; Choi, J.-M.; Doo, S. G.*, et al.*, *ACS Nano* **2012,** *6*, 303-309.

30. Hashimoto, Y.; Machida, N.; Shigematsu, T., *Solid State Ionics* **2004,** *175*, 177-180.

31. Wang, J.; Du, N.; Zhang, H.; Yu, J.; Yang, D., *J. Power Sources* **2012,** *208*, 434-439.

32. Flaherty, D. W.; Hahn, N. T.; May, R. A.; Berglund, S. P.; Lin, Y.-M.; Stevenson, K. J.; Dohnalek, Z.; Kay, B. D.; Mullins, C. B., *Acc. Chem. Res.* **2012,** *45*, 434–443.

33. Hawkeye, M. M.; Brett, M. J., *J. Vac. Sci. Technol., A* **2007,** *25*, 1317-1335.

34. Lin, Y.-M.; Abel, P. R.; Flaherty, D. W.; Wu, J.; Stevenson, K. J.; Heller, A.; Mullins, C. B., *J. Phys. Chem. C* **2011,** *115*, 2585-2591.

35. Berglund, S. P.; Rettie, A. J. E.; Hoang, S.; Mullins, C. B., *Phys. Chem. Chem. Phys.* **2012,** *14*, 7065-7075.

36. Berglund, S. P.; Flaherty, D. W.; Hahn, N. T.; Bard, A. J.; Mullins, C. B., *J. Phys. Chem. C* **2011,** *115*, 3794-3802.

37. Hahn, N. T.; Mullins, C. B., *Chem. Mater.* **2010,** *22*, 6474-6482.

38. Nakaiz, H.; Kubota, T.; Kita, A.; Kawashima, A., *J. Electrochem. Soc.* **2011,** *158*, A798-A801.

39. Lin, Y.-M.; Klavetter, K. C.; Abel, P. R.; Davy, N. C.; Snider, J. L.; Heller, A.; Mullins, C. B., *Chem. Commun.* **2012,** *48*, 7268-7270.

40. Etacheri, V.; Haik, O.; Goffer, Y.; Roberts, G. A.; Stefan, I. C.; Fasching, R.; Aurbach, D., *Langmuir* **2011,** *28*, 965-976.

41. Braunstein, R.; Moore, A. R.; Herman, F., *Phys. Rev.* **1958,** *109*, 695-710.

Chapter 4: Sub-Stoichiometric Germanium Selenide Nanocolumns for Lithium-Ion Battery Anodes Capable of Charging in Seconds

INTRODUCTION

The power density of lithium batteries is limited by the anode, as cathode materials such as $LiCoO_2$[1] and $LiMn_{1.5}Ni_{0.5}O_4$[2] support high charging and discharging rates, i.e., current densities. When graphite anodes are charged at a higher rate, their coulombic efficiency drops and, more importantly, they pose an increased risk of fire due to the formation of metallic lithium dendrites.[3-5] Anode materials such as Mo_3Sb_7[6] and $Li_4Ti_5O_{12}$[7-8] also support high rates, but at the cost of a greatly reduced battery voltage, as their redox potentials are respectively ~1 V and ~1.5 V oxidizing versus the reversible Li/Li^+ half-cell potentials. In contrast, the reversible potential of the most widely used graphite based anode is merely ~100 mV positive of the Li/Li^+ half-cell potential. The ideal anode material would have a redox potential close to Li/Li^+ yet still be able to support high current densities. Germanium based lithium-ion battery anodes of high lithium storage capacity have been extensively studied because their lithium insertion potential of ~300 mV suffices for reducing the likelihood of plating of metallic lithium and the associated risk of growth of dendrites, without excessive sacrifice of battery voltage.[9-13] The diffusivity of lithium in germanium is high, sufficient for high current densities. Nanostructured germanium supports lithium insertion rates of up to 40 C (55A g^{-1})[13] and lithium de-insertion rates of 100 C (138 A g^{-1}).[12]

While germanium and germanium-based materials have many desirable properties, germanium is ~1000 times more expensive than presently used graphite (~\$1 g^{-1} for germanium versus ~\$0.001 g^{-1} for graphite). While cost becomes exorbitant for stationary and vehicle-scale battery packs, the gram-scale quantities of germanium required for personal electronics-sized batteries is not prohibitively expensive.

Both Ag^+ and Li^+ diffuse rapidly in semiconducting germanium chalcogenides $GeSe_x$ and GeS_x ($x > 2$) and germanium chalcogenide glasses. The band gap of GeS_2 is larger than that of $GeSe_2$ and in $GeSe_x$ the band gap increases with x. The transport of Ag^+ in $GeSe_2$ has been extensively studied since the 1979 discovery of lithographic resists including photoresists, [14-16] e-beam resists, [17]and ion-beam resists consisting of a thin Ag_2Se film on semiconducting $GeSe_2$.[18] In these, photogenerated holes are captured by the Ag_2Se to produce Ag^+ ions, which drift to trapped photogenerated electrons in the $GeSe_2$ bulk. While the required deep electron traps in the resists necessitate their being electronic insulators, in lithium battery anodes a small band gap providing electronic conductivity is preferred, hence our preference for a high Ge: Se ratio.

Germanium chalcogenides glasses of the composition $(Li_2X)_y(GeX_2)_{(1-y)}$ (X = O, S, Se) have been shown to have exceptionally high Li^+ conductivity.[19-21] The nature of the enhanced conductivity has been attributed to a decrease in connectivity between adjacent germanium chalcogenide polyhedra in the glass forming network due to the presence of the modifying agent (Li_2X).[22] Such structural features significantly lower the activation energy required for Li^+ ions to hop between adjacent lattice sites. As such, the concentration of the modifying agent has a large effect on the material's ionic

conductivity.[20] Kim *et al.* studied lithium insertion/de-insertion in larger band gap germanium oxide and germanium sulfide glasses and found large first cycle irreversible capacities due to the formation of lithium chalcogenides. [23] GeS_2 outperforms GeO_2 because of the higher ionic conductivity of the Li_2S versus the Li_2O formed upon lithiation. The higher ionic conductivity of the Li_2S relative to Li_2O is attributed to the sulfide's larger polarizability.[20] Cho *et al.* reported that GeS and GeS_2 nanoparticles had good cycling stability and capacity retention at rates up to 5 C.[24] Additional work on nanocrystalline GeO_2 and GeS confirmed the superiority of the sulfur containing material, especially at high current densities.[25] The selenide system has not yet been applied to lithium-ion batteries, but it is of interest as the polarizability of selenium is even higher than that of sulfur.[19]

Sub-stoichiometric, nanocolumnar germanium selenide thin films were formed by glancing angle deposition (GLAD), in which evaporated gas-phase atoms were impinged on the substrate at an oblique angle. The surface of the substrate is roughened in the early stages of deposition due to stochastic variation in deposition rate. GLAD provides nanocolumnar films if the surface diffusion is limited.[26] The roughness created in the early stages of deposition is amplified by self-shadowing.[27] In GLAD, the morphology of the film is tuned by varying the deposition angle. Dense films are grown when the deposition angle is close to the surface normal while nanocolumnar films are grown at more oblique angles. [28] Details on GLAD and its applications can be found elsewhere.[9, 29-32]

EXPERIMENTAL METHODS

Material Synthesis

$GeSe_2$ was synthesized from its component elements (Germanium, 99.999% from Kurt J Lesker, and Selenium 99.999% from Alfa-Aesar) by heating them to 1000 ^oC in a sealed quartz tube for 24 hours followed by cooling at a rate of $1^oC\ min^{-1}$ until the ampule was below the material's glass-transition temperature. The resulting material was a mixture of crystalline and amorphous $GeSe_2$ as determined by XRD and EDX (See Supporting Information, Figure C.1). Germanium sub-selenide electrodes were vacuum deposited by diluting thermally evaporated $GeSe_2$ with additional germanium from a second evaporation source. Material was deposited on 15.6 mm diameter stainless steel substrates (Pred Materials) at an incident angle of 70^o from the surface normal. The substrates were cleaned by sonication in ethanol prior to deposition. The deposition rate of each evaporator was calibrated using a quartz crystal microbalance (Inficon), and the mass density of the electrodes was 50 $\mu g\ cm^{-2}$.

Material Characterization

SEM images of the electrodes were obtained with a Hitachi S5500 equipped with a Bruker x-ray detector for EDX measurements. TEM was performed on a JEOL 2010F. Samples for TEM were deposited on 10 μm thick copper foil. The TEM sample were prepared by ultramicrotome sectioning of of resin-embeded electrdes. A more detailed procedure is described elsewhere.[11] XRD was performed on a Bruker D8 powder x-ray diffractometer. Resistivity measurements were made with a Lucas four-point probe employing a Keithley 220 programmable current source.

Electrochemical testing

As-deposited films were assembled into 2032 coin cells in an argon-filled glove-box (MBraun Unilab) with oxygen and water levels held below 5 ppm. Lithium metal (Alfa Aesar 99%) was used as the counter/pseudoreference electrode and 1 M $LiPF_6$ (Sigma Aldrich, battery grade) in a 1:1 mixture of fluorinated ethylene carbonate (Solvay Chemicals) and diethyl carbonate (Sigma Aldrich, battery grade) as the electrolyte. Celgard 2400 polypropylene membrane was used as the separator. Cells were galvanically cycled using an Arbin BT2043 multichannel battery tester. Cells were cycled between 5 mV and either 1.5 V or 2V *versus* Li/Li^+. PITT was also performed on the Arbin BT2043 using voltage steps of 15mV. The voltage was held until the current decayed below C/250.

RESULTS AND DISCUSSION

Scanning electron microscope (SEM) images of a $Ge_{0.9}Se_{0.1}$ film deposited at a glancing angle of 70° versus normal are shown in Figure 4.1a-b. The film consists of a close-packed forest of nanocolumns that are 10 - 15 nm in diameter. The spaces between the individual columns accommodate the large volume expansion during lithium insertion and the nanocolumnar films are well retained on their stainless steel substrates. In contrast, dense films of silicon and germanium, deposited normally to the surface, are delaminated upon repeated lithiation and sodiation.[33-34] Figure 4.1c shows that the nanocolumnar film is amorphous, i.e., that its x-ray diffraction pattern is featureless. Nanocolumnar GLAD films tend to be amorphous because the formation of long-range order requires adatom mobility while the growth of nanocolumnar features requires that

surface diffusion be limited. The energy dispersive x-ray spectrum of the film (Figure 4.1d) shows that its germanium: selenium ratio is 10:1. The lesser EDX carbon, iron, nickel and chromium peaks derive of the stainless steel substrate.

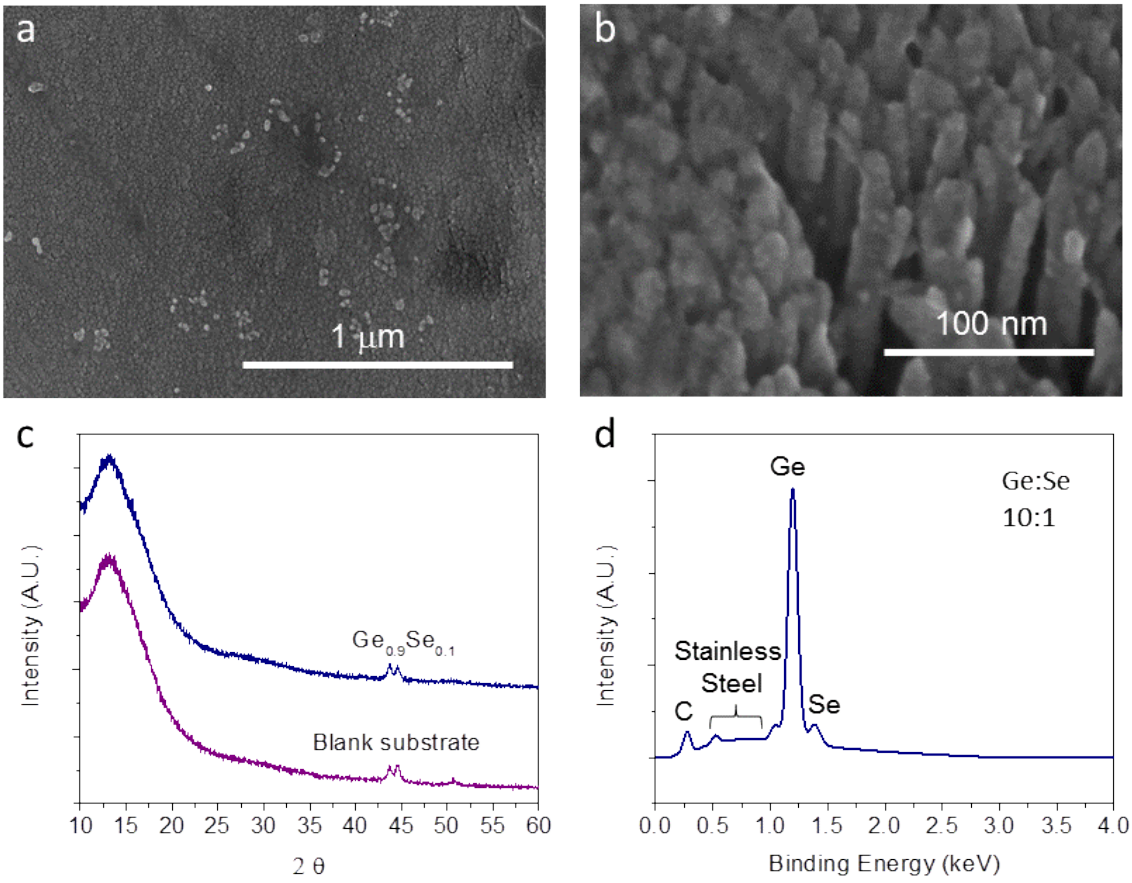

Figure 4.1. Morphology and chemical analysis of a $Ge_{0.9}Se_{0.1}$ electrode. a) Low and b) high magnification SEM images a $Ge_{0.9}Se_{0.1}$ electrode deposited a 70° from surface normal. c) XRD pattern a $Ge_{0.9}Se_{0.1}$ electrode compared to that of a blank substrate, and d) EDX of of a $Ge_{0.9}Se0.1$ electrode showing an elemental composition close to the nominal value.

The electrical resistivity of a dense $Ge_{0.9}Se_{0.1}$ film evaporatively deposited at normal incidence on glass as measured by four-point probe measurements was ~50 ohm-cm, less than the 100 ohm-cm resistivity measured for amorphous evaporated germanium[35] and much less than the $1.4x10^5$ ohm-cm resistivity for amorphous silicon[9] – two well-studied, high-capacity lithium-ion battery electrode materials. Electrode resistance contributes to the overpotential required to charge at a given rate; therefore low resistivity is advantageous for high-rate electrode materials.

The tested coin cells had nanocolumnar $Ge_{0.9}Se_{0.1}$ working electrodes and metallic lithium counter-electrodes. Assuming that only germanium contributes to the reversible capacity, the calculated specific capacity of the films is 1.25 Ah g^{-1}. As seen in Figure 3.2, this composition has better rate capability than structurally similar electrodes with either higher or lower selenium content. Pure germanium, $Ge_{0.9}Se_{0.1}$, and $Ge_{0.8}Se_{0.2}$ – all GLAD deposited at 70 º vs. normal – electrodes were electrochemically cycled for 10 cycles each at 1 C, 2 C, 5 C, and 10 C, followed by recovery at 1 C. The superior capacity retention of the $Ge_{0.9}Se_{0.1}$ becomes apparent at rates as low as 2C and is increasingly visible at higher rates. At 10 C, the $Ge_{0.9}Se_{0.1}$ retains 94% of its 1 C capacity while the electrodes with higher and lower selenium content retain only ~82% of their 1 C capacities. A comparison of the similar morphologies of the three compositions is found in the Supporting Information (Figure C.2).

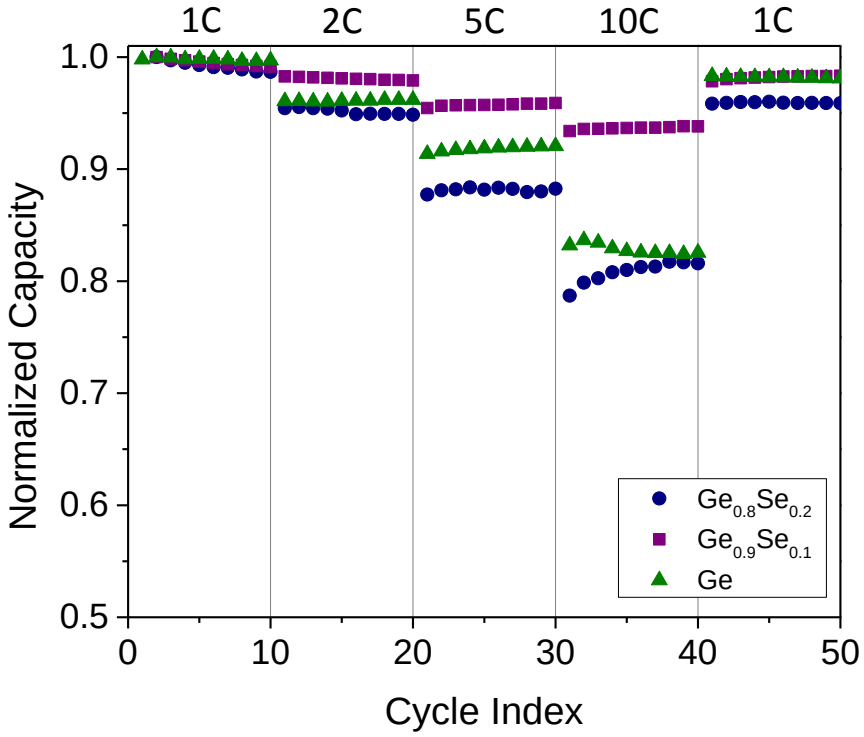

Figure 4.2. Electrochemical cycling of germanium sub-selenide films of various selenium content at rates up to 10 C.

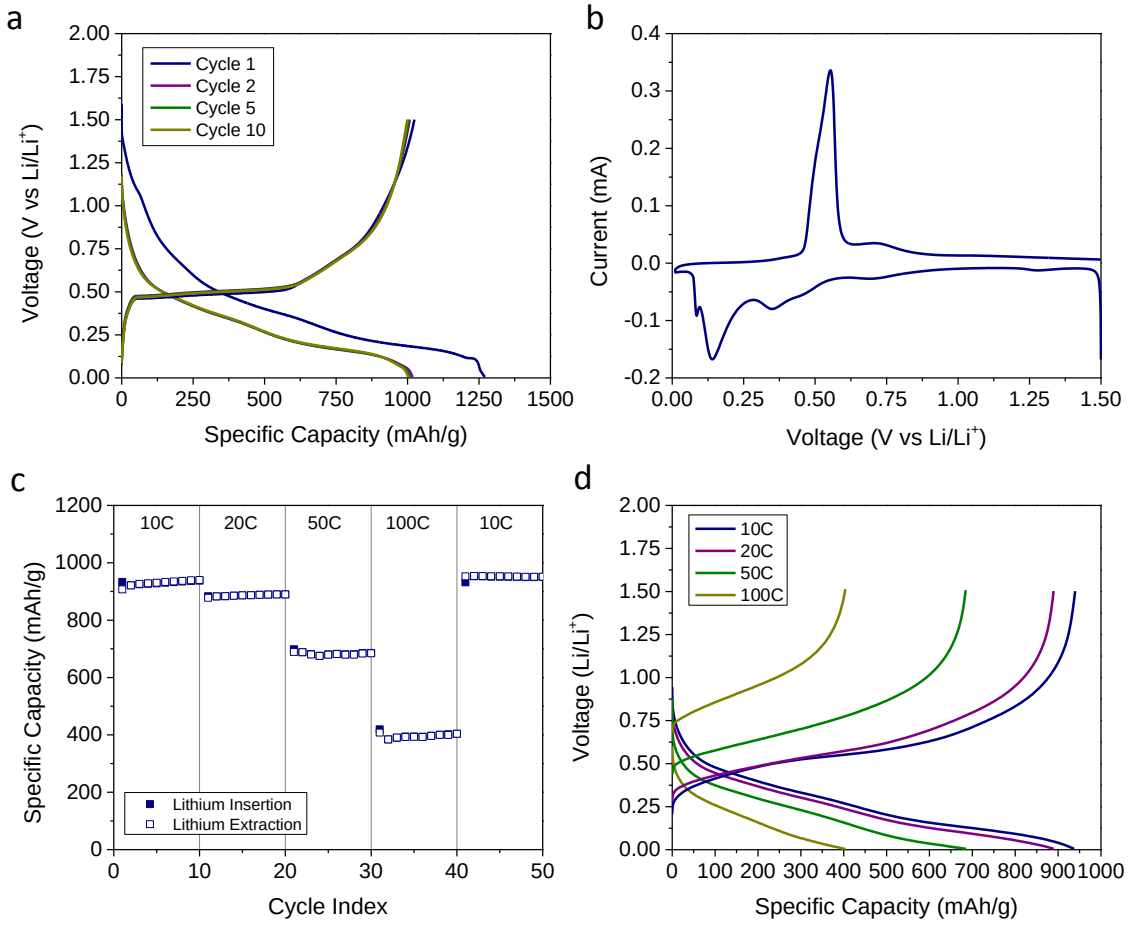

Figure 4.3. Electrochemical analysis of $Ge_{0.9}Se_{0.1}$ electrodes. a) Lithium insertion/extraction voltage profiles for cycles 1, 2, 5, and 10 at C/10, b) Cyclic voltammogram at a scan rate of 0.1 mV/s, c)specific capacity versus cycle number for cycling at rates from 10 C – 100 C, and d) voltage profiles for the 10th cycle at each C-rate for $Ge_{0.9}Se_{0.1}$.

Figure 4.3a shows the voltage profiles for the first, 2nd, 5th and 10th cycles at a slow, C/10, rate. In the first cycle Li-insertion step the $Ge_{0.9}Se_{0.1}$ alloy is converted to a mixture of non-cycling Li_2Se and a series of cycling Li-Ge alloys. Of these, LiGe, Li_9Ge_4, $Li_{16}Ge_5$, and $Li_{22}Ge_5$ were reported to persist at 400◦C, where their reversible potentials in

molten LiCl-KCl are between 62 mV and 580 mV vs. Li/Li^+. [36] As seen in the 25◦C, 0.1 mV s^{-1} voltammogram of Figure 4.3b, this range is well overlapped by the Li alloying peaks and shoulders at 0.08 V, 0.14 V, 0.33 V and 0.46 V and the de-alloying broad peak at 0.63 V and shoulder at 0.50 V. The first cycle lithium insertion profile shows a broad sloping region between 1 V and 0.5 V, attributed to non-cycling Li_2Se and SEI formation; below 0.5 V, the profile shows multiple broad pseudo-plateaus consistent with the expected staged lithiation of amorphous germanium (see below), including a small plateau at 100 mV consistent with that expected for crystalline $Li_{15}Ge_4$.[12] A flat lithium extraction plateau, seen only at very slow rates, suggests a slowly crystallizing lithiated germanium phase.

Figure 4.3c shows the cycling of the $Ge_{0.9}Se_{0.1}$ electrode for 10 cycles each at 10 C, 20 C, 50 C and 100 C rates. While the material is stable at these rates, the retained capacity drops at 50 and 100 C, ~70% of the 1C capacity being retained at 50 C and ~40% at 100 C. As seen in the 10^{th} cycle voltage profiles at each rate (Figure 4.3d), lithium insertion is slower than its extraction, as all inserted lithium is removed well before the upper cutoff voltage is reached. This is as expected for the rate limiting step being stripping of the Li^+ solvation shell or its diffusion through the SEI layer.

Figure 4.4 shows the discharge voltage profiles for $Ge_{0.9}Se_{0.1}$ lithiated at 1 C, and then delithiated at various rates between 1 and 1800 C up to a voltage cutoff of 2V. As the rate is increased, the lithium stripping voltage increases, but the capacity is little-affected up to a rate of 400 C, where 87% of the capacity is retained; at a rate of 1100 C, 75% is retained and 0.94 Ahr g^{-1} is discharged in 2.5 seconds; at an 1800 C rate, 36% of

the capacity is still retained. The well-retained capacity at high rates is indicative of fast lithium transport in the solid state. The polarization at the lithium counter electrode is necessarily included in the increased lithium stripping voltage at high rates due to the use of two-electrode coin-cells in this test.

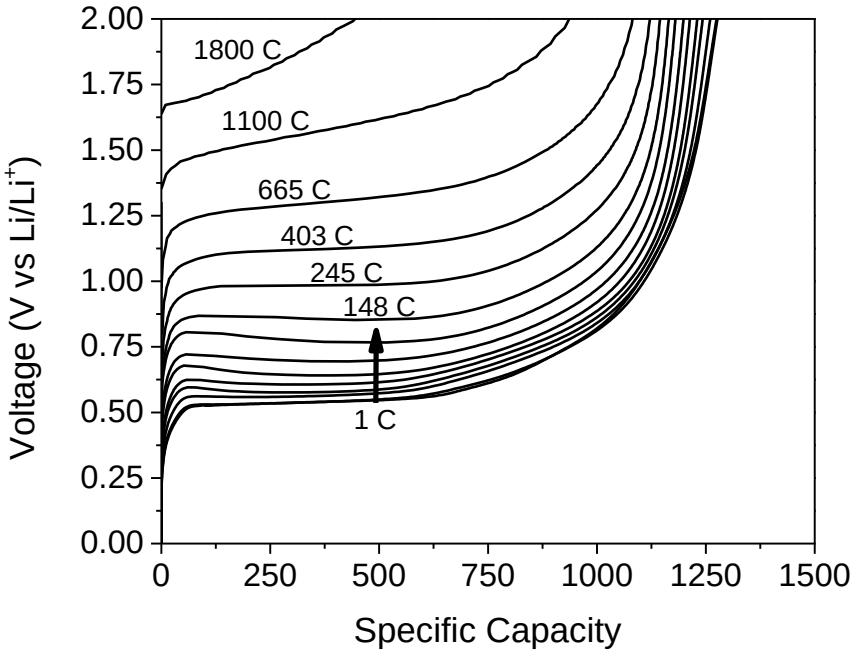

Figure 4.4. Electrochemical stripping at various rates.A $Ge_{0.9}Se_{0.1}$ electrode was lithiated at 1 C and the delithiated at rates ranging 1 C to 1800 C. 75% of the theoretical capacity is retained at 1100 C, or a current density of 1340 A/g.

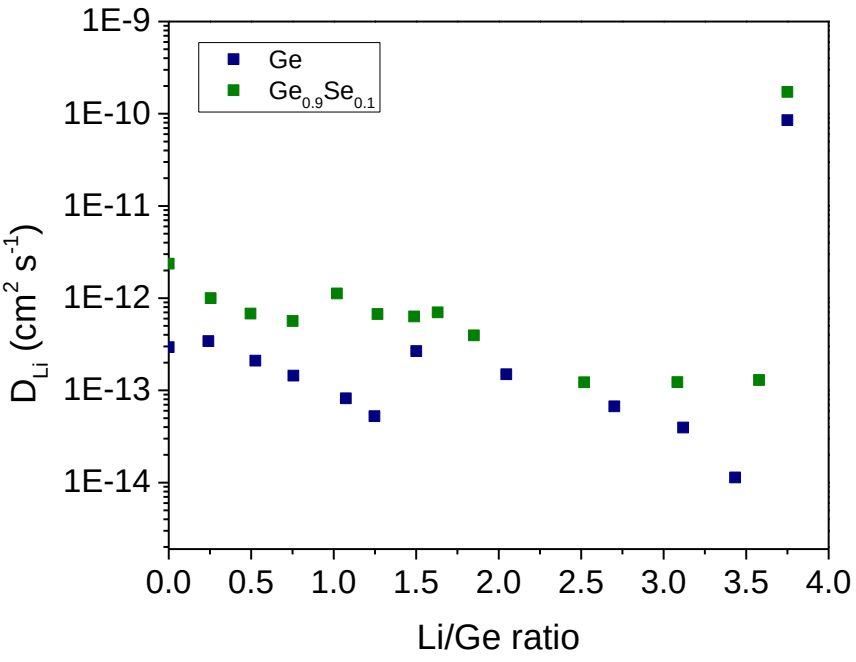

Figure 4.5. Lithium diffusion coefficient as measured by PITT with 15mV voltage steps.

Potentiostatic intermittent titration technique (PITT) was performed on both Ge and $Ge_{0.9}Se_{0.1}$ electrodes to determine the chemical diffusion coefficients for lithium in each material.[37] Figure 4.5 shows the lithium diffusion coefficients for each material as a function of the state of charge. The diffusion coefficient for lithium in $Ge_{0.9}Se_{0.1}$ was found to be an order of magnitude higher than for in pure germanium in the delithiated state ($2.5x10^{-12}$ cm^2 s^{-1} for $Ge_{0.9}Se_{0.1}$ *versus* $3x10^{-13}$ cm^2 s^{-1} for Ge). As the Li/Ge ratio is increased, the lithium diffusion coefficient in germanium passes through two local minima at Li/Ge = 1.25 and Li/Ge = 3.5. These features are absent in $Ge_{0.9}Se_{0.1}$. The diffusion of lithium has been decoupled from the state of charge of the germanium in the selenium containing sample due likely due to the presence of a fast lithium conducting

selenide phase present in the material. This lithium conducting phase provides an alternate pathway for lithium diffusion and shortens the effective lithium diffusion length in the sample. In the fully lithiated state, however, lithium diffusion in both samples was both more rapid and closer in magnitude ($1.7x10^{-10}$ cm^2 s^{-1} for $Ge_{0.9}Se_{0.1}$ *versus* $8.5x10^{-11}$ cm^2 s^{-1} for Ge). This is at a state of charge where the germanium would have crystallized into $Li_{15}Ge_4$. The similar diffusion coefficients indicate that lithium transport in $Li_{15}Ge_4$ is nearly as rapid as in the selenide phase present in $Ge_{0.9}Se_{0.1}$.

Cross-sectional TEM images of $Ge_{0.9}Se_{0.1}$ nanocolumnar films, both as-deposited and after one lithiation/delithiation cycle, are shown in Figure 4.6. The as-deposited material shown in figure 4.6a appears spatially homogeneous at the nanometer scale. The absence of diffraction pattern or lattice fringes confirms that the material is amorphous. The cycled material is shown in figure 4.6b. It remains amorphous, but domains of a second phase appear to have formed. From the images, the size of these domains is roughly 2 nm. Additional high-res images are shown in Figure C.3. $Ge_{0.9}Se_{0.1}$, the composition of the as-deposited material, is not thermodynamically stable, with Ge and GeSe being the stable coexisting phases at room temperature.[38] However, the phase segregation is induced by electrochemical lithium insertion and stripping, therefore the selenium-rich domains likely contain significant amounts of lithium as the reaction between lithium and chalcogenides are electrochemically irreversible. Glassy lithiated germanium selenides are known fast ion conductors,[19-20] and we attribute the high-rate performance of the $Ge_{0.9}Se_{0.1}$ electrodes to the presence of this phase. The selenium-rich phase forms isolated domains rather than a percolating network, so the increase in

diffusion coefficient in the composite material will be geometry dependent. If the length scale of the composite is much greater than the length scale of the selenium-rich domains, the reduction in effective lithium diffusion length will be small. PITT measurements on dense germanium and $Ge_{0.9}Se_{0.1}$ films revealed their lithium diffusion coefficients to be very similar over the entire Li/Ge compositional range. See Figure C.4**.**

The long-term stability of electrode materials is critical for the successful design of electrochemical devices. Figure 4.7 shows the cycling characteristics of the $Ge_{0.9}Se_{0.1}$ electrode cycled at a rate of 50 C for 1000 cycles. The capacity increases over the first 100 cycles likely due to ohmic heating of the coin cell during testing. After 1000 cycles at 50 C, approximately 70% of the maximum observed capacity is retained. The slow decline in capacity is likely due to loss of active material as a result of delamination of the nanocolumns from the current collector. Such a mechanism has been observed in electrodes with similar morphology.[29, 33] The coulombic efficiency remained unity throughout the 1000 cycles, and since charge is consumed during SEI formation, the high coulombic efficiency is an indication of a stable SEI layer. The stability of nanocolumnar germanium electrodes could not be investigated at this rate for comparison, as they did not retain any appreciable capacity at 50C.

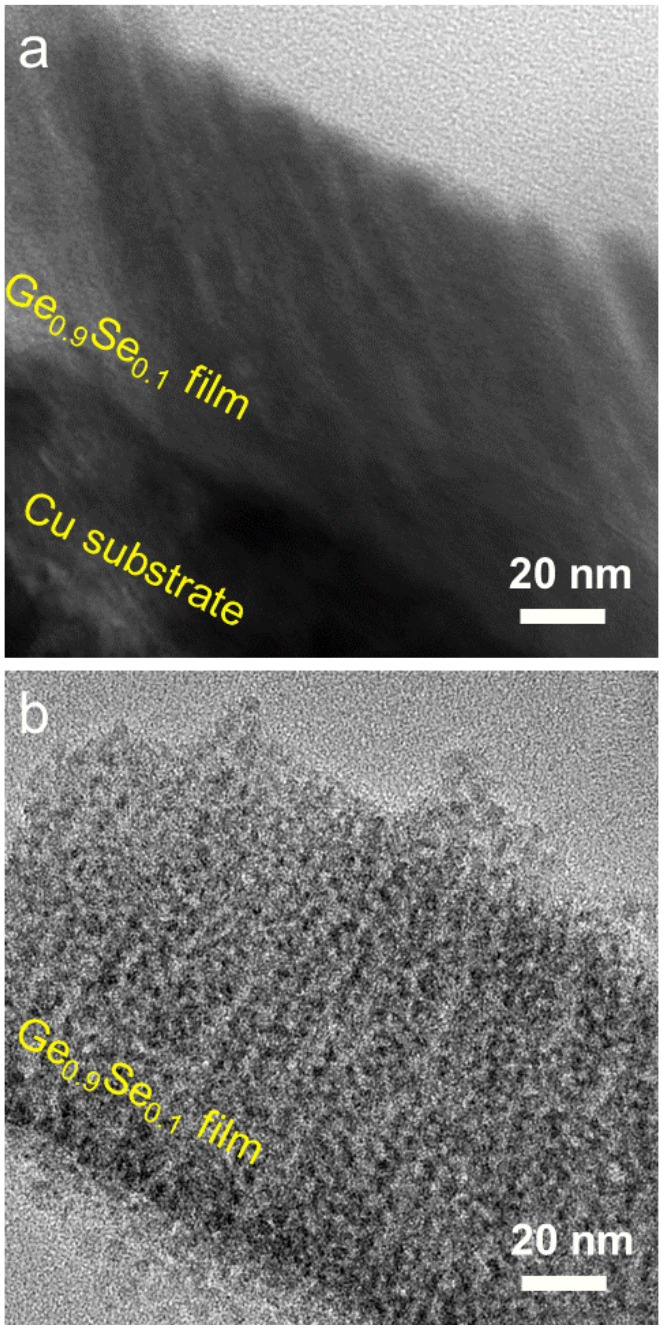

Figure 4.6. Cross-sectional TEM images of nanocolumnar $Ge_{0.9}Se_{0.1}$ electrodes a) as deposited and b) after one lithium insertion/extraction cycle.

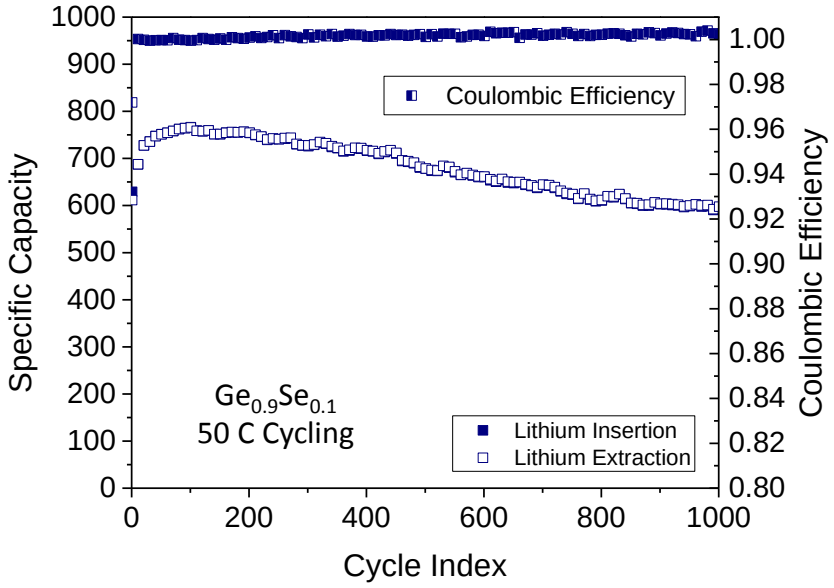

Figure 4.7. Cycle life testing of a $Ge_{0.9}Se_{0.1}$ electrode. Specific capacity *versus* cycle number for a $Ge_{0.9}Se_{0.1}$ electrode cycled at 50 C for 1000 cycles. The electrode retains ~70% of the maximum observed capacity at the 1000th cycle. The coulombic efficiency for each cycle was unity.

CONCLUSION

We have shown that the addition of small amounts of selenium to nanocolumnar germanium electrodes significantly enhances their high rate performance, allowing the material to support currents up to 1800 C (2200 A/g). In addition to performing well at high rates, the electrodes were stable over 1000 cycles at 50 C. TEM imaging shows that phase separation during the first cycle produces a lithium selenide based fast-ionic conducting phase within the material. The lithium-conducting phase forms in discrete domains rather than forming a percolating network, so the composite must be nanostructured in order to see significant improvements in the effective lithium diffusion

coefficient. Additionally, the high electrical conductivity of the material reduces the need for conducting carbon additives in a manufactured electrode, thus increasing the energy and power density of such an electrode. The performance of this material under challenging testing conditions warrants further investigation.

REFERENCES

1. Okubo, M.; Hosono, E.; Kim, J.; Enomoto, M.; Kojima, N.; Kudo, T.; Zhou, H.; Honma, I., *J. Am. Chem. Soc.* **2007,** *129*, 7444-7452.

2. Baggetto, L.; Unocic, R. R.; Dudney, N. J.; Veith, G. M., *J. Power Sources* **2012,** *211*, 108-118.

3. Ning, G.; Haran, B.; Popov, B. N., *J. Power Sources* **2003,** *117*, 160-169.

4. Takami, N.; Satoh, A.; Hara, M.; Ohsaki, T., *J. Electrochem. Soc.* **1995,** *142*, 371-379.

5. Bruce, P. G.; Scrosati, B.; Tarascon, J.-M., *Angew. Chem. Int. Ed.* **2008,** *47*, 2930-2946.

6. Baggetto, L.; Allcorn, E.; Unocic, R. R.; Manthiram, A.; Veith, G. M., *J. Mater. Chem. A* **2013,** *1*, 11163-11169.

7. Kim, H.-K.; Bak, S.-M.; Kim, K.-B., *Electrochem. Commun.* **2010,** *12*, 1768-1771.

8. Jung, H.-G.; Myung, S.-T.; Yoon, C. S.; Son, S.-B.; Oh, K. H.; Amine, K.; Scrosati, B.; Sun, Y.-K., *Energy & Environmental Science* **2011,** *4*, 1345-1351.

9. Abel, P. R.; Chockla, A. M.; Lin, Y.-M.; Holmberg, V. C.; Harris, J. T.; Korgel, B. A.; Heller, A.; Mullins, C. B., *ACS Nano* **2013,** *7*, 2249-2257.

10. Chockla, A. M.; Klavetter, K. C.; Mullins, C. B.; Korgel, B. A., *ACS Appl. Mater. Interfaces* **2012,** *4*, 4658-4664.

11. Klavetter, K. C.; Wood, S. M.; Lin, Y.-M.; Snider, J. L.; Davy, N. C.; Chockla, A. M.; Romanovicz, D. K.; Korgel, B. A.; Lee, J.-W.; Heller, A.*, et al.*, *J. Power Sources* **2013,** *238*, 123-136.

12. Baggetto, L.; Notten, P. H. L., *J. Electrochem. Soc.* **2009,** *156*, A169-A175.

13. Seng, K. H.; Park, M.-H.; Guo, Z. P.; Liu, H. K.; Cho, J., *Angew. Chem. Int. Ed.* **2012,** *51*, 5657-5661.

14. Heller, A.; Tai, K. L.; Vadimsky, R. G. Photoinduced Migration of Silver into Chalcogenide Layer. US 4,276,368, June 30, 1981, 1981.

15. Tai, K. L.; Vadimsky, R. G.; Kemmerer, C. T.; Wagner, J. S.; Lamberti, V. E.; Timko, A. G., *J. Vac. Sci. Technol.* **1980,** *17*, 1169-76.

16. Ong, E.; Tai, K. L.; Vadimsky, R. G.; Kemmerer, C. T., *Proc. SPIE-Int. Soc. Opt. Eng.* **1983,** *394*, 39-48.

17. Wagner, A.; Barr, D.; Venkatesan, T.; Crane, W. S.; Lamberti, V. E.; Tai, K. L.; Vadimsky, R. G., *J. Vac. Sci. Technol.* **1981,** *19*, 1363-7.

18. Venkatesan, T., *J. Vac. Sci. Technol.* **1981,** *19*, 1368-73.

19. Kikkawa, S.; Miyai, T.; Koizumi, M., *Solid State Ionics* **1988,** *28–30, Part 1*, 743-746.

20. Michel-Lledos, V.; Pradel, A.; Ribes, M., *Eur. J. Solid State Inorg. Chem.* **1992,** *29*, 301-310.

21. Souquet, J., *Solid State Ionics* **1981,** *3-4*, 317-321.

22. Price, D. L.; Ellison, A. J. G., *J. Non-Cryst. Solids* **1994,** *177*, 293-298.

23. Kim, Y.; Hwang, H.; Lawler, K.; Martin, S. W.; Cho, J., *Electrochim. Acta* **2008,** *53*, 5058-5064.

24. Cho, Y. J.; Im, H. S.; Myung, Y.; Kim, C. H.; Kim, H. S.; Back, S. H.; Lim, Y. R.; Jung, C. S.; Jang, D. M.; Park, J.*, et al.*, *Chem. Commun.* **2013,** *49*, 4661-4663.

25. Cho, Y. J.; Im, H. S.; Kim, H. S.; Myung, Y.; Back, S. H.; Lim, Y. R.; Jung, C. S.; Jang, D. M.; Park, J.; Cha, E. H.*, et al.*, *ACS Nano* **2013,** *7*, 9075-9084.

26. Robbie, K.; Sit, J. C.; Brett, M. J., *J. Vac. Sci. Technol., B* **1998,** *16*, 1115-1122.

27. Abelmann, L.; Lodder, C., *Thin Solid Films* **1997,** *305*, 1-21.

28. Krause, K. M.; Thommes, M.; Brett, M. J., *Microporous Mesoporous Mater.* **2011,** *143*, 166-173.

29. Abel, P. R.; Lin, Y.-M.; Celio, H.; Heller, A.; Mullins, C. B., *ACS Nano* **2012,** *6*, 2506-2516.

30. Lin, Y.-M.; Abel, P. R.; Flaherty, D. W.; Wu, J.; Stevenson, K. J.; Heller, A.; Mullins, C. B., *J. Phys. Chem. C* **2011,** *115*, 2585-2591.

31. Flaherty, D. W.; Hahn, N. T.; May, R. A.; Berglund, S. P.; Lin, Y.-M.; Stevenson, K. J.; Dohnalek, Z.; Kay, B. D.; Mullins, C. B., *Acc. Chem. Res.* **2012,** *45*, 434–443.

32. Hawkeye, M. M.; Brett, M. J., *J. Vac. Sci. Technol., A* **2007,** *25*, 1317-1335.

33. Abel, P. R.; Lin, Y.-M.; de Souza, T.; Chou, C.-Y.; Gupta, A.; Goodenough, J. B.; Hwang, G. S.; Heller, A.; Mullins, C. B., *J. Phys. Chem. C* **2013,** *117*, 18885-18890.

34. Maranchi, J. P.; Hepp, A. F.; Evans, A. G.; Nuhfer, N. T.; Kumta, P. N., *J. Electrochem. Soc.* **2006,** *153*, A1246-A1253.

35. Sharma, S. K.; Jain, S. C.; Aggarwal, S. S.; Bhide, V. G., *J. Non-Cryst. Solids* **1972,** *7*, 285-294.

36. St. John, M. R.; Furgala, A. J.; Sammells, A. F., *J. Electrochem. Soc.* **1982,** *129*, 246-50.

37. Weppner, W.; Huggins, R. A., *Annu. Rev. Mater. Sci.* **1978,** *8*, 269-311.

38. Ipser, H.; Gambino, M.; Schuster, W., *Monatsh Chem* **1982,** *113*, 389-398.

Chapter 5: Sub-Stoichiometric Germanium Sulfide as a High-Rate Lithium Storage Material

INTRODUCTION

The maximal rate of charging for a lithium-ion (Li-ion) battery is determined by the kinetics of the anode. If the rate of charge is faster than solid-state lithium diffusion in the anode, than lithium electrodeposition will occur rather than lithium insertion in the electrode. Lithium tends to form mossy, dendritic deposits rather than conformally deposited films.[1] This is the reason that lithium metal is not used in commercial devices – lithium dendrites can short the cell internally leading to thermal runaway and fire.[2] Additionally, graphite, which is presently used as the anode in commercial Li-ion batteries is limited in its rate capability by electrode stability – when cycled at rates higher than about 1C, the cell capacity fades rapidly.[3] For these reasons, alternative anode materials capable of supporting higher charging rates are sought.

Germanium has been studied as an anode material for Li-ion batteries because of its high gravimetric capacity (1384 mAh/g corresponding to the formation of $Li_{15}Ge_4$) and favorable lithium transport properties.[4-7] Germanium, like all lithium-alloy forming electrode materials, undergoes large volumetric expansion during cycling leading to rapid capacity fade. Use of nanostructuring has been used to stabilize the material,[8-10] as has using germanium chalcogens – GeO_x,[11-13] GeS,[14-15] GeS_2.[16] On lithiation, these materials form germanium embedded in a matric of Li_2X (X = O, S) which stabilizes the volumetric expansion of germanium on subsequent cycles. Kim *et al.* studied the lithium

electrochemistry of germanium oxide and germanium sulfide glasses.[16] Both materials had large first cycle irreversible capacities due to the formation of lithium chalcogenides. GeS_2 outperformed GeO_2 and the favorable performance was attributed to the higher ionic conductivity of the Li_2S versus the Li_2O formed upon lithiation. Sulfur's larger polarizability is credited for the higher lithium mobility in Li_2S relative to Li_2O.[17] Additionally, Cho *et al.* reported that GeS and GeS_2 nanoparticles had good cycling stability and capacity retention at rates up to 5 C.[14]

The Li_2X (X = O, S) matrix that forms during lithiation of these materials succeeds in stabilizing the material, but can also limits the high rate capability by creating additional diffusive barriers to lithium transport. Diffusion along grain boundaries is well known to be orders of magnitude faster than through bulk material. As such, intimately mixed, nano-scale materials may have very favorable lithium transport properties.

Sub-stoichiometric germanium selenide, which phase segregates to form nanoscale inclusions on lithiation, has previously been reported as a high-rate material.[18] The same phase segregation should also occur in sub-stoichiometric sulfides as well, suggesting that they should also be capable of charging at high rates. Like germanium selenide based glasses,[19] germanium sulfide glasses have been identified as fast ion conductors.[20] Sulfur has the advantage of being much more abundant than selenium. Additionally, sulfur is roughly half the atomic mass of selenium, so the same atomic fraction of sulfur in germanium is roughly half the mass fraction – this will increase the gravimetric capacity of sub-sulfides relative to a sub-selenides.

In this paper we deposit germanium and sub-stoichiometric germanium sulfide using glancing angle deposition (GLAD) to control the porosity of the deposited films. GLAD is a physical vapor deposition technique in which adatoms impinge on the substrate at an angle other than the surface normal (in our case, we use 70^{o} from the surface normal). GLAD can be used to produce nanostructured films if the surface diffusion of adatoms is limited.[21] Stochastic variations in the deposition rate roughen the surface in the early stages of deposition. The roughness is then amplified by self-shadowing and leads to the growth of porous films.[22] In GLAD films, the morphology is controlled by the deposition angle. Dense films are produced for deposition angles close to normal while porous, reticulated, and nanocolumnar films are produced as the deposition angle is increased.[23] Additional details, examples, and applications of GLAD can be found elsewhere.[24-27] We then investigate the electrochemical properties and phase evolution of the deposited materials.

MATERIALS AND METHODS

Material Synthesis

Germanium sub-sulfide electrodes were vacuum deposited by diluting thermally evaporated GeS_2 (MP Biomaterials) with additional germanium (Kurt Lesker, 99.999%) from a second evaporation source. A thermal evaporator was use to evaporate GeS_2 from an alumina crucible while an electron beam evaporator was used to evaporate Ge from a carbon crucible. Material was deposited on 15.6 mm diameter stainless steel substrates (Pred Materials) at an incident angle of 0^{o} or 70^{o} from the surface normal. The substrates

were cleaned by sonication in ethanol prior to deposition. The deposition rate of each evaporator was calibrated using a quartz crystal microbalance (Inficon), and the mass density of the electrodes was 50 μg cm^{-2}.

Material Characterization

SEM images of the electrodes were obtained with a Hitachi S5500. SEM images were analyzed using ImageJ.[28] EDX spectra were obtained with a Bruker detector on the same instrument. X-ray diffraction (XRD) was performed on a Philips XPERT theta-theta diffractometer. XPS was performed using a commercial X-ray photoelectron spectrometer (Kratos Axis Ultra), utilizing a monochromatic Al-Kα X-ray source (hν = 1486.5 eV). An automated charge neutralizer was employed for analysis. The surface of each sample was cleaned by argon ion sputtering before analysis in order to remove any surface oxide, contamination, or SEI layer formed during cycling. Casa XPS analysis software was used to determine the stoichiometry of samples from corrected peak areas. Sensitivity factors, either provided by Kratos or determined experimentally, were employed for quantitative analysis of each element of interest. The binding energies were calibrated to the C 1s signal from adventitious carbon taken to be 284.8 eV. TEM imaging and electron diffraction were performed on a JEOL 2010F. Samples for TEM were deposited on 10 μm thick copper foil. The TEM samples were prepared by ultramicrotome sectioning of resin-embeded electrodes. A more detailed procedure is described elsewhere.[4]

Electrochemical testing

As-deposited films were assembled into 2032 coin cells in an argon-filled glove-box (MBraun Unilab) with oxygen and water levels held below 5 ppm. Lithium metal (Alfa Aesar 99%) was used as the counter/pseudoreference electrode and 1 M $LiPF_6$ (Sigma Aldrich, battery grade) in a 1:1 mixture of fluorinated ethylene carbonate (Solvay Chemicals) and diethyl carbonate (Sigma Aldrich, battery grade) was employed as the electrolyte. A 25μm thick polypropylene film separator (Celgard 2400) was used. Cells were galvanically cycled using an Arbin BT2043 multichannel battery tester. Cells were cycled between 5 mV and 1.5 V *versus* Li/Li^+.

RESULTS AND DISCUSSION

Sub-stoichiometric germanium sulfide films were deposited by co-evaporating germanium and germanium disulfide. The deposition rates of Ge and GeS_2 could be independently controlled, so films with arbitrary sulfur content could be deposited. Evaporation of only GeS_2 led to the deposition of a severely sulfur deficient film (the composition of the films was close to GeS), so film compositions were correlated to deposition rates by x-ray photoelectron spectroscopy (XPS). Dense films for XPS analysis with various sulfur content were deposited normal to the surface. Evaporation of only germanium disulfide resulted in films with a composition of $Ge_{0.52}S_{0.48}$ as measured by XPS. The low sulfur content of the deposited film is likely due to decomposition of the germanium disulfide during evaporation. A fraction of the free sulfur created by the decomposition of GeS_2 would re-evaporate from the film's surface rather than being

incorporated into the film during deposition. Knowing the amount of sulfur incorporated into films deposited from evaporation of the GeS_2 precursor allowed the deposition of films with controlled sulfur content, and films with 5 or 10 at% sulfur were grown. The germanium 3d and sulfur 2p XPS features of films with 5, 10, or 48 at% sulfur are shown in Figure 5.1. These features were used for compositional analysis of each film. The position of the Ge 3d peak is seen to shift to higher binding energies as the sulfur content of the film is increased. This is consistent with sulfur drawing electron density away from the germanium atoms in the film. At the same time, the intensity of the feature decreases due to the lower concentration of germanium atoms at the surface while the sulfur 2p doublet increases in magnitude.

An SEM image of $Ge_{0.95}S_{0.05}$ deposited at 70° is shown in Figure 5.2a. The films are nanocolumnar, with an average column diameter of ~10 nm (See Figure D.1 and Table D.1 for statistical analysis of column size). The nanocolumnar morphology helps accommodate large strains that accompany the volumetric expansion that occurs during lithiation.[29] Additionally, a nanoscale dimension decreases the lithium diffusion length, and facilitates rapid lithium transport. The morphology of the $Ge_{0.95}S_{0.05}$ films is very similar to that of the pure germanium films shown in Figure 5.2b, such that differences in electrochemical performance can largely be attributed to the presence of sulfur in the films. The morphology of the film also did not change significantly when the sulfur content was increased to 10 at%.

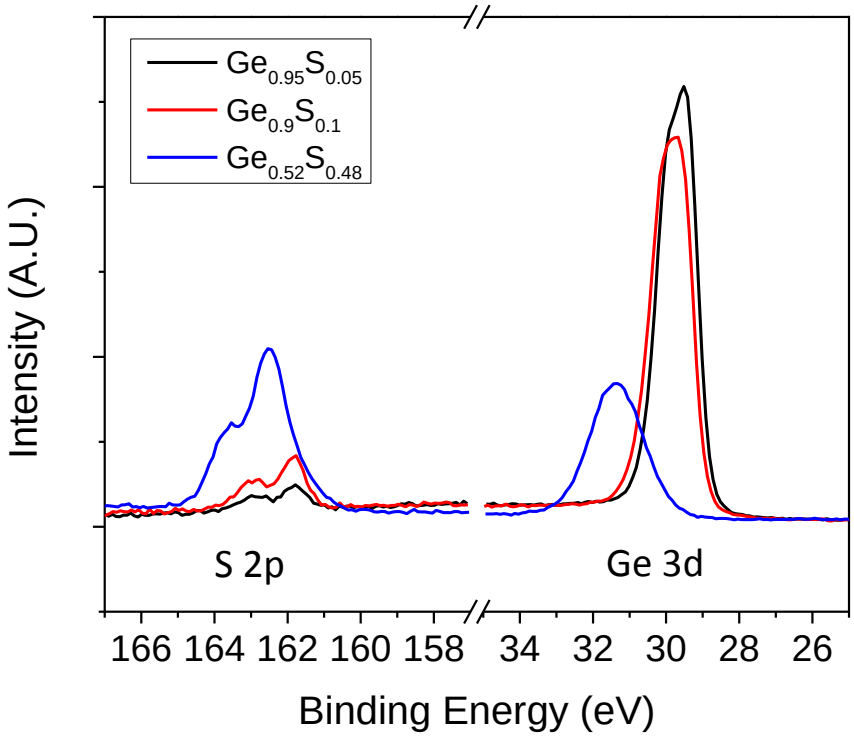

Figure 5.1. The Ge 3d and S2p XPS features of sub-stoichiometric germanium sulfide deposited at 0° on stainless steel substrates.

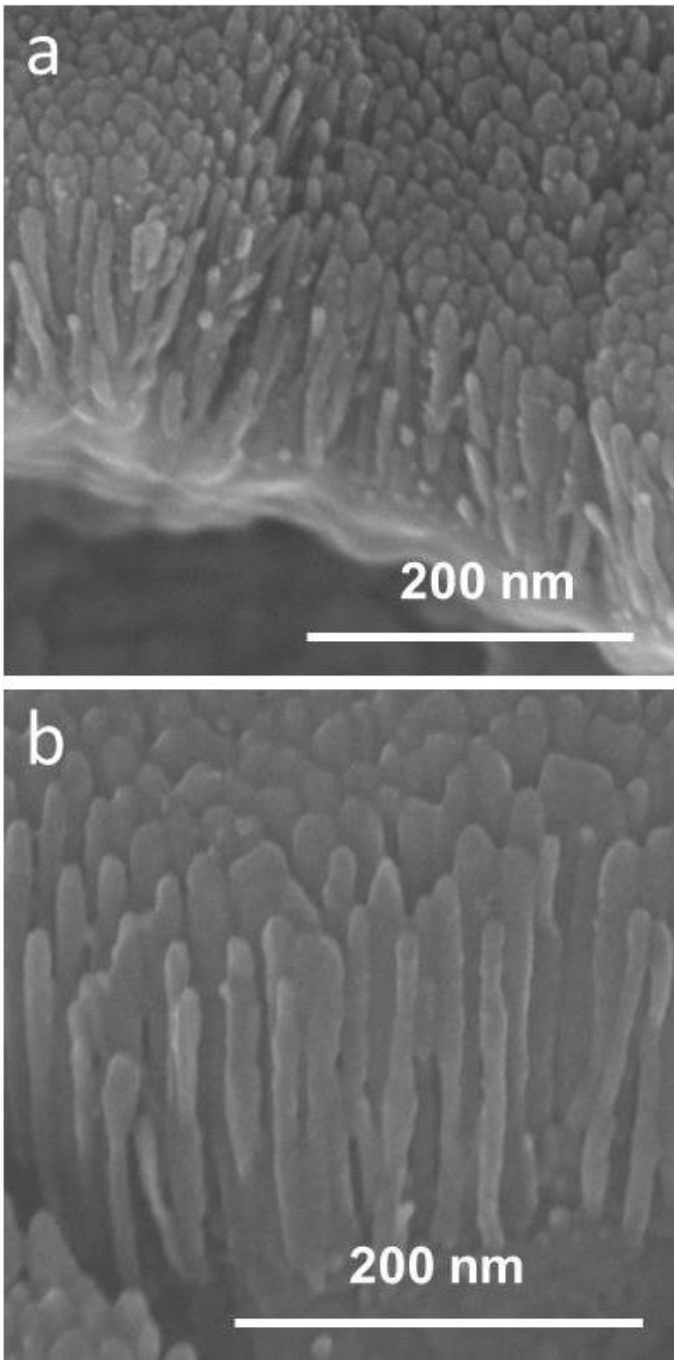

Figure 5.2. SEM images of a) 70° $Ge_{0.9}S_{0.1}$ and b) 70° Ge film. Both films show nanocolumnar morphology with a column diameter of ~10 nm.

TEM of an as-deposited $Ge_{0.95}S_{0.05}$ film is shown in Figure 5.3. The TEM image confirms the small ~10nm column diameter shown by SEM, and also shows the material to be amorphous. No lattice fringes are visible in the image. Additionally, the figure inset shows selected area electron diffraction (SAED) pattern from the sample. Only diffuse rings are present in the diffraction pattern which confirms that the material is amorphous. The amorphous nature of the as-deposited films is expected. The growth of crystalline films requires surface diffusion during deposition to allow adatoms to migrate to the equilibrium lattice points but the formation of nanocolumns during film deposition requires that adatom mobility be limited. The ability of nanocolumns to form during deposition suggests the film will be amorphous. X-ray diffraction (XRD) was also performed on an as deposited sample. No diffraction peaks from the film were observed (See figure D.2).

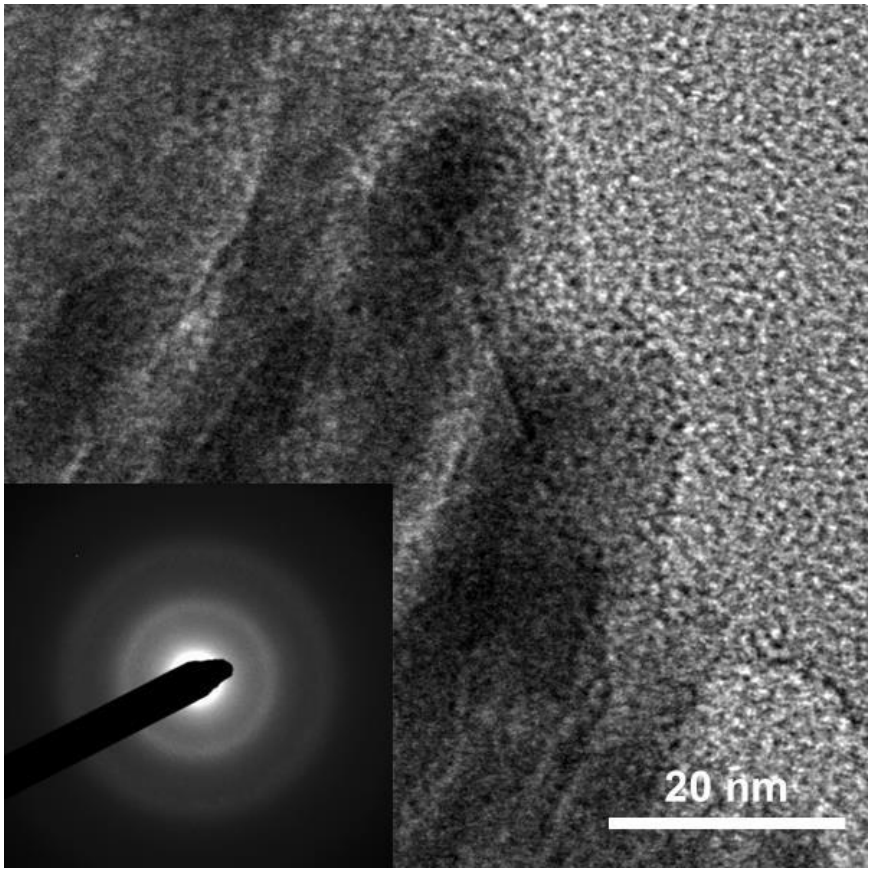

Figure 5.3. TEM and SAED of as-deposited films confirms the nanocolumnar morphology, small column diameter and amorphous nature of the material.

The electrochemistry of sub-stoichiometric germanium sulfide was investigated by galvanostatic cycling. C-rates for the sulfur containing films were calculated by assuming that only the germanium in the film contributes to the reversible capacity, but the specific capacity of the electrodes was calculated using the entire mass of the film (germanium plus sulfur). The first cycle voltage profiles of $Ge_{(1-x)}S_x$ films, as well as pure germanium films are shown in Figure 5.4a. This cycle was performed at a rate of C/10. The first cycle lithium insertion capacity for $Ge_{0.9}S_{0.1}$ is roughly 1750 mAh/g whereas the

capacity of the pure Ge film is just under 1500 mAh/g with the capacity of $Ge_{0.95}S_{0.05}$ falling in between. The higher lithium insertion capacity for the higher sulfur content films comes from a feature between 1.3 V and 0.6 V that grows in magnitude with increasing sulfur content. The pure germanium film shows a sloping feature in this same voltage range that is likely due to electrolyte decomposition to form a solid electrolyte interphase (SEI) layer on the electrode. Since the morphology of all three films is similar, the magnitude of charge consumed in SEI formation should be similar for each film. The increase in charge passed in this voltage range – for the sulfur-containing films – is therefore likely due to the reaction of lithium with the sulfur in the film. At potentials below 0.6 V, all three compositions behave similarly with lithiation pseudo-plateaus at 400 mV and 200 mV. The first cycle reversible capacities of the Ge, $Ge_{0.9}S_{0.1}$, and $Ge_{0.95}S_{0.05}$ films are 1230 mAh/g, 1160 mAh/g, and 1120 mAh/g respectively.

The voltage profiles for each composition at rates up to 10C are shown in Figure 5.4b-d. For pure germanium, shown in Figure 5.4b, significant overpotentials are required to drive lithiation at rates higher than ~2C. Above this rate, the material is not completely lithiated before the electrode reaching the lower cutoff voltage for the test. The overpotentials are significantly reduced for $Ge_{0.95}S_{0.05}$ (shown in Figure 5.4c), and $Ge_{0.9}S_{0.1}$ (shown in Figure 4d). $Ge_{0.95}S_{0.05}$ exhibits higher reversible capacities and lower overpotentials than the material with higher sulfur content.

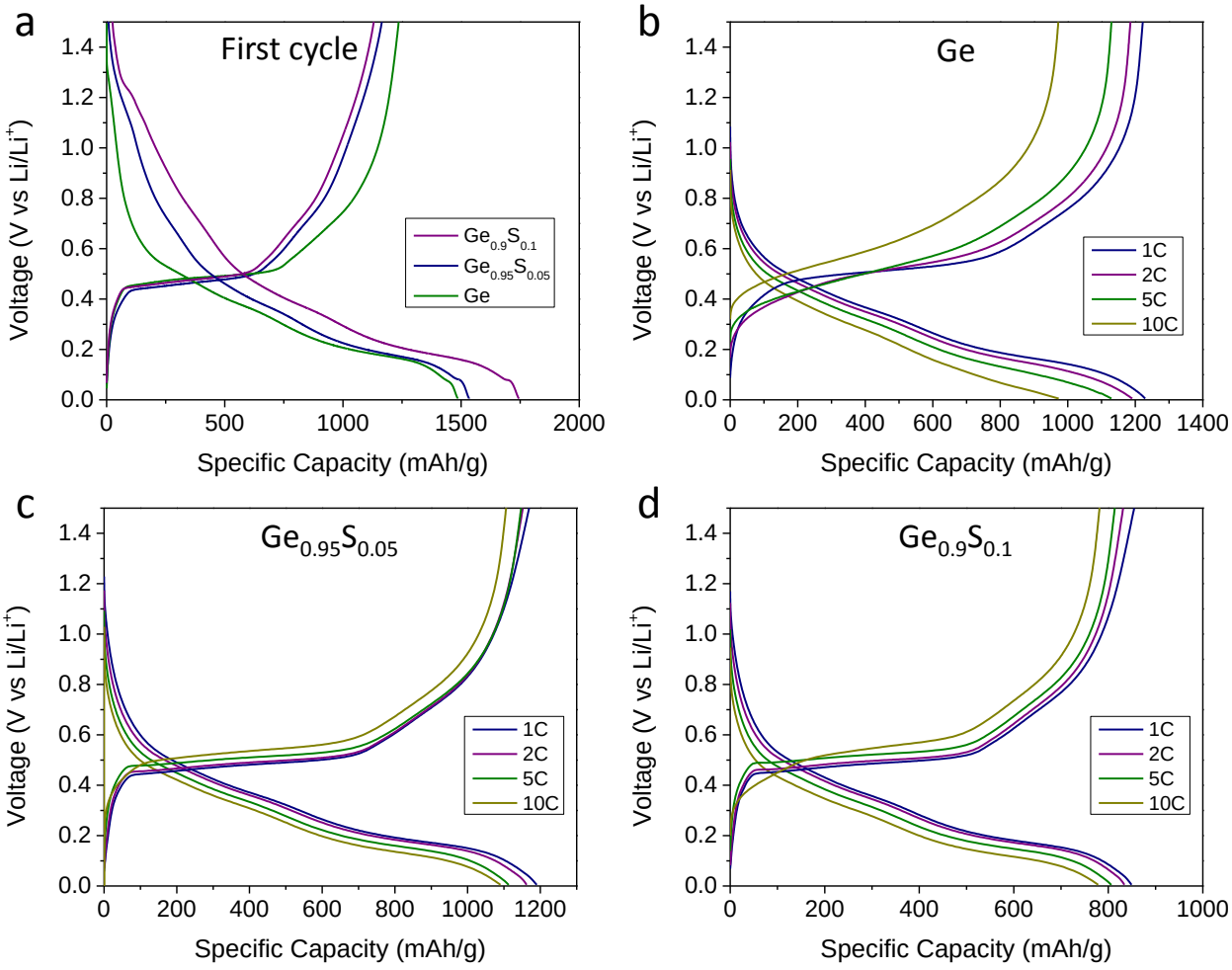

Figure 5.4. Voltage profiles for a) the first lithiation/delithiation cycle of $Ge_{(1-x)}S_x$ and pure Ge films, b) the voltage profiles for Ge at various c-rates, c) the voltage profiles for $Ge_{0.95}S_{0.05}$ at various C-rates, and d) he voltage profiles for $Ge_{0.9}S_{0.1}$ at various C-rates. All films were deposited at 70° from surface normal so have similar morphology.

The normalized capacity as a function of cycle number for $Ge_{(1-x)}S_x$ and pure Ge films is shown in Figure 5.5. All films have a C/10 conditioning cycle prior to the start of the C-rate test. The films were cycled for 10 cycles each at 1C, 2C, 5C, and 10C followed by a final 10 cycles at 1C to assess how the films recover from the high-rate cycling. The

pure germanium film exhibits the best stability over the duration of the test, with 98% of the initial capacity retained on cycle 50th. The sulfur-containing films show a gradual decline in capacity over the first 20 cycles before stable cycling is achieved. $Ge_{0.9}S_{0.1}$ retains 96% of its initial capacity on cycle 50, and $Ge_{0.8}S_{0.2}$ retains 95%. The superior high-rate capability of the sulfur-containing films becomes apparent at 5C and 10C despite the losses in capacity during the early cycles. At a rate of 10C, $Ge_{0.9}S_{0.1}$ retains 93% of its initial capacity while $Ge_{0.8}S_{0.2}$ retains 89% and pure germanium retains 82%.

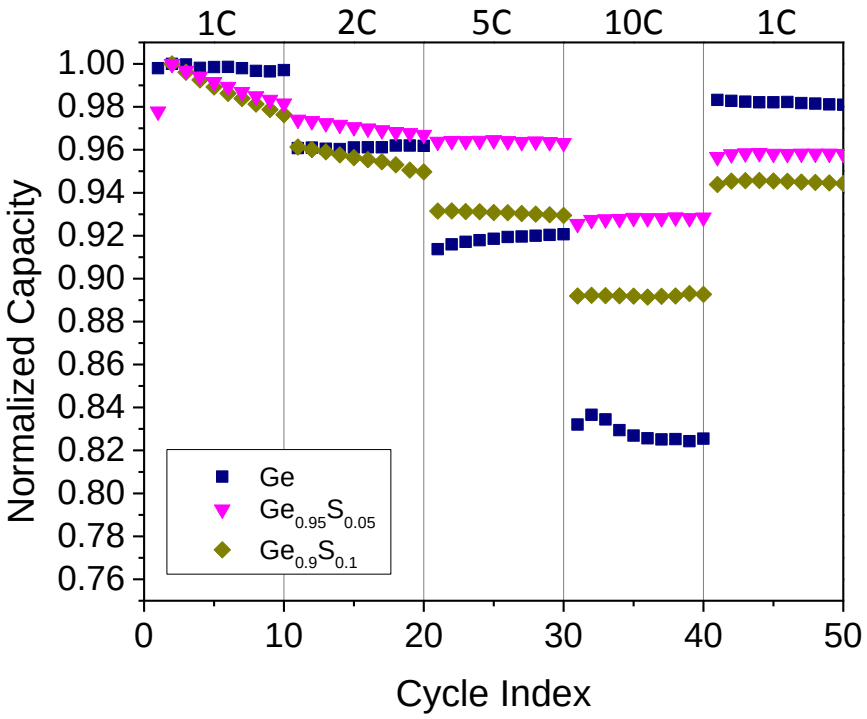

Figure 5.5. C-rate tests of Ge, $Ge_{0.95}S_{0.05}$, and $Ge_{0.9}S_{0.1}$ films at rates up to 10C.

The long-term stability of the highest performing composition ($Ge_{0.9}S_{0.1}$) was assessed by repeated cycling at 20C. The results of this test are shown in Figure 5.6. The electrode cycles stably for the first ~300 cycles with a specific capacity of just over 1000 mAh/g. After this point the capacity begins to slowly decay. The rate of decrease in capacity is approximately 0.5 mAh/g/cycle, or 0.05% per cycle. After 500 cycles, the capacity is 900 mAh/g, or about 88% of the initial capacity at 20C.

The voltage profiles for the 100th, 300th and 500th cycles are shown in Figure 5.6b. The 100th cycle voltage profile looks similar to the voltage profiles shown in figure 5.4 indicating that the high cycling rate doesn't fundamentally alter the lithiation mechanism of this material. As cycling continues, the capacity decreases and the overpotential increases. This is likely due to a loss of active material increasing the effective C-rate. A ratcheting mechanism, where stresses at the active material/current collector interface increases every cycle, has been shown to be responsible for capacity fade for thin films deposited on copper.[30] Previous studies on nanocolumnar Si and Ge electrodes deposited on stainless steel have shown that a similar failure mechanism was responsible for the capacity fade on repeated cycling.[24, 31]

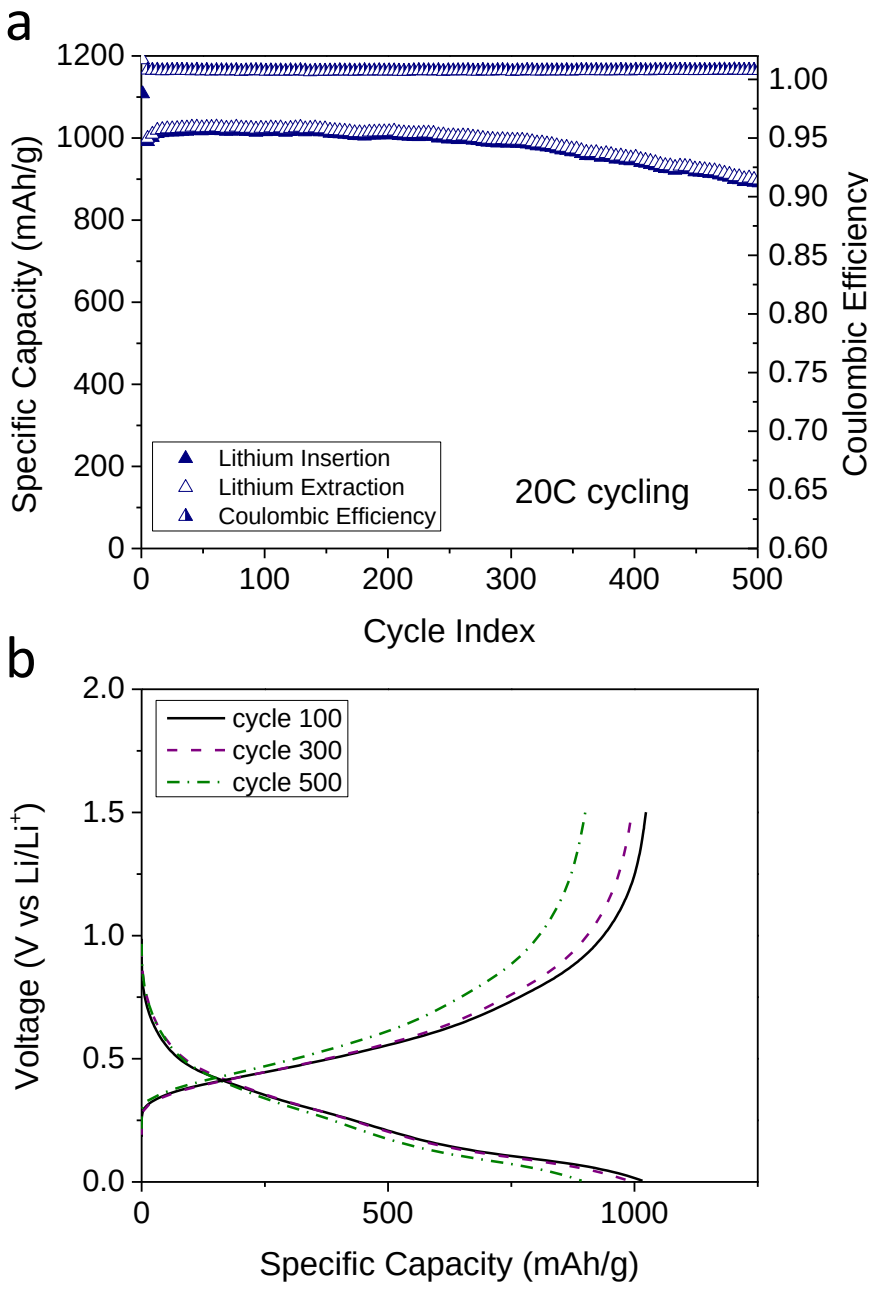

Figure 5.6. a) Cycle-life testing of $Ge_{0.9}S_{0.1}$ at 20C for 500 cycles, and b) voltage profiles for the 100th, 300th, and 500th cycle.

The as-deposited films are an amorphous mixture of germanium and sulfur. However, this composition is not thermodynamically stable, so the phase evolution of the material during cycling is of interest. Ex-situ TEM imaging was performed to assess the morphology of the electrode after a single cycle and the results are shown in Figure 5.7. Figure 5.7a shows that the nanocolumnar structure of the electrode is maintained and that a conformal layer, presumably SEI, has formed on the surfaces of the electrode which were exposed to the electrolyte. As opposed to the as-deposited films, which showed uniform contrast indicating a homogeneous material, the cycled material shows higher contrast inclusions which suggests that the material has phase separated. A high-resolution TEM image is shown in Figure 5.7b, and this confirms that the multiple phases are present. Small nanocrystalline inclusions a few nanometers in size are present in an amorphous matrix. The inclusions, while exhibiting visible lattice fringes, appear to be poorly crystallized. The lattice spacing was measured to be 2.85 Å which is in good agreement with the 2.86 Å spacing of the Li_2S (2 0 0) plane. The reaction between lithium and sulfur is reversible; however the reaction occurs at much more cathodic potentials (~2.2V *vs.* Li/Li^+) than occur at the anode during normal electrode cycling. The presence of the nanocrystalline Li_2S inclusions is likely responsible for the increased high-rate performance over that of pure germanium as the inclusions create phase boundaries throughout the electrode and diffusion along such boundaries is significantly faster than through the bulk material.

XRD was performed on the cycled electrodes, however no diffraction peaks were observed (see figure D.2). The lack of peaks in the x-ray diffraction pattern does not

necessarily contradict TEM observations – the poor degree of crystallinity, the low volume fraction, and the small size of the crystallites all contribute to making them difficult to detect by XRD.

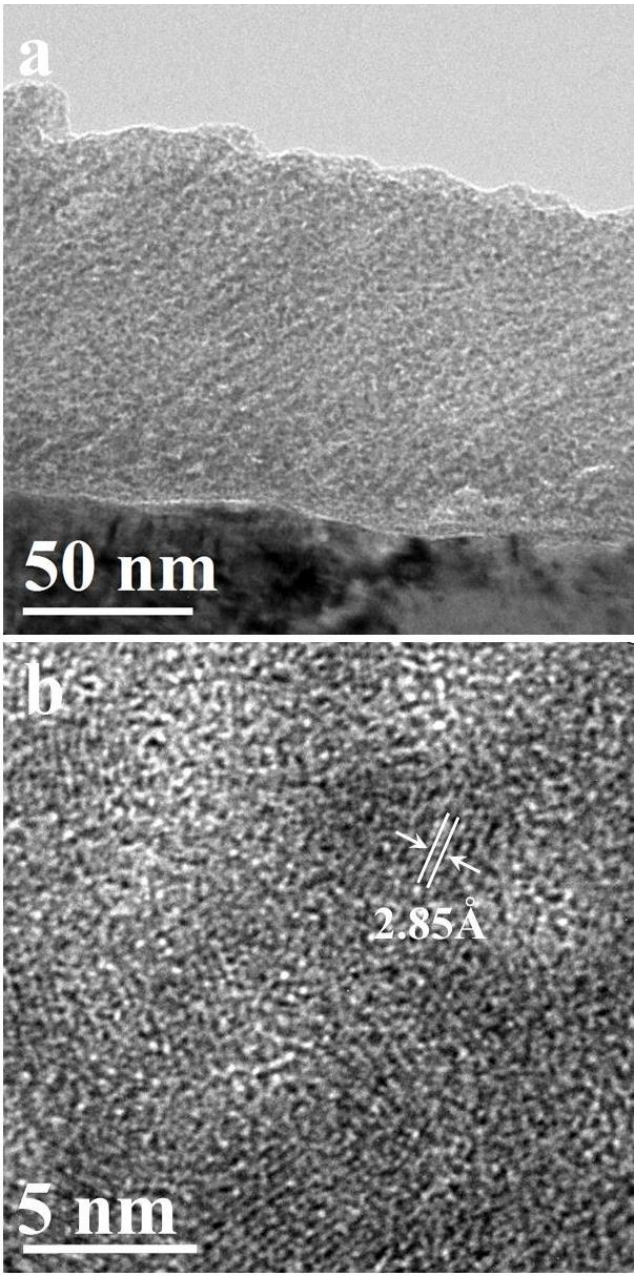

Figure 5.7. TEM images of a $Ge_{0.9}Se_{0.1}$ film cycled one time showing that a) the nanocolumnar morphology of the electrode is retained and b) nanocrystalline inclusions are present in the cycled electrode.

CONCLUSIONS

The co-evaporation of germanium and germanium disulfide at glancing angles was used to deposit nanocolunnar, sub-stoichiometric germanium sulfide films to test as Li-ion battery materials. The single-phase, amorphous films phase separated after one lithiation cycle resulting in poorly crystalized Li_2S nanoparticles embedded in amorphous germanium structures. This is the inverse structure of what is formed when stoichiometric germanium chalcogenides are lithiated. The result is superior high rate performance for $Ge_{0.95}S_{0.05}$, with ~93% of the low rate capacity retained when cycled at 10C compared to ~82% for pure germanium. The high performance is likely due to fast interfacial diffusion at the germanium/Li_2S nanocrystalline inclusion interfaces. Additionally, the films show good stability over 500 cycles at 20C. The fast lithium transport and stable cycling make sub-stoichiometric germanium sulfide a promising material for further study.

REFERENCES

1. Yamaki, J.-i.; Tobishima, S.-i.; Hayashi, K.; Keiichi, S.; Nemoto, Y.; Arakawa, M., J. Power Sources 1998, 74, 219-227.

2. Tarascon, J. M.; Armand, M., Nature 2001, 414, 359-367.

3. Ning, G.; Haran, B.; Popov, B. N., J. Power Sources 2003, 117, 160-169.

4. Klavetter, K. C.; Wood, S. M.; Lin, Y.-M.; Snider, J. L.; Davy, N. C.; Chockla, A. M.; Romanovicz, D. K.; Korgel, B. A.; Lee, J.-W.; Heller, A., et al., J. Power Sources 2013, 238, 123-136.

5. Chockla, A. M.; Panthani, M. G.; Holmberg, V. C.; Hessel, C. M.; Reid, D. K.; Bogart, T. D.; Harris, J. T.; Mullins, C. B.; Korgel, B. A., J. Phys. Chem. C 2012, 116, 11917-11923.

6. Baggetto, L.; Notten, P. H. L., J. Electrochem. Soc. 2009, 156, A169-A175.

7. Laforge, B.; Levan-Jodin, L.; Salot, R.; Billard, A., J. Electrochem. Soc. 2008, 155, A181-A188.

8. Lee, H.; Kim, M. G.; Choi, C. H.; Sun, Y.-K.; Yoon, C. S.; Cho, J., J. Phys. Chem. B 2005, 109, 20719-20723.

9. Liang, W.; Yang, H.; Fan, F.; Liu, Y.; Liu, X. H.; Huang, J. Y.; Zhu, T.; Zhang, S., ACS Nano 2013, 7, 3427-3433.

10. Chan, C. K.; Zhang, X. F.; Cui, Y., Nano Lett. 2007, 8, 307-309.

11. Peña, J. S.; Sandu, I.; Joubert, O.; Pascual, F. S.; Areán, C. O.; Brousse, T., Electrochem. Solid-State Lett. 2004, 7, A278-A281.

12. Wang, X.-L.; Han, W.-Q.; Chen, H.; Bai, J.; Tyson, T. A.; Yu, X.-Q.; Wang, X.-J.; Yang, X.-Q., J. Am. Chem. Soc. 133, 20692-20695.

13. Lin, Y.-M.; Klavetter, K. C.; Heller, A.; Mullins, C. B., J. Phys. Chem. Lett. 2013, 4, 999-1004.

14. Cho, Y. J.; Im, H. S.; Myung, Y.; Kim, C. H.; Kim, H. S.; Back, S. H.; Lim, Y. R.; Jung, C. S.; Jang, D. M.; Park, J., et al., Chem. Commun. 2013, 49, 4661-4663.

15. Cho, Y. J.; Im, H. S.; Kim, H. S.; Myung, Y.; Back, S. H.; Lim, Y. R.; Jung, C. S.; Jang, D. M.; Park, J.; Cha, E. H., et al., ACS Nano 2013, 7, 9075-9084.

16. Kim, Y.; Hwang, H.; Lawler, K.; Martin, S. W.; Cho, J., Electrochim. Acta 2008, 53, 5058-5064.

17. Michel-Lledos, V.; Pradel, A.; Ribes, M., Eur. J. Solid State Inorg. Chem. 1992, 29, 301-310.

18. Abel, P. R.; Klavetter, K. C.; Heller, A.; Mullins, C. B., J. Phys. Chem. C 2014.

19. Kikkawa, S.; Miyai, T.; Koizumi, M., Solid State Ionics 1988, 28–30, Part 1, 743-746.

20. Souquet, J., Solid State Ionics 1981, 3-4, 317-321.

21. Robbie, K.; Sit, J. C.; Brett, M. J., J. Vac. Sci. Technol., B 1998, 16, 1115-1122.

22. Abelmann, L.; Lodder, C., Thin Solid Films 1997, 305, 1-21.

23. Krause, K. M.; Thommes, M.; Brett, M. J., Microporous Mesoporous Mater. 2011, 143, 166-173.

24. Abel, P. R.; Lin, Y.-M.; Celio, H.; Heller, A.; Mullins, C. B., ACS Nano 2012, 6, 2506-2516.

25. Lin, Y.-M.; Abel, P. R.; Flaherty, D. W.; Wu, J.; Stevenson, K. J.; Heller, A.; Mullins, C. B., J. Phys. Chem. C 2011, 115, 2585-2591.

26. Flaherty, D. W.; Hahn, N. T.; May, R. A.; Berglund, S. P.; Lin, Y.-M.; Stevenson, K. J.; Dohnalek, Z.; Kay, B. D.; Mullins, C. B., Acc. Chem. Res. 2012, 45, 434–443.

27. Abel, P. R.; Chockla, A. M.; Lin, Y.-M.; Holmberg, V. C.; Harris, J. T.; Korgel, B. A.; Heller, A.; Mullins, C. B., ACS Nano 2013, 7, 2249-2257.

28. Rasband, W. S. ImageJ, U. S. National Institutes of Health: Bethesda, Maryland, USA, http://imagej.nih.gov/ij/, 1997-2014.

29. Arico, A. S.; Bruce, P.; Scrosati, B.; Tarascon, J.-M.; van Schalkwijk, W., Nat. Mater. 2005, 4, 366-377.

30. Maranchi, J. P.; Hepp, A. F.; Evans, A. G.; Nuhfer, N. T.; Kumta, P. N., J. Electrochem. Soc. 2006, 153, A1246-A1253.

31. Abel, P. R.; Lin, Y.-M.; de Souza, T.; Chou, C.-Y.; Gupta, A.; Goodenough, J. B.; Hwang, G. S.; Heller, A.; Mullins, C. B., J. Phys. Chem. C 2013, 117, 18885-18890.

Chapter 6: Nanocolumnar Germanium Thin Films as a High-Rate Sodium-Ion Battery Anode Material

INTRODUCTION

Existing commercially available sodium battery chemistries such as sodium-sulfur and sodium-nickel chloride use molten electrodes, a ceramic separator, and must operate above 300°C.[1-2] This requirement presents challenges for implementation at small scales and for on-demand applications. The development of room temperature sodium battery chemistries would therefore provide significant advantages and have the possibility to compete with currently available lithium-ion chemistries for stationary storage of electrical energy. [3]

The ongoing search for sodium insertion compounds suitable for room temperature sodium-ion batteries is impeded by the large size of the sodium ion; it is difficult to find materials that can reversibly store sodium ions with reasonable rates of charge and discharge. Layered metal oxides and phosphates similar to those used in Li-ion batteries have been shown to reversibly store the larger sodium ion.[4-8] Additionally, NASICON structured material[9-11] and cubic Prussian blue analogues[12-14] show promise as potential cathode materials. However, anode materials for room temperature sodium-ion batteries are more elusive. Unlike lithium, sodium ions do not intercalate reversibly into graphite; therefore alternative materials are sought. Non-graphitic carbons have been investigated, but they have been found to have high first-cycle irreversible capacities and low reversible capacities.[15-17] In analogy with their use in lithium-ion batteries, alloys

have been investigated to develop high-capacity sodium-ion battery anodes. Sodium is known to alloy with tin[3, 18-19] and antimony[20-21]. Additionally, the ternary sodium-tin-antimony alloy has been considered as an anode material.[22] Chevrier and Ceder, in a very interesting study, calculated that sodium should alloy with germanium up to NaGe, giving a theoretical capacity of 369mAh/g.[23]

Germanium has been extensively studied as an anode material for lithium-ion batteries as it has a high lithium storage capacity and high lithium diffusivity.[24-28] Sodium diffusion in crystalline germanium was studied at high temperature by Stojić *et al.* and found to be several orders of magnitude slower than that of lithium in germanium.[29-30] Both species are interstitial diffusers; however the larger radius of sodium in comparison to lithium results in a much higher activation energy for hopping between interstitial sites in the lattice (0.51 eV for lithium *versus* 1.5 eV for sodium). For sodium-ion batteries, solid state diffusion is a significant fraction of the total cell resistance. It is well established in the literature that surface diffusion and grain boundary diffusion are both much faster than bulk diffusion in solids. It is, therefore, desirable to utilize nanostructured germanium to overcome the low bulk diffusion coefficient of sodium in germanium in order to minimize the total cell resistance.

In this paper, we investigate the electrochemical properties of dense and nanocolumnar germanium thin films synthesized by glancing angle deposition (GLAD) as candidate anode materials for sodium-ion batteries. GLAD is a physical vapor deposition technique where adatoms impinge on a surface at an oblique angle. In the early stages of deposition, stochastic variation in deposition rate roughens the surface. If

surface diffusion is limited, the roughness is amplified by self-shadowing (see Abelmann and Lodder for additional details on this process)[31] and nanocolumnar films can be grown.[32] In GLAD, the morphology of the film is strongly dependent on deposition angle, with films deposited at angles close to the surface normal resulting in dense films and oblique angles resulting in highly porous,[33-34] nanocolumnar films.[35] More details on this technique can be found elsewhere.[24, 36-39] A previous study on how the deposition angle of TiO_2 GLAD electrodes for lithium-ion batteries affected electrochemical performance found diminishing returns in performance for angles greater than 70^o.[37] For this reason, this study is limited to comparing the performance of dense films and optimally nanostructured films deposited at 70^o.

MATERIALS AND METHODS

Material Synthesis

Germanium (Kurt J. Lesker, 99.999%) was vacuum deposited (by electron beam heating) onto a 15.6 mm diameter stainless steel substrate (Pred Materials) at an incident angle of either 0^o (dense films) or 70^o (nanocolumnar films) from the surface normal. The stainless steel substrates were cleaned by sonication in ethanol prior to deposition. The deposition rate was calibrated with a quartz crystal microbalance, and the mass density of all films was 50 $\mu g/cm^2$. The accuracy of the microbalance was checked by cross sectional SEM imaging of the films – see Figure S1.

Material Characterization

Imaging of germanium thin films was performed using a Hitachi S5500 microscope in SEM mode. TEM was performed using a JEOL 2010F transmission electron microscope. XPS was performed using a Kratos Axis Ultra X-ray photoelectron spectrometer utilizing a monochromatic Al-Kα X-ray source (hν = 1486.5 eV). A charge neutralizer was employed during analysis. Sample stoichiometry was determined using Casa XPS analysis software. Sensitivity factors for each element of interest were either provided by Kratos or experimentally determined.

Electrochemical Testing

As-deposited electrodes were held in a low humidity environment for 72 hours to allow for native oxide formation prior to assembly into 2032 coin cells in an argon filled glovebox (MBraud Unilab) with oxygen and water levels held below 2 ppm. Sodium metal (Alfa Aesar, 99%) was used as the counter/pseudo-reference electrode and 1M $NaPF_6$ (Sigma Aldrich, battery grade) in a 1:1 mixture of fluorinated ethylene carbonate (Solvay Chemicals) and diethyl carbonate (sigma Aldrich, battery grade) as the electrolyte. Coin cells were galvanically cycled in an Arbin BT2043 multi-channel battery tester. The cells were cycled between 5mV and 1.5V versus Na/Na+. Impedance spectroscopy was performed with a CHI 604D electrochemical workstation. The frequency was varied from 10^{-2} – 10^{6} Hz with an amplitude of 5 mV.

Quantum Mechanical Calculations

The quantum mechanical calculations reported herein were performed on the basis of DFT within the generalized gradient approximation (GGA-PW91)[40], as

implemented in the Vienna *Ab-initio* Simulation Package (VASP)[41-43]. The projector augmented wave (PAW) method with a planewave basis set was employed to describe the interaction between ion cores and valence electrons. Valence configurations employed are: $3s^1$ for Na and $4s^2 4p^2$ for Ge. An energy cutoff of 200 eV was applied for the planewave expansion of the electronic eigenfunctions. During geometry optimization, all atoms were fully relaxed using the conjugate gradient method until residual forces on constituent atoms become smaller than 5×10^{-2} eV/Å. For Brillouin zone sampling, a (2×2×2) *k*-point mesh in the scheme of Monkhorst-Pack[44] was used for all bulk amorphous samples, and for the corresponding slab models, a (2×2×1) *k*-point mesh was used.

RESULTS AND DISCUSSION

A scanning electron microscope (SEM) image of a germanium film deposited at 70° off-normal is shown in Figure 6.1. The film exhibits nanocolumnar morphology with individual columns having a diameter of ~20nm. The small diameter of the individual columns serves to buffer the volumetric expansion undergone during sodium insertion. Despite germanium's modest sodium capacity, the volumetric expansion associated with the formation of NaGe is greater than 100%.[45] Additionally, the small columnar diameter provides a short ion-diffusion length, which facilitates rapid sodium insertion and extraction. An HRTEM image of a bundle of individual columns is shown in Figure 1b. No lattice fringes are visible, indicating that the as-deposited material is amorphous.

Amorphous nanocolumns are expected, as the growth of crystalline or poly-crystalline material requires adatom surface diffusion in order to build long-range order into the structures. This requirement for crystalline growth contradicts the requirements required for the growth of nanocolumnar films by GLAD.[39] The amorphous nature of the material was confirmed by selected-area electron diffraction, shown in the insert in Figure 1b. Only diffuse rings are present indicating the lack of any long-range order in the sample. SEM images of the dense films deposited at 0° as well as a clean stainless steel substrate are shown in Figure S2. These films do not exhibit nanostructuring. Any features in the film are the result of substrate roughness being conformally coated during deposition.

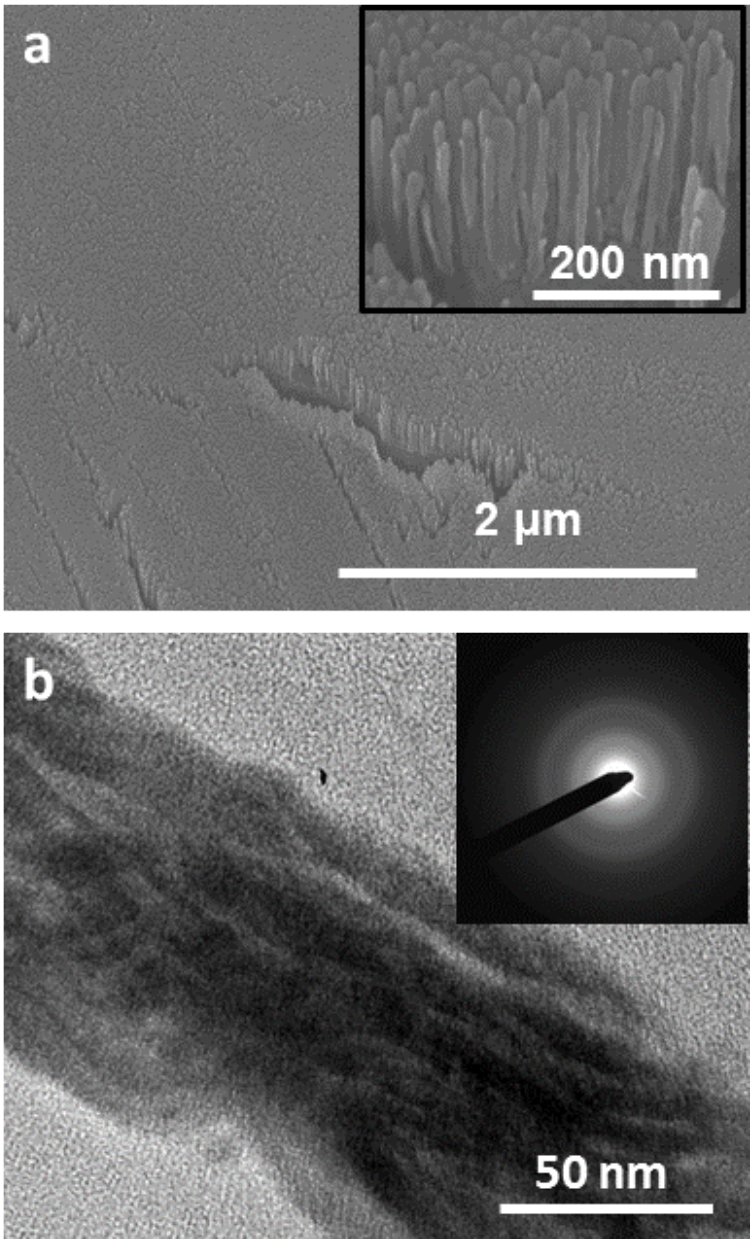

Figure 6.1. a) SEM image of germanium nanocolumns deposited at 70°. b) HRTEM image of a bundle of nanocolumns. The insert shows the electron diffraction pattern from the material.

Coin cells were made with both nanocolumnar and dense germanium film anodes charged/discharged *versus* sodium metal counterelectrodes. The cycle life testing results are shown in Figure 6.2a. The cycling was at C/5 after an initial conditioning cycle at C/20. While the initial capacities of the dense and nanocolumnar films are similar (430 mAh/g for the nanocolumnar films *versus* 400 mAh/g for the dense films), the stability of the two morphologies are markedly different. The nanocolumnar film, deposited at 70°, shows excellent capacity retention, maintaining 88% of initial capacity after 100 cycles. The dense film, however, begins to show significant capacity fade after only 15 cycles. SEM imaging of cycled dense electrodes revealed significant cracking after a single cycle with additional cracking and delamination occurring by the fifth cycle (See Figure S3). The dense films also have a lower average coulombic efficiency than the nanocolumnar films (93% *versus* 95%). This is additional evidence of the dense film's pulverization, which exposes new surfaces for SEI formation. Maranchi *et al.* investigated the behavior of the a-Si/copper current collector interface, and concluded that the cracking and subsequent delamination of the active material was due to the accumulated plastic deformation of the substrate after multiple cycles.[46] The same mechanism is likely responsible for the failure of the dense films in this study. The cycling stability of the nanocolumnar film, deposited at 70°, is therefore the result of the nanoscale dimensions effectively buffering the stresses resulting from the volumetric expansion undergone during cycling both in the bulk and at the active material/substrate interface.

The voltage profiles for the reversible sodiation of germanium films deposited at 70° are shown in Figure 6.2b. The first sodium insertion shows a distinct voltage plateau

at 130 mV *versus* sodium. This voltage is lower than the nearly 400 mV calculated by Chevrier and Ceder.[23] While the magnitude of the 130 mV plateau is too large to be consistent with the formation of the NaGe phase, it is consistent with the reversible capacity of the system as seen in subsequent cycles. The sodium stripping plateau is located at ~600 mV. A large irreversible reaction during the first cycle sodiation includes a shoulder in the voltage profile at ~900 mV which we attribute to the onset of the formation of a passivating SEI layer. The shape of the sodiation and desodiation voltage profiles are quite flat which indicates that the sodiation reaction procedes *via* a two phase reaction mechanism: a reaction front separating the sodium-rich and sodium-poor phases propagates through the material as the reaction progresses.

There is very little change in the shape of the sodiation curves between the first cycle and the 50th cycle, indicating that the sodiation reaction is reversible and that nanocolumnar germanium has good stability when cycled at a slow rate. Between the 50th and 100th cycle, the capacity is lowered and there is a slight increase in the desodiation potential. The sodiation reaction terminates at Na_xGe with $x \approx 1.17$, and the small feature size in the nanocolumnar films is able to effectively buffer the large volumetric expansion associated with sodiation.[45] The product of electrochemical sodiation is not an equilibrium phase, as there are no phases between NaGe and Na_3Ge reported on the phase diagram. It is likely, as is the case with electrochemical lithiation of silicon, that the sodiation of germanium reaches a metastable terminal phase not found on the equilibrium phase diagram.[47-48]

X-ray photoelectron spectroscopy (XPS) was used to investigate the final composition of the sodiated electrodes. A dense germanium electrode was sodiated to 5 mV *vs.* Na/Na^+ at a rate of C/10 and held at that voltage until the current decayed below C/100. The composition of the material was found to be 54 at% sodium and 46 at% germanium. These atomic ratios correspond to a sodium insertion capacity of 433 mAh/g, which is in very good agreement with the electrochemically derived value. The XPS spectrum for sodiated germanium is shown in Figure S4. Details on the elemental analysis can also be found in the supporting information. X-ray diffraction indicated that the sodiated germanium remained amorphous, precluding structural characterization of the sodiated germanium.

The sodium insertion capacity is consistently higher than the extraction capacity indicating that even though the electrode is stable, the SEI layer is not. While the addition of fluorinated ethylene carbonate as an electrolyte co-solvent for lithium-ion batteries significantly improves the coulombic efficiency for silicon and germanium electrodes owing to its formation of a superior SEI layer,[25-26, 49-50] the SEI layer formed from a sodium-salt electrolyte appears to be less stable.

Figure 6.2c shows the cycling behavior of nanocolumnar germanium anodes cycled at various C-rates. After an initial conditioning cycle at C/20, the rate was increased to 3.7C, 7.4C, 18.4C and 27C for 10 cycles each. The electrode exhibited a capacity of 307 mAh/g at 3.7C, 287 at 7.4C, 236 mAh/g at 18.4C and 164 mAh/g at 27C. 27C corresponds to a current density of 10 A/g. The high capacity retention at high charge rates indicates that sodium diffusion is rapid in amorphous germanium despite the

large radius of the sodium ion. Additionally, the high current capability on sodium insertion provides a measure of safety by making it difficult to electrodeposit sodium on the electrode surface. A C-rate test performed on a dense film is shown in figure S5. The voltage profile for the last cycle at each C-rate is shown in Figure 6.2d. At the two highest current densities, a nucleation overpotential becomes apparent at the beginning of sodiation as a result of the two-phase reaction mechanism for the sodiation of germanium.

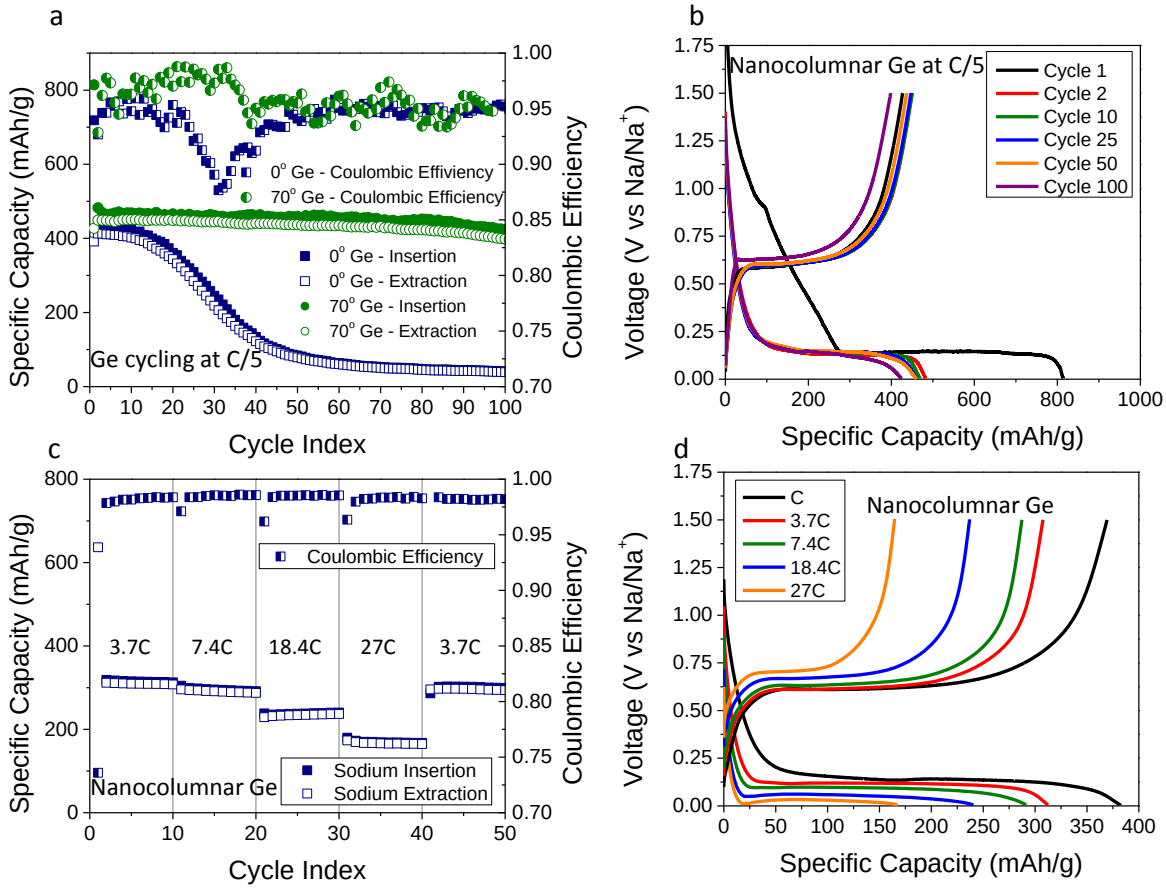

Figure 6.2. a) Cycling results for germanium thin films deposited at an incident angle of 0° and 70°. Cycling was performed at C/5 after an initial conditioning cycle of C/20. b) Voltage profiles for the 1st, 2nd, 10th, 25th, 50th, and 100th sodium insertion cycles in nanocolumnar germanium deposited at 70°. c) C-rate testing of 70° germanium thin films with 10 cycles each at 3.7C, 7.4C, 18.4C, and 27C (10 A/g), and d) voltage profiles for sodium insertion cycles at each rate in the C-rate test.

The impedance spectra of fully sodiated and fully desodiated dense germanium films are shown in Figure 6.3. 20 nm thick dense films were used so that the electrode would have a well-defined surface area and a well-known finite diffusion length. The impedance spectra were fit to a modified Randle's circuit employing a constant phase

element to account for surface roughness and a finite Warburg element to account for the solid state diffusion. From this model, the diffusion coefficient for sodium in the dense germanium film was found to be ~$9x10^{-14}$ cm^2 s^{-1}, and the diffusion coefficient for sodium in sodiated germanium was found to be $1.6x10^{-13}$ cm^2 s^{-1}. This is much faster than what is predicted by extrapolation from high temperature diffusion data for single-crystalline germanium.[29] The measured diffusion coefficient is not directly comparable to values for single-crystalline materials as the presence of surface and grain-boundary diffusion, as well as the amorphous nature of the material, have a significant impact on the apparent diffusion rate. Defects in amorphous semiconductors tend to trap interstitial diffusors such as sodium, thus slowing diffusion. However, the nanoscale thickness of the electrodes used for the impedance measurements results in a large surface area to volume ratio, thus making surface diffusion a dominant effect.

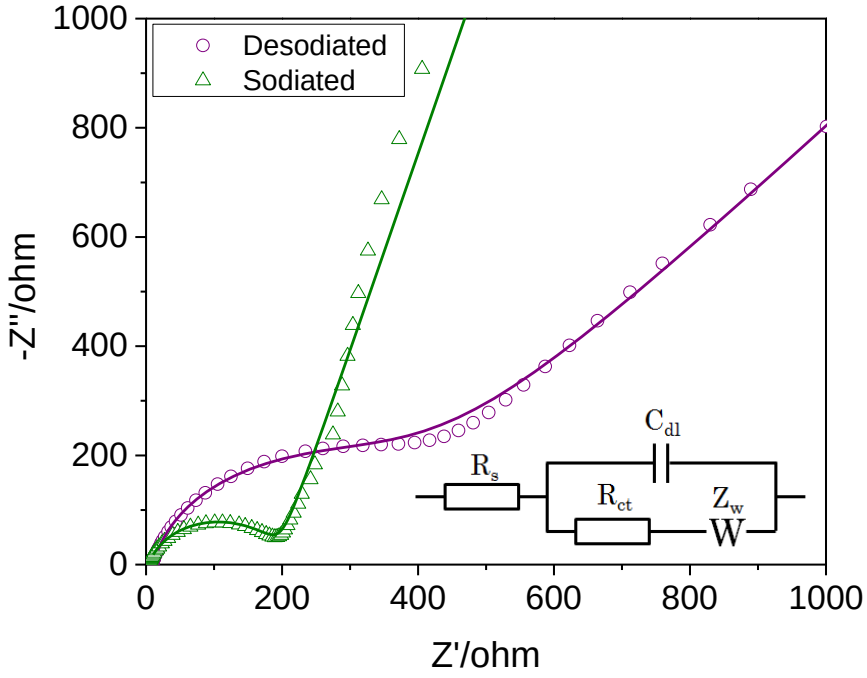

Figure 6.3. Impedance spectra of both fully sodiated (at 10mV *versus* Na/Na^+) and fully desodiated (at 1 V *versus* Na/Na^+) 20nm thick dense germanium films. The data were modeled using a Randles circuit. The data are shown as open symbols and the model fit is shown as solid lines.

To examine the surface effects on the mobility of Na atoms in sodiated Ge, *ab initio* molecular dynamics (AIMD) simulations were performed at 1000 K to calculate Na diffusivities (D_{Na}) in slab and bulk amorphous $Na_{0.25}Ge_{0.75}$ alloy (*a*-$Na_{0.25}Ge_{0.75}$) systems. The bulk model structure for *a*-$Na_{0.25}Ge_{0.75}$ consisting of 16 Na and 48 Ge atoms was created with AIMD simulations. Detailed computational methods can be found elsewhere.[51-52] The slab models had a 15-Å-thick vacuum gap inserted into the *a*-$Na_{0.25}Ge_{0.75}$ bulk alloys in the *z* direction. To simulate a laterally extended surface in the *x* and *y* directions, we employed the repeated-slab approach by applying periodic boundary

conditions to the unit cell. The unit cells for the bulk and slab systems are illustrated in Figure 6.4.

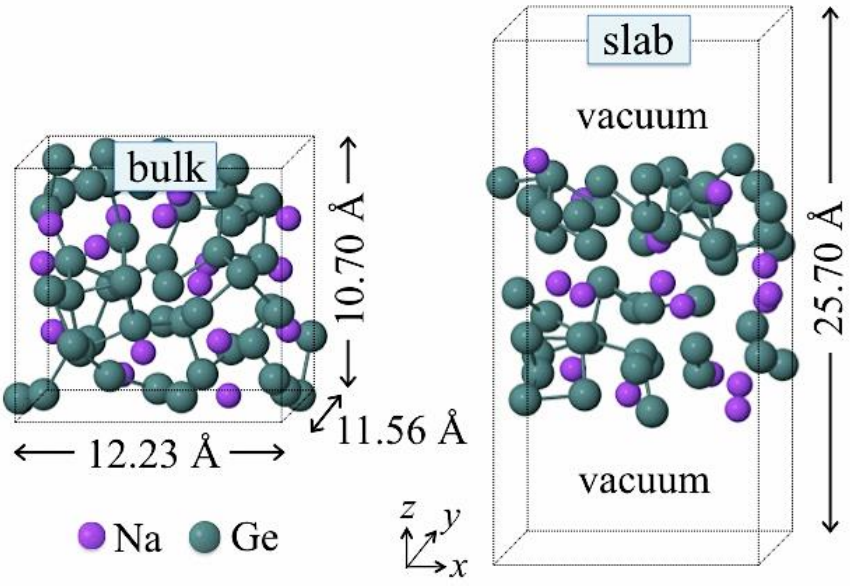

Figure 6.4. Side View of a-Na0.25Ge0.75 bulk and slab systems each containing 64 atoms. The laterally extended surface in the x and y directions is simulated using the repeated slab approach with a vacuum layer inserted in the z direction.

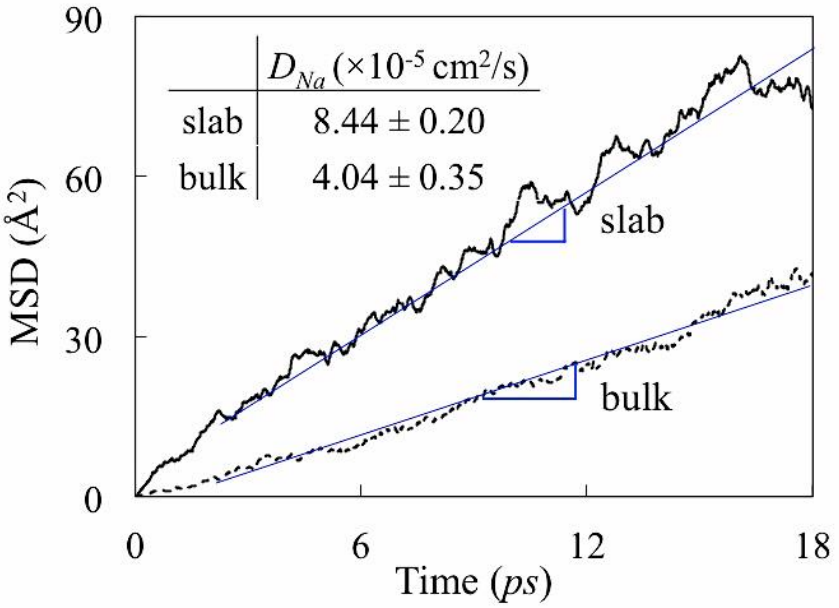

Figure 6.5. Variation in the mean square displacements (MSDs) of Na atoms in a-Na0.25Ge0.75 bulk and slab systems at 1000 K.

For each system, three samples were averaged to calculate the mean-square displacements of Na atoms (MSD = $|R_i(t) - R_i(0)|^2$, where $R_i(t)$ is the position of atom i at time t). From the MSD profiles shown in Figure 6.5, D_{Na} values were obtained from the Einstein relation, D = <MSD>/6t; the angular bracket denotes an averaged value. Here, the MD duration of 18 *ps* appears to be sufficient to obtain well-converged results; disregarding the first 2 *ps*, linear fits over a time interval of the following 16 *ps* yield D_{Na} = 8.44 ± 0.20 and 4.03 ± 0.35 × 10^{-5} cm^2/s for the slab and bulk systems, respectively. Although the slabs employed in our calculations were fairly thin, we could not exclude the contribution of the (bulk-like) subsurface/center regions; hence, the diffusivities calculated here should not be viewed as pure surface diffusivities. Nevertheless, the

results clearly show that Na diffusion along the surface is much more facile than bulk diffusion. As a result, the nanocolumnar Ge thin films with a relatively large surface-area-to-volume ratio are able to sustain reversible charge/discharge rates as high as 27 C (10 A/g).

CONCLUSIONS

We have demonstrated the reversible electrochemical storage of sodium in nanocolumnar germanium electrodes with an initial sodium storage capacity of 430 mAh/g. After 100 cycles at C/5, 88% of this capacity is retained. The material also exhibits high capacity retention at rates up to 27C (10 A/g), Dense germanium films exhibit significant capacity fade when cycled at the same rate. *Ab initio* molecular dynamics simulations of the Na-Ge system indicate that near-surface diffusion is significantly faster than bulk diffusion. Nano-scale dimensions, therefore, are critical for stable, reversible, and high-rate sodiation of germanium.

REFERENCES

1. Wen, Z.; Hu, Y.; Wu, X.; Han, J.; Gu, Z., *Adv. Funct. Mater.* **2012,** *23*, 1005–1018.

2. Lu, X.; Li, G.; Kim, J. Y.; Lemmon, J. P.; Sprenkle, V. L.; Yang, Z., *J. Power Sources* **2012,** *215*, 288-295.

3. Ellis, B. L.; Nazar, L. F., *Curr. Opin. Solid State Mater. Sci.* **2012,** *16*, 168-177.

4. Moreau, P.; Guyomard, D.; Gaubicher, J.; Boucher, F., *Chem. Mater.* **2010,** *22*, 4126-4128.

5. Liu, Y.; Xu, Y.; Han, X.; Pellegrinelli, C.; Zhu, Y.; Zhu, H.; Wan, J.; Chung, A. C.; Vaaland, O.; Wang, C.*, et al.*, *Nano Lett.* **2012,** *12*, 5664-5668.

6. Kim, D.; Lee, E.; Slater, M.; Lu, W.; Rood, S.; Johnson, C. S., *Electrochem. Commun.* **2012,** *18*, 66-69.

7. Xia, X.; Dahn, J. R., *Electrochem. Solid-State Lett.* **2012,** *15*, A1-A4.

8. Barpanda, P.; Ye, T.; Nishimura, S.-I.; Chung, S.-C.; Yamada, Y.; Okubo, M.; Zhou, H.; Yamada, A., *Electrochem. Commun.* **2012,** *24*, 116-119.

9. Sun, Q.; Ren, Q.-Q.; Fu, Z.-W., *Electrochem. Commun.* **2012,** *23*, 145-148.

10. Jian, Z.; Zhao, L.; Pan, H.; Hu, Y.-S.; Li, H.; Chen, W.; Chen, L., *Electrochem. Commun.* **2012,** *14*, 86-89.

11. Lim, S. Y.; Kim, H.; Shakoor, R. A.; Jung, Y.; Choi, J. W., *J. Electrochem. Soc.* **2012,** *159*, A1393-A1397.

12. Lu, Y.; Wang, L.; Cheng, J.; Goodenough, J. B., *Chem. Commun.* **2012,** *48*, 6544-6546.

13. Wessells, C. D.; Peddada, S. V.; Huggins, R. A.; Cui, Y., *Nano Lett.* **2011,** *11*, 5421-5425.

14. Wessells, C. D.; McDowell, M. T.; Peddada, S. V.; Pasta, M.; Huggins, R. A.; Cui, Y., *ACS Nano* **2012,** *6*, 1688-1694.

15. Alcántara, R.; Jiménez-Mateos, J. M.; Lavela, P.; Tirado, J. L., *Electrochem. Commun.* **2001,** *3*, 639-642.

16. Wenzel, S.; Hara, T.; Janek, J.; Adelhelm, P., *Energy & Environmental Science* **2011,** *4*, 3342-3345.

17. Cao, Y.; Xiao, L.; Sushko, M. L.; Wang, W.; Schwenzer, B.; Xiao, J.; Nie, Z.; Saraf, L. V.; Yang, Z.; Liu, J., *Nano Lett.* **2012,** *12*, 3783-3787.

18. Datta, M. K.; Epur, R.; Saha, P.; Kadakia, K.; Park, S. K.; Kumta, P. N., *J. Power Sources* **2013,** *225*, 316-322.

19. Lin, Y.-M.; Abel, P. R.; Gupta, A.; Goodenough, J. B.; Heller, A.; C. Buddie Mullins, *ACS Appl. Mater. Interfaces - accepted*.

20. Qian, J.; Chen, Y.; Wu, L.; Cao, Y.; Ai, X.; Yang, H., *Chem. Commun.* **2012,** *48*, 7070-7072.

21. Darwiche, A.; Marino, C.; Sougrati, M. T.; Fraisse, B.; Stievano, L.; Monconduit, L., *J. Am. Chem. Soc.* **2012,** *134*, 20805-20811.

22. Xiao, L.; Cao, Y.; Xiao, J.; Wang, W.; Kovarik, L.; Nie, Z.; Liu, J., *Chem. Commun.* **2012,** *48*, 3321-3323.

23. Chevrier, V. L.; Ceder, G., *J. Electrochem. Soc.* **2011,** *158*, A1011-A1014.

24. Abel, P. R.; Chockla, A. M.; Lin, Y.-M.; Holmberg, V. C.; Harris, J. T.; Korgel, B. A.; Heller, A.; Mullins, C. B., *ACS Nano* **2013,** *7*, 2249-2257.

25. Chockla, A. M.; Klavetter, K. C.; Mullins, C. B.; Korgel, B. A., *ACS Appl. Mater. Interfaces* **2012,** *4*, 4658-4664.

26. Klavetter, K. C.; Wood, S. M.; Lin, Y.-M.; Snider, J. L.; Davy, N. C.; Chockla, A. M.; Romanovicz, D. K.; Korgel, B. A.; Lee, J.-W.; Heller, A.*, et al.*, *J. Power Sources* **2013,** *238*, 123-136.

27. Graetz, J.; Ahn, C. C.; Yazami, R.; Fultz, B., *J. Electrochem. Soc.* **2004,** *151*, A698-A702.

28. Chan, C. K.; Zhang, X. F.; Cui, Y., *Nano Lett.* **2007,** *8*, 307-309.

29. Stojić, M.; Kostić, D.; Stošić, B., *Physica B+C* **1986,** *138*, 125-128.

30. Fuller, C. S.; Severiens, J. C., *Phys. Rev.* **1954,** *96*, 21-24.

31. Abelmann, L.; Lodder, C., *Thin Solid Films* **1997,** *305*, 1-21.

32. Robbie, K.; Sit, J. C.; Brett, M. J., *J. Vac. Sci. Technol., B* **1998,** *16*, 1115-1122.

33. Flaherty, D. W.; Dohnálek, Z.; Dohnálková, A.; Arey, B. W.; McCready, D. E.; Ponnusamy, N.; Mullins, C. B.; Kay, B. D., *J. Phys. Chem. C* **2007,** *111*, 4765-4773.

34. Krause, K. M.; Thommes, M.; Brett, M. J., *Microporous Mesoporous Mater.* **2011,** *143*, 166-173.

35. Fleischauer, M. D.; Li, J.; Brett, M. J., *J. Electrochem. Soc.* **2009,** *156*, A33-A36.

36. Abel, P. R.; Lin, Y.-M.; Celio, H.; Heller, A.; Mullins, C. B., *ACS Nano* **2012,** *6*, 2506-2516.

37. Lin, Y.-M.; Abel, P. R.; Flaherty, D. W.; Wu, J.; Stevenson, K. J.; Heller, A.; Mullins, C. B., *J. Phys. Chem. C* **2011,** *115*, 2585-2591.

38. Flaherty, D. W.; Hahn, N. T.; May, R. A.; Berglund, S. P.; Lin, Y.-M.; Stevenson, K. J.; Dohnalek, Z.; Kay, B. D.; Mullins, C. B., *Acc. Chem. Res.* **2012,** *45*, 434–443.

39. Hawkeye, M. M.; Brett, M. J., *J. Vac. Sci. Technol., A* **2007,** *25*, 1317-1335.

40. Blöchl, P. E., *Phys. Rev. B* **1994,** *50*, 17953-17979.

41. Kresse, G.; Hafner, J., *Phys. Rev. B* **1993,** *47*, 558-561.

42. Kresse, G.; Furthmüller, J., *Comput. Mater. Sci.* **1996,** *6*, 15-50.

43. Kresse, G.; Furthmüller, J., *Phys. Rev. B* **1996,** *54*, 11169-11186.

44. Monkhorst, H. J.; Pack, J. D., *Phys. Rev. B* **1976,** *13*, 5188-5192.

45. Witte, J.; Schnering, H. G.; Klemm, W., *Z. Anorg. Allg. Chem.* **1964,** *327*, 260-273.

46. Maranchi, J. P.; Hepp, A. F.; Evans, A. G.; Nuhfer, N. T.; Kumta, P. N., *J. Electrochem. Soc.* **2006,** *153*, A1246-A1253.

47. Hatchard, T. D.; Dahn, J. R., *J. Electrochem. Soc.* **2004,** *151*, A838-A842.

48. Obrovac, M. N.; Christensen, L., *Electrochem. Solid-State Lett.* **2004,** *7*, A93-A96.

49. Lin, Y.-M.; Klavetter, K. C.; Abel, P. R.; Davy, N. C.; Snider, J. L.; Heller, A.; Mullins, C. B., *Chem. Commun.* **2012,** *48*, 7268-7270.

50. Nakai, H.; Kubota, T.; Kita, A.; Kawashima, A., *J. Electrochem. Soc.* **2011,** *158*, A798-A801.

51. Chou, C.-Y.; Hwang, G. S., *Surf. Sci.* **2013,** *612*, 16-23.

52. Kim, H.; Chou, C.-Y.; Ekerdt, J. G.; Hwang, G. S., *J. Phys. Chem. C* **2011,** *115*, 2514-2521.

Chapter 7: Tin-Germanium Alloys as Anode Materials for Sodium-Ion Batteries

INTRODUCTION

Sodium batteries have the potential for significant cost advantages over lithium batteries and are attractive for stationary applications where cost is a limiting factor. The Na-S and Na-$NiCl_2$ batteries offer such an advantage, but they utilize liquid electrodes, require ceramic electrolytes, and operate at temperatures on the order of 300ºC.[1-2] Their high operating temperature makes them less attractive for intermittent or on-demand applications. Recent identification of new intercalation materials for Na-ion battery cathodes has refreshed the effort to develop Na chemistries that operate at room-temperature.[3-12] Many sodium intercalation compounds behave similarly to their lithium analogues,[6, 13-14] however Na-ions will typically not intercalate into graphite although other carbon allotropes show a small reversible capacity.[15-17] This has led to a presently ongoing search for safe, abundant and robust materials for Na-ion battery anodes.

Group IV elements have been well studied as anode materials for lithium-ion batteries.[18-32] In their recent study Chevrier and Ceder calculated the voltages at which that the heavier group IV elements alloy with sodium.[15] Experimental data are available for germanium,[33-34] tin,[35-37] and lead.[38] Sodium alloys with Sn up to a thermodynamic limit of $Na_{15}Sn_4$, providing a theoretical capacity of 847 mAh g^{-1}, making it an attractive candidate. However, the capacity is not well retained on cycling, particle aggregation and electrode/electrolyte instability being cited as causes of degradation.[39-42] While limiting

the potential range of cycling improves the stability, [41] operating anode potentials in actually functioning batteries is rarely well-defined. Additionally, active/inactive matrices,[43-44] composites,[45-46] and alloys have been investigated as methods for stabilizing tin electrodes.[47-48]

The technology of alloying elements to change material properties is nearly as old as civilization itself. The Bronze Age is named after one of the first metallurgical discoveries, the alloying of copper and tin, resulting in a much harder metal. By alloying tin with other elements, physical, chemical, and electrochemical properties can be significantly altered, and by appropriate selection of Sn-alloying element(s), anode materials can be improved. This principle has been demonstrated in the literature with the addition of copper to tin electrodes for sodium-ion batteries. Sn-Cu compounds will have a melting point that is significantly higher than that of pure tin, and as a result, the Sn-Cu alloys are more resistant to agglomeration and electrochemical sintering. As expected, the Sn-Cu electrodes show significant improvements in stability; however, the specific capacity is decreased by the additional weight of the inactive Cu in the electrode.[47]

Alloying tin with other sodium-active elements is a possible way to improve the electrode stability without sacrificing capacity. Other group IV elements such as Ge have limited solubility in tin at room temperature,[49] but metastable amorphous alloys of tin and germanium have been synthesized for study as semiconductor materials. Vacuum evaporative deposition and sputtering allowed the growth of single phase, amorphous tin-germanium alloys of over a much wider compositional range than allowed by traditional processing techniques.[50-51] Furthermore, such alloys exhibit tetrahedral short range order

as well as random arrangement of their constituent elements. Group IV alloys such as Si-Ge[19] and Sn-Ge[52-54] have been investigated as lithium-ion batteries anodes and Sn-Ge-Sb ternary alloys have recently been investigated for sodium-ion batteries,[55] but the electrochemical properties of alloy systems are still not well understood.

Here we grow well-defined thin films of Sn-Ge alloys of various compositions by vacuum deposition and test them as sodium-ion battery anodes. Additionally, we use glancing angle deposition (GLAD) for microstructural and porosity control. GLAD is a physical vapor deposition technique in which adatoms impinge on the substrate at a glancing angle (in our case, we use 70^{o} from surface normal). GLAD will produce nanostructured films if the surface diffusion of adatoms is limited.[56] In the early stages of deposition, stochastic variations in the deposition rate tend to roughen the surface. That roughness is amplified by self-shadowing and leads to the growth of porous films.[57] In these films, morphology is controlled by the deposition angle, and ranges from dense at angles close to normal, to porous, reticulated, and then nanocolumnar as the deposition angle is increased. [58] If surface diffusion is possible, however, the shadowed regions of the substrate are accessible to the adatoms through diffusional processes and dense films result independent of deposition angle. Adatom surface diffusion is related to substrate temperature with growth of non-equilibrium structures possible if the substrate temperature is held below approximately 1/3 of the melting point of the deposited material.[59] We use the ability of the alloys to support nanostructured growth as a proxy for stability and correlate electrochemical stability to the ability to hold nanostructure

during deposition. Additional details, examples and applications of GLAD can be found elsewhere.[18-19, 60-61]

EXPERIMENTAL METHODS

Material Synthesis

Tin-Germanium alloy electrodes were vacuum deposited by co-evaporation of Tin (Alfa Aesar 99.999%) and Germanium (Kurt J. Lesker 99.999%) using electron beam evaporators. The composition of the Sn-Ge alloys was controlled by varying the ratio of the fluxes from the individual evaporators. The deposition rate for each element was independently measured and balanced to grow a film of the desired composition. The base pressure of the chamber was $<1x10^{-7}$ Torr, but increased to $\sim5x10^{-7}$ Torr during deposition. Material for electrochemical testing and SEM imaging was deposited on 15.6 mm diameter stainless steel substrates (Pred Materials) at an incident angle of 0^{o} or 70^{o} from the surface normal, while material for resistivity measurements was deposited on glass slide covers (Fisher Scientific). The substrates were cleaned by sonication in ethanol prior to deposition. The deposition rate of each evaporator was calibrated using a quartz crystal microbalance (QCM) (Inficon SQM-160 with cool-drawer sensor feed-through), and the ratio of deposition rates was used to calculate film composition. The total mass density of the electrodes was 50 $\mu g\ cm^{-2}$.

Material Characterization

SEM images of the electrodes were obtained with a Hitachi S5500 equipped with a Bruker x-ray detector for EDX measurements. XRD was performed on a Philips X-

PERT theta-theta diffractometer. Resistivity measurements were made with a Lucas four-point probe employing a Keithley 220 programmable current source. The composition was measured by XPS using a commercial X-ray photoelectron spectrometer (Kratos Axis Ultra), utilizing a monochromatic Al-Kα X-ray source (hν = 1486.5 eV). An automated charge neutralizer was employed for analysis. Casa XPS analysis software was used to determine the stoichiometry of samples from corrected peak areas, employing Kratos sensitivity factors for each element of interest.

Electrochemical testing

As-deposited films were assembled into 2032 coin cells in an argon-filled glove-box (MBraun Unilab) with oxygen and water levels held below 5 ppm. Sodium metal (Sigma-Aldrich, ACS Reagent) was used as the counter/pseudoreference electrode and 1 M $NaPF_6$ (Alfa Aesar, 99+%) in a 1:1 mixture of fluorinated ethylene carbonate (Solvay Chemicals) and diethyl carbonate (Sigma Aldrich, battery grade) as the electrolyte. Celgard 2400 polypropylene membrane was used as the separator. Cells were galvanically cycled using an Arbin BT2043 multichannel battery tester. Cells were cycled between 5 mV and either 0.75V or 1.5 V *versus* the Na/Na^+ redox couple.

RESULTS AND DISCUSSION

Films with nominal compositions Ge, $Ge_{0.75}Sn_{0.25}$, $Ge_{0.5}Sn_{0.5}$, $Ge_{0.25}Sn_{0.75}$, and Sn, all deposited at 0^o, were analyzed by XPS in order to verify the final composition of the films. Quantitative analysis of the Ge $2p_{1/2}$ feature at 1248 eV and the Sn $3d_{5/2}$ feature at 485 eV was used to determine the film compositions. These features are shown in Figure

7.1. Quantitative analysis of the features provided film compositions very close to the nominal values calculated from QCM measured fluxes. The measured values for the intermediate compositions were $Ge_{0.79}Sn_{0.21}$, $Ge_{0.45}Sn_{0.55}$, $Ge_{0.26}Sn_{0.74}$. For simplicity, we continue to label the films by their nominal compositions. Both the tin and germanium show measurable oxidation, with a germanium oxide peak at 1251 eV and a tin oxide peak at 487 eV. XPS, however, is a surface sensitive technique, and no precautions were taken to prevent surface oxidation on the samples.

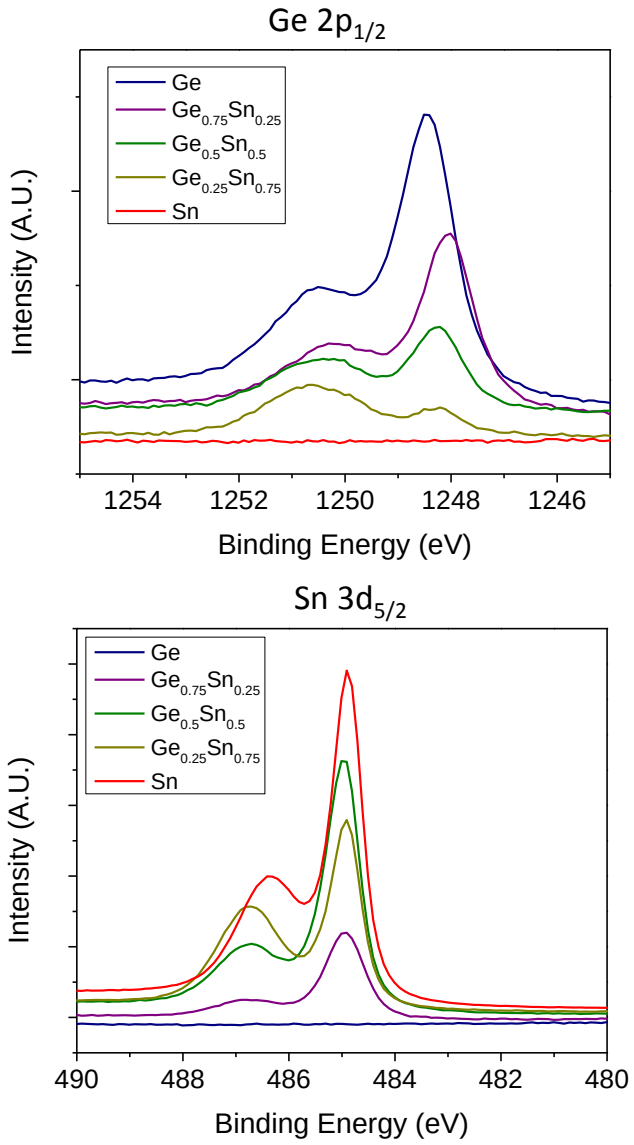

Figure 7.1. XPS on Sn-Ge alloy electrodes. The Ge $2p_{1/2}$ and Sn $3d_{5/2}$ features are shown. Quantitative analysis was used to determine the elemental composition of each film.

SEM images of Sn-Ge films deposited at 0° as well as 70° are shown in Figure 7.2. While there is a marked difference in morphology between the films deposited at different angles for pure germanium, the two pure tin films look identical. This is due to

the difference in surface mobility between the two species. The substrate is radiatively heated by the evaporators, and tin is much more mobile than germanium at the substrate temperature of ~50°C during deposition. The substrate temperature is high enough for tin adatoms to migrate into any shadowed regions by surface diffusion when the tin is deposited at a glancing angle. This absolute substrate temperature is roughly 64% of tin's absolute melting point; in comparison, the absolute substrate temperature is only 26% of the absolute melting point of Ge. The deposited alloys are metastable phases not represented on the phase diagram, and thus do not have a well-defined melting point. The liquid species, however, are completely miscible and if we use substrate temperature as a fraction of the liquidus as a predictor of stability, we get values of 29%, 31%, and 36% for $Ge_{0.75}Sn_{0.25}$, $Ge_{0.5}Sn_{0.5}$, and $Ge_{0.25}Sn_{0.75}$ respectively. This analysis agrees with the SEM images of films deposited at 70° (Figure 7.2) where Ge and $Ge_{0.75}Sn_{0.25}$ are nanostructured while $Ge_{0.25}Sn_{0.75}$ and pure Sn are dense. $Ge_{0.5}Sn_{0.5}$ appears to be a transition case where there is significant porosity in the film, but it is not nanostructured to the degree of the higher germanium content films. This is consistent with the surface atoms being increasingly mobile as the mole fraction of tin is increased. We therefore expect the films with the highest tin content to be the least stable on cycling. The morphology of the films deposited at 0° also changes with composition. Tin does not wet the stainless steel substrates used in this study and formed isolated islands rather than a conformal film during deposition. The film roughness and prevalence of such islands increased with the film's tin content.

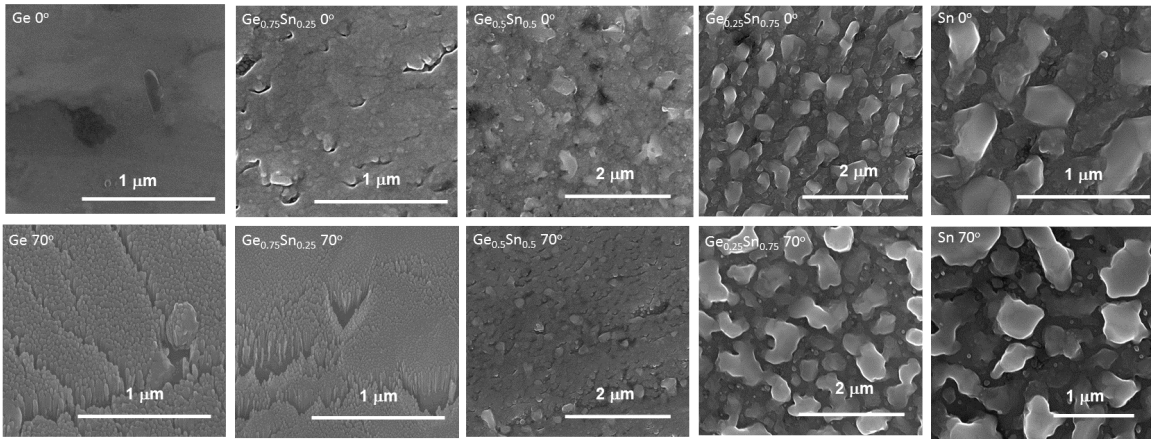

Figure 7.2. SEM images of Sn-Ge alloy films. Films of each composition are shown deposited at both 0° and 70° from surface normal.

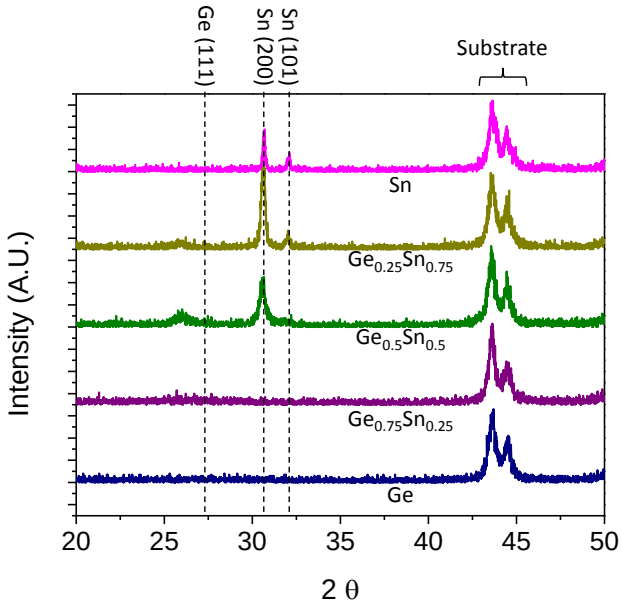

Figure 3. XRD patterns of as-deposited Sn-Ge films of each composition.

Figure 7.3 shows x-ray diffraction patterns for thin films of each composition. The only visible features in the Ge and $Ge_{0.75}Sn_{0.25}$ films at 43.6° and 44.5° are due to the stainless steel substrate. The high melting point of germanium leads to the deposition of completely amorphous films, and high concentrations of germanium decrease the mobility of tin. Crystalline peaks for b-tin are observed for $Ge_{0.5}Sn_{0.5}$, $Ge_{0.25}Sn_{0.75}$ and pure Sn. This is consistent with the findings of Maruyama and Akagi, who found that crystalline b-tin formed for compositions with more than 38 at% tin.[62] The intensity of the Sn [101] peak at 32° decreases while the Sn [200] peak at 30° broadens and shifts to lower angles with increasing germanium content. This indicates that the tin lattice is increasingly strained as the germanium content of the film is increased. A detailed view of the tin [101] and [200] is shown in Figure F.1 in the supporting information.

Thin films of each alloy, deposited at 0° in order to have consistent morphology for all samples, were cycled as a constant current C/2 between 5mV and either 0.75V, or 1.5V in order to investigate the cycling stability of each composition. The cycling results are shown in Figure 7.4. When cycled up to 1.5V, the capacity of both the tin and the $Ge_{0.25}Sn_{0.75}$ electrodes degraded rapidly. The tin electrode only survived for four cycles before the capacity dropped significantly while the $Ge_{0.25}Sn_{0.75}$ survived for ~20 cycles before it began to degrade appreciably. At germanium compositions of 50 at% and higher, however, the capacity remained stable for the full 100 cycles. The stability of the films and the ability of that material to form non-equilibrium structures during deposition follow the same trend; this suggests that the observed electrode degradation is related to

the mobility of the electrode material. By increasing the liquidus of the alloy, the mobility of the constituent atoms is decreased and the stability of the electrode is increased.

If the upper cutoff voltage is reduced from 1.5 V to 0.75 V, all compositions remain stable for the duration of the 100 cycle test with the exception of pure tin. While the tin electrode is not perfectly stable, its stability is greatly increased. For the 0.75 V case, the tin electrode retains 83% of its initial capacity whereas only 5% is retained when the cutoff voltage is 1.5V. The decrease in upper cutoff voltage also reduced the reversible capacity of all electrode compositions. This indicates that some sodium remains alloyed with the electrode at the upper cutoff voltage, i.e., the sodium is incompletely stripped from the electrode.

Voltage profiles for the second cycles for all of the compositions are shown in Figure 5a. The tin electrode shows voltage plateaus for sodium stripping at 660 mV, 530 mV, 270 mV, 210 mV, and 150 mV. The plateaus at 660 mV, 530 mV, 270 mV and 150 mV have been indexed by Ellis *et al.* to the following reactions respectively:[35]

$$3Sn + Na <-> NaSn_3 \quad (7.1)$$

$$1/3\ NaSn_3 + 2/3Na <-> a\text{-}NaSn \quad (7.2)$$

$$4\ a\text{-}NaSn + 5\ Na <-> Na_9Sn_4 \quad (7.3)$$

$$Na_9Sn_4 + 6\ Na <-> Na_{15}Sn_4 \quad (7.4)$$

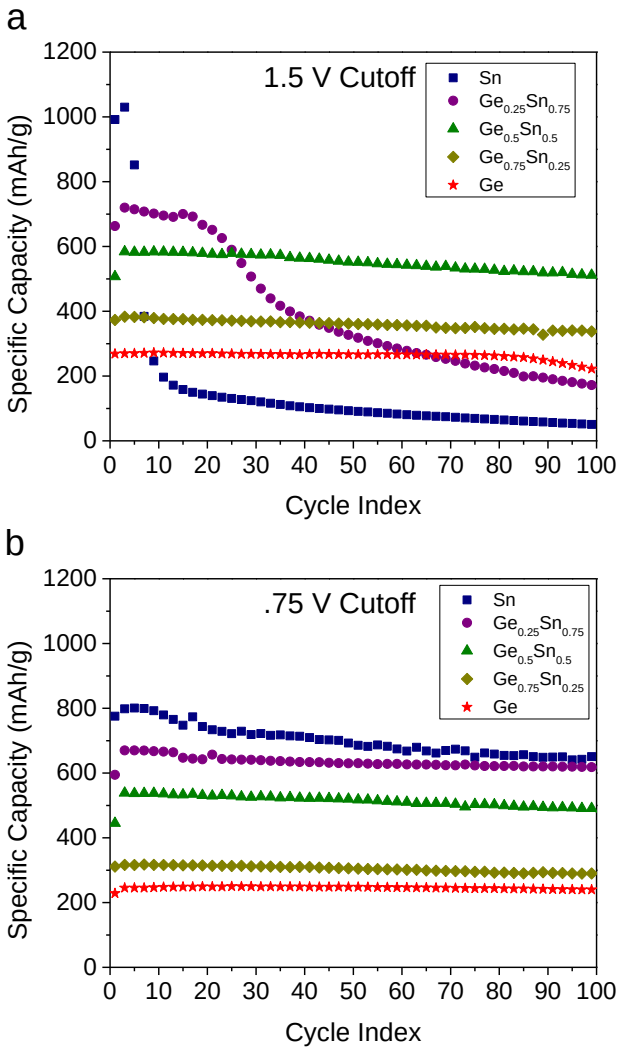

Figure 7.4. Stability of Sn-Ge alloy films cycled at C/2 between a lower cutoff voltage of 5 mV and an upper cutoff voltage of either a) 1.5 V, or b) 0.75 V.

As germanium is added, the redox potential of the phase transformations are changed and the formation of certain phases are suppressed. The voltage of each phase transformation for each composition is shown in Figure 7.5b. When 25 at% germanium is added to tin, the potential for reaction 1 shifts from 660 mV to 745 mV, and the reaction

is completely suppressed in $Ge_{0.5}Sn_{0.5}$ and alloys with higher germanium content. Both tin and germanium form 1:1 alloys with sodium; however, germanium does not form any intermediate phase between Ge and NaGe,[4] explaining the disappearance of a plateau for reaction 7.1 in germanium rich alloys while the plateau for reaction 7.2 merely shifts from 530 mV for tin, to 550 mV for $Ge_{0.25}Sn_{0.75}$, to 590 mV for $Ge_{0.5}Sn_{0.5}$, to 610 mV to $Ge_{0.75}Sn_{0.25}$. Reaction 7.3 does not exhibit significant changes in potential with composition, remaining near 270 mV for all tested compositions; only the magnitude of the plateau changes. The magnitude, however, drops faster than would be expected from the percentage of tin in the alloy. For $Ge_{0.25}Sn_{0.75}$, the capacity of this plateau dropped from 278 mAh/g, for pure tin, to 174 mAh/g, a reduction of 37% whereas the tin content has only been reduced by 25%. For $Ge_{0.5}Sn_{0.5}$ the magnitude has been reduced to 50 mAh/g, a reduction of 82%. The feature completely disappears in the $Ge_{0.75}Sn_{0.25}$ electrode. The feature for reaction 4 also remains at a constant voltage of ~150mV for $Ge_{0.5}Sn_{0.5}$, $Ge_{0.25}Sn_{0.75}$ and pure tin. It then increases to ~200 mV for $Ge_{0.75}Sn_{0.25}$ and is absent for pure germanium films.

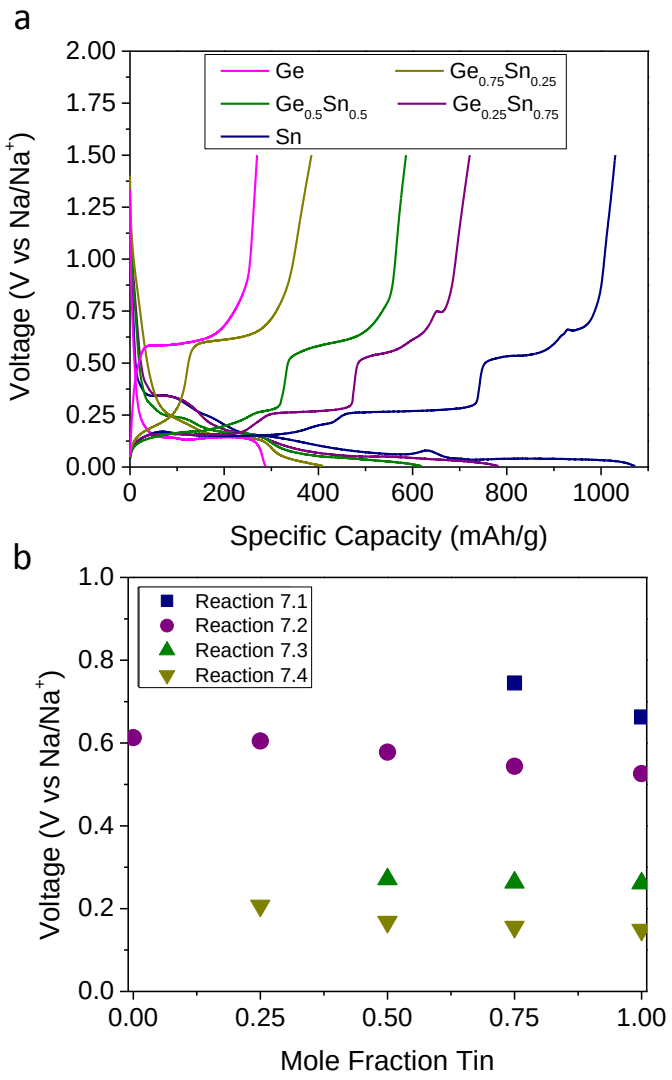

Figure 7.5. a)Voltage profiles of tin-germanium alloys on the second cycle at C/2 and b) the sodium stripping voltages for each of the four reactions proposed by Ellis *et al.*.[35]

C-rate tests were performed on electrodes of each composition. After a conditioning cycle at C/10, each electrode was tested for 10 cycles each at 1C, 2C, 5C, and 10C. The capacity of each composition on the 10th cycle at each C-rate was

normalized to the C/10 capacity for that composition and the normalized capacity as a function of C-rate for each composition is shown in Figure 7.6. The complete series of C-rate tests are shown in Figure F.2 in the supporting information, and voltage profiles for each composition at each rate are shown in Figure F.3. For germanium, the capacity remains nearly constant for rates up to 2C. Above this rate, the capacity drops quickly, with only 50% of the C/10 capacity retained at 10C. The loss in capacity accelerates with increasing C-rate. $Ge_{0.75}Sn_{0.25}$ shows a similar trend, however the normalized capacity is significantly lower at each C-rate.

Tin shows a different trend as the C-rate is increased. While there is a loss in capacity when the rate is increased from C/10 to 1C, the largest decrease in capacity is between 1C and 2C, and the rate of capacity loss decreases as the C-rate is increased beyond that point. The large drop in capacity between 1C and 2C is partially due to the highest voltage sodium stripping feature is pushed outside the voltage window of the test (See Figure F.3 in the supporting information). $Ge_{0.25}Sn_{0.75}$ follows the same trend as pure tin, but with an improved normalized capacity at each C-rate.

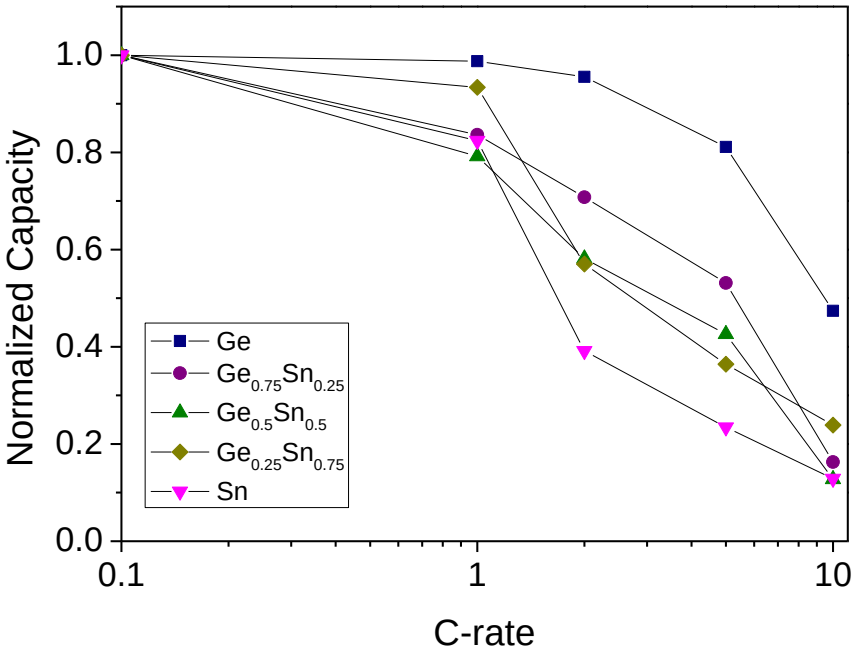

Figure 7.6. Normalized capacity as a function of C-rate for each composition of Sn-Ge alloy.

The stable phase of tin, at room temperature, is metallic β-tin. However a semimetal, diamond-cubic phase, α-tin, is stable below 13.2°C. The stable phase of germanium is diamond-cubic, and the amorphous alloy of the two elements was found to have the diamond-cubic short-range order. Additionally, adding tin to germanium narrows the bandgap of the material.[64] This trend is reflected in the resistivity measurements shown in Figure 7.7. The resistivity of the alloy decreases with increasing tin content, from a value of 84 ohm-cm for pure germanium to 9×10^{-3} ohm-cm for $Ge_{0.25}Sn_{0.75}$. We were unable to measure the resistivity of the pure tin film, as tin does not wet the glass substrates that we were using. Instead, the tin formed individual, isolated

domains on the surface. As such, the measurements returned the resistivity of the substrate rather than the film. However, the resistivity of tin, as reported in the literature is $1x10^{-5}$ ohm-cm for the tetragonal β-tin phase[65] and $2.0x10^{-4}$ ohm-cm for the diamond-cubic α-tin phase.[66] Regression and extrapolation to zero germanium content from the experimental resistivity data matches closely with the reported resistivity value for β-tin suggesting that the local order in the alloy films is diamond cubic.

Because the sodiation reaction is electron mediated, materials with low resistivity are desirable. While pure tin has the lowest resistivity, it is also the least stable composition in this study. The electrodes with high germanium content were much more stable than tin, and additionally performed better at high c-rates. This indicates that for all of the compositions studied electrical resistivity was not a limiting factor.

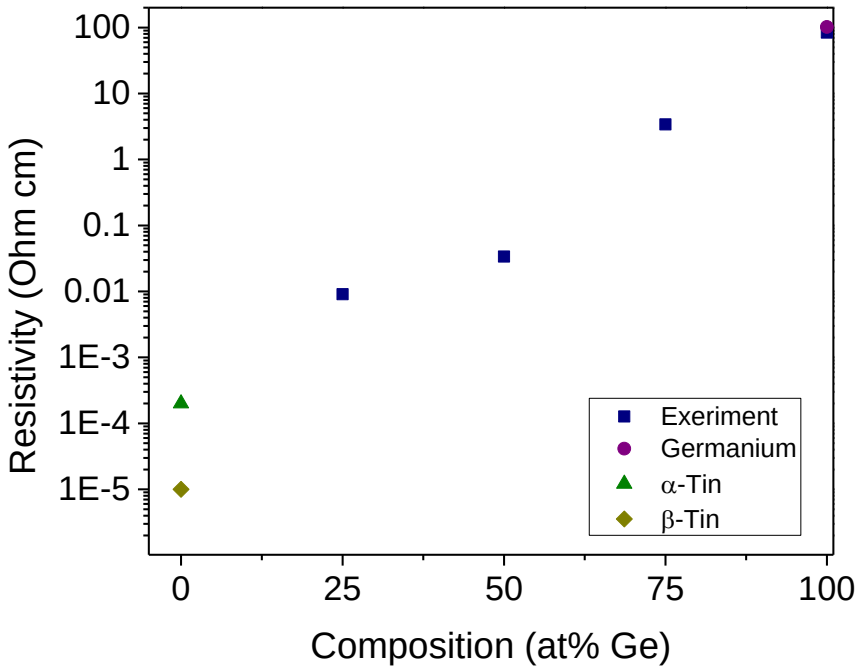

Figure 7.7. Electrical resistivity measurements for tin-germanium alloys as well as literature values for amorphous germanium,[144] α-tin,[52] and β-tin

CONCLUSIONS

Tin is a promising sodium-ion battery material, but suffers from poor cycling stability. Alloying tin with germanium improves the cycling stability. The addition of germanium to tin raises the liquidus of the melt, reducing the surface mobility of atoms at room temperature and improving the cycling stability of the anodes. Limiting the cycling upper cutoff voltage to 0.75V also increases the stability of the anodes.

REFERENCES

1. Sudworth, J. L., *J. Power Sources* **1994,** *51*, 105-114.

2. Lu, X.; Xia, G.; Lemmon, J. P.; Yang, Z., *J. Power Sources* **2010,** *195*, 2431-2442.

3. Lu, Y.; Wang, L.; Cheng, J.; Goodenough, J. B., *Chem. Commun.* **2012,** *48*, 6544-6546.

4. Barpanda, P.; Ye, T.; Nishimura, S.-I.; Chung, S.-C.; Yamada, Y.; Okubo, M.; Zhou, H.; Yamada, A., *Electrochem. Commun.* **2012,** *24*, 116-119.

5. Jian, Z.; Zhao, L.; Pan, H.; Hu, Y.-S.; Li, H.; Chen, W.; Chen, L., *Electrochem. Commun.* **2012,** *14*, 86-89.

6. Kim, D.; Lee, E.; Slater, M.; Lu, W.; Rood, S.; Johnson, C. S., *Electrochem. Commun.* **2012,** *18*, 66-69.

7. Lee, H.; Kim, Y.-I.; Park, J.-K.; Choi, J. W., *Chem. Commun.* **2012,** *48*, 8416-8418.

8. Lim, S. Y.; Kim, H.; Shakoor, R. A.; Jung, Y.; Choi, J. W., *J. Electrochem. Soc.* **2012,** *159*, A1393-A1397.

9. Sun, Q.; Ren, Q.-Q.; Fu, Z.-W., *Electrochem. Commun.* **2012,** *23*, 145-148.

10. Wessells, C. D.; McDowell, M. T.; Peddada, S. V.; Pasta, M.; Huggins, R. A.; Cui, Y., *ACS Nano* **2012,** *6*, 1688-1694.

11. Wessells, C. D.; Peddada, S. V.; Huggins, R. A.; Cui, Y., *Nano Lett.* **2011,** *11*, 5421-5425.

12. Xia, X.; Dahn, J. R., *Electrochem. Solid-State Lett.* **2012,** *15*, A1-A4.

13. Moreau, P.; Guyomard, D.; Gaubicher, J.; Boucher, F., *Chem. Mater.* **2010,** *22*, 4126-4128.

14. Liu, Y.; Xu, Y.; Han, X.; Pellegrinelli, C.; Zhu, Y.; Zhu, H.; Wan, J.; Chung, A. C.; Vaaland, O.; Wang, C.*, et al.*, *Nano Lett.* **2012,** *12*, 5664-5668.

15. Chevrier, V. L.; Ceder, G., *J. Electrochem. Soc.* **2011,** *158*, A1011-A1014.

16. Alcántara, R.; Jiménez-Mateos, J. M.; Lavela, P.; Tirado, J. L., *Electrochem. Commun.* **2001,** *3*, 639-642.

17. Stevens, D. A.; Dahn, J. R., *J. Electrochem. Soc.* **2001,** *148*, A803-A811.

18. Abel, P. R.; Lin, Y.-M.; Celio, H.; Heller, A.; Mullins, C. B., *ACS Nano* **2012,** *6*, 2506-2516.

19. Abel, P. R.; Chockla, A. M.; Lin, Y.-M.; Holmberg, V. C.; Harris, J. T.; Korgel, B. A.; Heller, A.; Mullins, C. B., *ACS Nano* **2013,** *7*, 2249-2257.

20. Lin, Y.-M.; Klavetter, K. C.; Abel, P. R.; Davy, N. C.; Snider, J. L.; Heller, A.; Mullins, C. B., *Chem. Commun.* **2012,** *48*, 7268-7270.

21. Klavetter, K. C.; Wood, S. M.; Lin, Y.-M.; Snider, J. L.; Davy, N. C.; Chockla, A. M.; Romanovicz, D. K.; Korgel, B. A.; Lee, J.-W.; Heller, A.*, et al.*, *J. Power Sources* **2013,** *238*, 123-136.

22. Chockla, A. M.; Klavetter, K. C.; Mullins, C. B.; Korgel, B. A., *ACS Appl. Mater. Interfaces* **2012,** *4*, 4658-4664.

23. Beattie, S. D.; Larcher, D.; Morcrette, M.; Simon, B.; Tarascon, J.-M., *J. Electrochem. Soc.* **2008,** *155*, A158-A163.

24. Dimov, N.; Kugino, S.; Yoshio, M., *Electrochim. Acta* **2003,** *48*, 1579-1587.

25. Maranchi, J. P.; Hepp, A. F.; Kumta, P. N., *Electrochem. Solid-State Lett.* **2003,** *6*, A198-A201.

26. Chan, C. K.; Peng, H.; Liu, G.; McIlwrath, K.; Zhang, X. F.; Huggins, R. A.; Cui, Y., *Nat. Nanotechnol.* **2008,** *3*, 31-35.

27. Seo, M.-H.; Park, M.; Lee, K. T.; Kim, K.; Kim, J.; Cho, J., *Energy & Environmental Science* **2011,** *4*, 425-428.

28. Liang, W.; Yang, H.; Fan, F.; Liu, Y.; Liu, X. H.; Huang, J. Y.; Zhu, T.; Zhang, S., *ACS Nano* **2013,** *7*, 3427-3433.

29. Baggetto, L.; Notten, P. H. L., *J. Electrochem. Soc.* **2009,** *156*, A169-A175.

30. Derrien, G.; Hassoun, J.; Panero, S.; Scrosati, B., *Adv. Mater.* **2007,** *19*, 2336-2340.

31. Winter, M.; Besenhard, J. O., *Electrochim. Acta* **1999,** *45*, 31-50.

32. Courtney, I. A.; McKinnon, W. R.; Dahn, J. R., *J. Electrochem. Soc.* **1999,** *146*, 59-68.

33. Abel, P. R.; Lin, Y.-M.; de Souza, T.; Chou, C.-Y.; Gupta, A.; Goodenough, J. B.; Hwang, G. S.; Heller, A.; Mullins, C. B., *J. Phys. Chem. C* **2013,** *117*, 18885-18890.

34. Baggetto, L.; Keum, J. K.; Browning, J. F.; Veith, G. M., *Electrochem. Commun.* **2013,** *34*, 41-44.

35. Ellis, L. D.; Hatchard, T. D.; Obrovac, M. N., *J. Electrochem. Soc.* **2012,** *159*, A1801-A1805.

36. Datta, M. K.; Epur, R.; Saha, P.; Kadakia, K.; Park, S. K.; Kumta, P. N., *J. Power Sources* **2013,** *225*, 316-322.

37. Yamamoto, T.; Nohira, T.; Hagiwara, R.; Fukunaga, A.; Sakai, S.; Nitta, K.; Inazawa, S., *J. Power Sources* **2012,** *217*, 479-484.

38. Jow, T. R.; Shacklette, L. W.; Maxfield, M.; Vernick, D., *J. Electrochem. Soc.* **1987,** *134*, 1730-1733.

39. Li, H.; Shi, L.; Lu, W.; Huang, X.; Chen, L., *J. Electrochem. Soc.* **2001,** *148*, A915-A922.

40. Kim, C.; Noh, M.; Choi, M.; Cho, J.; Park, B., *Chem. Mater.* **2005,** *17*, 3297-3301.

41. Komaba, S.; Matsuura, Y.; Ishikawa, T.; Yabuuchi, N.; Murata, W.; Kuze, S., *Electrochem. Commun.* **2012,** *21*, 65-68.

42. Beattie, S. D.; Hatchard, T.; Bonakdarpour, A.; Hewitt, K. C.; Dahn, J. R., *J. Electrochem. Soc.* **2003,** *150*, A701-A705.

43. Gu, M.; Kushima, A.; Shao, Y.; Zhang, J.-G.; Liu, J.; Browning, N. D.; Li, J.; Wang, C., *Nano Lett.* **2013,** *13*, 5203-5211.

44. Wang, Y.-X.; Lim, Y.-G.; Park, M.-S.; Chou, S.-L.; Kim, J. H.; Liu, H.-K.; Dou, S.-X.; Kim, Y.-J., *J. Mater. Chem. A* **2014,** *2*, 529-534.

45. Wu, L.; Hu, X.; Qian, J.; Pei, F.; Wu, F.; Mao, R.; Ai, X.; Yang, H.; Cao, Y., *J. Mater. Chem. A* **2013,** *1*, 7181-7184.

46. Xu, Y.; Zhu, Y.; Liu, Y.; Wang, C., *Adv. Energy Mater.* **2013,** *3*, 128-133.

47. Lin, Y.-M.; Abel, P. R.; Gupta, A.; Goodenough, J. B.; Heller, A.; Mullins, C. B., *ACS Appl. Mater. Interfaces* **2013,** *5*, 8273-8277.

48. Thorne, J. S.; Dunlap, R. A.; Obrovac, M. N., *Electrochim. Acta* **2013,** *112*, 133-137.

49. Olesinski, R. W.; Abbaschian, G. J., *Bulletin of Alloy Phase Diagrams* **1984,** *5*, 265-271.

50. Temkin, R. J.; Connell, G. A. N.; Paul, W., *Solid State Commun.* **1972,** *11*, 1591-1595.

51. Tamura, K.; Fukushima, J.; Endo, H.; Minomura, S.; Shimomura, O.; Asaumi, K., *J. Phys. Soc. Jpn.* **1974,** *36*, 558-564.

52. Bodnarchuk, M. I.; Kravchyk, K. V.; Krumeich, F.; Wang, S.; Kovalenko, M. V., *ACS Nano* **2014**.

53. Fan, S.; Lim, L. Y.; Tay, Y. Y.; Pramana, S. S.; Rui, X.; Samani, M. K.; Yan, Q.; Tay, B. K.; Toney, M. F.; Hng, H. H., *J. Mater. Chem. A* **2013,** *1*, 14577-14585.

54. Cho, Y. J.; Kim, C. H.; Im, H. S.; Myung, Y.; Kim, H. S.; Back, S. H.; Lim, Y. R.; Jung, C. S.; Jang, D. M.; Park, J.*, et al.*, *Phys. Chem. Chem. Phys.* **2013,** *15*, 11691-11695.

55. Farbod, B.; Cui, K.; Kalisvaart, W. P.; Kupsta, M.; Zahiri, B.; Kohandehghan, A.; Lotfabad, E. M.; Li, Z.; Luber, E. J.; Mitlin, D., *ACS Nano* **2014**.

56. Robbie, K.; Sit, J. C.; Brett, M. J., *J. Vac. Sci. Technol., B* **1998,** *16*, 1115-1122.

57. Abelmann, L.; Lodder, C., *Thin Solid Films* **1997,** *305*, 1-21.

58. Krause, K. M.; Thommes, M.; Brett, M. J., *Microporous Mesoporous Mater.* **2011,** *143*, 166-173.

59. Hawkeye, M. M.; Brett, M. J., *J. Vac. Sci. Technol., A* **2007,** *25*, 1317-1335.

60. Lin, Y.-M.; Abel, P. R.; Flaherty, D. W.; Wu, J.; Stevenson, K. J.; Heller, A.; Mullins, C. B., *J. Phys. Chem. C* **2011,** *115*, 2585-2591.

61. Flaherty, D. W.; Hahn, N. T.; May, R. A.; Berglund, S. P.; Lin, Y.-M.; Stevenson, K. J.; Dohnalek, Z.; Kay, B. D.; Mullins, C. B., *Acc. Chem. Res.* **2012,** *45*, 434–443.

62. Maruyama, T.; Akagi, H., *J. Electrochem. Soc.* **1998,** *145*, 1303-1305.

63. Abel, P. R.; Lin, Y.-M.; de Souza, T.; Chou, C.-Y.; Gupta, A.; Goodenough, J. B.; Hwang, G. S.; Heller, A.; Mullins, C. B., *J. Phys. Chem. C* **2013,** *117*, 18885-18890.

64. Kolodzey, J.; Coppinger, M.; Kim, S.; Bhargava, N.; Gupta, J.; Chaoying, N.; Yung Kee, Y. In *The Properties of Germanium-Tin Alloys for Infrared Device Applications*, Semiconductor Device Research Symposium (ISDRS), 2011 International, 7-9 Dec. 2011; 2011; pp 1-1.

65. Hall, L. A., *Survey of Electrical Resistivity Measurements on 16 Pure Metals in the Temperature Range 0 to 273 K*. U.S. Dept. of Commerce, National Bureau of Standards: Washington, D.C., 1968; p 111 p.

66. Ewald, A. W.; Tufte, O. N., *J. Phys. Chem. Solids* **1959,** *8*, 523-525.

67. Sharma, S. K.; Jain, S. C.; Aggarwal, S. S.; Bhide, V. G., *J. Non-Cryst. Solids* **1972,** *7*, 285-294.

Chapter 8: Conclusion

Overview of Completed Work

This dissertation presented the results of several studies on potential lithium- and sodium-ion battery materials synthesized by evaporative deposition. Chapter 1 introduced the current and possible future applications of electrochemical energy storage as well as discussing the limitations and shortcomings of battery technology. Various methods for improving battery performance were also discussed.

Chapter 2 presented a study where partially oxidized silicon thin films grown by RBD were tested as a lithium-ion battery anode material. The introduction of small amounts of oxygen (>20 at%) during synthesis significantly increased the cycling stability of the films, and low temperature annealing further improved the stability. Both surface oxidation and homogeneous oxygen incorporation in the bulk of the material improved performance, but the optimal material contained both surface and bulk oxide. Even though the capacity of the partially oxidized films was lower than that of pristine silicon, it was almost 6 times higher than the capacity of graphite which is currently used as the anode material in lithium-ion batteries. While fully oxidized silicon dioxide performed poorly as an anode material, partial oxidation of silicon significantly improved its performance.

In chapter 3, silicon-germanium alloys of different compositions were studied as anode materials for lithium-ion batteries. By changing the composition of the alloy, the electrochemical properties could be tuned between the extremes presented by each pure

material. Germanium-rich compositions offered good high-rate performance (up to 20C), whereas silicon-rich alloys offered higher specific capacities. The electronic conductivity of the alloy also increased as the germanium content increased. While the silicon films in this study retained almost zero capacity when cycled at 5C, the germanium films retained ~90% their initial capacity, $Si_{0.25}Ge_{0.75}$ retained ~75%, and $Si_{0.5}Ge_{0.5}$ retained ~68%. Silicon alloying can be used to mitigate the high cost of germanium and increases the specific capacity of the material, and these benefits can outweigh the loss of high rate performance – particularly if the maximum charge/discharge rate for the cell is below 5C. This study has shown that alloy composition is a previously unexplored parameter when optimizing an anode material for a specific application.

Chapter 4 describes the electrochemical properties of sub-stoichiometric germanium selenide. The addition of small amounts of selenium to nanocolumnar germanium electrodes significantly enhances their high rate performance. Whereas pure germanium can support current densities of ~27A/g, nanocolumnar $Ge_{0.9}Se_{0.1}$ could support current densities of up to 2200 A/g. In addition to supporting high current densities, the electrodes were stable over 1000 cycles at 50 C. TEM imaging showed that phase separation during the first cycle produces a lithium selenide based fast-ionic conducting phase within the material. The effective lithium diffusion coefficient of $Ge_{0.9}Se_{0.1}$, as measured by PITT, was roughly an order of magnitude higher than that of pure germanium. The electrical conductivity of the sub-selenide was also found to be higher than that of pure germanium. The performance of this material under challenging testing conditions demonstrates a new method for improving electrode performance.

Chapter 5, like Chapter 4, deals with sub-stoichiometric germanium chalcogenides, but investigates the electrochemical properties of the germanium sulfide rather than the selenide. Single-phase, amorphous, sub-stoichiometric germanium sulfide films phase separated after one lithiation cycle resulting in poorly crystalized Li_2S nanoparticles embedded in amorphous germanium structures. This is the inverse structure of what is formed when stoichiometric germanium chalcogenides are lithiated. The result is superior high rate performance for $Ge_{0.95}S_{0.05}$, with ~93% of the low rate capacity retained when cycled at 10C compared to ~82% for pure germanium. The high performance is likely due to fast interfacial diffusion at the germanium/Li_2S nanocrystalline inclusion interfaces. Additionally, the films show good stability over 500 cycles at 20C. The fast lithium transport and stable cycling make sub-stoichiometric germanium sulfide a promising material for further study.

Chapters 6 and 7 were dedicated to anode materials for sodium-ion batteries. Chapter 6 presented experimental confirmation of the reversible electrochemical storage of sodium in germanium. Nanocolumnar germanium electrodes had an initial sodium storage capacity of 430 mAh/g. After 100 cycles at C/5, 88% of this capacity was retained. The material also exhibited high capacity retention at rates up to 27C (10 A/g), Dense germanium films exhibited significant capacity fade when cycled at the same rate. *Ab initio* molecular dynamics simulations of the Na-Ge system indicate that near-surface diffusion is significantly faster than bulk diffusion. Nano-scale dimensions, therefore, are critical for stable, reversible, and high-rate sodiation of germanium.

Chapter 7 returned to the idea of using alloys to improve electrode performance. Tin is a promising sodium-ion battery material, but suffers from poor cycling stability. The study showed that alloying tin with germanium improves the cycling stability. The addition of germanium to tin raises the liquidus of the melt, thus reducing the surface mobility of atoms at room temperature. This improved the cycling stability of the electrodes by preventing agglomeration of the active material. This study suggested that tin must be effectively immobilized in order to engineer stable electrodes.

ONGOING AND FUTURE WORK

Vacuum deposition is a powerful tool to synthesize new and novel materials, but it is also a time consuming and costly technique. With current laboratory equipment, it is completely impractical to deposit more than microgram quantities of material. This is enough material for preliminary electrochemical investigations, but much less than the milligram quantities used in traditional slurry cast electrodes. Sub-stoichiometric germanium sulfide and germanium selenide have shown promise as lithium-ion battery anode materials and tin-germanium alloys are promising for sodium-ion batteries. These materials, however, are not thermodynamically stable which makes synthesis by many traditional methods impossible. Ongoing and future work includes developing methods to synthesize these materials in the quantities required for the next stage of testing in traditional slurry cast electrodes.

Vapor deposition is only one method by which metastable, non-equilibrium materials can be created. An energy diagram for the process of creating metastable phases

is shown in Figure 8.1. In addition to vapor deposition, melt quenching and mechanical milling are identified as methods for the formation of such materials.

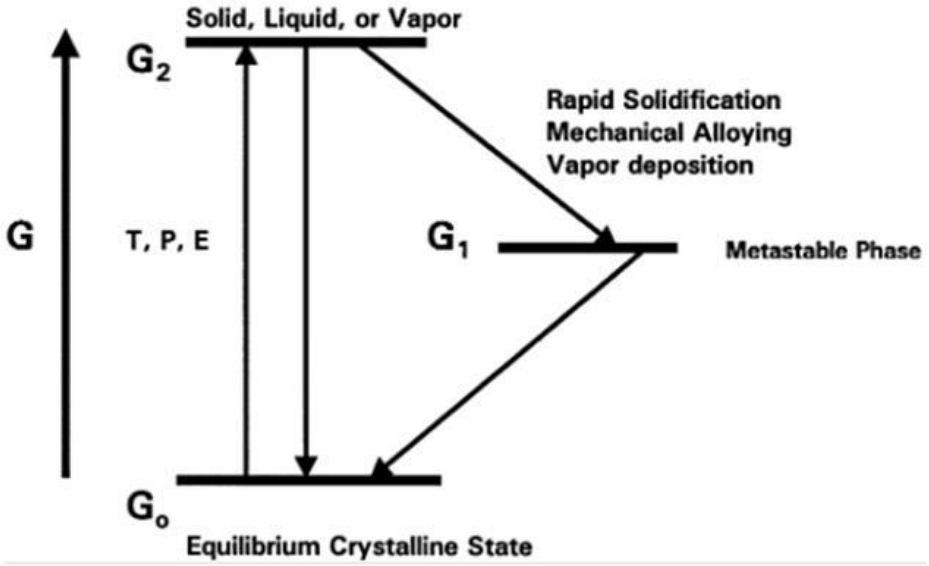

Figure 8.1. Schematic energy diagram for metastable materials and methods for their formation.[1]

Melt quenching has been used extensively in the study of amorphous materials and glasses. The technique employs rapid cooling in order to avoid crystallization or phase separation. The cooling rate must be faster than the kinetics of crystallization or phase segregation, and the cooled product must lack the thermal energy to overcome the energetic barrier to transform into the thermodynamically stable form. Liquid germanium is miscible with either selenium or sulfur at high temperatures,[2-3] so sufficiently fast cooling of the melt may yield a metastable, homogenous sub-stoichiometric sulfide or

selenide of similar atomic structure to what is obtained from evaporative deposition. Both sulfur and selenium are volatile at the temperatures necessary for melt-processing germanium, so the processing must be carried out in a sealed ampule. This precludes many high cooling rate techniques such as splat quenching, and limits on how quickly the melt can be cooled. Germanium chalcogenide based glasses synthesized by melt quenching have been well studied.[4-8] In the case of these materials, quenching an ampule in a water bath provides sufficient cooling rates to make vitreous samples, and it is hoped that homogeneous, non-stoichiometric samples could be made by the same techniques.

The germanium-selenium phase diagram is shown in Figure 8.1.[3] A monotectic at 1177K with approximately 12 at% selenium is near the optimal composition for the sub-stoichiometric germanium selenide determined in chapter 4, and quenching from this monotectic, represented by the arrow, and may result in a homogeneous material of the desired composition.

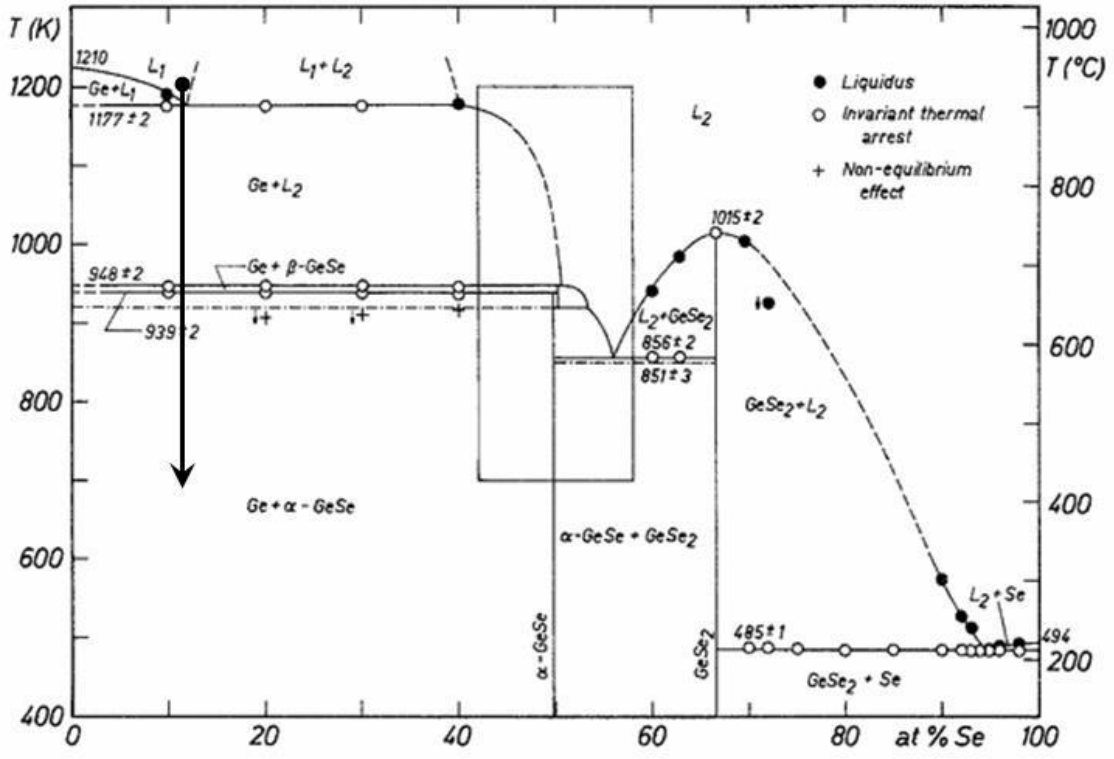

Figure 8.2 The germanium-selenium phase diagram with the proposed path to form bulk samples of sub stoichiometric germanium selenide.3

Another technique which may be suitable for preparing bulk samples of sub-stoichiometric sulfides and selenides is high-energy mechanical milling. In mechanical milling, the kinetic energy of collisions between grinding media is used to fracture particles. The process also imparts defects in the material leading to partial or complete amorphization and provides energy to promote chemical reactions between different species present in the grinding bowl.[1] A schematic of the process is shown in Figure 8.3.[9]

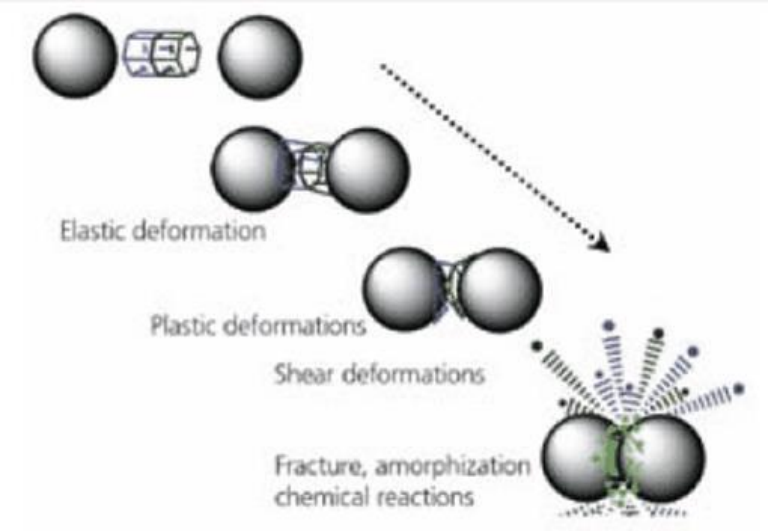

Figure 8.3. A schematic of mechanical milling showing the physical and chemical processes which occur during collisions between grinding media.[9]

Mechanical milling has previously been employed in the synthesis of composites and alloys for battery applications.[10-13] It is likely that successful synthesis of sub-stoichiometric materials will involve both melt processing and mechanical milling to obtain the desired composition and morphology.

The studies on thin films in this dissertation have identified new materials with enhanced electrochemical properties. The electrochemical performance of these materials warrants further investigation, however, it must still be tested whether the desirable characteristics can be maintained when material synthesis and electrode processing techniques compatible with large-scale manufacturing are employed. This question is the focus of ongoing and future work.

REFERENCES

1. Suryanarayana, C., *Prog. Mater Sci.* **2001,** *46*, 1-184.

2. Predel, B., Ge-S (Germanium-Sulfur). In *Ga-Gd – Hf-Zr*, Madelung, O., Ed. Springer Berlin Heidelberg: 1996; Vol. 5f, pp 1-2.

3. Ipser, H.; Gambino, M.; Schuster, W., *Monatsh Chem* **1982,** *113*, 389-398.

4. Zhilinskaya, E. A.; Valeev, N. K.; Oblasov, A. K., *J. Non-Cryst. Solids* **1992,** *146*, 285-293.

5. Marchese, D.; De Sario, M.; Jha, A.; Kar, A. K.; Smith, E. C., *J. Opt. Soc. Am. B* **1998,** *15*, 2361-2370.

6. Souquet, J., *Solid State Ionics* **1981,** *3-4*, 317-321.

7. Kikkawa, S.; Miyai, T.; Koizumi, M., *Solid State Ionics* **1988,** *28–30, Part 1*, 743-746.

8. Michel-Lledos, V.; Pradel, A.; Ribes, M., *Eur. J. Solid State Inorg. Chem.* **1992,** *29*, 301-310.

9. Balema, V. P., **2007,** *Materials Matters*, 16.

10. Wu, J.; Zhu, Z.; Zhang, H.; Fu, H.; Li, H.; Wang, A.; Zhang, H.; Hu, Z., *J. Alloys Compd.* **2014,** *596*, 86-91.

11. Yu, H. T.; Loka, C.; Lee, K.-S.; Cho, J. S.; Lee, S. H., *Mater. Sci. Eng., B* **2013,** *178*, 1422-1428.

12. Allcorn, E.; Manthiram, A., *ACS Appl. Mater. Interfaces* **2014**.

13. Yu, B.-C.; Hwa, Y.; Kim, J.-H.; Sohn, H.-J., *J. Power Sources* **2014,** *260*, 174-179.

Appendix A: Supplemental Information for Improving the Stability of Nanostructured Silicon Thin Film Lithium-Ion Battery Anodes Through Their Controlled Oxidation

QCM measurements were used to determine total film mass, and thusly the specific capacity of the deposited materials. Cross sectional SEM measurements were used in order to independently verify the accuracy of the QCM measurements. Silicon GLAD films were deposited on thermally oxidized silicon wafers. The 120nm thermal oxide layer provided increased contrast between the silicon substrate and the deposited film. Three silicon GLAD films with 50 $\mu g/cm^2$ mass density, grown on silicon wafer fragments, are shown in Figure A.1. They show very consistent thicknesses. The standard deviation in thickness is ~5nm or ~1.1% of the total. This gives confidence that the QCM measurements give tight control over total amount of material deposited. Using the bulk density of silicon and the measured thickness of the films, the porosity is ~50%, which is in good agreement with expected value based on studies of other materials deposited by RBD.

XPS is a surface sensitive technique, and therefore is sensitive to species adsorbed on the surface of samples. It was observed that carbon collects on the surface of silicon samples after sputtering. Care was taken during the measurements to minimize the signal from surface adsorbed species. With the use of a liquid nitrogen cryo-shroud and a titanium sublimation pump, the pressure in the XPS analysis chamber was reduced to $1x10^{-9}$ Torr. A measurement taken immediately following argon ion sputter cleaning of the surface shows ~2 at% carbon. It had increased to ~9 at% after 45 minutes and 16 at%

after two hours. Figure A.2 shows the time dependent XPS signal. The measured oxygen content does not increase significantly indicating that the surface contamination is due to hydrocarbon adsorption rather than small molecules such as CO or CO_2.

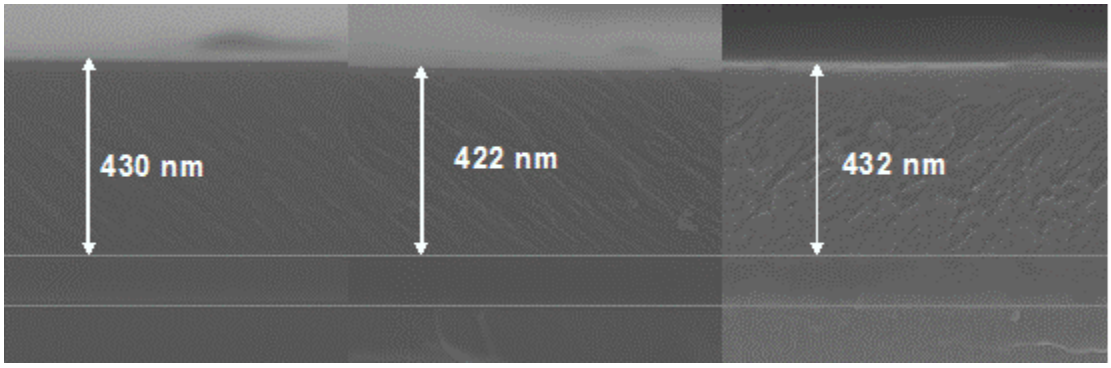

Figure A.1. Cross sectional SEM micrographs of three silicon GLAD films grown on silicon wafer fragments show very consistent thicknesses. The standard deviation in thickness is ~5nm or ~1.1% of the total. This gives confidence in the consistency of this deposition technique. A 120 nm thick thermal oxide layer was grown on the wafer fragments prior to depositing the film to provide contrast in the image. The nominal mass of each film is 50 $\mu g/cm^2$ as measured by QCM. Using the bulk density of silicon and the measured thickness of the films, the porosity is ~50%, which is in good agreement with expected value based on studies of other materials deposited by RBD.

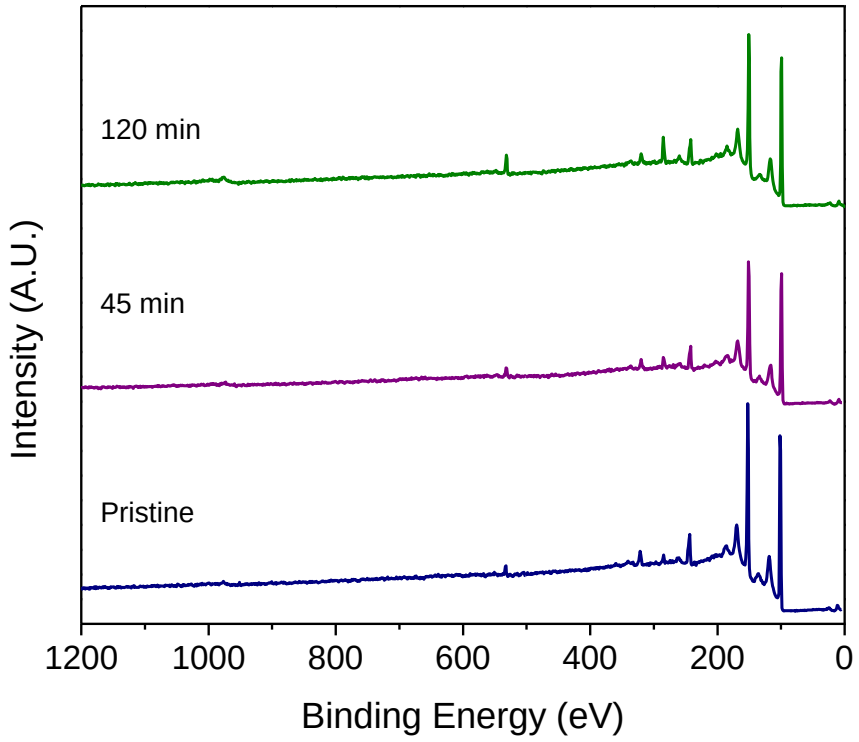

Figure A.2. Time dependent XPS spectra of a pristine silicon film after cleaning by argon ion sputtering. Carbon collects on the surface after sputtering with a measured concentration of 2 at% immediately following cleaning, 9 at% after 45 minutes, and 16 at% after 2 hours. The measured oxygen content does not increase significantly indicating that the surface contamination is due to hydrocarbon adsorption rather than small molecules such as CO or CO_2.

The concentration of oxygen contained in the bulk of the film can be estimated using the electrochemical reaction with lithium in the first cycle if we assume a reaction mechanism. A differential capacity plot showing the first lithium insertion for a pristine film as well as films deposited in $2x10^{-6}$ Torr and $4x10^{-6}$ Torr H_2O background is shown in Figure A.3. The area of the feature centered at ~400mV is attributed to the reaction of lithium with oxygen incorporated homogeneously into the film. We believe that it is due

to the reaction between lithium and oxygen rather than SEI formation because the feature is absent in the pristine film and increases in magnitude with increasing background oxygen pressure during deposition. We assume that the reaction proceeds according to the following stoichiometry: $O + 2Li^+ + e^- \rightarrow Li_2O$. Integration of this feature indicates that the films grown in $2x10^{-6}$ and $4x10^{-6}$ Torr H_2O contain 14 at% and 20 at% oxygen respectively. This is in good agreement with the oxygen content measured by XPS and QCM. We assume that the pristine film contains no oxygen, and use it as a baseline to eliminate the charge consumed in SEI formation and Li-Si alloy formation in the same voltage range.

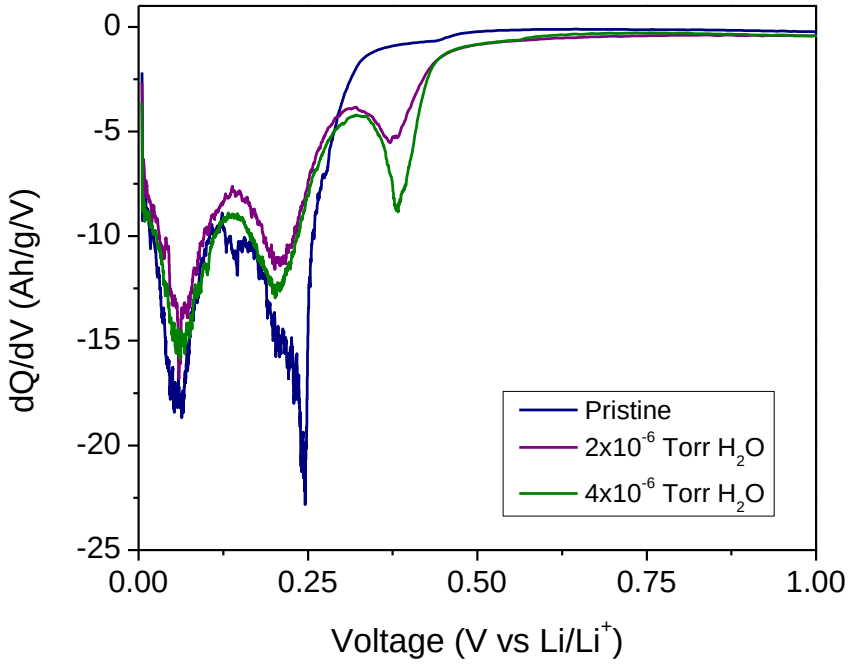

Figure A.3. Differential capacity plot showing the first lithium insertion for a pristine film as well as films deposited in $2x10^{-6}$ Torr and $4x10^{-6}$ Torr H_2O background. The area of the feature centered at ~400mV is attributed to the reaction of lithium with oxygen incorporated homogeneously into the film. Integration of this feature indicates that the films grown in $2x10^{-6}$ and $4x10^{-6}$ Torr H_2O contain 14 at% and 20 at% oxygen respectively.

The oxygen content of air-annealed films was estimated using the method described above. The un-annealed pristine film was again used as the baseline. A pristine film as well as films deposited in $2x10^{-6}$ Torr and $4x10^{-6}$ Torr H_2O background, and then annealed in air for two hours were found to contain 22 at%, 38 at% and 39 at% respectively. The differential capacity plot detailing the first lithium insertion for these films is shown in Figure A.4. Native oxide formation is self-limiting and diffusion controlled. Taking the 22 at% oxygen content of the air annealed pristine film as contribution from the native oxide layer, 14% of the silicon atoms in the film are

consumed in the formation of the native oxide layer. The oxygen content does not increase from the film deposited in $2x10^{-6}$ Torr H_2O to the film deposited in $4x10^{-6}$ Torr H_2O. This may be due to incomplete lithiation of the partially oxidized films. The capacity of the material decreases and the positions of the lithium insertion features shift to lower potentials with increasing bulk oxygen content indicating that the resistivity of the material increases with oxygen content.

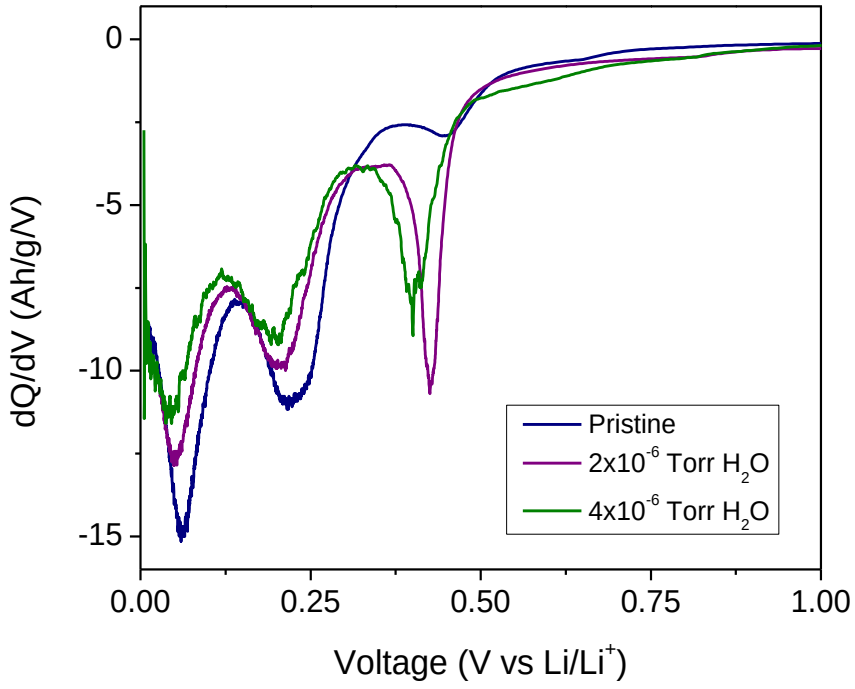

Figure A.4. Differential capacity plot showing the first lithium insertion for a pristine film as well as films deposited in $2x10^{-6}$ Torr and $4x10^{-6}$ Torr H_2O background, and then annealed in air for two hours. The feature centered at ~400 mV is present in the film deposited with no background gas indicating that native oxide reacts with lithium. This feature increases in magnitude for the film deposited in $2x10^{-6}$ Torr H_2O, but does not increase further for the film deposited in $4x10^{-6}$ Torr H_2O. This feature has a broad tail at higher voltages. The magnitude of this tail increases slightly with increasing bulk oxygen content.

Appendix B: Supplemental Information for Nanostructured $Si_{(1-x)}Ge_x$ for Tunable Thin Film Anodes

Surface oxides play an important but not well studied role in the electrochemical alloying reaction between silicon or germanium and lithium. Figures B.1-B.5 show the cycling behavior and first cycle differential capacity plot for Ge, $Si_{0.25}Ge_{0.75}$, $Si_{0.5}Ge_{0.5}$, $Si_{0.75}Ge_{0.25}$ and Si films that were exposed to atmosphere for 72 hours in order to grow a terminal native oxide layer as well as films that were assembled into coin cells with minimum exposure to atmosphere. The minimally air exposed films were exposed to atmosphere for less than a minute during transfer from the deposition chamber to the glovebox. Data for the fully surface oxidized films is presented in the main text of the paper.

Figure B.1a shows that germanium films with a terminal native oxide layer have a lower reversible capacity, but higher capacity retention at high rates. At this point, the experimental data are not sufficient to determine the cause of this phenomenon, however, the two effects may be related. A lower reversible capacity will lead to a smaller volumetric expansion which will lead to less structural damage and better cyclability. There will also be differences in the surface energies between the clean semiconductor and oxide terminated films. This will lead to differences in the quality and thickness of SEI which forms on each surface. Additionally, localized negative charge on the oxygen atoms could facilitate the desolvation of the lithium ions. Figure B.1b shows the first

cycle differential capacity plot for surface oxidized and minimally oxidized germanium. The air exposed film has a peak at 1.23V that is absent in the minimally oxidized film. We attribute this peak to the reduction of germanium oxide. The inset is a magnification of this feature.

In Figure B.2, B.3, B.4, and B.5, data for $Si_{0.25}Ge_{0.75}$, $Si_{0.5}Ge_{0.5}$, $Si_{0.75}Ge_{0.25}$ and Si films are presented. $Si_{0.25}Ge_{0.75}$, $Si_{0.5}Ge_{0.5}$, $Si_{0.75}Ge_{0.25}$ and pure silicon have analogous oxide reduction peaks at 1.15 V, 0.960 V, 0.630 V, and 0.420 V respectively. The magnitude of the peak becomes larger as the silicon content of the film increases. This indicates that the terminal native oxide layer thickness increases with silicon content. Additionally, the peak is present in the silicon and $Si_{0.75}Ge_{0.25}$ minimally air exposed films. This indicates that the kinetics of oxide layer formation increase with increasing silicon content. The capacity retention at high rates is again better for the more oxidized films, with the exception of the pure silicon film. For silicon, we argue that the oxide layer becomes thick enough to hinder lithium transport, thus becoming detrimental at high rates.

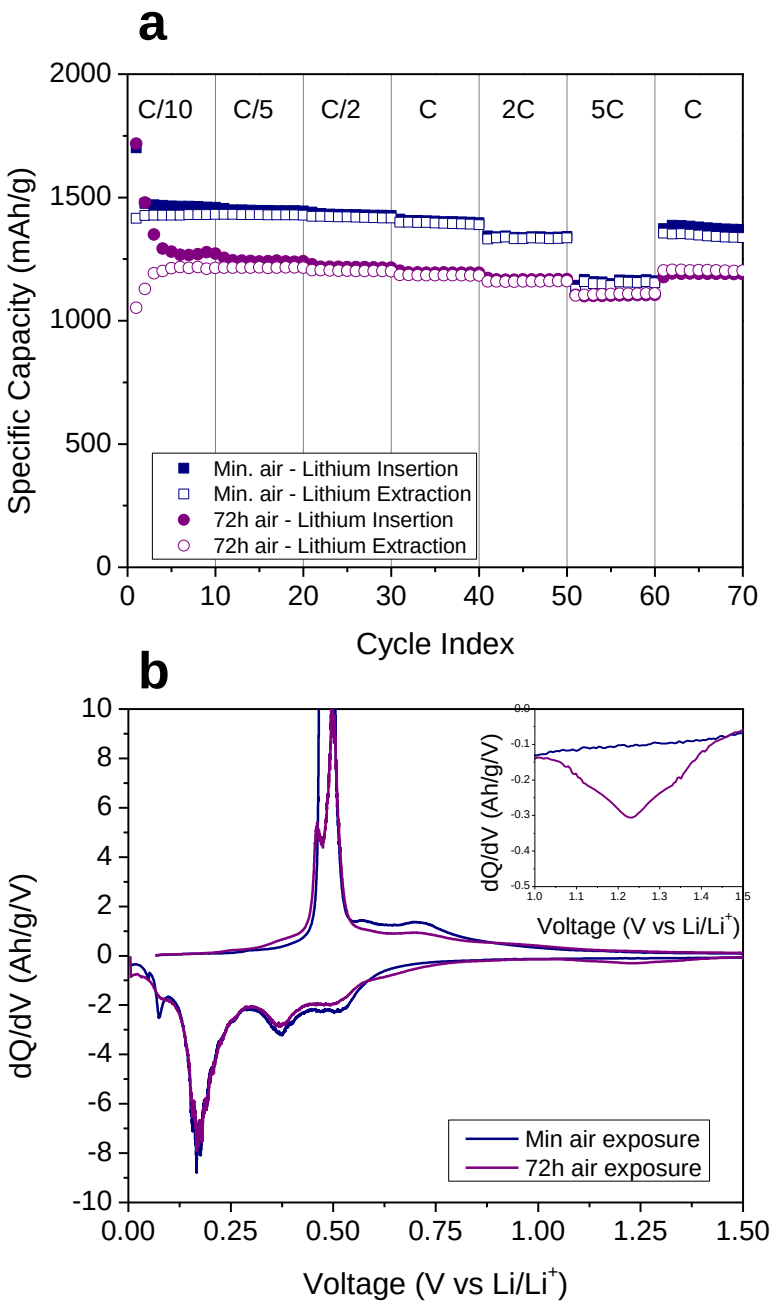

Figure B.1. a) Cycling data and b) first cycle differential capacity plots for germanium films with minimal air exposure and 72h air exposure.

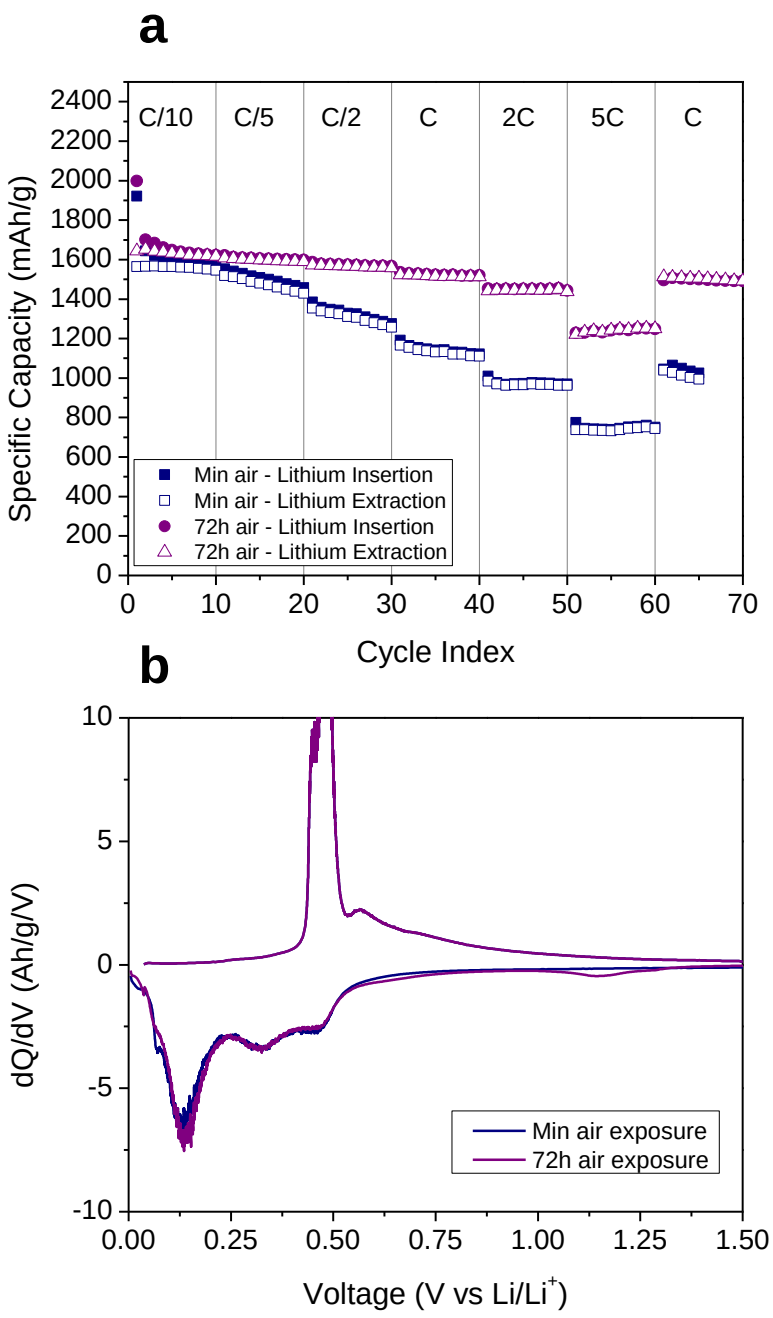

Figure B.2. a) Cycling data and b) first cycle differential capacity plots for $Si_{0.25}Ge_{0.75}$ films with minimal air exposure and 72h air exposure.

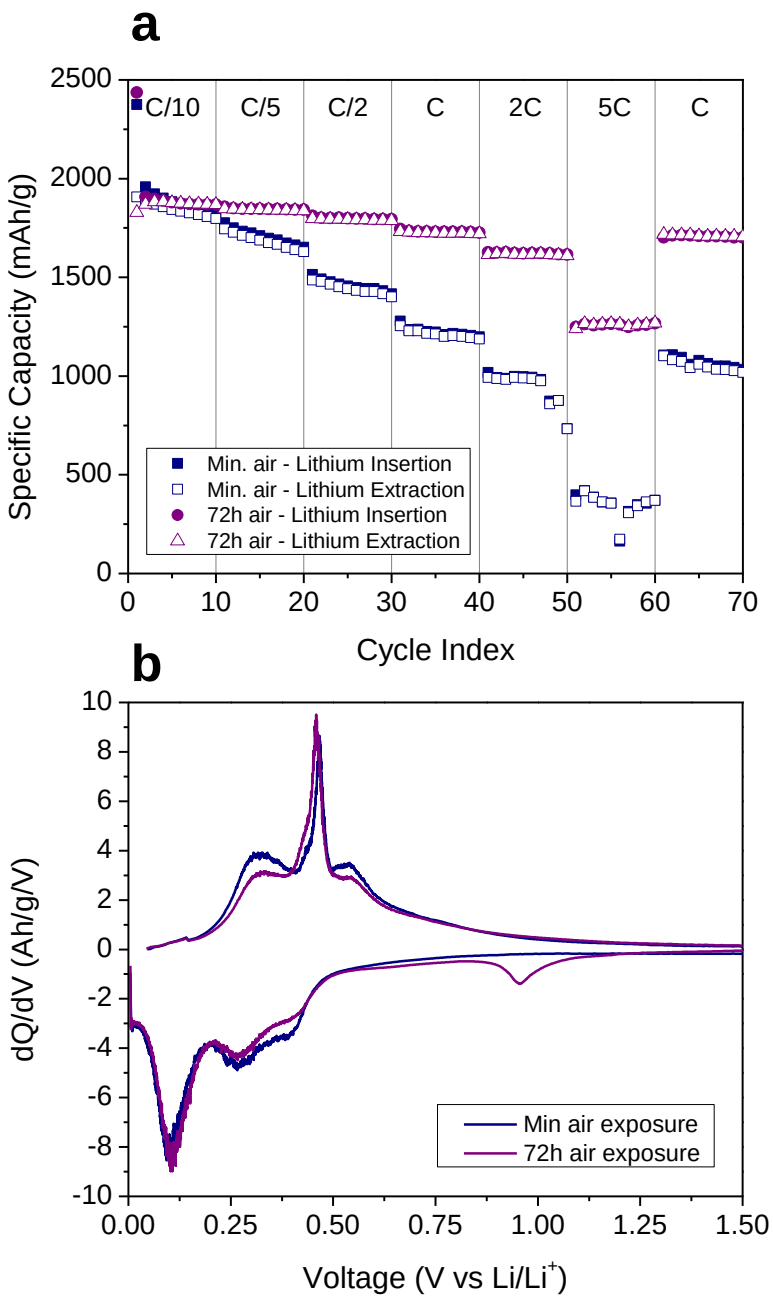

Figure B.3. a) Cycling data and b) first cycle differential capacity plots for $Si_{0.5}Ge_{0.5}$ films with minimal air exposure and 72h air exposure

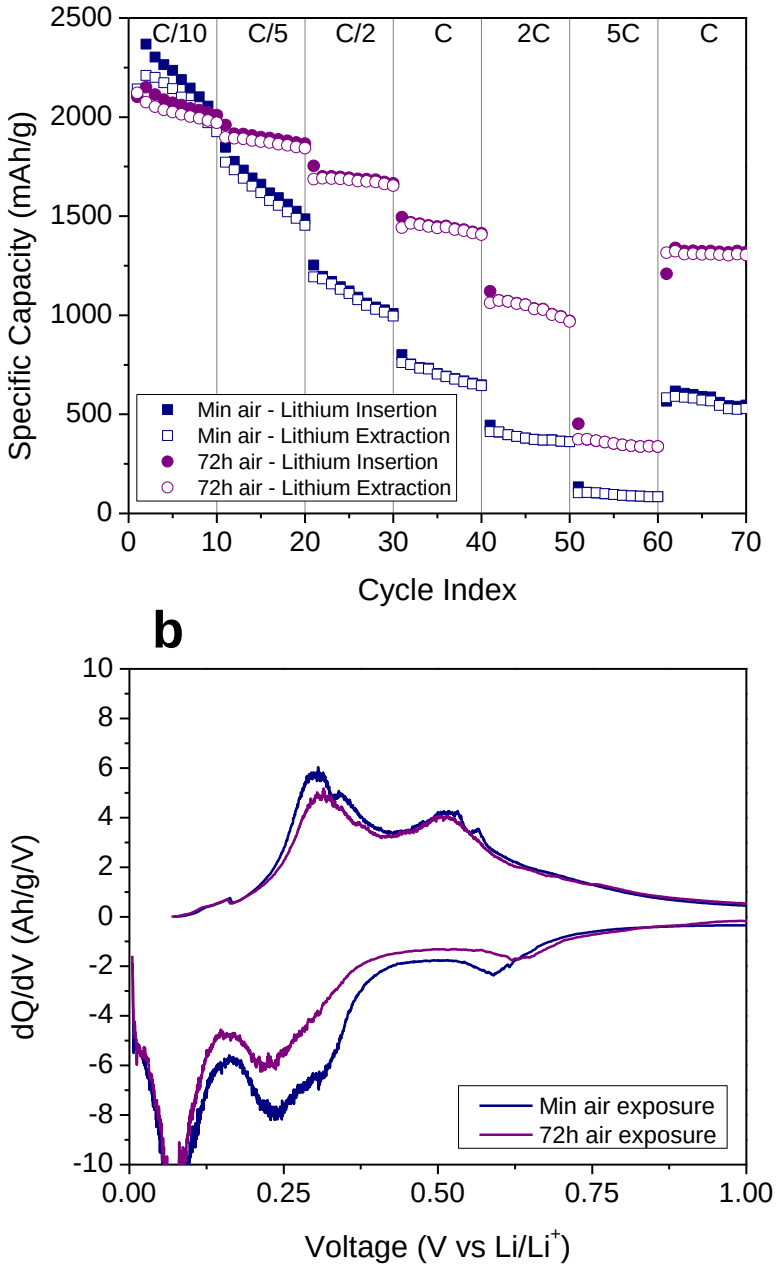

Figure B.4. a) Cycling data and b) first cycle differential capacity plots for $Si_{0.75}Ge_{0.25}$ films with minimal air exposure and 72h air exposure

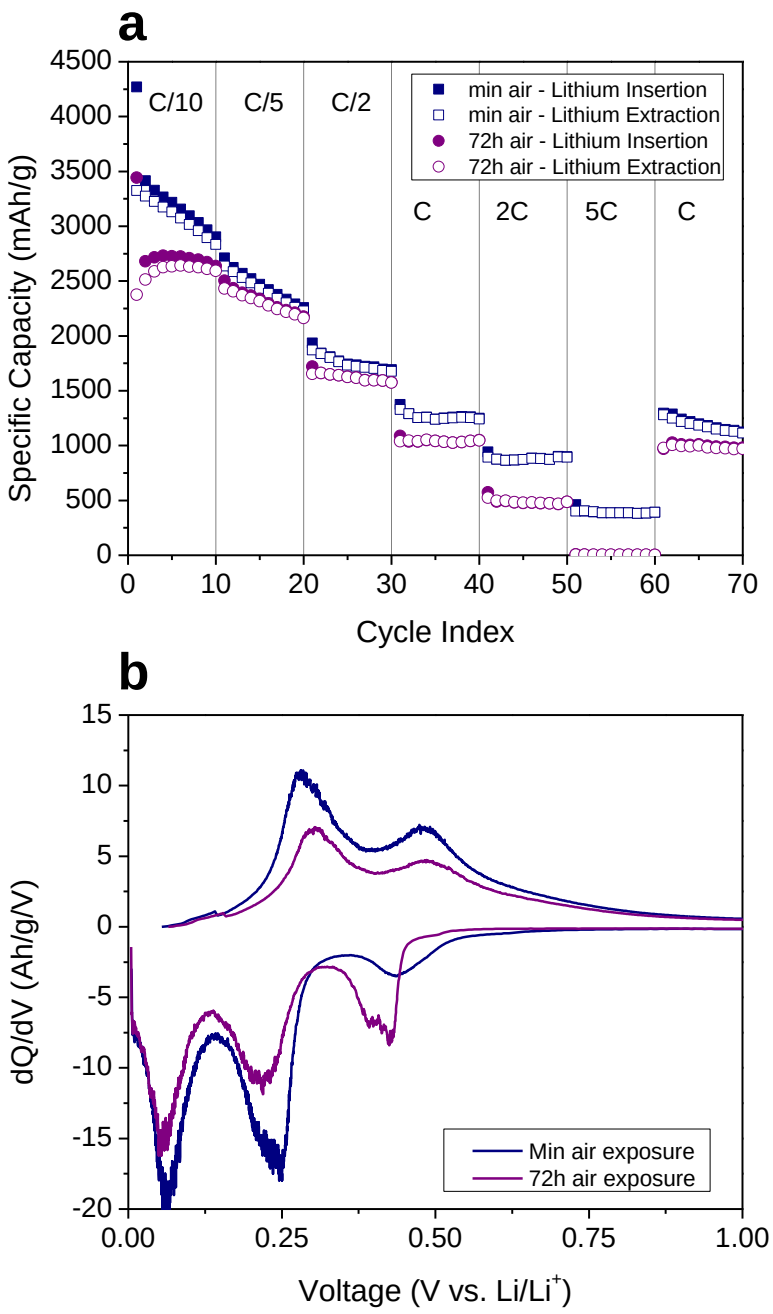

Figure B.5. a) Cycling data and b) first cycle differential capacity plots for silicon films with minimal air exposure and 72h air exposure

Appendix C: Supplemental Information for Sub-Stoichiometric Germanium Selenide for Lithium-Ion Battery Anodes Capable of Charging in Seconds

Figure C.1 shows chemical analysis of the synthesized $GeSe_2$. EDX analysis of the amorphous and crystalline reaction products indicated that both contained the stoichiometric ratios of germanium and selenium. The x-ray diffractions pattern for the crystalline phase, shown in Figure C.1b, is consistent with the reference pattern for the $GeSe_2$.

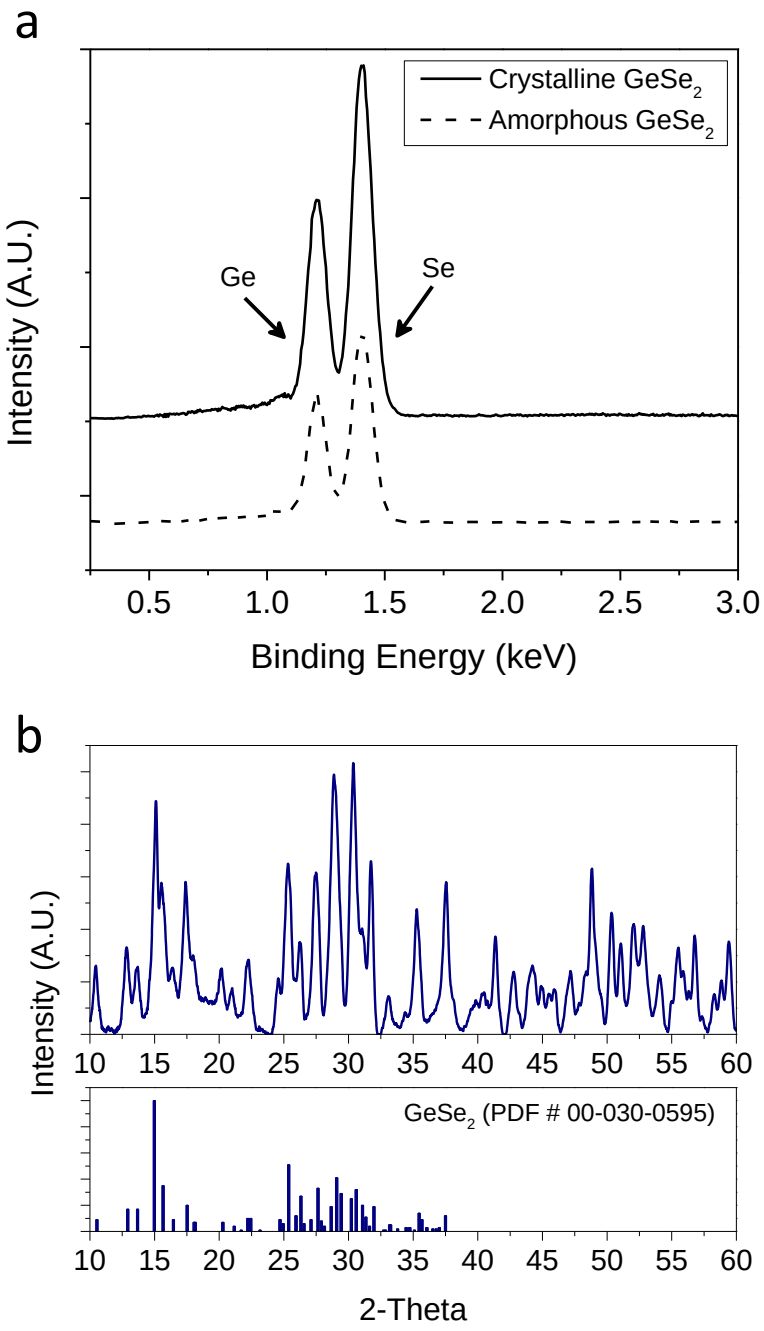

Figure C.1. Chemical characterization of sealed tube synthesized GeSe2. b) EDX of orange crystalline and gray amorphous $GeSe_2$. Integration of the germanium and selenium peaks gives a Ge:Se ratio of 1:2 in both cases. b) XRD of the orange crystalline $GeSe_2$ phase.

Figure C.2 shows SEM images of nanocolumnar Ge, $Ge_{0.9}Se_{0.1}$, and $Ge_{0.8}Se_{0.2}$. There are slight morphological differences across the compositions. Pure germanium has the smoothest nanocolumns and the roughness of the columns increases with increasing selenium content. The diameters of the nanocolumns of different composition are, however, very similar.

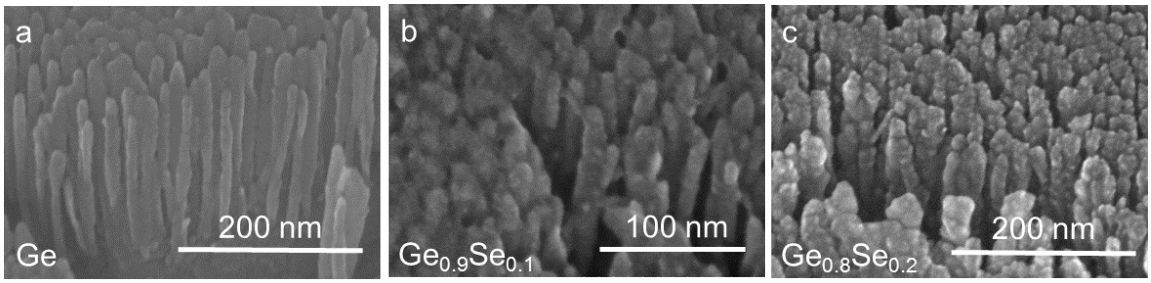

Figure C.2. Characterization of germanium sub-selenide films of various selenium content.SEM images of a) Ge, b) $Ge_{0.9}Se_{0.1}$, and c) $Ge_{0.8}Se_{0.2}$ deposited on at an incident angle of 70^{o}

High resolution TEM images of individual $Ge_{0.9}Se_{0.1}$ nanocolumns are shown in Figure C.3. The un-cycled nanocolumn appears amorphous and homogenous. After one cycle, domains of a second phase appear to have formed in the nanocolumn. The size of the domains is approximately 2 nm. An SEI layer is also visible around the cycled nanocolumn. It is conformal and roughly 5 nm in thickness.

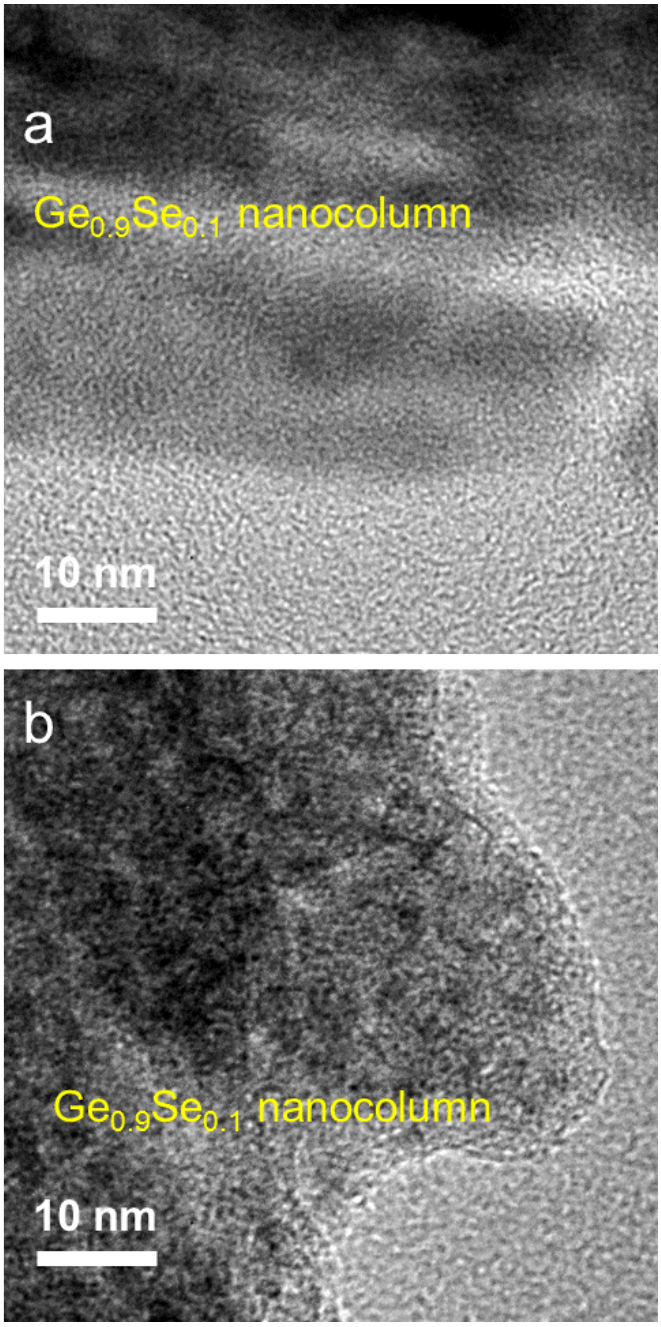

Figure C.3. TEM images of $Ge_{0.9}Se_{0.1}$ nanocolumns a) as deposited and b) after one lithium insertion/extraction cycle.

Diffusion coefficients for lithium in dense Ge and $Ge_{0.9}Se_{0.1}$ films as estimated from PITT measurements are shown in Figure C.4. The diffusion coefficients are very similar over the entire compositional range. Nanocolumnar $Ge_{0.9}Se_{0.1}$ films showed enhanced diffusion because of the presence of a fast ion-conducting phase. This phase should also be present in the dense films, however enhancement in diffusivity will be much smaller in the dense films because the fast ion-conducting domains do not form a percolating network, and the size of the domains is much smaller than the film thickness.

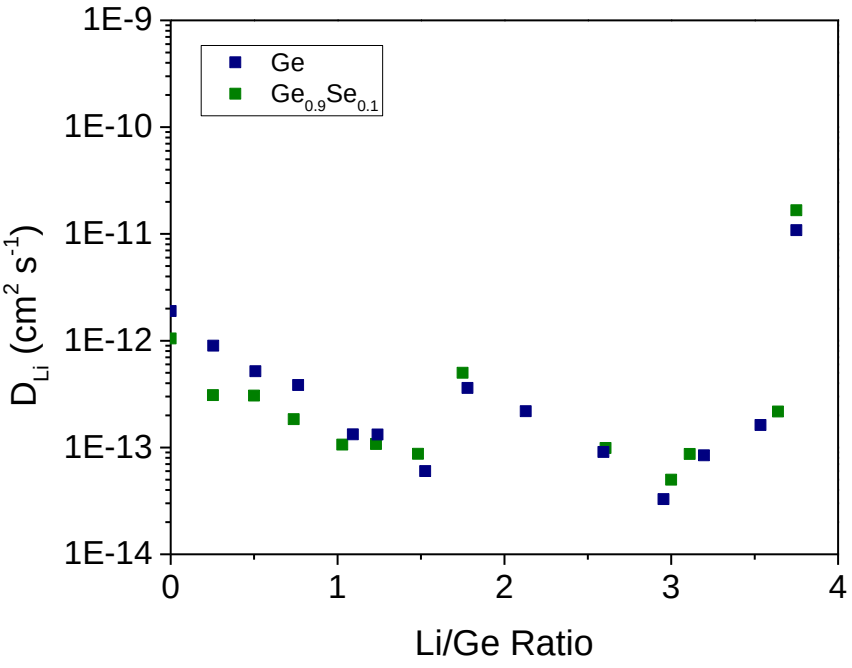

Figure C.4. Diffusion coefficients of dense Ge and Ge0.9Se0.1 electrodes as measured by PITT.

Appendix D: Supporting Information for Sub-Stoichiometric Germanium Sulfide as a High-Rate Lithium Storage Material

ImageJ was used to determine the column diameter and size distribution from SEM images of films deposited at 70°. The two images used for this analysis are shown in Figure S1. The columns identified by ImageJ are numbered in each image, and the diameter of each numbered column is given in Table D.1. Both images indicate that the mean column diameter is just over 10 nm with a standard deviation of 2.46 nm for Figure D.1a, and 0.86 nm for Figure D.1b.

XRD was used to characterize the crystallinity of as-deposited and cycled $Ge_{0.95}S_{0.05}$ films. A blank stainless steel substrate exhibited three broad peaks between 43° and 51°, and these peaks persisted through the deposited films. Crystalline germanium would give peaks at 27.4°, and 45.5°, and Li_2S would give peaks at 26.9°, 31.2°, and 44.8°, but no features are present for the as deposited or cycled films. The XRD patterns are shown in Figure D.2.

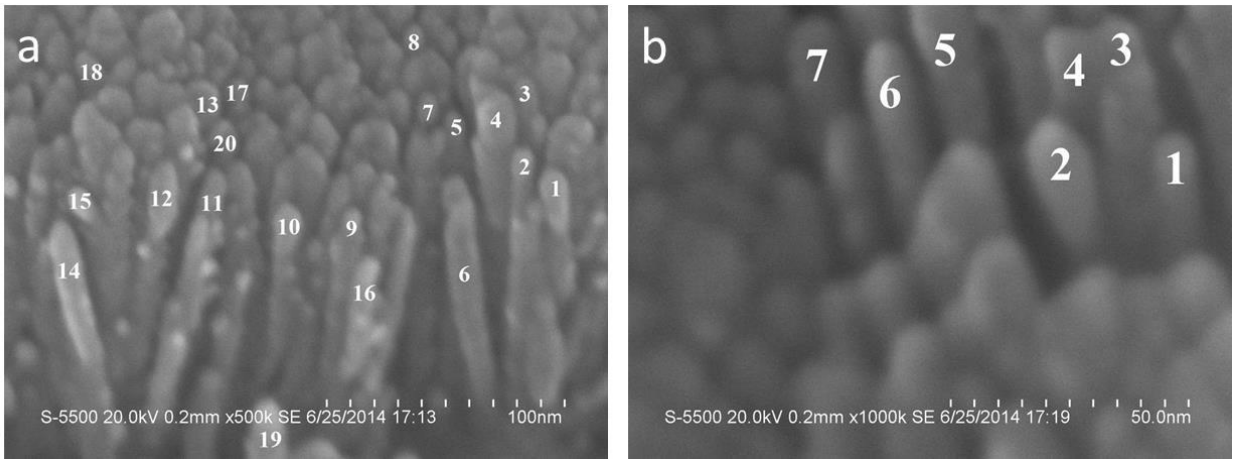

Figure D.1. Analysis of two SEM images of $Ge_{0.95}S_{0.05}$ films deposited at 70° shows that the average column diameter is ~10nm. The numbered columns were identified and analyzed by ImageJ.[1] 20 columns are identified in a) while 7 are identified in b).

Table D.1. Column diameters and statistical analysis of size distribution from two images analyzed by ImageJ.[1]

Measurements from Figure S1a

Column number	Diameter (nm)
1	9.832
2	7.93
3	8.719
4	15.854
5	8.491
6	12.488
7	9.018
8	8.52
9	8.296
10	9.079
11	9.037
12	11.209
13	14.509
14	12.032
15	8.626
16	9.693
17	10.126
18	10.637
19	15.062
20	13.526
Average	10.63
Std. Dev.	2.46

Measurements from Figure S1b

Column number	Diameter (nm)
1	8.269
2	10.685
3	9.756
4	10.43
5	10.779
6	10.175
7	10.331
Average	10.06
Std. Dev.	0.86

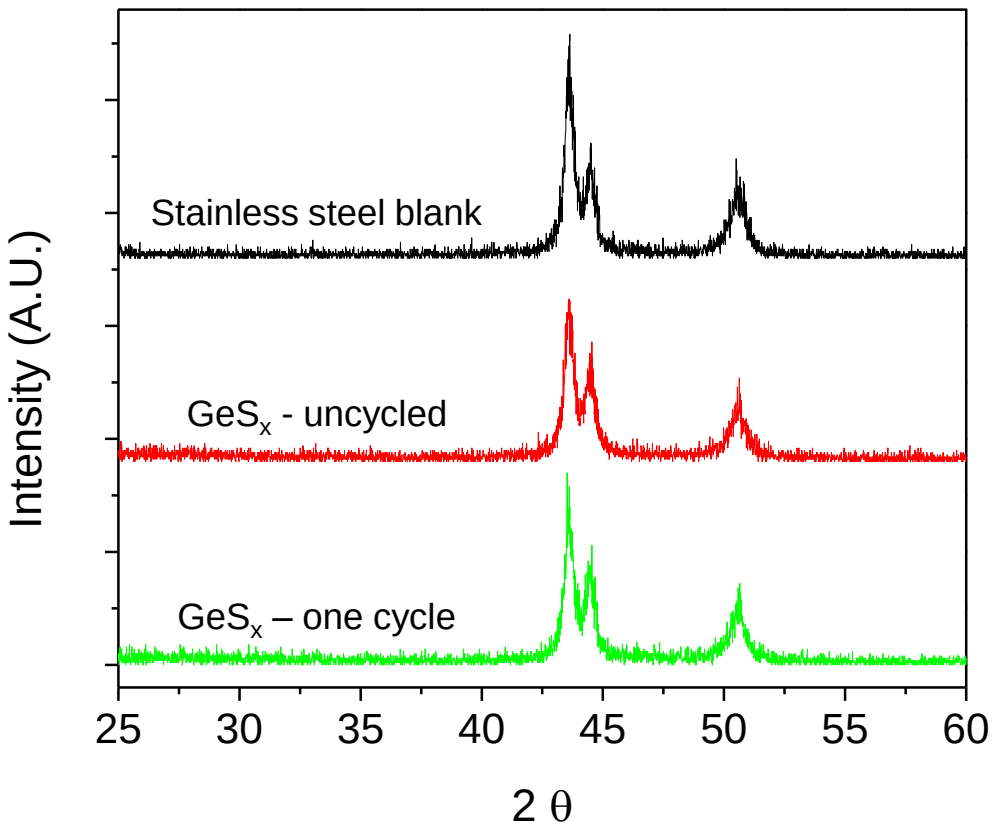

Figure D.2. XRD patterns for a blank stainless steel substrate, an uncycled $Ge_{0.95}S_{0.05}$ film, and a $Ge_{0.95}S_{0.05}$ film after one cycle.

REFERENCES

1. Rasband, W. S. *ImageJ*, U. S. National Institutes of Health: Bethesda, Maryland, USA, http://imagej.nih.gov/ij/, 1997-2014.

Appendix E: Supplemental Information for Nanocolumnar Germanium Thin Films as a High-Rate Sodium-Ion Battery Anode Material

Figure E.1 shows cross sections of three individual germanium films deposited on silicon wafers. The target mass of each film was 50 ▫g/cm2. If the density of the films is assumed to be that of bulk germanium, this mass translates to a thickness of 93 nm. Using the quartz crystal microbalance to calibrate the deposition rate provides an accurate and repeatable method for controlling the mass of germanium deposited on the substrate, and it gives us confidence that the specific capacities reported in this study are not overestimated due to errors in film mass.

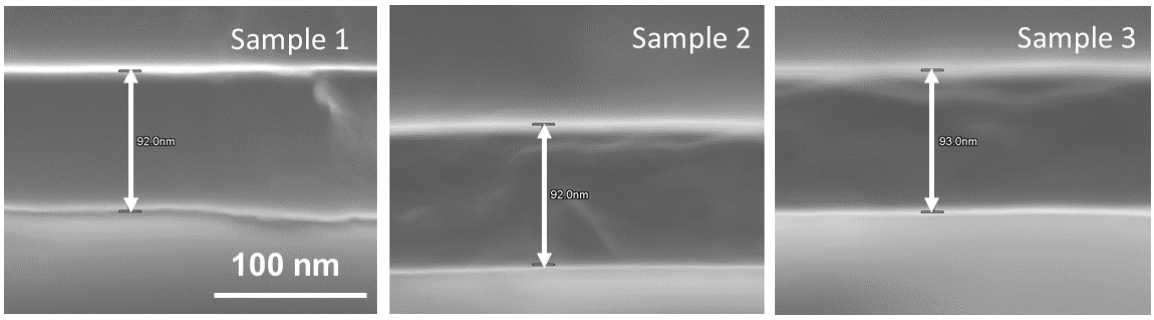

Figure E.1. Cross sectional SEM images of dense germanium films deposited on silicon wafers demonstrate the accuracy and precision of the deposition technique. The target thickness for the three samples was 50 μg/cm^2, or 93 nm thick assuming the film density is identical to that of bulk germanium.

The dependence of film morphology on deposition angle was confirmed by SEM imaging of films deposited on stainless steel substrates. While the films deposited at 70^o exhibited nanocolumnar morphology, films deposited at 0^o were observed to be dense.

Figure E.2a shows an SEM image of a bare stainless steel substrate and Figure E.2b shows an SEM Image of the dense germanium film. There was no observable nanostructuring in the film, and any roughness was the result of the film conformally coating the rough stainless steel substrate.

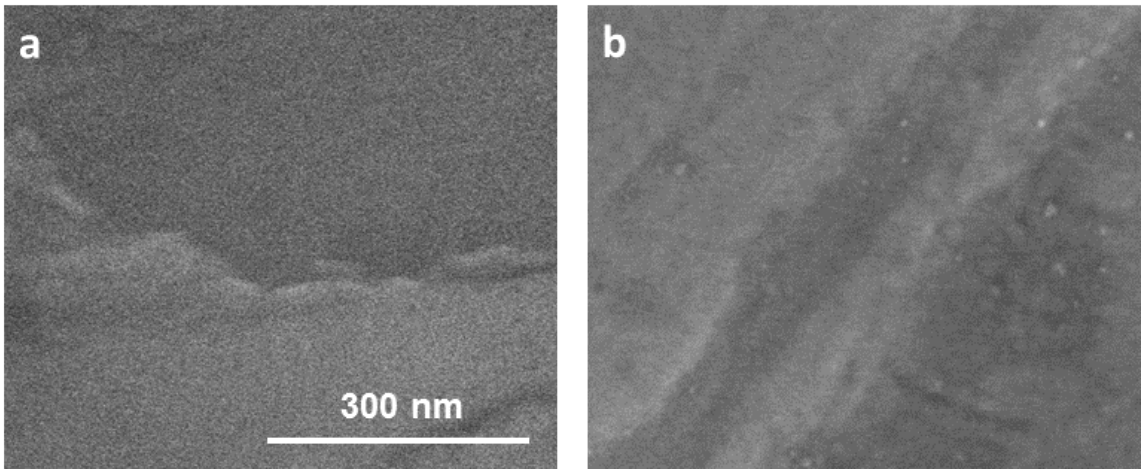

Figure E.2. SEM image of a) stainless steel substrate and b) dense germanium film deposited on the substrate at 0° from the surface normal. The scale bar applies to both images.

Figure E.3 shows SEM and EDX mapping of dense germanium electrodes after one cycle and five cycles. After a single sodiation cycle, the electrode exhibits significant cracking as seen in Figure E.3a. The germanium EDX map shown in Figure E.3b reveals that the cracks observed in the SEM image propagate through the entire thickness of the electrode and expose the substrate beneath. The EDX map for sodium is shown in Figure E.3c. An SEM image as well as EDX maps for germanium and sodium for an electrode after five cycles is shown in Figure E.3d-f. The electrode exhibits a greater amount of

cracking. Patches of the substrate are exposed due to delamination of the active material. From these images, we can conclude that the failure mechanism for dense germanium films is pulverization and loss of active material.

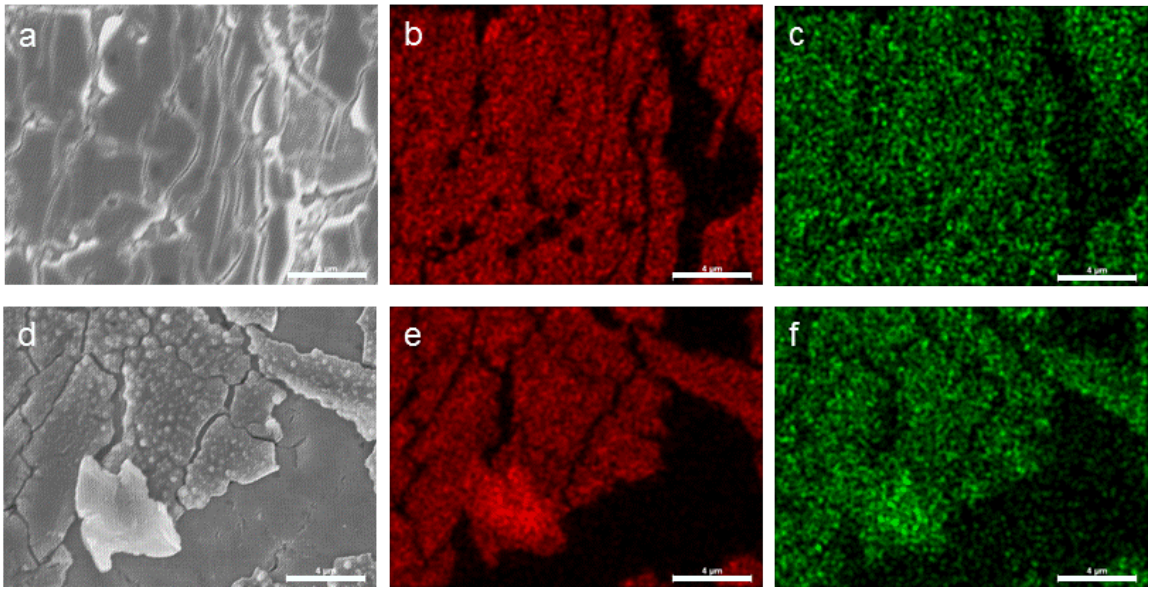

Figure E.3. SEM imaging and EDX mapping of cycled germanium electrodes. a) SEM image of a dense germanium electrode after a single cycle. The corresponding EDX map for germanium is shown in b) and for sodium is shown in c). The cracks observed in the SEM image are mirrored in the elemental maps. An SEM image and EDX maps for germanium and sodium for and electrode after five cycles are shown in d), e), and f) respectively. Quantitative analysis revealed that each electrode contained ~4 at% sodium.

XPS was used to independently verify the final composition of sodiated electrodes. A dense germanium electrode was sodiated to 5 mV *vs.* Na/Na^+ at a rate of C/10 and held at that voltage until the current decayed below C/100. The coin cell was disassembled in an argon environment and soaked overnight in DMC to remove any

lithium salt from the electrode surface. The electrode was then transferred to XPS using a vacuum transfer arm to avoid exposure to atmosphere. Ar^+ sputtering was used to remove SEI from the surface of the electrode, and the C 1s peak was used as a marker to determine the cleanliness of the surface. The intensity of the C 1s signal was attenuated below the noise threshold after 2 minutes of sputtering, indicating that the SEI had been completely removed. The F 1s signal, however, was not completely removed indicating residual fluorine contamination on the surface. The F 2s peak at 30 eV overlaps with the Ge 3d signal which extends from 29 – 33 eV due to the multiple valence states of germanium present in the sample. For this reason, the Ge 2p doublet was used to quantify the material composition, as was the Na 2s peak at 64 eV. Casa XPS analysis software was used to determine the stoichiometry of sample. Both experimentally derived and Kratos sensitivity factors were used. The material was found to be 54 at% sodium and 46 at% germanium. The XPS spectrum is shown in Figure E.4.

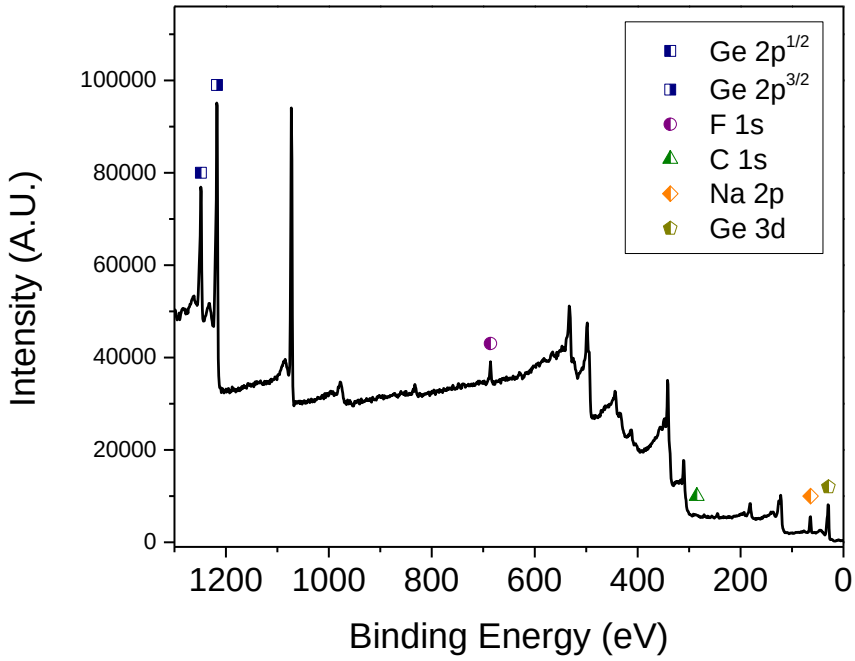

Figure E.4. XPS spectrum for a sodiated germanium electrode. Fearures relevant to the quantitative analysis are marked.

Figure E.5 shows C-rate tests of nanocolumnar germanium deposited at 70° and dense germanium deposited at 0°. While the specific capacity of the nanocolumnar film is stable for 50 cycles at rates up to 1C, the dense film begins to degrade after ~15 cycles. This degradation makes it difficult to determine how cycling rate affects the specific capacity of dense films.

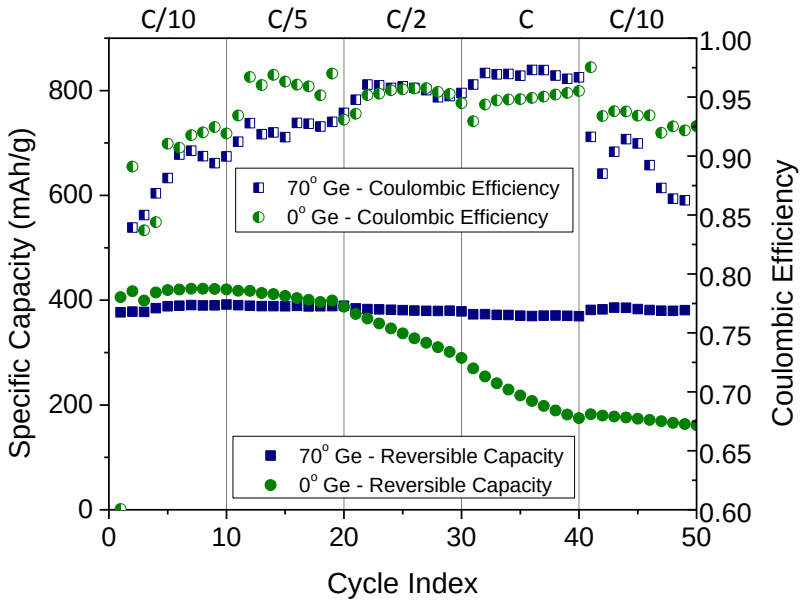

Figure E.5. C-Rate testing of dense and nanocolumnar germanium films deposited at 0° and 70°.

Appendix F: Supplemental Information for Tin-Germanium Alloys as Anode Materials for Sodium-Ion Batteries

A detailed view of the tin [200] and [101] x-ray diffraction peaks is shown in Figure F.1. The tin [200] peak is shown to shift from 30.685° for pure tin to 30.585° for $Ge_{0.5}Sn_{0.5}$. Additionally the width of the feature increases. The simultaneous decrease in diffraction angle and broadening of the feature indicate that the tin lattice becomes increasingly strained as the germanium content of the film is increased. The strain could either be caused by germanium being incorporated in the tin phase, or by interfacial strain at the tin phase boundary. If interfacial strain is the cause, the individual tin domains must be small in order for a large volume fraction of tin to experience strain.

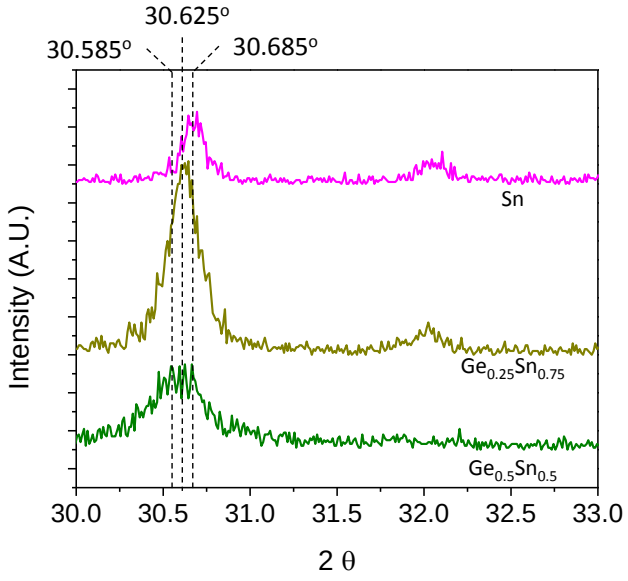

Figure F1. Detailed view of the tin [200] and [101] XRD features for Sn, $Ge_{0.25}Sn_{0.75}$ and $Ge_{0.5}Sn_{0.5}$ films.

Figure F.2 shows C-rate tests for all of the tin-germanium compositions. After a conditioning cycle at C/10, each cell is cycled for 10 cycles each at 1C, 2C, 5C, and 10C followed by 10 cycles back at 1C to see how the material recovers. The voltage profiles for each material at each C-rate are shown in Figure F.3.

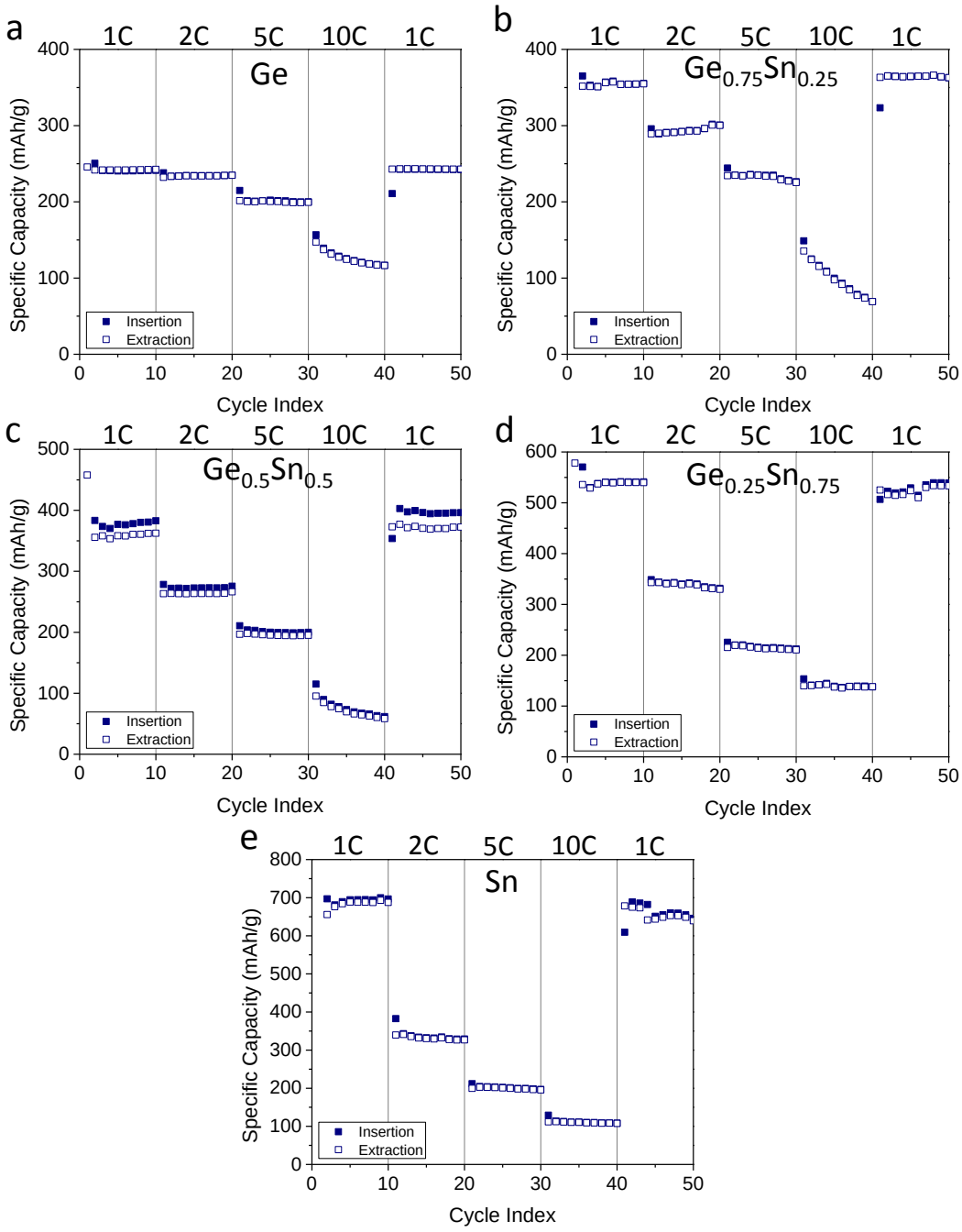

Figure F.2. C-rate tests for a) Ge, b) $Ge_{0.75}Sn_{0.25}$, c) $Ge_{0.5}Sn_{0.5}$, d) $Ge_{0.25}Sn_{0.75}$, and e) Sn. The cells are cycled for 10 cycles each at 1C, 2C, 5C, and 10C followed by 10 cycles back at 1C to see how the cells recover.

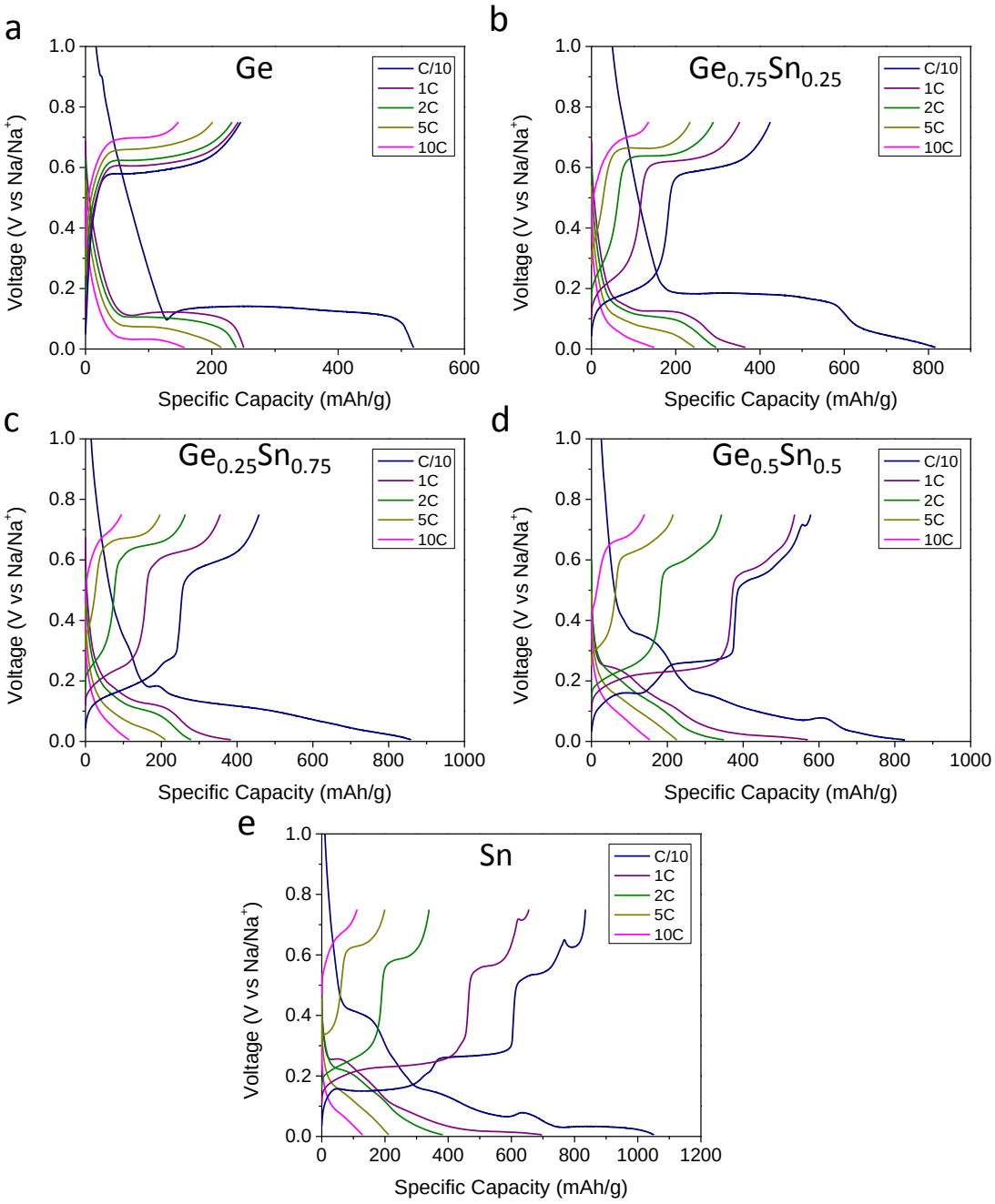

Figure F.3. Voltage profiles for a) Ge, b) $Ge_{0.75}Sn_{0.25}$, c) $Ge_{0.5}Sn_{0.5}$, d) $Ge_{0.25}Sn_{0.75}$, and e) Sn at rates ranging from C/10 to 10C.

Bibliography

Abel, P. R.; Lin, Y.-M.; Celio, H.; Heller, A.; Mullins, C. B., *ACS Nano* **2012,** *6*, 2506-2516.

Abel, P. R.; Chockla, A. M.; Lin, Y.-M.; Holmberg, V. C.; Harris, J. T.; Korgel, B. A.; Heller, A.; Mullins, C. B., *ACS Nano* **2013,** *7*, 2249-2257.

Abel, P. R.; Lin, Y.-M.; de Souza, T.; Chou, C.-Y.; Gupta, A.; Goodenough, J. B.; Hwang, G. S.; Heller, A.; Mullins, C. B., *J. Phys. Chem. C* **2013,** *117*, 18885-18890.

Abel, P. R.; Klavetter, K. C.; Heller, A.; Mullins, C. B., *J. Phys. Chem. C* **2014**. Accepted

Abelmann, L.; Lodder, C., *Thin Solid Films* **1997,** *305*, 1-21.

Ainger, F. W., *J. of Mater. Sci.* **1966,** *1*, 1-13.

Alcántara, R.; Jiménez-Mateos, J. M.; Lavela, P.; Tirado, J. L., *Electrochem. Commun.* **2001,** *3*, 639-642.

Allcorn, E.; Manthiram, A., *ACS Appl. Mater. Interfaces* **2014**.

Arico, A. S.; Bruce, P.; Scrosati, B.; Tarascon, J.-M.; van Schalkwijk, W., *Nat Mater* **2005,** *4*, 366-377.

Atabaev, I.; Matchanov, N.; Bakhranov, É., *Phys. Solid State* **2001,** *43*, 2234-2236.

Aurbach, D.; Gamolsky, K.; Markovsky, B.; Gofer, Y.; Schmidt, M.; Heider, U., *Electrochim. Acta* **2002,** *47*, 1423-1439.

Baggetto, L.; Notten, P. H. L., *J. Electrochem. Soc.* **2009,** *156*, A169-A175.

Baggetto, L.; Unocic, R. R.; Dudney, N. J.; Veith, G. M., *J. Power Sources* **2012,** *211*, 108-118.

Baggetto, L.; Allcorn, E.; Unocic, R. R.; Manthiram, A.; Veith, G. M., *J. Mater. Chem., A* **2013,** *1*, 11163-11169.

Baggetto, L.; Keum, J. K.; Browning, J. F.; Veith, G. M., *Electrochem. Commun.* **2013,** *34*, 41-44.

Balema, V. P., **2007,** *Materials Matters*, 16.

Barpanda, P.; Ye, T.; Nishimura, S.-I.; Chung, S.-C.; Yamada, Y.; Okubo, M.; Zhou, H.; Yamada, A., *Electrochem. Commun.* **2012,** *24*, 116-119.

Bazin, L.; Mitra, S.; Taberna, P. L.; Poizot, P.; Gressier, M.; Menu, M. J.; Barnabé, A.; Simon, P.; Tarascon, J. M., *J. Power Sources* **2009,** *188*, 578-582.

Beattie, S. D.; Hatchard, T.; Bonakdarpour, A.; Hewitt, K. C.; Dahn, J. R., *J. Electrochem. Soc.* **2003,** *150*, A701-A705.

Beattie, S. D.; Larcher, D.; Morcrette, M.; Simon, B.; Tarascon, J.-M., *J. Electrochem. Soc.* **2008,** *155*, A158-A163.

Beattie, S. D.; Larcher, D.; Morcrette, M.; Simon, B.; Tarascon, J. M., *J. Electrochem. Soc.* **2008,** *155*, A158-A163.

Berglund, S. P.; Flaherty, D. W.; Hahn, N. T.; Bard, A. J.; Mullins, C. B., *J. Phys. Chem. C* **2011,** *115*, 3794-3802.

Berglund, S. P.; Flaherty, D. W.; Hahn, N. T.; Bard, A. J.; Mullins, C. B., *J. Phys. Chem. C* **2011,** *115*, 3794-3802.

Berglund, S. P.; Rettie, A. J. E.; Hoang, S.; Mullins, C. B., *Phys. Chem. Chem. Phys.* **2012,** *14*, 7065-7075.

Blöchl, P. E., *Phys. Rev. B* **1994,** *50*, 17953-17979.

Braunstein, R.; Moore, A. R.; Herman, F., *Phys. Rev.* **1958,** *109*, 695-710.

Bruce, P. G.; Scrosati, B.; Tarascon, J.-M., *Angew. Chem. Int. Ed.* **2008,** *47*, 2930-2946.

Cabana, J.; Monconduit, L.; Larcher, D.; Palacín, M. R., *Adv. Mater.* **2010,** *22*, E170-E192.

Cao, Y.; Xiao, L.; Sushko, M. L.; Wang, W.; Schwenzer, B.; Xiao, J.; Nie, Z.; Saraf, L. V.; Yang, Z.; Liu, J., *Nano Lett.* **2012,** *12*, 3783-3787.

Champion, Y.; Langlois, C.; Guérin-Mailly, S.; Langlois, P.; Bonnentien, J.-L.; Hÿtch, M. J., *Science* **2003,** *300*, 310-311.

Chan, C. K.; Zhang, X. F.; Cui, Y., *Nano Lett.* **2007,** *8*, 307-309.

Chan, C. K.; Peng, H.; Liu, G.; McIlwrath, K.; Zhang, X. F.; Huggins, R. A.; Cui, Y., *Nat. Nanotechnol.* **2008,** *3*, 31-35.

Chan, C. K.; Patel, R. N.; O'Connell, M. J.; Korgel, B. A.; Cui, Y., *ACS Nano* **2010,** *4*, 1443-1450.

Chen, H.; Xiao, Y.; Wang, L.; Yang, Y., *J. Power Sources 196*, 6657-6662.

Chen, H.; Dong, Z.; Fu, Y.; Yang, Y., *J. Solid State Electrochem.* **2010,** *14*, 1829-1834.

Chen, L.; Wang, K.; Xie, X.; Xie, J., *J. Power Sources* **2007,** *174*, 538-543.

Chevrier, V. L.; Ceder, G., *J. Electrochem. Soc.* **2011,** *158*, A1011-A1014.

Cho, Y. J.; Im, H. S.; Kim, H. S.; Myung, Y.; Back, S. H.; Lim, Y. R.; Jung, C. S.; Jang, D. M.; Park, J.; Cha, E. H.*, et al.*, *ACS Nano* **2013,** *7*, 9075-9084.

Cho, Y. J.; Im, H. S.; Myung, Y.; Kim, C. H.; Kim, H. S.; Back, S. H.; Lim, Y. R.; Jung, C. S.; Jang, D. M.; Park, J.*, et al.*, *Chem. Commun.* **2013,** *49*, 4661-4663.

Cho, Y. J.; Kim, C. H.; Im, H. S.; Myung, Y.; Kim, H. S.; Back, S. H.; Lim, Y. R.; Jung, C. S.; Jang, D. M.; Park, J.*, et al.*, *Phys. Chem. Chem. Phys.* **2013,** *15*, 11691-11695.

Chockla, A. M.; Bogart, T. D.; Hessel, C. M.; Klavetter, K. C.; Mullins, C. B.; Korgel, B. A., *J. Phys. Chem. C* **2012,** *116*, 18079-18086.

Chockla, A. M.; Klavetter, K.; Mullins, C. B.; Korgel, B. A., *Chem. Mater.* **2012**.

Chockla, A. M.; Klavetter, K. C.; Mullins, C. B.; Korgel, B. A., *ACS Appl. Mater. Interfaces* **2012,** *4*, 4658-4664.

Chockla, A. M.; Panthani, M. G.; Holmberg, V. C.; Hessel, C. M.; Reid, D. K.; Bogart, T. D.; Harris, J. T.; Mullins, C. B.; Korgel, B. A., *J. Phys. Chem. C* **2012,** *116*, 11917-11923.

Choi, J. W.; McDonough, J.; Jeong, S.; Yoo, J. S.; Chan, C. K.; Cui, Y., *Nano Lett. 10*, 1409-1413.

Chou, C.-Y.; Hwang, G. S., *Surf. Sci.* **2013,** *612*, 16-23.

Conwell, E. M., *Proc. IRE* **1952,** *40*, 1327-1337.

Courtney, I. A.; McKinnon, W. R.; Dahn, J. R., *J. Electrochem. Soc.* **1999,** *146*, 59-68.

Darwiche, A.; Marino, C.; Sougrati, M. T.; Fraisse, B.; Stievano, L.; Monconduit, L., *J. Am. Chem. Soc.* **2012,** *134*, 20805-20811.

Datta, M. K.; Epur, R.; Saha, P.; Kadakia, K.; Park, S. K.; Kumta, P. N., *J. Power Sources* **2013,** *225*, 316-322.

Derrien, G.; Hassoun, J.; Panero, S.; Scrosati, B., *Adv. Mater.* **2007,** *19*, 2336-2340.

Dimov, N.; Kugino, S.; Yoshio, M., *Electrochim. Acta* **2003,** *48*, 1579-1587.

Dohnálek, Z.; Kimmel, G. A.; McCready, D. E.; Young, J. S.; Dohnálková, A.; Smith, R. S.; Kay, B. D., *J. Phys. Chem. B* **2002,** *106*, 3526-3529.

Ellis, B. L.; Nazar, L. F., *Curr. Opin. Solid State Mater. Sci.* **2012,** *16*, 168-177.

Ellis, L. D.; Hatchard, T. D.; Obrovac, M. N., *J. Electrochem. Soc.* **2012,** *159*, A1801-A1805.

Etacheri, V.; Haik, O.; Goffer, Y.; Roberts, G. A.; Stefan, I. C.; Fasching, R.; Aurbach, D., *Langmuir* **2011,** *28*, 965-976.

Ewald, A. W.; Tufte, O. N., *J. Phys. Chem. Solids* **1959,** *8*, 523-525.

Fan, S.; Lim, L. Y.; Tay, Y. Y.; Pramana, S. S.; Rui, X.; Samani, M. K.; Yan, Q.; Tay, B. K.; Toney, M. F.; Hng, H. H., *J. Mater. Chem. A* **2013,** *1*, 14577-14585.

Farbod, B.; Cui, K.; Kalisvaart, W. P.; Kupsta, M.; Zahiri, B.; Kohandehghan, A.; Lotfabad, E. M.; Li, Z.; Luber, E. J.; Mitlin, D., *ACS Nano* **2014**.

Flaherty, D. W.; Dohnálek, Z.; Dohnálková, A.; Arey, B. W.; McCready, D. E.; Ponnusamy, N.; Mullins, C. B.; Kay, B. D., *J. Phys. Chem. C* **2007,** *111*, 4765-4773.

Flaherty, D. W.; Dohnálek, Z.; Dohnálková, A.; Arey, B. W.; McCready, D. E.; Ponnusamy, N.; Mullins, C. B.; Kay, B. D., *J. Phys. Chem. C* **2007,** *111*, 4765-4773.

Flaherty, D. W.; Hahn, N. T.; Ferrer, D.; Engstrom, T. R.; Tanaka, P. L.; Mullins, C. B., *J. Phys. Chem. C* **2009,** *113*, 12742-12752.

Flaherty, D. W.; May, R. A.; Berglund, S. P.; Stevenson, K. J.; Mullins, C. B., *Chem. Mater.* **2009,** *22*, 319-329.

Flaherty, D. W.; Hahn, N. T.; May, R. A.; Berglund, S. P.; Lin, Y.-M.; Stevenson, K. J.; Dohnalek, Z.; Kay, B. D.; Mullins, C. B., *Acc. Chem. Res.* **2011**.

Flaherty, D. W.; Hahn, N. T.; May, R. A.; Berglund, S. P.; Lin, Y.-M.; Stevenson, K. J.; Dohnalek, Z.; Kay, B. D.; Mullins, C. B., *Acc. Chem. Res.* **2012,** *45*, 434–443.

Fleischauer, M. D.; Li, J.; Brett, M. J., *J. Electrochem. Soc.* **2009,** *156*, A33-A36.

Fuller, C. S.; Severiens, J. C., *Phys. Rev.* **1954,** *96*, 21-24.

Gao, B.; Sinha, S.; Fleming, L.; Zhou, O., *Adv. Mater.* **2001,** *13*, 816-819.

Goodenough, J. B.; Kim, Y., *Chem. Mater.* **2009,** *22*, 587-603.

Graetz, J.; Ahn, C. C.; Yazami, R.; Fultz, B., *J. Electrochem. Soc.* **2004,** *151*, A698-A702.

Gu, M.; Kushima, A.; Shao, Y.; Zhang, J.-G.; Liu, J.; Browning, N. D.; Li, J.; Wang, C., *Nano Lett.* **2013,** *13*, 5203-5211.

Hahn, N. T.; Mullins, C. B., *Chem. Mater.* **2010,** *22*, 6474-6482.

Hahn, N. T.; Ye, H.; Flaherty, D. W.; Bard, A. J.; Mullins, C. B., *ACS Nano* **2010,** *4*, 1977-1986.

Hall, L. A., *Survey of Electrical Resistivity Measurements on 16 Pure Metals in the Temperature Range 0 to 273 K*. U.S. Dept. of Commerce, National Bureau of Standards: Washington, D.C., 1968; p 111 p.

Hariharan, S.; Saravanan, K.; Balaya, P., *Electrochem. Solid-State Lett.* **2010,** *13*, A132-A134.

Hashimoto, Y.; Machida, N.; Shigematsu, T., *Solid State Ionics* **2004,** *175*, 177-180.

Hatchard, T. D.; Dahn, J. R., *J. Electrochem. Soc.* **2004,** *151*, A838-A842.

Hawkeye, M. M.; Brett, M. J., *J. Vac. Sci. Technol., A* **2007,** *25*, 1317-1335.

Heller, A.; Tai, K. L.; Vadimsky, R. G. Photoinduced Migration of Silver into Chalcogenide Layer. US 4,276,368, June 30, 1981, 1981.

Hieu, N. S.; Lim, J. C.; Lee, J. K., *Microelectron. Eng.* **2011**.

Hu, Y.-S.; Demir-Cakan, R.; Titirici, M.-M.; Mueller, J.-O.; Schloegl, R.; Antonietti, M.; Maier, J., *Angew. Chem., Int. Ed.* **2008,** *47*, 1645-1649.

Huang, H.; Kelder, E. M.; Schoonman, J., *J. Power Sources* **2001,** *97–98*, 114-117.

Hwang, C.-M.; Lim, C.-H.; Park, J.-W., *Thin Solid Films* **2011,** *519*, 2332-2338.

Hwang, C.-M.; Park, J.-W., *Electrochim. Acta* **2011,** *56*, 6737-6747.

Ipser, H.; Gambino, M.; Schuster, W., *Monatsh Chem* **1982,** *113*, 389-398.

Islam, M. S.; Fisher, C. A. J., *Chem. Soc. Rev.* **2014,** *43*, 185-204.

Jeong, S.-K.; Inaba, M.; Mogi, R.; Iriyama, Y.; Abe, T.; Ogumi, Z., *Langmuir* **2001,** *17*, 8281-8286.

Jian, Z.; Zhao, L.; Pan, H.; Hu, Y.-S.; Li, H.; Chen, W.; Chen, L., *Electrochem. Commun.* **2012,** *14*, 86-89.

Johnson, Q.; Smith, G. S.; Wood, D., *Acta Crystallogr.* **1965,** *18*, 131-132.

Jow, T. R.; Shacklette, L. W.; Maxfield, M.; Vernick, D., *J. Electrochem. Soc.* **1987,** *134*, 1730-1733.

Jung, H.-G.; Myung, S.-T.; Yoon, C. S.; Son, S.-B.; Oh, K. H.; Amine, K.; Scrosati, B.; Sun, Y.-K., *Energy & Environmental Science* **2011,** *4*, 1345-1351.

Kasavajjula, U.; Wang, C.; Appleby, A. J., *J. Power Sources* **2007,** *163*, 1003-1039.

Kikkawa, S.; Miyai, T.; Koizumi, M., *Solid State Ionics* **1988,** *28–30, Part 1*, 743-746.

Kim, C.; Noh, M.; Choi, M.; Cho, J.; Park, B., *Chem. Mater.* **2005,** *17*, 3297-3301.

Kim, D.; Lee, E.; Slater, M.; Lu, W.; Rood, S.; Johnson, C. S., *Electrochem. Commun.* **2012,** *18*, 66-69.

Kim, H.-K.; Bak, S.-M.; Kim, K.-B., *Electrochem. Commun.* **2010,** *12*, 1768-1771.

Kim, H.; Seo, M.; Park, M.-H.; Cho, J., *Angew. Chem., Int. Ed.* **2010,** *49*, 2146-2149, S2146/1-S2146/4.

Kim, H.; Chou, C.-Y.; Ekerdt, J. G.; Hwang, G. S., *J. Phys. Chem. C* **2011,** *115*, 2514-2521.

Kim, J.-B.; Lee, H.-Y.; Lee, K.-S.; Lim, S.-H.; Lee, S.-M., *Electrochem. Commun.* **2003,** *5*, 544-548.

Kim, K.; Park, J.-H.; Doo, S.-G.; Kim, T., *Thin Solid Films* **2010,** *518*, 6547-6549.

Kim, Y.; Hwang, H.; Lawler, K.; Martin, S. W.; Cho, J., *Electrochim. Acta* **2008,** *53*, 5058-5064.

Klavetter, K. C.; Wood, S. M.; Lin, Y.-M.; Snider, J. L.; Davy, N. C.; Chockla, A. M.; Romanovicz, D. K.; Korgel, B. A.; Lee, J.-W.; Heller, A.*, et al.*, *J. Power Sources* **2013,** *238*, 123-136.

Kolodzey, J.; Coppinger, M.; Kim, S.; Bhargava, N.; Gupta, J.; Chaoying, N.; Yung Kee, Y. In *The Properties of Germanium-Tin Alloys for Infrared Device Applications*, Semiconductor Device Research Symposium (ISDRS), 2011 International, 7-9 Dec. 2011; 2011; pp 1-1.

Komaba, S.; Matsuura, Y.; Ishikawa, T.; Yabuuchi, N.; Murata, W.; Kuze, S., *Electrochem. Commun.* **2012,** *21*, 65-68.

Krause, K. M.; Thommes, M.; Brett, M. J., *Microporous and Mesoporous Materials* **2011,** *143*, 166-173.

Kresse, G.; Hafner, J., *Physical Review B* **1993,** *47*, 558-561.

Kresse, G.; Furthmüller, J., *Comput. Mater. Sci.* **1996,** *6*, 15-50.

Kresse, G.; Furthmüller, J., *Physical Review B* **1996,** *54*, 11169-11186.

Kromer, M. A.; Heywood, J. B. *Electric Powertrains: Opportunities and*

Challenges in the U.S. Light-Duty Vehicle Fleet Massachusetts Institute of Technology: Sloan Automotive Laboratory, 2007.

Laforge, B.; Levan-Jodin, L.; Salot, R.; Billard, A., *J. Electrochem. Soc.* **2008,** *155*, A181-A188.

Landi, B. J.; Ganter, M. J.; Cress, C. D.; DiLeo, R. A.; Raffaelle, R. P., *Energy & Environmental Science* **2009,** *2*, 638-654.

Lee, H.; Kim, M. G.; Choi, C. H.; Sun, Y.-K.; Yoon, C. S.; Cho, J., *J. Phys. Chem. B* **2005,** *109*, 20719-20723.

Lee, H.; Kim, Y.-I.; Park, J.-K.; Choi, J. W., *Chem. Commun.* **2012,** *48*, 8416-8418.

Lee, S.; Bondi, R. J.; Hwang, G. S., *Phys.Rev. B* **2011,** *84*, 045202.

Levinshtein, M. E. R., Sergey L.; Shur, Michael S., *Properties of Advanced Semiconductor Materials: GaN, AlN, InN,NB,SiC, SiGe*. John Wiley and Sons: New York, 2001.

Li, H.; Huang, X.; Chen, L.; Zhou, G.; Zhang, Z.; Yu, D.; Jun Mo, Y.; Pei, N., *Solid State Ionics* **2000,** *135*, 181-191.

Li, H.; Shi, L.; Lu, W.; Huang, X.; Chen, L., *J. Electrochem. Soc.* **2001,** *148*, A915-A922.

Liang, W.; Yang, H.; Fan, F.; Liu, Y.; Liu, X. H.; Huang, J. Y.; Zhu, T.; Zhang, S., *ACS Nano* **2013,** *7*, 3427-3433.

Lim, S. Y.; Kim, H.; Shakoor, R. A.; Jung, Y.; Choi, J. W., *J. Electrochem. Soc.* **2012,** *159*, A1393-A1397.

Lin, Y.-M.; Abel, P. R.; Gupta, A.; Goodenough, J. B.; Heller, A.; Mullins, C. B., ACS Appl. Mater. Interfaces 2013, 5, 8273-8277.

Lin, Y.-M.; Abel, P. R.; Flaherty, D. W.; Wu, J.; Stevenson, K. J.; Heller, A.; Mullins, C. B., *J. Phys. Chem. C* **2011,** *115*, 2585-2591.

Lin, Y.-M.; Abel, P. R.; Heller, A.; Mullins, C. B., *J. Phys. Chem. Lett.* **2011,** *2*, 2885-2891.

Lin, Y.-M.; Klavetter, K. C.; Abel, P. R.; Davy, N. C.; Snider, J. L.; Heller, A.; Mullins, C. B., *Chem. Commun.* **2012,** *48*, 7268-7270.

Lin, Y.-M.; Klavetter, K. C.; Heller, A.; Mullins, C. B., *J. Phys. Chem. Lett.* **2013,** *4*, 999-1004.

Liu, X. H.; Huang, S.; Picraux, S. T.; Li, J.; Zhu, T.; Huang, J. Y., *Nano Lett.* **2011,** *11*, 3991-3997.

Liu, Y.; Xu, Y.; Han, X.; Pellegrinelli, C.; Zhu, Y.; Zhu, H.; Wan, J.; Chung, A. C.; Vaaland, O.; Wang, C.*, et al.*, *Nano Lett.* **2012,** *12*, 5664-5668.

Lu, X.; Xia, G.; Lemmon, J. P.; Yang, Z., *J. Power Sources* **2010,** *195*, 2431-2442.

Lu, X.; Li, G.; Kim, J. Y.; Lemmon, J. P.; Sprenkle, V. L.; Yang, Z., *J. Power Sources* **2012,** *215*, 288-295.

Lu, Y.; Wang, L.; Cheng, J.; Goodenough, J. B., *Chem. Commun.* **2012,** *48*, 6544-6546.

Magasinski, A.; Dixon, P.; Hertzberg, B.; Kvit, A.; Ayala, J.; Yushin, G., *Nat. Mater.* **2010,** *9*, 353-358.

Manthiram, A., *J. Phys. Chem. Lett.* **2011,** *2*, 176-184.

Maranchi, J. P.; Hepp, A. F.; Kumta, P. N., *Electrochem. Solid-State Lett.* **2003,** *6*, A198-A201.

Maranchi, J. P.; Hepp, A. F.; Evans, A. G.; Nuhfer, N. T.; Kumta, P. N., *J. Electrochem. Soc.* **2006,** *153*, A1246-A1253.

Marchese, D.; De Sario, M.; Jha, A.; Kar, A. K.; Smith, E. C., *J. Opt. Soc. Am. B* **1998,** *15*, 2361-2370.

Maruyama, T.; Akagi, H., *J. Electrochem. Soc.* **1998,** *145*, 1303-1305.

McDowell, M. T.; Lee, S. W.; Ryu, I.; Wu, H.; Nix, W. D.; Choi, J. W.; Cui, Y., *Nano Lett.* **2011**, 4018–4025.

Michel-Lledos, V.; Pradel, A.; Ribes, M., *Eur. J. Solid State Inorg. Chem.* **1992,** *29*, 301-310.

Mizushima, K.; Jones, P. C.; Wiseman, P. J.; Goodenough, J. B., *Mater. Res. Bull.* **1980,** *15*, 783-789.

Monkhorst, H. J.; Pack, J. D., *Phys. Rev. B* **1976,** *13*, 5188-5192.

Moreau, P.; Guyomard, D.; Gaubicher, J.; Boucher, F., *Chem. Mater.* **2010,** *22*, 4126-4128.

Morita, T.; Takami, N., *J. Electrochem. Soc.* **2006,** *153*, A425-A430.

Nakai, H.; Kubota, T.; Kita, A.; Kawashima, A., *J. Electrochem. Soc.* **2011,** *158*, A798-A801.

Nakaiz, H.; Kubota, T.; Kita, A.; Kawashima, A., *J. Electrochem. Soc.* **2011,** *158*, A798-A801.

Ning, G.; Haran, B.; Popov, B. N., *J. Power Sources* **2003,** *117*, 160-169.

Noh, M.; Kwon, Y.; Lee, H.; Cho, J.; Kim, Y.; Kim, M. G., *Chem. Mater.* **2005,** *17*, 1926-1929.

Obrovac, M. N.; Christensen, L., *Electrochem. Solid-State Lett.* **2004,** *7*, A93-A96.

Okubo, M.; Hosono, E.; Kim, J.; Enomoto, M.; Kojima, N.; Kudo, T.; Zhou, H.; Honma, I., *J. Am. Chem. Soc.* **2007,** *129*, 7444-7452.

Olesinski, R. W.; Abbaschian, G. J., *Bulletin of Alloy Phase Diagrams* **1984,** *5*, 265-271.

Ong, E.; Tai, K. L.; Vadimsky, R. G.; Kemmerer, C. T., *Proc. SPIE-Int. Soc. Opt. Eng.* **1983,** *394*, 39-48.

Padhi, A. K.; Nanjundaswamy, K. S.; Goodenough, J. B., *J. Electrochem. Soc.* **1997,** *144*, 1188-1194.

Park, C.-M.; Choi, W.; Hwa, Y.; Kim, J.-H.; Jeong, G.; Sohn, H.-J., *J. Mater. Chem.* **2010,** *20*, 4854-4860.

Park, M.-H.; Cho, Y.; Kim, K.; Kim, J.; Liu, M.; Cho, J., *Angew. Chem. Int. Ed.* **2011,** *50*, 9647-9650.

Peña, J. S.; Sandu, I.; Joubert, O.; Pascual, F. S.; Areán, C. O.; Brousse, T., *Electrochem. Solid-State Lett.* **2004,** *7*, A278-A281.

Poizot, P.; Laruelle, S.; Grugeon, S.; Dupont, L.; Tarascon, J. M., *Nature* **2000,** *407*, 496-499.

Predel, B., Ge-S (Germanium-Sulfur). In *Ga-Gd – Hf-Zr*, Madelung, O., Ed. Springer Berlin Heidelberg: 1996; Vol. 5f, pp 1-2.

Price, D. L.; Ellison, A. J. G., *J. Non-Cryst. Solids* **1994,** *177*, 293-298.

Qian, J.; Chen, Y.; Wu, L.; Cao, Y.; Ai, X.; Yang, H., *Chem. Commun.* **2012,** *48*, 7070-7072.

Rasband, W. S. *ImageJ*, U. S. National Institutes of Health: Bethesda, Maryland, USA, http://imagej.nih.gov/ij/, 1997-2014.

Robbie, K.; Sit, J. C.; Brett, M. J., *J. Vac. Sci. Technol., B* **1998,** *16*, 1115-1122.

Rowsell, J. L. C.; Pralong, V.; Nazar, L. F., *J. Am. Chem. Soc.* **2001,** *123*, 8598-8599.

Ryu, J. H.; Kim, J. W.; Sung, Y.-E.; Oh, S. M., *Electrochem. Solid-State Lett.* **2004,** *7*, A306-A309.

Scrosati, B., *J. Electrochem. Soc.* **1992,** *139*, 2776-2781.

Seng, K. H.; Park, M.-H.; Guo, Z. P.; Liu, H. K.; Cho, J., *Angew. Chem. Int. Ed.* **2012,** *51*, 5657-5661.

Seo, M.-H.; Park, M.; Lee, K. T.; Kim, K.; Kim, J.; Cho, J., *Energy & Environmental Science* **2011,** *4*, 425-428.

Sharma, S. K.; Jain, S. C.; Aggarwal, S. S.; Bhide, V. G., *J. Non-Cryst. Solids* **1972,** *7*, 285-294.

Shodai, T.; Okada, S.; Tobishima, S.-i.; Yamaki, J.-i., *Solid State Ionics* **1996,** *86–88, Part 2*, 785-789.

Song, T.; Cheng, H.; Choi, H.; Lee, J.-H.; Han, H.; Lee, D. H.; Yoo, D. S.; Kwon, M.-S.; Choi, J.-M.; Doo, S. G.*, et al.*, *ACS Nano* **2012,** *6*, 303-309.

Souquet, J., *Solid State Ionics* **1981,** *3-4*, 317-321.

St. John, M. R.; Furgala, A. J.; Sammells, A. F., *J. Electrochem. Soc.* **1982,** *129*, 246-50.

Stevens, D. A.; Dahn, J. R., *J. Electrochem. Soc.* **2001,** *148*, A803-A811.

Stojić, M.; Kostić, D.; Stošić, B., *Physica B + C* **1986,** *138*, 125-128.

Sudworth, J. L., *J. Power Sources* **1994,** *51*, 105-114.

Sun, Q.; Ren, Q.-Q.; Fu, Z.-W., *Electrochem. Commun.* **2012,** *23*, 145-148.

Suryanarayana, C., *Prog. Mater Sci.* **2001,** *46*, 1-184.

Tai, K. L.; Vadimsky, R. G.; Kemmerer, C. T.; Wagner, J. S.; Lamberti, V. E.; Timko, A. G., *J. Vac. Sci. Technol.* **1980,** *17*, 1169-76.

Takami, N.; Satoh, A.; Hara, M.; Ohsaki, T., *J. Electrochem. Soc.* **1995,** *142*, 371-379.

Tamura, K.; Fukushima, J.; Endo, H.; Minomura, S.; Shimomura, O.; Asaumi, K., *J. Phys. Soc. Jpn.* **1974,** *36*, 558-564.

Tarascon, J. M.; Armand, M., *Nature* **2001,** *414*, 359-367.

Temkin, R. J.; Connell, G. A. N.; Paul, W., *Solid State Commun.* **1972,** *11*, 1591-1595.

Thorne, J. S.; Dunlap, R. A.; Obrovac, M. N., *Electrochim. Acta* **2013,** *112*, 133-137.

U. S. Geological Mineral Commodity Summaries 2013. Survey, U. S. G., Ed. U.S. Geological Survey: 2013.

Venkatesan, T., *J. Vac. Sci. Technol.* **1981,** *19*, 1368-73.

Wagner, A.; Barr, D.; Venkatesan, T.; Crane, W. S.; Lamberti, V. E.; Tai, K. L.; Vadimsky, R. G., *J. Vac. Sci. Technol.* **1981,** *19*, 1363-7.

Wang, J.; Zhao, H.; He, J.; Wang, C.; Wang, J., *J. Power Sources* **2011,** *196*, 4811-4815.

Wang, J.; Du, N.; Zhang, H.; Yu, J.; Yang, D., *J. Power Sources* **2012,** *208*, 434-439.

Wang, X.-L.; Han, W.-Q.; Chen, H.; Bai, J.; Tyson, T. A.; Yu, X.-Q.; Wang, X.-J.; Yang, X.-Q., *J. Am. Chem. Soc. 133*, 20692-20695.

Wang, Y.-X.; Lim, Y.-G.; Park, M.-S.; Chou, S.-L.; Kim, J. H.; Liu, H.-K.; Dou, S.-X.; Kim, Y.-J., *J. Mater. Chem. A* **2014,** *2*, 529-534.

Wen, C. J.; Huggins, R. A., *J. Solid State Chem.* **1981,** *37*, 271-278.

Wen, Z.; Hu, Y.; Wu, X.; Han, J.; Gu, Z., *Adv. Funct. Mater.* **2012,** *23*, 1005–1018.

Wenzel, S.; Hara, T.; Janek, J.; Adelhelm, P., *Energy & Environmental Science* **2011,** *4*, 3342-3345.

Weppner, W.; Huggins, R. A., *Annu. Rev. Mater. Sci.* **1978,** *8*, 269-311.

Wessells, C. D.; Peddada, S. V.; Huggins, R. A.; Cui, Y., *Nano Lett.* **2011,** *11*, 5421-5425.

Wessells, C. D.; McDowell, M. T.; Peddada, S. V.; Pasta, M.; Huggins, R. A.; Cui, Y., *ACS Nano* **2012,** *6*, 1688-1694.

Winter, M.; Besenhard, J. O., *Electrochim. Acta* **1999,** *45*, 31-50.

Witte, J.; Schnering, H. G.; Klemm, W., *Z. Anorg. Allg. Chem.* **1964,** *327*, 260-273.

Wu, B.; Heidelberg, A.; Boland, J. J., *Nat. Mater.* **2005,** *4*, 525-529.

Wu, J.; Zhu, Z.; Zhang, H.; Fu, H.; Li, H.; Wang, A.; Zhang, H.; Hu, Z., *J. Alloys Compd.* **2014,** *596*, 86-91.

Wu, L.; Hu, X.; Qian, J.; Pei, F.; Wu, F.; Mao, R.; Ai, X.; Yang, H.; Cao, Y., *Journal of Materials Chemistry A* **2013,** *1*, 7181-7184.

Xia, X.; Dahn, J. R., *Electrochem. Solid-State Lett.* **2012,** *15*, A1-A4.

Xiao, L.; Cao, Y.; Xiao, J.; Wang, W.; Kovarik, L.; Nie, Z.; Liu, J., *Chem. Commun.* **2012,** *48*, 3321-3323.

Xu, W.; Vegunta, S. S. S.; Flake, J. C., *J. Power Sources* **2011,** *196*, 8583-8589.

Xu, Y.; Zhu, Y.; Liu, Y.; Wang, C., *Adv. Energy Mater.* **2013,** *3*, 128-133.

Xun, S.; Song, X.; Grass, M. E.; Roseguo, D. K.; Liu, Z.; Battaglia, V. S.; Liu, G., *Electrochem. Solid-State Lett.* **2011,** *14*, A61-A63.

Yamaki, J.-i.; Tobishima, S.-i.; Hayashi, K.; Keiichi, S.; Nemoto, Y.; Arakawa, M., *Journal of Power Sources* **1998,** *74*, 219-227.

Yamamoto, T.; Nohira, T.; Hagiwara, R.; Fukunaga, A.; Sakai, S.; Nitta, K.; Inazawa, S., *J. Power Sources* **2012,** *217*, 479-484.

Yang, J.; Takeda, Y.; Imanishi, N.; Capiglia, C.; Xie, J. Y.; Yamamoto, O., *Solid State Ionics* **2002,** *152-153*, 125-129.

Yao, Y.; McDowell, M. T.; Ryu, I.; Wu, H.; Liu, N.; Hu, L.; Nix, W. D.; Cui, Y., *Nano Lett.* **2011,** *11*, 2949-2954.

Yazami, R.; Touzain, P., *J. Power Sources* **1983,** *9*, 365-371.

Yoo, H.; Lee, J.-I.; Kim, H.; Lee, J.-P.; Cho, J.; Park, S., *Nano Lett. 11*, 4324-4328.

Yu, B.-C.; Hwa, Y.; Kim, J.-H.; Sohn, H.-J., *J. Power Sources* **2014,** *260*, 174-179.

Yu, H. T.; Loka, C.; Lee, K.-S.; Cho, J. S.; Lee, S. H., *Mater. Sci. Eng., B* **2013,** *178*, 1422-1428.

Zaghib, K.; Brochu, F.; Guerfi, A.; Kinoshita, K., *J. Power Sources* **2001,** *103*, 140-146.

Zhang, X.; Kostecki, R.; Richardson, T. J.; Pugh, J. K.; Ross, P. N., *J. Electrochem. Soc.* **2001,** *148*, A1341-A1345.

Zhilinskaya, E. A.; Valeev, N. K.; Oblasov, A. K., *J. Non-Cryst. Solids* **1992,** *146*, 285-293.

Zhong, C.; Wang, J.; Chen, Z.; Liu, H., *J. Phys. Chem. C* **2011,** *115*, 25115-25120.

Zhou, S.; Liu, X.; Wang, D., *Nano Lett.* **2010,** *10*, 860-863.

Zu, C.-X.; Li, H., *Energy & Environmental Science* **2011,** *4*, 2614-2624.

Vita

Paul Abel graduated from Aloha High school in 2004. Paul then attended the Massachusetts Institute of Technology where he conducted undergraduate research under Professor William Green, studying the role of organic radicals in combustion chemistry. Paul graduated with a B.S. in chemical engineering in 2008.

Paul then enrolled in the chemical engineering Ph.D. program at The University of Texas at Austin where he worked with Professor C. Buddie Mullins. He was awarded the Thrust 2000 - Harry P. Whitworth Endowed Graduate Fellowship in Engineering in 2008, and the Hertz Foundation Fellowship in 2009.

Email Address: paulx.abel@gmail.com

This dissertation was typed by the author.